Aston University

If you have discovered material in AURA which is unlawful e.g. breaches copyright, (either yours or that of a third party) or any other law, including but not limited to those relating to patent, trademark, confidentiality, data protection, obscenity, defamation, libel, then please read our Takedown Policy and contact the service immediately

Exploitation of Fibre Characteristics in Temperature Sensing and Radio-over-Fibre Applications

PEI CHIN WON

Doctor of Philosophy

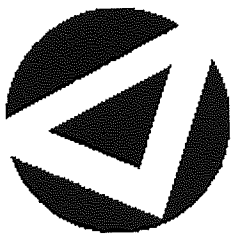

ASTON UNIVERSITY

September 2005

ASTON UNIVERSITY

Exploitation of Fibre Characteristics in Temperature Sensing and Radio-over-Fibre Applications

PEI CHIN WON

Doctor of Philosophy, 2005

Thesis Summary

The development of sensing devices is one of the instrumentation fields that has grown rapidly in the last decade. Corresponding to the swift advance in the development of micro-electronic sensors, optical fibre sensors are widely investigated because of their advantageous properties over the electronics sensors such as their wavelength multiplexing capability and high sensitivity to temperature, pressure, strain, vibration and acoustic emission. Moreover, optical fibre sensors are more attractive than the electronics sensors as they can perform distributed sensing, in terms of covering a reasonably large area using a single piece of fibre. Apart from being a responsive element in the sensing field, optical fibre possesses good assets in generating, distributing, processing and transmitting signals in the future broadband information network. These assets include wide bandwidth, high capacity and low loss that grant mobility and flexibility for wireless access systems. Among these core technologies, the fibre optic signal processing and transmission of optical and radio frequency signals have been the subjects of study in this thesis.

Based on the intrinsic properties of single-mode optical fibre, this thesis aims to exploit the fibre characteristics such as thermal sensitivity, birefringence, dispersion and nonlinearity, in the applications of temperature sensing and radio-over-fibre systems. By exploiting the fibre thermal sensitivity, a fully distributed temperature sensing system consisting of an apodised chirped fibre Bragg grating has been implemented. The proposed system has proven to be efficient in characterising grating and providing the information of temperature variation, location and width of the heat source applied in the area under test.

To exploit the fibre birefringence, a fibre delay line filter using a single high-birefringence optical fibre structure has been presented. The proposed filter can be reconfigured and programmed by adjusting the input azimuth of launched light, as well as the strength and direction of the applied coupling, to meet the requirements of signal processing for different purposes in microwave photonic and optical filtering applications.

To exploit the fibre dispersion and nonlinearity, experimental investigations have been carried out to study their joint effect in high power double-sideband and single-sideband modulated links with the presence of fibre loss. The experimental results have been theoretically verified based on the in-house implementation of the split-step Fourier method applied to the generalised nonlinear Schrödinger equation. Further simulation study on the inter-modulation distortion in two-tone signal transmission has also been presented so as to show the effect of nonlinearity of one channel on the other.

In addition to the experimental work, numerical simulations have also been carried out in all the proposed systems, to ensure that all the aspects concerned are comprehensively investigated.

Keywords: fibre gratings, temperature sensing, delay line filter, radio-over-fibre, fibre nonlinearity

To my parents, sisters and friends.

Acknowledgements

First and foremost I am grateful to my supervisor Dr John Williams for his patience, understanding, sparkling discussions and thorough explanations he gave me whenever I needed them.

Being a member of Photonics Research Group, I profited a lot from the discussions during the years I was at Aston University. With this regard, special thanks are dedicated to Dr Wei Zhang, Dr Yicheng Lai and Dr Jinsong Leng, whom I have spent time doing experiments with.

I would like to express my appreciation to Mr Bert Biggs for his assistance in the lab.

My sincere acknowledgement also goes to my fellow colleagues in the group, especially Amós Martinez, Jovana Petrovic, Zahariah Zakaria, Helen Dobb, Tim Ellingham, Xianfeng Chen, Dr Youfang Hu and Irina Nasieva.

I would also like to thank Dr Tom Allsop, Dr Nayot Kurukitkoson, Dr Juan Diego Ania-Castañón, Dr Zhijian Huang and Dr Vladimir Mezentsev for their external assistance in the fields of sensing and optical communications.

My deepest gratitude also goes to all my friends in Aston University who make my stay in Birmingham a beautiful and fruitful one.

For the remote and indispensable spiritual support, I thank my family and my friends in Malaysia and Singapore, without whom the completion of this thesis would have been much harder.

Contents

List of Figures

List of Tables

Chapter 1

Introduction

The field of measurement and instrumentation, and particularly sensor development, is one of those that has expanded rapidly in the last decade. The need for high quality sensors to be integrated into sophisticated measurements and control systems is clear as they provide high resolution and high accuracy. In parallel with the rapid advance in the development of sensors based on microelectronics, those sensors based on optical techniques have also expanded drastically. They are widely investigated because of their advantageous properties over the conventional sensors, such as their multiplexing capability using wavelength, i.e. the ability to string a set of sensors in one length of fibre, and their high sensitivity to the disturbance of temperature, pressure, strain, vibration and acoustic emission. However, they remain at the prototype stage in the laboratory and only have resulted few real commercial successes due to the proven reliability record and low manufacturing cost of conventional electro-mechanical sensors. Nevertheless, optical fibre sensors do offer new capabilities, such as distributed sensing, which have distinct advantages over the competition [1].

Another field of interest that has witnessed intense research in the recent years is the millimetre-wave/microwave photonic technology. The amount of information dealt with and required each day has been rapidly increasing. The broadband wireless network systems have become a promising candidate to support this trend because they offer mobility, relocatability and cost effective installation [2]. Towards wide coverage and low cost implementation of this network, integration of millimetre-wave/microwave photonic technology is inevitable. This technology overcomes the difficulties faced by the conventional wireless technologies, such as bandwidth and capacity limitations [3].

For these reasons, this thesis focuses in exploiting the transmission characteristics of optical fibre, a transmission medium with enormous potential bandwidth, light weight, small diameter, low transmission loss, immunity to electromagnetic interference (EMI) and crosstalk,

non-conductivity, signal security, ruggedness, flexibility, system reliability and ease of maintenance [4,5]. Particularly, the thermal sensitivity, birefringence, dispersion and nonlinearity of optical fibre are exploited in three challenges, which are distributed temperature sensing, microwave and optical signals filtering and radio-over-fibre, respectively.

1.1 Challenges

1.1.1 Distributed Temperature Sensing

Optical fibre distributed temperature monitoring is significantly attractive in several situations, such as, when electrical temperature monitoring is impractical or unsafe, when there is no prior knowledge of sensor placement and when there are a large number of sensors to be placed. As most of the applications need efficient, fast and accurate temperature monitoring over the area under test, fibre-optic intracore Bragg gratings functioning as mirrors with wavelength-selective reflectivities have emerged as a promising candidate in distributed temperature sensing.

The key issue of these fibre Bragg grating (FBG) sensors is the high resolution detection of the Bragg wavelength shift due to the temperature change onto the grating. In most of the FBG temperature sensing schemes, the typical value of temperature sensitivity of fibre is about 10 pm/K at 1550 nm [6], which means that a change of 100 K in temperature causes an 1-nm shift of Bragg wavelength near the 1550 nm region. This inevitably limits the resolution of a FBG sensor for measuring temperature change if a conventional optical spectrum analyser with typical resolution 0.06–0.1 nm is used to detect the wavelength shift. This implies that a FBG sensor, which uses an optical spectrum analyser with a wavelength resolution of 0.1 nm as a demodulation system, can not evaluate the temperature change within 10 K [7] if the direct wavelength shift method is used.

Many reports have been presented with different FBG structures and numerical models. However, some of them are limited for point sensing, whilst those which are able to provide distributed sensing are only suitable for monotonically increasing or decreasing disturbance profiles with fairly large gradients. Thus, apart from designing a distributed sensing element based on the thermal sensitivity of optical fibre, there is paramount interest to build up an interrogation system that can provide an accurate information about the non-monotonic temperature change over the area under test.

1.1.2 Microwave and Optical Signals Filtering

Fibre based microwave photonic signal processors have stimulated the interest among researchers for decades. These devices are attractive due to the inherent advantages of optical fibres such as light weight, small diameter, low cost, low transmission loss and immunity to electromagnetic interference (EMI) and crosstalk. Optical filters, in particular, are of interest due to the fact that they offer the capability of processing microwave signals in the optical domain and therefore, have the compatibility with radio-over-fibre systems [8]. Needless to say that they are competent in processing optical signals. Thus, while single-mode optical fibre has been widely used in the sensing and communication systems, it is used in configurations for microwave and optical signals filtering.

The most common objectives for the design of the optical filter include low loss, reconfigurable transfer characteristics, wide operation bandwidth and good isolation. A number of filters and signal processing structures have been reported [8–10]. Many of them use the combinations of optical fibre delay line to realise the various signal processing function [11]. In principle, a delay line structure that involves coherent addition of the tapped signals is of interest because it realises negative taps that is able to produce more complex transfer functions. However, much care from environmental disturbance is required. Coherent detection with less isolation from environmental perturbation is always the challenge in the design of optical fibre delay line filter. Thus, the photonic processing of radio and optical signals using a fibre based filter remains of considerable research interest.

1.1.3 Radio-over-Fibre

The introduction of new multimedia services in the residential and business environments requires a broadband that can bear with the access network. Nevertheless, the growing demand in narrowband services in the actual radio systems has reduced the possibilities of lodging in the radioelectric spectrum that demanded by the great capacity of wireless broadband systems. To overcome this limitation, the utilisation of radio link at frequencies of 1–100GHz is being considered for the applications in micro/picocellular broadband systems, fixed point-to-multipoint distribution system and local wireless area network. In fact, only a few of the bands around 60 GHz have been assigned for future broadband service provision. For instance, 62–63 GHz and 65-66 GHz bands have been identified by the European Radiocommunications Office for mobile broadband applications [12].

The main candidate to permit these broadband services is, indisputably, the optical fibre, which has an enormous bandwidth of about 4 THz for the 1550 nm wavelength region which also beneficial from the effective use of erbium doped fibre amplifier (EDFA) [13–15]. The

complexity of radio-over-fibre link can then be simplified by sharing the transmitting and receiving devices of millimetre/microwave or RF frequencies between different channels at the central station by using the subcarrier multiplexing technique. On top of that, the base stations can even be more simplified because the need for electro-opto and opto-electro signal conversion at each base station can be omitted. The only possible disadvantage is the cost of the efficient transmitter and broadband photodetector. Due to the trade-off between the bandwidth and responsivity of a photodetector [16] and the high demand in the signal multiplexing systems, as frequencies increase (e.g. to > 60 GHz for micro-cellular applications), there is a need to increase the optical power in the fibre link to maintain an adequate signal-to-noise performance at the receiver [17, 18]. This usually involves the use of an optical amplifier, such as an EDFA in order to reach the desired optical power.

Consequently, optical fibres in telecommunication systems now carry more channels as well as with higher optical powers than ever before. Systems are operating at a high optical power that increases the power density of fibre, and henceforth excels the nonlinear properties of the optical fibre. An optical channel will then affect the signal propagation in its own channel as well as in other channels through the fibre leading to nonlinear effects. Thus, nonlinear effects have become much more crucial since the development of the optical fibre amplifier. These amplifiers can boost the power in a number of channels at different wavelengths simultaneously rather than having a separate repeater for each channel. This allows many more channels to be multiplexed into a single fibre than was economically viable with optoelectronics repeaters. Although the individual power in each channel may be below that needed to produce nonlinearities, the combination of high total optical power and a large number of channels at closely spaced wavelengths is ideal for many kinds of nonlinear effects, such as self-phase modulation, cross-phase modulation, stimulated Brillouin scattering, stimulated Raman scattering, four-wave mixing and intermodulation distortion.

In spite of the fibre nonlinearity being often regarded as a problem, it may also be useful in a variety of applications. All these nonlinear processes have been studied in detail in the context of optical digital system. One of the useful and beautiful phenomena is the creation of soliton in optical pulse propagation [19]. Nevertheless, minor attention has been given to the analogue communication systems. Furthermore, most of these studies have focused on analysing mainly on the degradation produced by these nonlinear effects without analysing their potential applications when they interplay with the fibre dispersion, an undesired fibre characteristic in low power transmission. Therefore, the joint effect of fibre dispersion and fibre nonlinearity emerges as an important field of research in the area of radio-over-fibre system.

1.2 Objectives of the Thesis

The objectives of the thesis are:

1 To exploit the thermal sensitivity of optical fibre through the in-fibre structure, which is fibre Bragg grating, in distributed temperature sensing system

2 To exploit the birefringence of optical fibre in microwave/millimetre-wave as well as optical signals filtering systems

3 To exploit the joint effect of fibre dispersion and fibre nonlinearity in radio-over-fibre system

1.3 Thesis Outline

This thesis aims to exploit the fibre characteristics, which are the thermal sensitivity, birefringence, dispersion and nonlinearity of fibre, in the applications of temperature sensing and radio-over-fibre systems.

Chapter 2 gives a brief introduction to the transmission characteristics of optical fibre, starting from the very fundamental but yet vital information on materials, losses and birefringence, to its essential properties in radio-over-fibre transmission, which are fibre dispersion and fibre nonlinearities.

Since fibre Bragg gratings are used in most of the experiments carried out in this thesis, Chapter 3 seeks to introduce the fibre Bragg grating technology, in which its working principle, fabrication techniques and spectra measurement arrangement are highlighted. Brief introductions to the coupled-mode theory and transfer matrix method used to simulate the responses of fibre Bragg gratings are also included. Various types of gratings are presented and their roles as temperature sensing element, sideband filter and dispersion compensator in this thesis are highlighted.

Chapter 4 describes the exploitation of fibre thermal sensitivity by introducing an apodised chirped fibre Bragg grating based temperature sensor. The proposed sensing system whose working principle is based on the Fabry-Perot effect induced by the internal wavelength shift is presented. Two synthesis models based on the coupled-mode theory and implemented by the transfer matrix method are described in detail. A brief introduction to the algorithm used for the synthesis models is also given. The experimental results are presented together with the simulated results from the proposed synthesis models. Detailed discussions on the repeatability, capability of measuring multiple heated regions, factors that affect the algorithm speed, ripple problem and coverage are also included.

Chapter 5 seeks to exploit the birefringent characteristic of fibre by presenting a fibre delay line filter on the use of a single length of segmented high-birefringence optical fibre structure. This proposed coherent system is able to provide bipolar tap signals that allow more complex transfer function and flattop bandpass response. Due to the nature of the fibre, it is stable from environmental disturbance. A simulation model based on the proposed segmented structure is detailed. Experimental and simulated results in microwave and optical signals filtering responses are superimposed.

Chapter 6 relates to the exploitation of the joint effect of fibre dispersion and fibre nonlinearity in radio-over-fibre transmission links. Fibre dispersion induced modulation suppression and fibre nonlinearities are not welcome. However, the joint effect between them gives interesting and remarkable responses in transmission link. This chapter experimentally demonstrates the joint effect between the fibre dispersion and fibre nonlinearity with the presence of fibre loss and the results are theoretically verified based on the in-house implementation of split-step Fourier method applied to the generalised nonlinear Schrödinger equation. The effect with the inclusion of fibre gratings based dispersion compensator is also incorporated in the investigations. Further study on the intermodulation distortion in two-tone signals transmission is also carried out in order to investigate the influence of the joint effect from one channel to the others.

Lastly, Chapter 7 concludes the exploitation of fibre characteristics in three aspects. Some steps are also recommended for the future work in order to improve the proposed systems.

Chapter 2

Transmission Characteristics of Optical Fibres

2.1 Introduction

Sensing and communication technologies using an optical wave guided along a length of glass fibre have a number of extremely attractive properties over conventional methods. Advantages provided by optical fibre include light weight, small diameter, low cost, low transmission loss, immunity to electromagnetic interference (EMI) and crosstalk, enormous potential bandwidth, higher capacity, non-conductivity, signal security, ruggedness, flexibility, system reliability and ease of maintenance [4, 5, 20].

There are three basic types of fibre used in sensing and communication systems, which are step-index single-mode fibre, step-index multi-mode fibre and graded-index fibre. Step-index fibre has an index of refraction profile that steps from high to low measured from core to cladding whilst refractive index of graded-index fibre decreases parabolically from the core centre towards the cladding. Multi-mode fibre has larger core diameter than single-mode fibre and it allows multiple modes or paths to propagate through the fibre. Multi-mode graded-index fibre, on the other hand, has a lower intermodal dispersion than step-index multi-mode fibre [4, 5].

Step-index multi-mode fibre is used in applications that require bandwidth of <1 GHz over relatively short distance (<3 km) such as a local area network or a campus network backbone. Single-mode step-index fibre allows only one mode or path for light to travel within the fibre. It is used in applications that need low signal loss and high data rates. Owing to the single-mode fibre not suffering modal dispersion as in multi-mode fibre, it can provide long haul high bandwidth transmission. For this reason, it is more commonly used

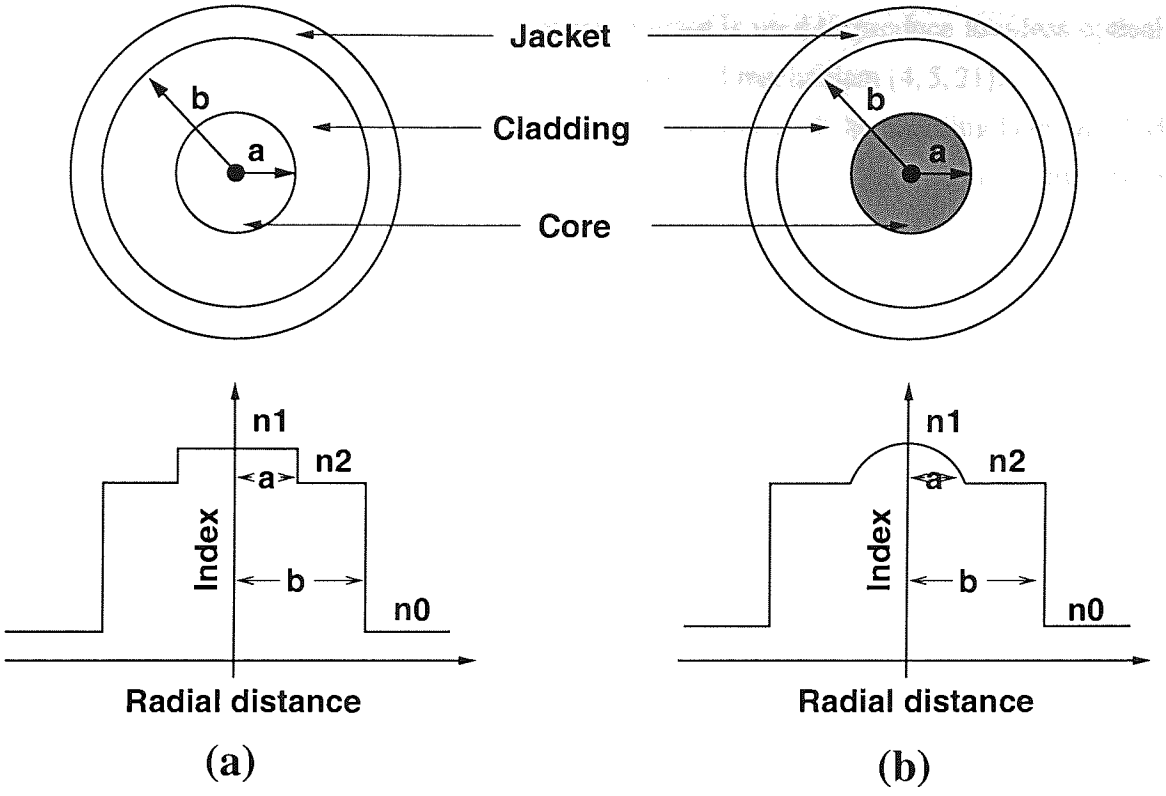

Figure 2.1: Schematic diagram of the cross sections and refractive index profiles of (a) step-index and (b) graded-index fibres.

in long distance communication systems [4].

In order to give a basic review about single-mode fibre as a sensing element and transmission medium in optical communication systems, the principal transmission characteristics that influence the performance of fibre such as its materials, losses, birefringence and dispersion are introduced in this chapter. Modulation suppression in radio-over-fibre links due to the fibre chromatic dispersion will also be highlighted. As nonlinear phenomena have become more important within the development of low loss single-mode fibre as a transmission medium in radio-over-fibre links, effects induced by fibre nonlinearities are discussed. These nonlinear effects include stimulated Brillouin scattering, stimulated Raman scattering, self-phase modulation, cross-phase modulation and four-wave mixing.

2.2 Materials

An optical fibre is composed of a dielectric core with relatively small diameter compared with the cladding layer that surrounds it. Figure 2.1 illustrates the schematic diagram of the cross sections and refractive index profiles of step-index and graded-index fibres [5]. Typical single-mode fibre used in the current communication systems has a core diameter a of 9 μm

and a cladding diameter b of 125 μm. Pure silica glass is used to produce low-loss optical fibres through the drawing process using a precision-feed mechanism [4, 5, 21].

In order to form a guiding waveguide, the refractive index of the cladding layer, n_2, has to be slightly lower than the refractive index of the core, n_1. This refractive index difference can be achieved by the selective use of dopants during the fabrication process. GeO_2 and P_2O_5 are usually used to increase the refractive index of the core whilst materials such as boron and fluorine are used for the cladding. Additional dopants can be used for specific applications, for example, Erbium (Er^{3+}) and Erbium/Ytterbium (Er/Yb) are added in the core of fibre to make fibre amplifier and fibre laser [22, 23].

It is worth noting that the refractive index of glass depends on the density of the material. When there is a change in the volume through thermally induced relaxation of the glass, there will be a change in the refractive index n as

$$\frac{\Delta n}{n} \approx \frac{\Delta V}{V} \approx \frac{3n}{2}\varepsilon, \tag{2.1}$$

where the fractional change ε in linear dimension of glass is proportional to the ratio of volumetric change ΔV and original volume V [24]. Equation (2.1) indicates that refractive index changes when fibre is exposed to disturbances like temperature, strain, bending and so on.

2.3 Fibre Losses

The measure of power loss during transmission of optical signals inside the fibre is a significant limiting factor in lightwave communication systems because it decreases the signal power reaching the receiver. To recover the signal accurately, a certain minimum amount of power above the noise level in an optical receiver is imperative.

Thus, the transmission link distance is always constrained by the fibre losses. However, as the loss has been reduced to only 0.2 dB/km near the 1.55 μm region, optical fibre is still the prevailing medium in the field of long link transmission technology compared to the coaxial cable which has about 1000 dB/km of loss.

If P_0 is the initial power launched at the input of a fibre of length L, the transmitted power P_T is defined as

$$P_T = P_0 \exp(-\alpha L), \tag{2.2}$$

where the attenuation constant α is a measure of total fibre losses from all sources, for instance, material absorption, Rayleigh scattering, imperfections at the core-cladding interface

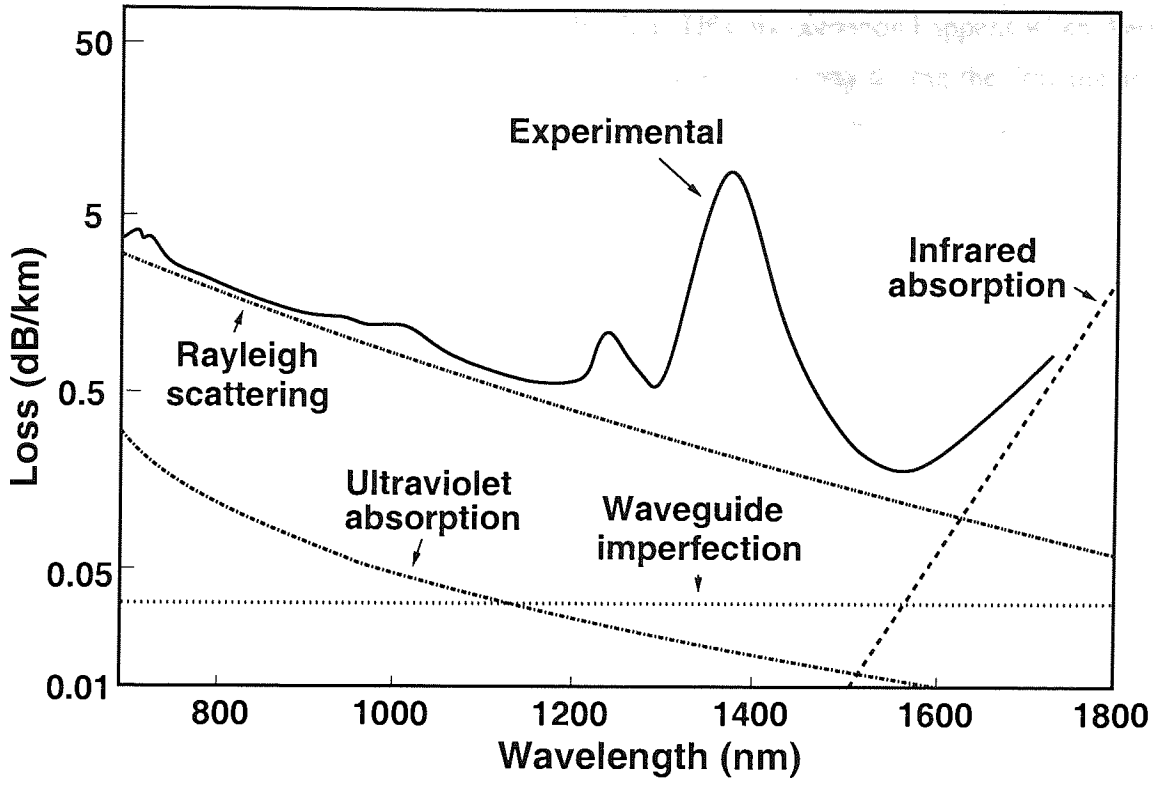

Figure 2.2: Schematic diagram of the loss spectrum of a single-mode fibre.

and externally induced losses such as microbending [4, 5, 21]. It is also usual to express α in units of dB/km using the relation

$$\alpha_{dB} = -\frac{10}{L}\log_{10}\left(\frac{P_T}{P_0}\right), \tag{2.3}$$

and α_{dB} is always referred as the fibre-loss parameter.

Fibre losses are wavelength-dependent, as can be seen from the typical plot of loss spectrum $\alpha(\lambda)$ in figure 2.2 [4]. It shows that there is a local loss maximum around 1.39 μm and there are several smaller peaks. The primary minimum is found at the region of 1.55 μm with only a loss of 0.2 dB/km. This makes 1.55 μm the main operation band for current long distance fibre-optic communication systems. The secondary minimum occurs near 1.3 μm where the fibre loss is below 0.5 dB/km. This low-loss window was used for second-generation lightwave systems since the minimum fibre dispersion is found to be there.

2.4 Birefringence

Strictly speaking, a non-ideal single-mode fibre is not truly single mode due to the fact that it can transmit light in two polarisation modes. It means, in reality, light propagates in two

polarisation modes that are orthogonal to each other. This phenomenon happens when there exist random variations in core shape and stress induced anisotropy during the drawing and cabling processes. The break of mode degeneracy causes the injected light propagates in two polarisation modes with different phase velocity and produces a time delay between two polarisation components when they reach the receiver.

Consequently, there is a slight difference in mode propagation constant β between the modes polarised in x and y directions which is called modal birefringence and is defined as

$$B_m = \frac{|\beta_x - \beta_y|}{k_0} = |n_x - n_y|, \tag{2.4}$$

where k_0 is the wave propagation constant of vacuum, n_x and n_y are the modal refractive indices for the two orthogonally polarised states [21]. As light propagates along the fibre, the two modes exchange their powers in a periodic fashion with the period

$$L_B = \frac{2\pi}{|\beta_x - \beta_y|} = \frac{\lambda}{B_m}, \tag{2.5}$$

where L_B is the beat length. The axis with smaller refractive index is referred to as the fast axis, because light propagates faster in material with lower refractive index and vice versa.

Generally, random changes in polarisation mode are not welcome because it introduces polarisation-mode dispersion (PMD), a phenomenon when group velocities change randomly corresponding to random changes in fibre birefringence. While change of polarisation does not give impact to continuous-wave (CW) light because of the irresponsive of most of the photodetectors to polarisation changes, it is an important parameter for short pulse propagation in long haul transmission link which it may cause pulse broadening [21].

However, for some applications, high modal birefringence is desired and is maintained. Such polarisation maintaining (PM) fibres can be classified into two main groups, namely high-birefringence (Hi-Bi) and low-birefringence (Lo-Bi) fibres. Conventional fibres normally has birefringence of the order of 10^{-6} or 10^{-5} while an order of $> 10^{-5}$ is required for Hi-Bi fibres [25]. Hi-Bi fibres have been used in many applications such as the construction of delay line filters [26], birefringence induced fibre grating laser [27, 28] and polarimetric sensor [29, 30].

2.5 Dispersion

When analogue and digital optical signals are transmitted in optical fibre, elements such as numerical aperture, refractive index profile, laser linewidth, wavelength and core diameter cause them to disperse and distort [4]. This phenomenon is called dispersion and usually it

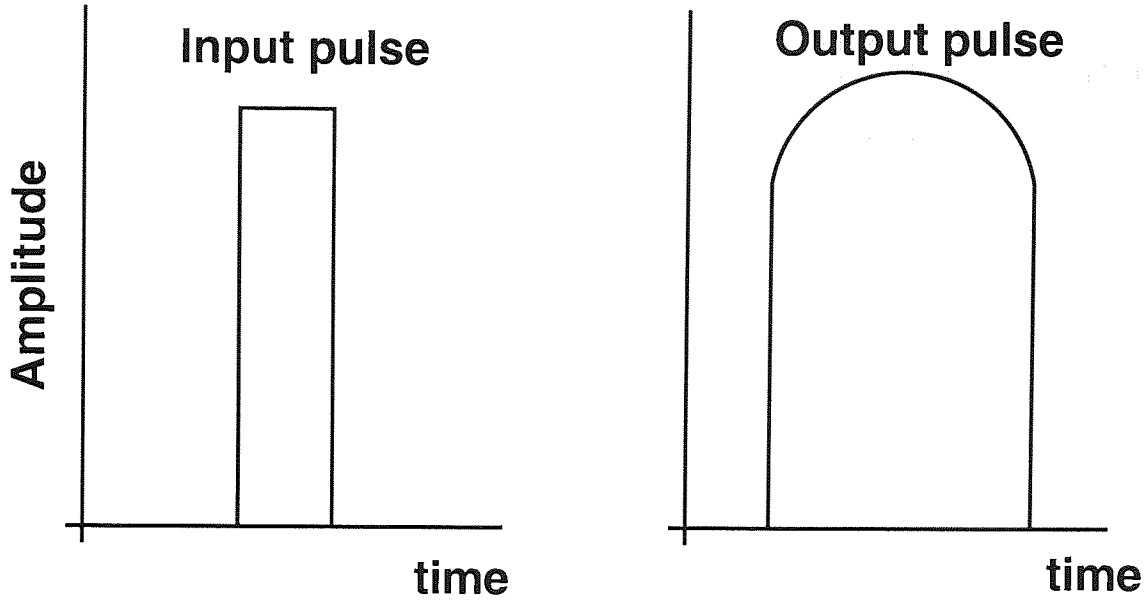

Figure 2.3: Schematic diagram of pulse broadening caused by dispersion in digital optical signal transmission.

is expressed in terms of the symbol D. It causes pulse broadening in digital optical signal transmission, as can be seen from figure 2.3, and poses limitations on the overall bandwidth of the fibre.

The effects of fibre dispersion are accounted for by expanding the mode propagation constant β in a Taylor series about the frequency ω_0 at which the spectrum is centered [21]:

$$\beta(\omega) = \beta_0 + \beta_1(\omega - \omega_0) + \frac{1}{2}\beta_2(\omega - \omega_0)^2 + \cdots, \tag{2.6}$$

where

$$\beta_m = \left(\frac{d^m\beta}{d\omega^m}\right)_{\omega=\omega_0} \qquad (m = 0, 1, 2, \ldots). \tag{2.7}$$

Parameters β_1 and β_2 are given as

$$\beta_1 = \frac{1}{v_g} = \frac{n_g}{c} = \frac{1}{c}\left(n + \omega\frac{dn}{d\omega}\right), \tag{2.8}$$

$$\beta_2 = \frac{1}{c}\left(2\frac{dn}{d\omega} + \omega\frac{d^2n}{d\omega^2}\right), \tag{2.9}$$

where n_g is the group index and v_g is the group velocity.

From equation (2.9), it clearly shows that β_2 represents the dispersion of the group velocity, a phenomenon which is known as group-velocity dispersion (GVD). β_2 is therefore always referred as the GVD parameter and is related to dispersion D, by the relation

$$D = -\frac{2\pi c}{\lambda^2}\beta_2, \tag{2.10}$$

where c is the velocity of light in vacuum and λ is the wavelength of light. Dispersion D is commonly used in fibre optic literature in place of β_2. β_3 is third-order-dispersion parameter and is only included when wavelength approaches zero-dispersion wavelength λ_D to within a few nanometres. λ_D is about 1310 nm for standard fibres. This will be discussed in the text later.

Generally, dispersion D can be divided into two classes, which are intermodal dispersion and intramodal dispersion or chromatic dispersion. Since intermodal dispersion is caused by the time delay between the lower modes and higher modes of rays propagating through the fibre which only happens in multi-mode fibre, it is not problematic in single-mode fibre, the fibre which only allows one mode to propagate and is used widely in optical communication systems.

Chromatic dispersion, which is often expressed in units of nanoseconds or picoseconds per kilometre per nanometre (ns/km/nm or ps/km/nm), can be resulted from material dispersion and waveguide dispersion. Material dispersion is caused by the dependency of refractive index of glass on the wavelength. It manifests through the frequency dependent refractive index $n(\omega)$ causing different wavelengths of light propagate at slightly different velocities through the fibre. Since the index of glass fibre is a wavelength-dependent quantity, all laser sources, laser or LED, bring chromatic dispersion to the system due to the fact that they have finite linewidth.

On the other hand, waveguide dispersion is due to the physical structure of the waveguide in which it can be expressed by

$$D_W = -\frac{2\pi\Delta}{\lambda^2}\left[\frac{n_{2g}^2}{n_2\omega}\frac{Vd^2(Vb)}{dV^2} + \frac{dn_{2g}}{d\omega}\frac{d(Vb)}{dV}\right], \tag{2.11}$$

where λ is the operating wavelength, Δ is the fractional index change at the core-cladding interface, n_{2g} is the group index of the cladding material, $\omega = 2\pi c/\lambda$, V is the normalised frequency and b is the normalised propagation constant. Since both derivatives in equation (2.11) are always positive [5], thus waveguide dispersion is usually negative for a given single-mode fibre in the wavelength range of $0.0 - 1.6$ μm.

The magnitude of waveguide dispersion increases with an increase in wavelength and changes with the core radius and difference in the core-cladding refractive index. For instance, if the core radius is made smaller and the value of Δ is made larger, the magnitude of the waveguide dispersion increases. Thus, waveguide dispersion can be tailored for specific requirements. Both components of chromatic dispersion can have opposite signs depending

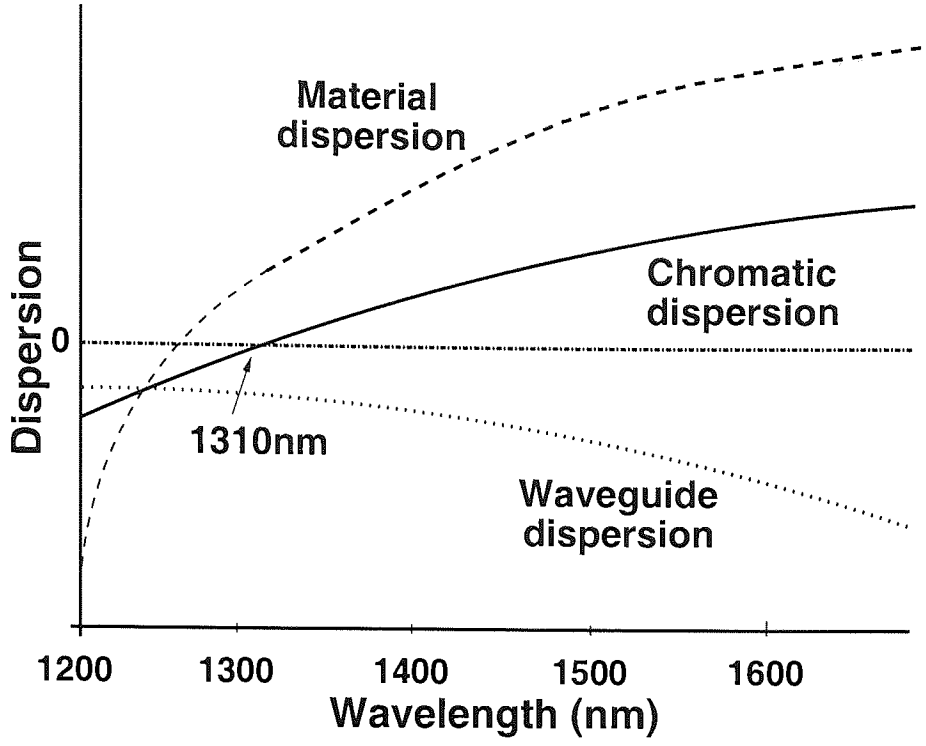

Figure 2.4: Schematic diagram of chromatic dispersion for standard fibre.

on the transmission wavelength. For standard step-index single-mode fibre, they cancel each other at 1310 nm producing zero-dispersion, as shown in figure 2.4. 1310 nm is therefore referred as zero-dispersion wavelength λ_D for standard fibre as discussed earlier.

As waveguide dispersion can be changed to meet specific applications, the zero-dispersion wavelength λ_D can be shifted to coincide with the 1550 nm transmission window where fibre loss is minimum, as shown in figure 2.5, to realise high-bandwidth long distance communication. This type of fibre is called zero-dispersion-shifted fibre. Physically, due to waveguide dispersion, longer wavelengths travel more slowly than shorter wavelengths. And due to material dispersion, longer wavelengths travel faster than shorter wavelengths. These two effects compensate for each other and produce zero total dispersion around 1550 nm. It is also possible to make nonzero-dispersion-shifted fibre where $D \approx 0$ is not at 1550 nm. Some other types of fibre such as dispersion-compensating fibre and dispersion-flattened fibre may also be made by changing the properties of waveguide dispersion [21].

Optical fibre gives different nonlinear effects corresponding to the sign of the GVD parameter, β_2. It exhibits normal dispersion as $\beta_2 > 0$ in the region of $\lambda < \lambda_D$ where high-frequency (blue-shifted) components of an optical pulse travel slower than low-frequency (red-shifted) components. On the contrary, anomalous dispersion $\beta_2 < 0$ occurs in the region of $\lambda > \lambda_D$ showing an opposite response. In this region, high-frequency components of

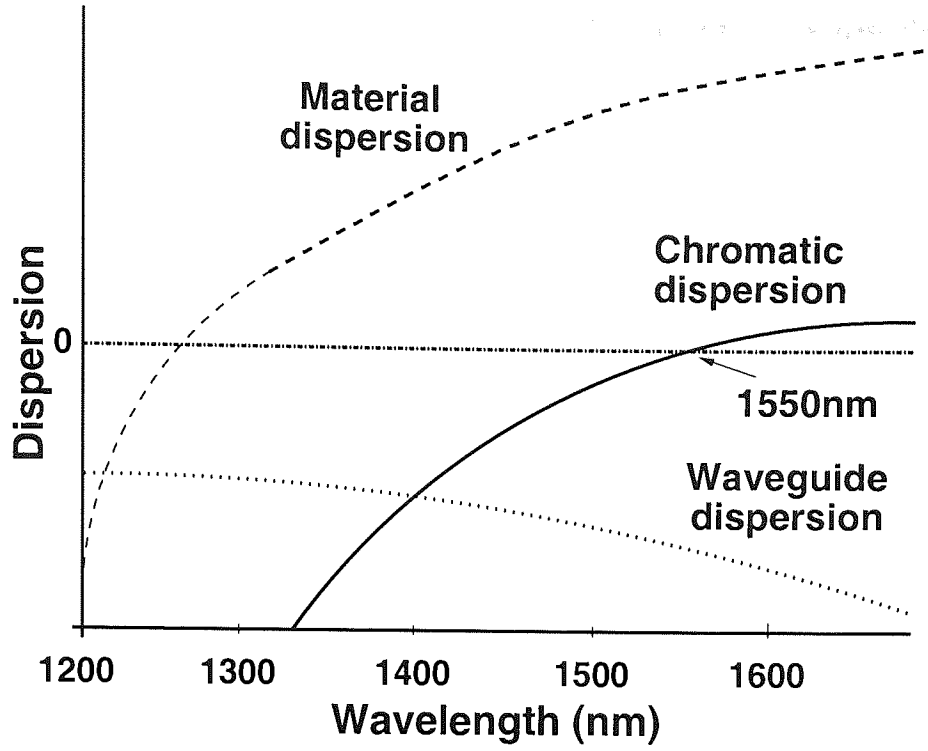

Figure 2.5: Schematic diagram of chromatic dispersion for dispersion-shifted fibre.

an optical pulse travel faster than low-frequency components. The anomalous dispersion is of interest in current optical communication systems because the combination of fibre dispersion and nonlinearity can result in a qualitatively different behaviour. The joint effect will be discussed in more detail in the later chapter.

2.5.1 Modulation Suppression Induced by Fibre Chromatic Dispersion in Radio-over-Fibre Link

In radio-over-fibre (RoF) link, when an optical carrier is intensity-modulated by a radio frequency signal, the two modulation sidebands and the optical carrier propagate with different velocities in the fibre due to the chromatic dispersion. In the photodetector, the modulation sidebands and the optical carrier are mixed, generating a heterodyne signal component at the modulation frequency. At certain modulation frequencies, the chromatic dispersion $\times$ length product causes the two modulation sidebands to be in counter phase thereby producing a zero in the amplitude of the signal from the photodetector [31].

The optical field coupled into the fibre under test by an amplitude modulation signal can be described with only two modulation sidebands, which is a good approximation for small modulation index values ($m < 0.5$). Neglecting the fibre loss, the propagation of the

modulated signal in the fibre as a function of time t, and distance z, can be described by the electrical field [32]

$$\vec{E}(t,z) = \vec{E}_0 \cdot [\cos(\omega_0 t - \beta_0 z) + \frac{m}{2}[\cos((\omega_0 + \omega_m)t - \beta_+ z) + \cos((\omega_0 - \omega_m)t - \beta_- z)]], \tag{2.12}$$

where ω_0 is the angular optical carrier frequency and the two last terms are the modulation sidebands at the frequencies $\pm\omega_m (= 2\pi f_m)$ relative to the optical carrier frequency. β_0, β_- and β_+ are the propagation constant at the respective frequencies.

Due to the change in the refractive index as a function of wavelength, the propagation constant is different for the two modulation sidebands as denoted by the subscript. The propagation constant, $\beta(\omega)$, is described by the Taylor expression

$$\beta(\omega) = \beta_0 + \beta_1(\omega - \omega_0) + \frac{1}{2}\beta_2(\omega - \omega_0)^2, \tag{2.13}$$

where the higher order dispersion terms are neglected. The optical signal propagates in the fibre with the group velocity of $1/\beta_1$ and the fibre dispersion D is related to the group velocity dispersion parameter β_2 by

$$D = -\frac{2\pi c \beta_2}{\lambda^2}, \tag{2.14}$$

where $\lambda = c/f_0$ is the wavelength of the laser source with c is the light speed in vacuum and f_0 is the frequency of the laser source.

After transmission in a fibre of length L, the current generated in the photo-detector is proportional to the intensity (the square of the electrical field). The electrical spectral RF component generated at the modulation frequency, $i_{\omega_m}(t)$, can be found from equation (2.12) and equation (2.14)

$$i_{\omega_m}(t) = i_0 \cdot m \cdot \cos(\frac{1}{2}\beta_2 L \omega_m^2) \cdot \cos(\omega_m t) \cdot e^{j\beta_1 L \omega_m}, \tag{2.15}$$

where i_0 is a constant proportional to the average optical power. The amplitude of the signal component in equation (2.15) varies as the cosine to an argument, which depends on the dispersion, the fibre length and the square of the modulation frequency. The amplitude is zero whenever the argument is equal to an odd number times $\pi/2$, which implies the intensity at frequency

$$f_m = f_0 \sqrt{\frac{N}{2LDc}}, \tag{2.16}$$

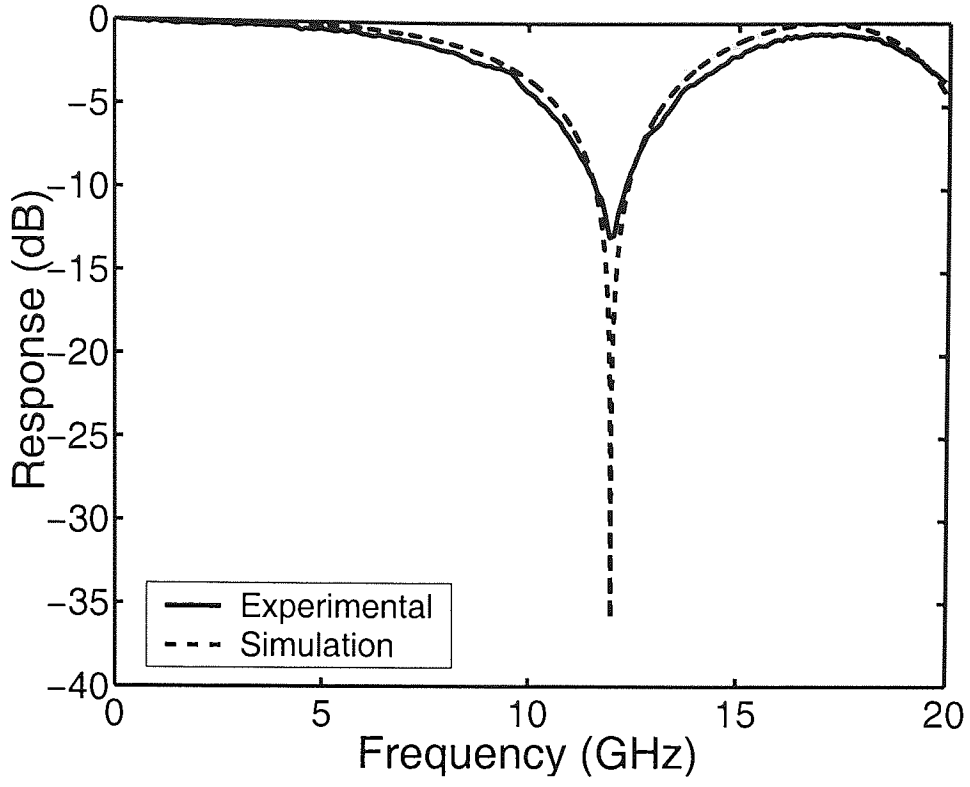

Figure 2.6: Measured and simulated frequency responses in 25 km of single-mode fibre.

vanishes with N=1, 3, 5, ...

The modulation suppression in the frequency transfer function of a 25-km of single-mode fibre is illustrated in figure 2.6. It shows that the f_m at the first dip is about 12.0 GHz with a measured strength of 12.8 dB. This clearly indicates that the performance of analogue signal transmission in single-mode fibre is severely limited by chromatic dispersion of standard single-mode fibre. Phase cancellation between the two modulation sidebands in double-sideband (DSB) modulated signal at the photodetector [32, 33] sharply limits the frequency-length product of fibre-optic links.

As can be seen from figure 2.6, there is, however, a clear discrepancy in the notch depth between the measured and simulated results. Further investigation has been done to investigate this discrepancy [34]. It claimed that the above-mentioned equations are based on the assumption that the two modulation sidebands have the same amplitude. With unequal amplitude of modulation sidebands input, the amplitude of the signal component in equation (2.15) varies as

$$\sqrt{p^2+q^2-2pq\cos\theta} \tag{2.17}$$

to the argument, where p and q is the amplitude of the two modulation sidebands and θ is

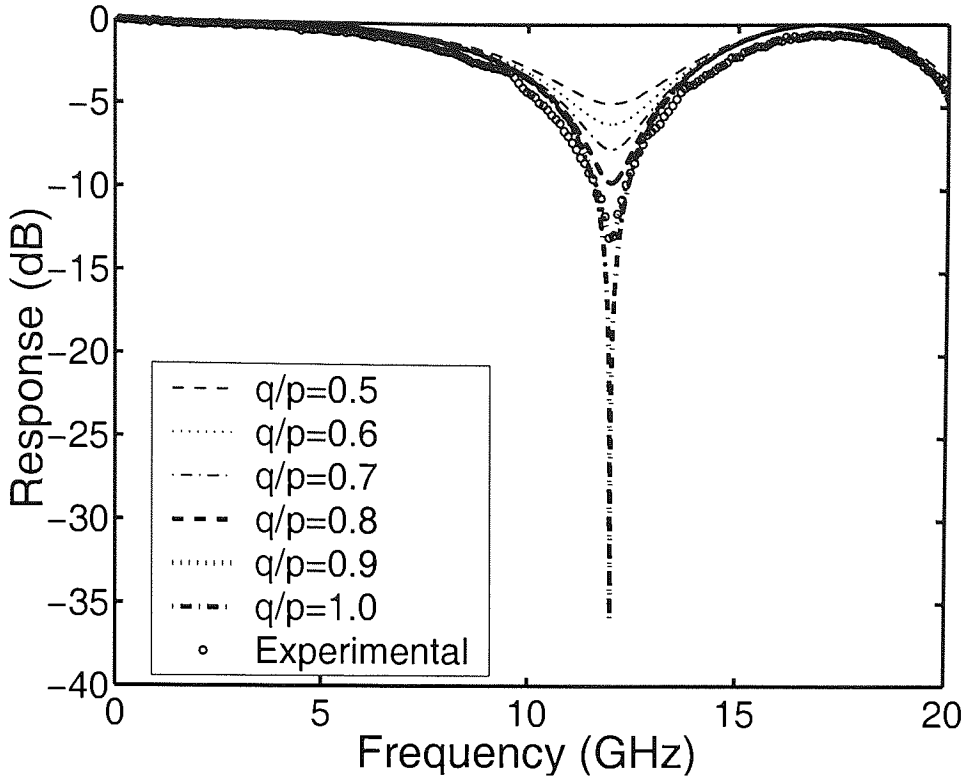

Figure 2.7: Simulated frequency responses in 25 km of single-mode fibre with different q/p.

$$\theta = \frac{2\pi LcDf_m^2}{f_0^2}. \tag{2.18}$$

Based on this study, the reviewed frequency transfer function is depicted in figure 2.7. From the fitted simulation result based on equation (2.17), it is found that the ratio of the amplitude of the two modulation sidebands $q/p = 0.9$ gives the matched profile to the measured result. Inequality in the amplitude of the two modulation sidebands of the modulated laser decreases the depth of the notch response and henceforth degrades the performance of the notch filter. To obtain the maximum notch depth, the ratio of the amplitude of the two modulation sidebands has to be unity, regardless of their amplitudes.

2.6 Fibre Nonlinearities

Consider a dielectric material in the presence of an electromagnetic field: the field causes the electrons within the material to become polarised with respect to the nuclei, which causes an overall polarisation within the dielectric. If the electromagnetic field is small, the response of the dielectric is linear as in

$$\mathbf{P} = \varepsilon_0 \chi^{(1)} \cdot \mathbf{E}, \tag{2.19}$$

where $\mathbf{P}$ is the induced electric polarisation, $\chi^{(1)}$ is the linear susceptibility of the medium and ε_0 is the permittivity of the free space [21, 35]. When electromagnetic fields become more intense, where the electric field strength is comparable to the inter-atomic electric field, as with the laser radiation, the linear relation between the $\mathbf{P}$ and $\mathbf{E}$ is no longer sufficient and a power series expansion in the field must be used. The response of dielectric to light becomes nonlinear, and optical fibres are no exception.

Even though silica, the material of fibre, is intrinsically not a highly nonlinear material, the small fibre cross section and long fibre length make nonlinearity an important issue in the design of modern lightwave systems. The total polarisation $\mathbf{P}$ induced by the electric dipoles is not linear in the electric field $\mathbf{E}$, but satisfies the more general relation

$$\mathbf{P} = \varepsilon_0 \left(\chi^{(1)} \cdot \mathbf{E} + \chi^{(2)} : \mathbf{E}^2 + \chi^{(3)} \vdots \mathbf{E}^3 + \cdots \right), \tag{2.20}$$

where $\chi^{(j)}$ (j=1, 2, $\cdots$) is the jth order susceptibility. In general, $\chi^{(j)}$ is a tensor of rank $j+1$ [21]. The linear susceptibility $\chi^{(1)}$ represents the dominant contribution to $\mathbf{P}$. Its effects are included through the refractive index n and the attenuation coefficient α. The second-order susceptibility $\chi^{(2)}$ is responsible for such nonlinear effects as second-harmonic generation and sum- and difference frequency generation. It is nonzero only for media that lack an inversion symmetry at the molecular level. As SiO_2 is a symmetric molecule, $\chi^{(2)}$ vanishes for silica glasses. As a result, optical fibres do not normally exhibit second-order nonlinear effects. Nonetheless, the electric-quadrupole and magnetic-dipole moments can generate weak second-order nonlinear effects. Defects or color centres inside the fibre core can also contribute to second-order harmonic generation under certain conditions.

$\chi^{(3)}$ gives rise to third-harmonic generation, four-wave mixing and nonlinear refraction [35, 36]. Third-harmonic generation and four-wave mixing, which are the processes that involve new frequency generations, are not efficient in optical fibres unless special efforts are made to achieve phase matching. With the phase matching condition, most of the nonlinear effects in optical fibre originate from nonlinear refractions that manifested by $\chi^{(3)}$.

Fibre nonlinearities can be divided into elastic and inelastic processes. Elastic processes do not exchange energy between the electromagnetic fields in the dielectric medium and are generally caused by the nonlinear refractive index. Inelastic processes exchange energy and are caused by stimulated scattering. In the following sections, these phenomena will be described in which more attention will be given to inelastic processes that are more related to the research work in the later chapter.

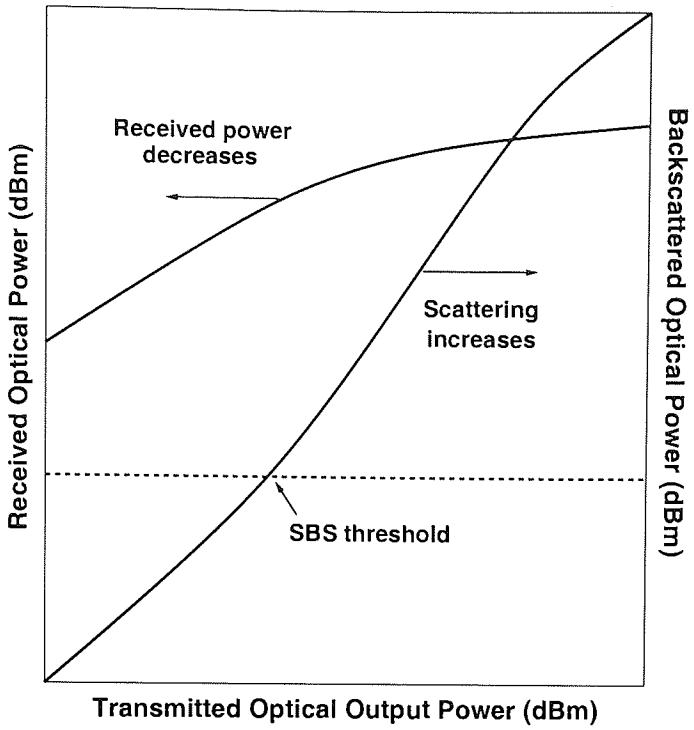

Figure 2.8: Schematic diagram of the effect of stimulated Brillouin scattering.

2.6.1 Stimulated Inelastic Scattering

When the frequency (or the photon energy) of scattered light remains unchanged, it is called elastic scattering. One of the examples is Rayleigh scattering which consistently contributes loss in optical fibre for a window of wavelength. On the contrary, in inelastic scattering, the frequency of the scattered light is shifted upward. The stimulated inelastic scattering can be categorised into two classes, stimulated Brillouin scattering (SBS) and stimulated Raman scattering (SRS). In these processes, part of the energy from electromagnetic fields is transferred to their constituent materials. A photon is annihilated to give another photon and a phonon. The main difference between SBS and SRS is that optical phonons participate in SRS while acoustic phonons participate in SBS.

SBS basically involves the light modulation through thermal molecular vibrations within the fibre. It scatters the light into upper and lower sidebands which are separated equally from the incident light by the modulation frequency. The frequency shift is a maximum in the backward direction reducing to zero to in the forward direction making SBS a mainly backward process with a frequency shift of $\approx$10 GHz.

SBS sets an upper limit on the optical power that can be gainfully launched into optical fibre, as illustrated in figure 2.8 [37], in which the threshold power P_B in watts is given by

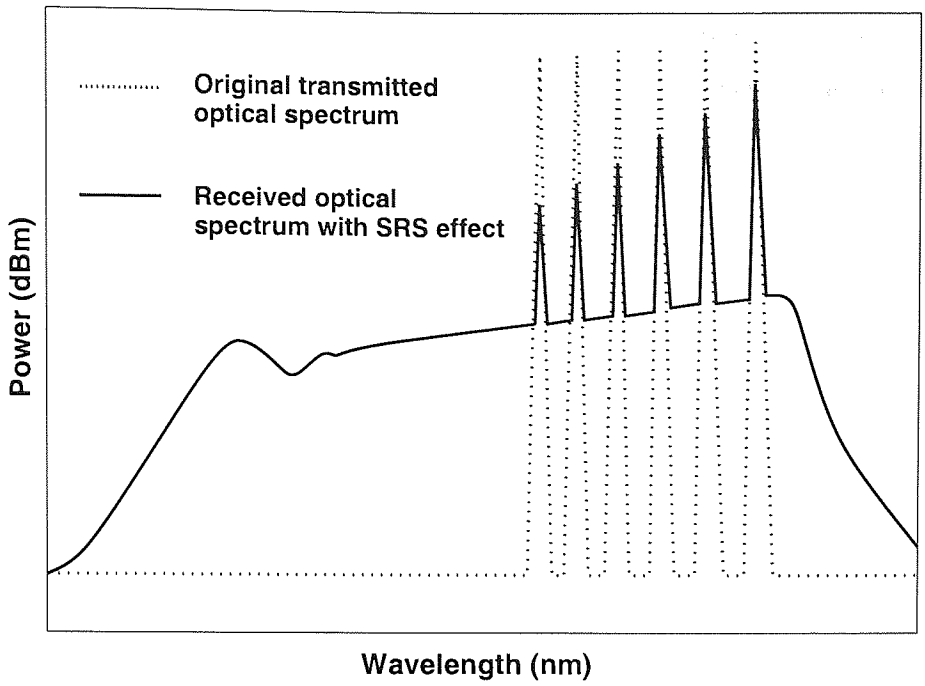

Figure 2.9: Schematic diagram of the effect of stimulated Raman scattering.

$$P_B = 4.4 \times 10^{-3} d^2 \lambda^2 \alpha_{dB} \nu, \tag{2.21}$$

where d is the fibre core diameter in micrometres, λ operating wavelength in micrometres and ν is the bandwidth of the laser source in gigahertz [4]. When launched power exceeds the SBS threshold, the periodic variations in the refractive index, caused by the high power incident lightwave, induce backreflection similar to the effect of Bragg gratings. This causes a saturation of optical power in the receiver and a saturation of noise that degrades bit-error-rate performance.

As can be seen from equation (2.21), the two parameters that govern the threshold for the onset of SBS effect are wavelength and the linewidth of the transmitter. Optical sources with narrower linewidth have lower SBS threshold. Thus, broadening the effective spectral width of the optical source minimises SBS. It is also noteworthy that the SBS threshold is lower at 1550 nm than 1310 nm. Typical values for directly modulated optical sources operating at 1550 nm are +8 dBm to +10 dBm over standard single-mode fibre.

SRS is similar to SBS except a high frequency optical phonon rather than an acoustic phonon is generated. The scattered light is shifted by 13 THz and its threshold optical power in watts is given as

$$P_R = 5.9 \times 10^{-2} d^2 \lambda^2 \alpha_{dB}, \tag{2.22}$$

where d and λ are as specified in equation (2.21) [4]. Comparatively, the threshold of SRS is nearly 1 Watt, which is a lot higher than SBS. Consequently, it is much less of a problem. This limit drops proportionally by the number of the optical amplifiers in the link. SRS can cause scattering like SBS. However, the usual effect is that the shorter wavelength channels are robbed of power, and that power is transferred to the longer wavelength channels, as shown in figure 2.9 [37]. It is much like the operation of Erbium-doped fibre amplifier (EDFA) where energy is transferred from 980 nm wavelength window to amplify 1550 nm wavelength window. This SRS effect leads to the idea of Raman amplifiers which are now becoming mainstream additions to long-haul telecommunication system.

2.6.2 Fibre Nonlinear Refraction

Nonlinear effects caused by the intensity dependent refractive index of fibre are commonly referred to as Kerr nonlinearities [4]. In practise, the refractive index of all materials is power dependent. It increases with intensity and causes materials to behave nonlinearly. To take this nonlinear refraction in account, the effective refractive index n' is modified as

$$n' = n_0 + n_2 \frac{P_0}{A_{\text{eff}}}, \tag{2.23}$$

where n_0 is the linear refractive index, n_2 is the nonlinear-index coefficient, P_0 is the optical incident power and A_{eff} is the effective core area of the fibre. n_2 is about 2.60×10^{-20} m^2/W for silica fibres and can be varied with dopants used in the core [5]. As can be seen from equation (2.23), even if the n_2 value is very small, high optical power and small core area can cause fibre to behave nonlinearly in long haul lightwave systems.

Two interesting manifestations of nonlinear refraction effect that are widely studied are self-phase modulation (SPM) and cross-phase modulation (XPM). In these phenomena, the mode propagation constant becomes power dependent and can be written as

$$\beta' = \beta_0 + \beta_1 \omega + \frac{\beta_2 \omega^2}{2} + \gamma P = \beta + \gamma P, \tag{2.24}$$

where

$$\gamma = \frac{n_2 \omega}{c A_{\text{eff}}} = \frac{2\pi n_2}{A_{\text{eff}} \lambda}, \tag{2.25}$$

which is a key parameter with values ranging from 1 to 5 W^{-1}/km based on the values of A_{eff} and λ [21].

In SPM, the optical field propagated in optical fibres experiences self-induced phase shift due to this γ term and this nonlinear phase shift increases linearly with fibre length as [5]

$$\Delta\phi = \int_0^L (\beta' - \beta)dz = \int_0^L \gamma P(z)dz = \gamma P_{in} L_{\text{eff}}, \tag{2.26}$$

where $P(z) = P_{in}\exp(-\alpha z)$ accounts for fibre losses where P_{in} is the input optical power and L_{eff} is

$$L_{\text{eff}} = \frac{1-\exp(-\alpha L)}{\alpha}. \tag{2.27}$$

Since frequency is the derivative of phase, $\omega = -d\phi/dt$, the phase delay results in a frequency chirp, $\Delta\omega$, across the phase is

$$\Delta\omega = -\frac{d(\Delta\phi)}{dt}. \tag{2.28}$$

Hence, the nonlinear refractive index of the optical fibre results in self-phase modulation of the optical signal.

When there are two or more optical signals with different wavelength, direction or state of polarisation are transmitted inside an optical fibre, nonlinear phase shift for a specific channel depends not only on the power of that channel but also on the power of other channel. This phenomenon is called cross-phase modulation and it is always accompanied by the SPM. The phase shift for the jth channel will be [5]

$$\phi_j^{NL} = \gamma L_{\text{eff}}\left(P_j + 2\sum_{m\neq j} P_m\right), \tag{2.29}$$

where the summation extends over the number of the channels. The total phase shift depends on the powers in all channels. The factor 2 implies that the nonlinear effect from XPM is two times that of SPM for the same applied optical power.

A general way to investigate the effect of SPM and XPM is based on the generalised nonlinear Schrödinger (GNLS) equation [38]

$$i\frac{\delta A}{\delta z} + i\frac{\alpha}{2}A - \frac{\beta_2}{2}\frac{\delta^2 A}{\delta T^2} + \gamma|A|^2 A = 0, \tag{2.30}$$

where $A = A(z,T)$ is the slowly varying field envelope, z is the propagation distance, α is the fibre attenuation coefficient and $T = t - z/v_g$ is the normalised time in a frame moving at the group velocity v_g. This GNLS equation takes dispersion, nonlinearity and fibre losses into account for designing lightwave systems. And to solve this equation, the split-step Fourier method is commonly used where the dispersive and nonlinear effects are assumed to act independently in propagating the optical field over a small distance [39]. The algorithms of GNLS based on the split-step Fourier method will be discussed in more detail in the later chapter.

2.6.3 Four-Wave Mixing

As stated earlier, four-wave mixing (FWM) is one of the nonlinear phenomena induced by $\chi^{(3)}$ which involves new frequencies generation. When three optical fields with frequencies ω_1, ω_2 and ω_3 copropagate in the fibre at the same time, the fourth frequency ω_4 will be generated by a relation of $\omega_4 = \omega_1 + \omega_2 + \omega_3$ or $\omega_3 + \omega_4 = \omega_1 + \omega_2$ [5, 21]. The first term refers to energy transfer from three photons to a single photon. When $\omega_1 = \omega_2 = \omega_3$, this term refers to third-harmonic generation, or it refers to frequency conversion when $\omega_1 = \omega_2 \neq \omega_3$. Practically, it is hard to build up because of the phase-matching requirement which can only be reached when the channel wavelength is close to the zero-dispersion wavelength λ_D. The latter term corresponds to the scattering process in which two photons are destroyed to form two new photons. The phase-matching requirement for this process to happen is

$$\Delta k = k_3 + k_4 - k_1 - k_2 = (n_3\omega_3 + n_4\omega_4 - n_1\omega_1 - n_2\omega_2)/c = 0, \tag{2.31}$$

where k_1, k_2, k_3, k_4 and n_1, n_2, n_3, n_4 are the wave propagation constants and refractive indices for the four wavelengths. $\omega_1 = \omega_2$ is usually the dominant process that gives most impact to the system performance because it is relatively easy to achieve the mismatch $\Delta k = 0$ in this case for the wavelength difference in the microwave frequency region.

Since the mismatch can be contributed by material dispersion, waveguide dispersion and nonlinear effects, the phase-matching condition can be expressed as

$$\kappa = \Delta k_M + \Delta k_W + \Delta k_{NL}, \tag{2.32}$$

where Δk_M, Δk_W and Δk_{NL} represent the phase mismatch due to the material dispersion, waveguide dispersion and nonlinear effects. In single-mode fibres, it is possible to realise phase-matching conditions by using small frequency shifts and low pump power to reduce Δk_M and Δk_{NL}, operating near λ_D so that Δk_{NL} nearly cancels $\Delta k_M + \Delta k_W$, or working in the anomalous GVD regime so that Δk_M is negative and can be cancelled by $\Delta k_W + \Delta k_{NL}$.

The third option is relatively interesting because it involves the compensation from fibre nonlinearity to achieve phase-matching requirement. This phenomenon can be interpreted as modulation instability which is induced by the interplay between dispersion and nonlinearity in terms of FWM process that is phase-matched by the nonlinear process of SPM. In this case, if two CW waves propagate at frequency ω_0 and $\omega_1 = \omega_0 + \Omega$, the energy of two photons from the intense beam will create two different photons, one at frequency $2\omega_1 - \omega_0$ and the other at the idler frequency $2\omega_0 - \omega_1$ as long as $|\Omega| < \Omega_c$ where

$$\Omega_{max} = \pm\frac{\Omega_c}{\sqrt{2}} = \pm\sqrt{\frac{2\gamma P_0}{|\beta_2|}}. \tag{2.33}$$

Even if there is only one CW beam which propagates by itself, modulation instability can lead to a breakup of the CW beam into a pulse train. As largest gain occurs for frequencies $\omega_0 \pm \Omega_{max}$, these frequency components are amplified the most. Thus, the fibre output will give two spectral sidebands located at $\pm\Omega_{max}$ on each side of the beam frequency ω_0 as a result of FWM that is phase matched by the nonlinear process of SPM. The frequency shifts are in the range of 1 – THz for optical incident power ranging from 1 – 100 W. This FWM is similar to the nature of intermodulation distortion in radio-over-fibre system that involves radio frequency [5, 40]. As the frequency difference between channels is always in the condition of $|\Omega| < \Omega_c$ in radio-over-fibre systems, the spectrum exhibits peaks at multiples of the beat frequency because of the fibre induced self phase modulation.

In general, FWM is undesirable because it leads to inter-channel crosstalk in wavelength division multiplexing (WDM) systems and imposes limitations on transmission in fibre with low dispersion, which is dispersion-shifted fibre. However, it can be suppressed by using dispersion management wherein fibre with high anomalous dispersion is used. It can be used for wavelength conversion and to generate a spectrally inverted signal through the process of optical phase conjugation which is useful for dispersion compensation.

2.7 Conclusion

This chapter has given the background of the fibre characteristics including materials, losses, birefringence, dispersion of optical fibres, as well as the modulation suppression induced by the fibre chromatic dispersion in radio-over-fibre links. Various nonlinear effects that can be induced in optical fibres and their significant impacts in lightwave systems have also been outlined. The significance of these joint effects will be covered in the later chapter.

Chapter 3

Fibre Bragg Gratings

3.1 Introduction

The exploitation of optical fibre Bragg gratings (FBGs) has grown exponentially in the field of telecommunications and sensing. They have been an area of intense research and development since the discovery of photosensitivity in fibre by Hill *et al.* in 1978 [41]. The demand for increased bandwidth has rapidly expanded the development of optical components and devices. Bragg gratings have been vital in the phenomenal growth of some of these products, and are recognised as one of the most significant enabling technologies for fibre optic communications in the last decade.

FBGs are simple intrinsic elements, which can be "photo-imprinted" into photosensitive fibre. The photosensitivity is primarily due to the germanium dopant used in the core of the commercial fibres. It can be increased by raising the germanium doping level or by the in-diffusing of molecular hydrogen which acts as a catalyst to the reaction of the germanium with ultra-violet (UV) light and greatly reduces the exposure time. FBGs can be made by producing periodic variations in the index of refraction along a short section in the core of an optical fibre non-destructively. These periodic changes in index could effectively be used to form intracore Bragg gratings to reflect a predetermined narrow or broad range of wavelength of light incident on the gratings, while passing all the other wavelengths of the light, as can be seen from figure 3.1.

By exposing the side of the fibre to an interference pattern of intersecting coherent beams of UV source, the Bragg wavelength can be easily varied and located along a length of a fibre [42]. Multiple fibre gratings can now be written at arbitrary locations along a single optical fibre, with reflectivities ranging from 0.1 % to approaching 99.97 % and the spectral width can be tailored from 0.1 nm to a few tens of nm. Besides, this external exposure

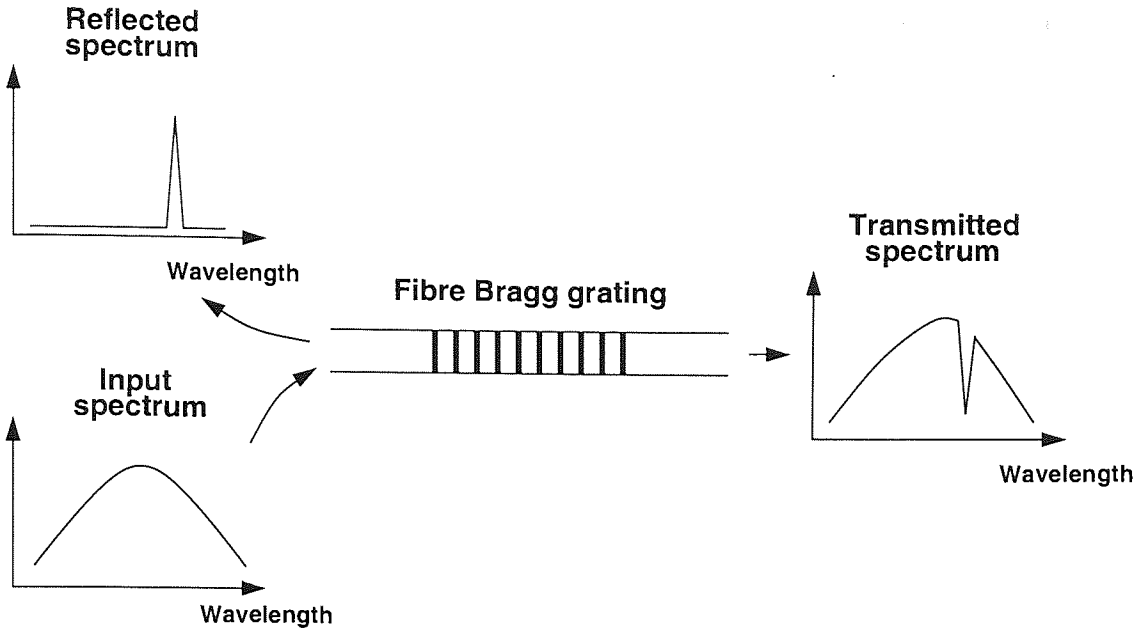

Figure 3.1: Schematic diagram of the working principle of fibre Bragg gratings.

allows the fibre to retain its intrinsically high compressive and tensile strength, if coated properly after fabrication [43]. They have proven to be attractive as optical devices for many applications such as wavelength selective filters, tunable filters, dispersion compensator, narrowband fibre laser, optical fibre mode converters, optical sensors etc.

This chapter aims to introduce the basic working principle of a Bragg grating, as well as the coupled-mode theory and the transfer matrix method used to simulate the reflecting grating. Three different grating fabrication techniques, which are holographic, point-by-point direct writing and phase mask scanning, are discussed followed by the arrangement for spectra measurement. Finally, three types of commonly used gratings are presented with their measured and simulated spectra.

3.2 The Working Principle

A repetitive array of diffracting elements, either apertures or obstacles, that has the effect of producing periodic variations in the phase, amplitude, or both of an emergent wave is said to be a diffraction grating. According to the diffraction theory of gratings [44], the relationship between the incident and diffracted light can be expressed as

$$\sin\theta_i - \sin\theta_r = m\frac{\lambda}{n\Lambda}, \tag{3.1}$$

where θ_i and θ_r are the incident and diffracted angles measured with respect to the planes

of constant refractive index, Λ is the grating period, λ/n is the wavelength of light in the medium with refractive index n, and m is the order of Bragg diffraction. This condition is similar to the phase-matching condition in four-wave mixing. It can be written as

$$\mathbf{k}_i - \mathbf{k}_d = m\mathbf{k}_g, \tag{3.2}$$

where $\mathbf{k}_i$ and $\mathbf{k}_d$ are the wave vectors of incident and diffracted light, $\mathbf{k}_g$ has the value of $2\pi/\Lambda$ and points in the direction in which the refractive index of the medium is changing [36]. As these three vectors lie along the fibre axis in single-mode fibres, $\mathbf{k}_d = -\mathbf{k}_i$ and the diffracted light propagates backwards.

When phase-matching condition is achieved, the fibre grating acts as a reflector with $\theta_i = \pi/2$ and $\theta_r = -\pi/2$. Weak reflections in the gratings accumulate in phase to produce a strong reflection at the resonance wavelength. If $m = 1$, the period of grating Λ is

$$\Lambda = \frac{\lambda_B}{2n}. \tag{3.3}$$

This condition is known as the Bragg condition. The gratings are hereafter referred to as Bragg gratings and λ_B is the Bragg wavelength. From $\lambda_B = 2n\Lambda$, grating period Λ of about 0.5 μm gives reflected light wavelength near 1.5 μm, which is the commonly used transmission window.

3.3 Coupled-Mode Theory

In a guided mode reflection grating, light propagated in fibre interacts with the periodic structures and reflects due to the periodic structures. The interaction between the forward-propagating mode and an identical backward-propagating mode in the general approach of the coupled-mode equation can be simplified as [24]

$$\frac{\partial A_v}{\partial z} = -ik_{dc}A_v - ik_{ac}^* B_\mu e^{i(\Delta\beta z - \phi(z))}, \tag{3.4}$$

$$\frac{\partial B_\mu}{\partial z} = ik_{dc}B_\mu + ik_{ac}A_v e^{-i(\Delta\beta z - \phi(z))}, \tag{3.5}$$

where A_v and B_μ denote the slowly varying amplitudes of the forward and backward travelling modes and

$$\Delta\beta = \beta_\mu + \beta_v - \frac{2\pi N}{\Lambda}, \tag{3.6}$$

where β_μ and β_v are the wave propagation constants for forward- and backward-propagating modes, and k_{dc} and k_{ac} are the dc and ac coupling constants.

In order to solve the coupled-mode equations in equation (3.4) and equation (3.5), the forward propagating mode F and backward propagating mode B are assumed as

$$F = A_v e^{-(i/2)[\Delta\beta z - \phi(z)]} \tag{3.7}$$

and

$$B = B_\mu e^{(i/2)[\Delta\beta z - \phi(z)]}. \tag{3.8}$$

These two equations are then differentiated and substituted into equation (3.4) and equation (3.5). Coupled-mode equations can then be written as

$$\frac{dF}{dz} + i\left[\kappa_{dc} + \frac{1}{2}\left(\Delta\beta - \frac{d\phi(z)}{dz}\right)\right]F = -i\kappa_{ac}^{*}B \tag{3.9}$$

and

$$\frac{dB}{dz} - i\left[\kappa_{dc} + \frac{1}{2}\left(\Delta\beta - \frac{d\phi(z)}{dz}\right)\right]B = i\kappa_{ac}F. \tag{3.10}$$

By analytically solving equation (3.9) and equation (3.10), the transmissivity τ and reflectivity ρ of the whole grating are [24]

$$\tau = \frac{S}{S\cosh(S\delta l_j) - i\delta_0 \sinh(S\delta l_j)} \tag{3.11}$$

and

$$\rho = \frac{i\kappa\sinh(S\delta l_j)}{S\cosh(S\delta l_j) - i\delta_0 \sinh(S\delta l_j)}, \tag{3.12}$$

respectively. From the analysis, the effective detuning S of the gratings can be defined as

$$S = \sqrt{\kappa^2 - {\delta_0}^2}, \tag{3.13}$$

where

$$\delta_0 = 2\pi n_{eff}\left[\frac{1}{\lambda} - \frac{1}{\lambda_B}\right] \tag{3.14}$$

is the difference between the propagation constant and gratings resonance. n_{eff} is the effective refractive index, $\kappa = \kappa_{ac}$ is the coupling constant of the grating, λ is the wavelength of the light source, and λ_B is the Bragg wavelength. Equation (3.11) and equation (3.12) are important expressions for fibre Bragg gratings and were employed by the author to simulate all the uniform gratings used in the research work.

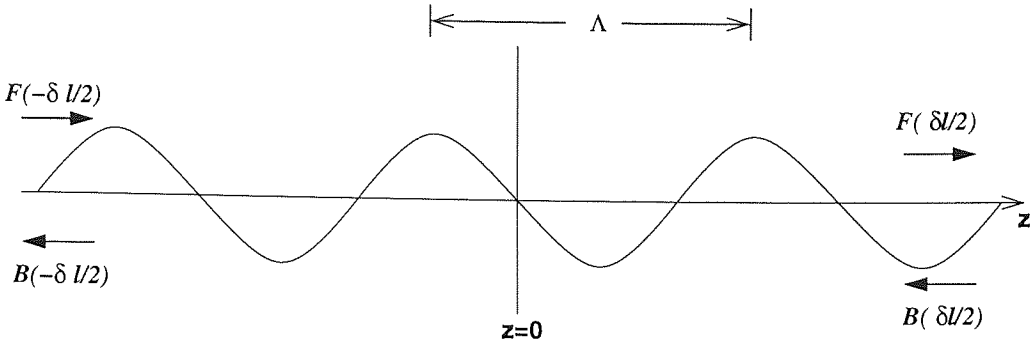

Figure 3.2: Refractive index modulation in the fibre core.

3.4 Transfer Matrix Method

Practically, there are many techniques for calculating the spectrum of fibre Bragg gratings, for instance, numerical integration of coupled-mode equations and Rouard's transfer matrix method [24]. Among them, Rouard's transfer matrix method is the faster technique and thus it is extensively implemented.

In this method, coupled-mode equations are used to calculate the output fields of a short section δl_1 of grating for which the gratings length L_g, the coupling constant $\kappa(z)$ and chirp $\Lambda(z)$ are assumed to be constant. Each may possess a unique and independent functional dependence on the spatial parameter z. For such a grating with an integral number of periods, the analytical solution results in the amplitude reflectivity, transmission and phase. These quantities are then used as the input parameters for the adjacent section of grating of length δl_2.

Assuming that the grating has input fields of $F(-\delta l_1/2)$ and $F(\delta l_1/2)$ and output fields of $B(-\delta l_1/2)$ and $B(\delta l_1/2)$ respectively in a short grating section δl_1, as can be seen from figure 3.2, the transfer matrix can be written as

$$\begin{bmatrix} F(-\delta l_1/2) \\ B(-\delta l_1/2) \end{bmatrix} = [T^1] \begin{bmatrix} F(\delta l_1/2) \\ B(\delta l_1/2) \end{bmatrix}, \tag{3.15}$$

where matrix

$$[T^1] = \begin{bmatrix} T_{11} & T_{12} \\ T_{21} & T_{22} \end{bmatrix} \tag{3.16}$$

denotes the fundamental transfer matrix. By applying the boundary conditions onto equation (3.16), the transmitted and reflected amplitudes can be written as

$$F(\delta l_1/2) = \frac{1}{T_{11}} \tag{3.17}$$

and

$$B(-\delta l_1/2) = \frac{T_{21}}{T_{11}}. \tag{3.18}$$

These resultant fields become the new fields for the adjacent grating section δl_2 by another transfer matrix T^2. This results the entire N sections grating with $L = \sum_{i=1}^{N} \delta l_i$ is

$$\begin{bmatrix} F(-L/2) \\ B(-L/2) \end{bmatrix} = [\mathbf{T}] \begin{bmatrix} F(L/2) \\ B(L/2) \end{bmatrix}, \tag{3.19}$$

where the matrix $\mathbf{T}$ is given as

$$[\mathbf{T}] = \prod_{i=1}^{N} [T^i]. \tag{3.20}$$

According to the solution of coupled-mode theory in equation (3.11) and equation (3.12), the transfer matrix elements for ith section are [24]

$$T_{11} = \cosh(S\delta l_i) - \frac{i\delta_0 \sinh(S\delta l_i)}{S}, \tag{3.21}$$

$$T_{22} = \cosh(S\delta l_i) + \frac{i\delta_0 \sinh(S\delta l_i)}{S}, \tag{3.22}$$

$$T_{12} = -\frac{i\kappa_{ac} \sinh(S\delta l_i)}{S}, \tag{3.23}$$

$$T_{21} = \frac{i\kappa_{ac} \sinh(S\delta l_i)}{S}. \tag{3.24}$$

To simulate the non-uniform grating, which is the chirped grating, used in the work, the Bragg wavelength λ_B has to be modified to

$$\lambda_B(z) = \lambda_c + \gamma z, \tag{3.25}$$

where λ_c is the central wavelength of the grating, γ is the chirped rate and z is in the range of $-L/2$ to $L/2$ with L is the length of the grating. This z-dependent Bragg wavelength will then be substituted into equation (3.14) and equation (3.13) and subsequently into equation (3.11) and equation (3.12) to calculate the transmissivity and reflectivity of the grating.

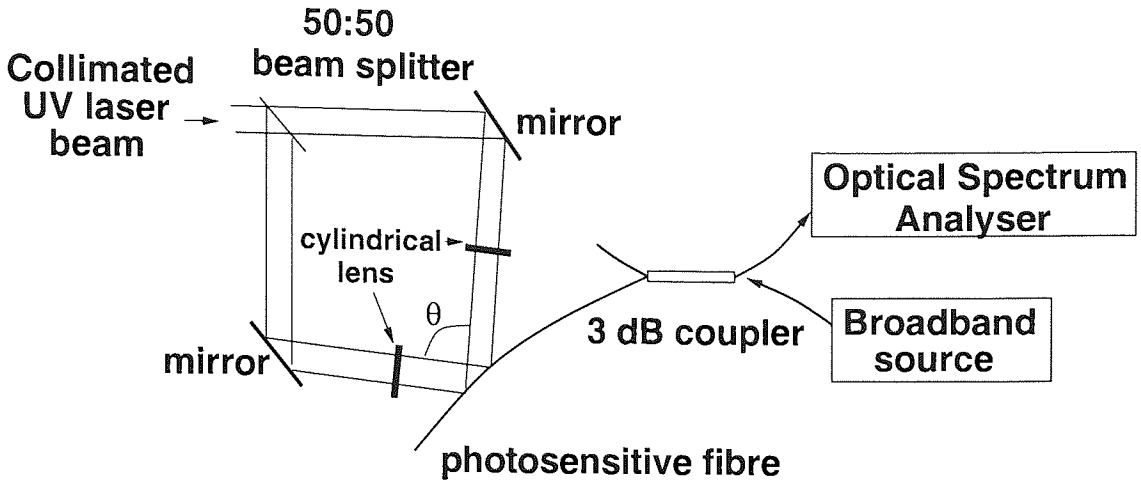

Figure 3.3: Arrangement for transverse two-beam interferometric exposure of a fibre.

3.5 Fabrication Techniques

Many techniques have been studied widely in order to produce higher-quality fibre gratings. Basically, they can be classified into three categories, which are holographic, point-by-point direct writing and phase mask techniques. The holographic technique uses a beam splitter to divide a single input UV beam into two, interfering them at the fibre whilst the point-by-point technique involves inscription of one grating pitch at a time. The phase mask technique is based on the simple periodic exposure to UV-radiation or through a spatially periodic mask along a piece of fibre [24,45,46].

The arrangement for writing uniform-period gratings into optical fibre by the transverse UV two-beam interferometric holographic technique is shown in figure 3.3. In this setup, cylindrical lenses are usually adopted in the arrangement in order to increase the intensity of the UV beams and to ensure that the beams are focused on to the fibre core in the direction along to the fibre. As non-uniform beam exposure onto the fibre core creates non-uniformity in effective refractive index and hence gives undesired self-chirping, an aperture is needed to ensure that the central portion of the Gaussian beam profile is selected in order to produce a more uniform intensity profile.

Undeniably, free-space holographic exposure has the capability of producing gratings of highest flexibility, in which the Bragg wavelength, λ_B, can be selected arbitrarily by the angle between the interfering beams since

$$\lambda_B = 2n\Lambda = n\frac{\lambda_{UV}}{\sin(\frac{\theta}{2})}, \tag{3.26}$$

where θ denotes the angle between the two interfering beams of wavelength λ_{UV} [47]. How-

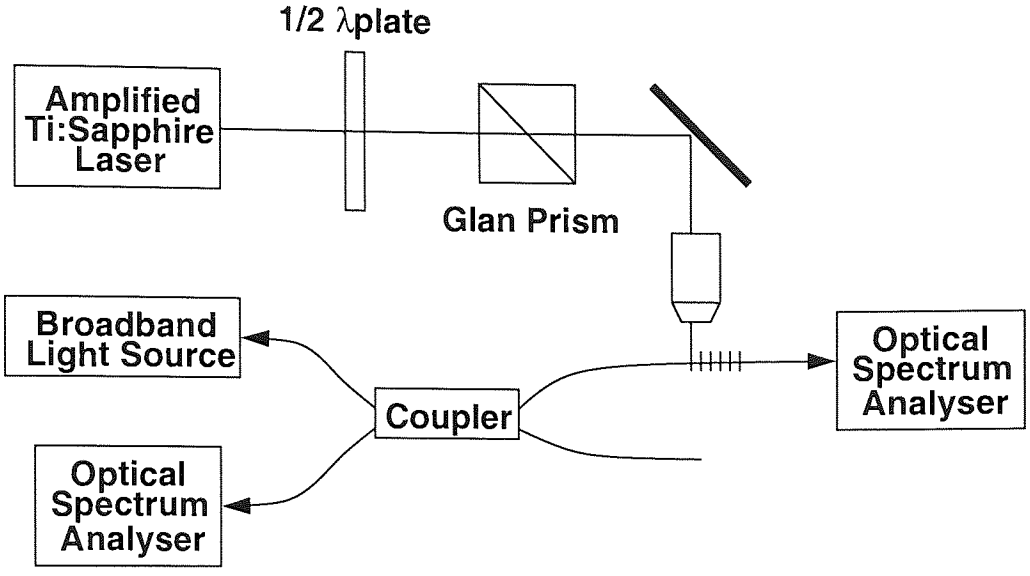

Figure 3.4: Arrangement for the point-by-point fibre Bragg grating inscription method.

ever, high spatially and temporally coherent laser sources, high stability of optical path difference and extreme isolation from air turbulence are needed. Moreover, this technique imposes more stringent requirements such as the size and the uniformity of the interfering UV beams during the fabrication of long period gratings. This fabrication process takes minutes to hours to make a certain length of long period gratings.

Point-by-point direct writing fabrication is based on the inscription of one grating pitch at a time. Therefore it offers a number of distinctive advantages such as great flexibility to inscribe gratings with any periodicity and length. In principle, it is also possible to inscribe highly complex structures, since the induced refractive index modulation and pitch period can be altered for each grating pitch. This level of control is unavailable for either the diffractive or the holographic method.

Despite its potential advantages, the point-by-point method using the UV laser source is mainly considered only for the inscription of long period gratings. Very long process time, complex alignment and errors in the grating periodicity due to thermal and strain changes in the fibre have allowed only the inscription of weak gratings of low quality [48]. However, recently, highly reflective gratings have been inscribed using the point-by-point method based on tightly focused femtosecond laser, as shown in figure 3.4 [49]. Unlike the UV point-by-point method, the femtosecond laser point-by-point method offers rapid inscription and the potential of making gratings with highly complex structures and improved thermal robustness [50]. Nevertheless, this technique requires expensive setup and since it is a relatively new technique, the inscription of chirped Bragg gratings has not been reported so far.

To achieve a more repeatable and flexible writing setup, an alternate method based on

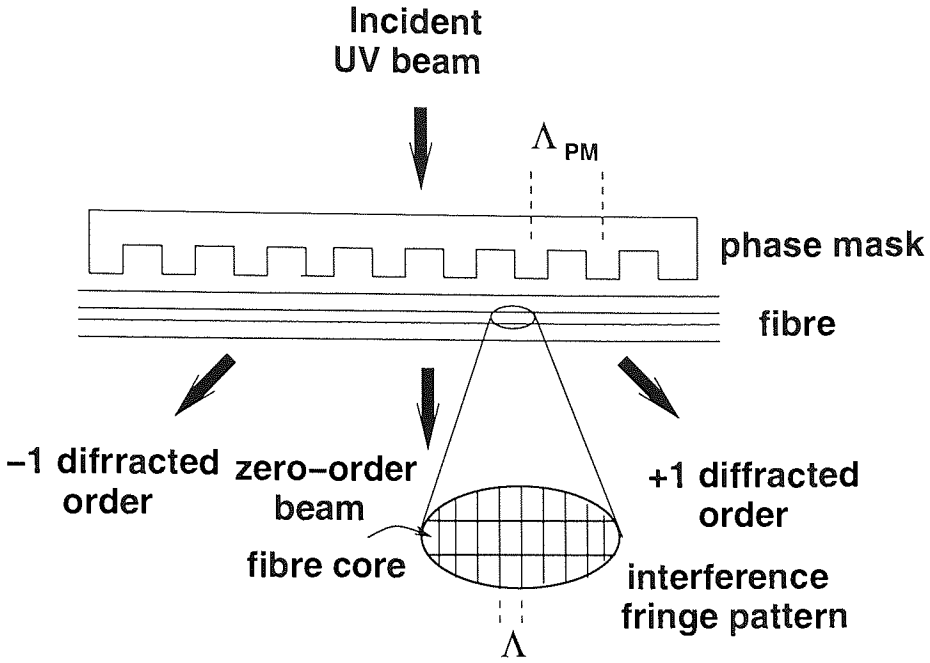

Figure 3.5: Arrangement for UV exposure through a phase mask.

the near-contact exposure through a phase mask is used. This technique is attractive for its simplicity and reproducibility. It has proven to be the preferred method for gratings fabrication in most cases [51, 52]. A phase mask is typically a relief grating etched in a silica plate with a carefully controlled mark-space ratio as well as depth. It can be fabricated by exposure of a photoresist overcoated, silica maskplate to an electron beam to form the pattern, or by holographic exposure [24].

A phase mask with period Λ_{PM} is designed to have corrugations so that a normal incident beam exposing on the mask is entirely diffracted with 0 % of light transmitted in the zero-order beam and 50 % of the total light diffracted to the +1 and -1 orders, as can be seen in figure 3.5. Typically, there is less than 5 % of light transmitted in the zero-order beam and about 45 % of the total light diffracted to the +1 and -1 orders.

The grating is written with a period $\Lambda = \Lambda_{PM}/2$ by the interference patterns between the +1 and -1 orders of the phase mask. It is worth noting that the period of the gratings is independent of the exposure source wavelength λ_{UV}. This enables greater flexibility in using the phase mask although it may not be efficient in terms of different phase masks with different periods being needed for different Bragg wavelengths.

Several laser sources with wavelengths range from 190 nm to 280 nm have been used for gratings written by this techniques. The choice is made based on the requirement that the radiation can be strongly absorbed by the fibre core but not by the cladding. Some examples are, KrF (248 nm) and ArF (193 nm) excimer lasers, tunable excimer-pumped frequency-

doubled dye lasers, frequency-quadrupled Nd:YAG (266 nm) and Nd:YLF (262 nm), and the continuous-wave (CW) frequency-doubled argon-ion laser.

This method does face a trade-off in the need to have different phase mask patterns for each desired Bragg wavelength since the gratings created in the fibre is purely determined by the phase mask. This makes the method costly. Nevertheless, some experiments have been demonstrated that the λ_B can be varied almost 2 nm from the unmagnified value by using a magnifying lens placed before the mask patterns [53] or up to 2.5 nm by stretching the fibre during the fabrication process by means of changing the tension applied on to the fibre during the process [54, 55].

To obtain more flexibility in the phase mask technique, a technique of moving fibre/phase mask scanning beam technique has been demonstrated [56, 57]. This technique allows fabrication of more complex gratings such as apodised gratings, phase shifted gratings and chirped gratings. It is accomplished with a highly stable CW Argon laser operating at 244 nm with a high resolution movement translation stage. This stage is attached with a piezo-electric transducer (PZT) allowing movement with step size of up to sub-μm. The relative movement between the fibre and phase mask is then controlled by the computer.

The gratings used for the research work in this thesis were fabricated using the fibre/phase mask scanning technique. Relative shifts between fibre and phase mask on the order of a mask pitch period, which is 1 μm, were achieved easily by remotely controlled computer. In this technique, the length of the gratings was basically restricted by the length of the phase mask and the high stability of the high power laser ensured a uniformity in the exposure.

3.6 Spectra Measurement

Real-time monitoring can be carried out during the writing process by illuminating the gratings with a broadband source covering the gratings reflection spectrum. It is normal to have either a circulator or a combination of isolator and 50:50 fibre coupler between the source and the gratings to be measured in order to prevent any backreflection to the source. As the most sensitive method for detecting gratings is in reflection, it is best to measure gratings in reflection for diagnostics purposes and display the reflected signal on an optical spectrum analyser (OSA), as shown in figure 3.6 [24]. The inset shows an alternate arrangement that uses a coupler. However, the reflection spectrum obtained in this way does not give the absolute reflectivity of the gratings. To get the absolute reflectivity, transmission spectrum is needed since the relationship between transmissivity τ and reflectivity ρ is given by

$$\rho = 1 - \tau. \tag{3.27}$$

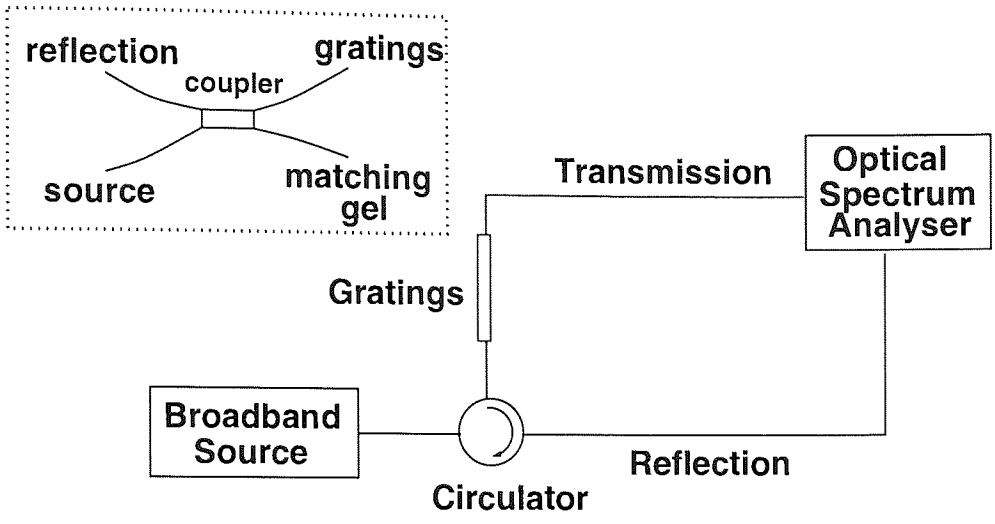

Figure 3.6: Apparatus to measure the transmission and reflection spectra of Bragg gratings.

3.7 Types of FBGs and Their Applications

Many types of gratings have been studied and fabricated recently. Basically, they can be classified as uniform gratings, chirped gratings and apodised gratings. These gratings can be fabricated in standard, Hi-Birefringence or other special-treated fibres, such as Erbium-doped fibre, dependent on the applications. This section seeks to give a brief introduction of these gratings and to present their sample spectra. Their simulated spectra obtained from the coupled-mode theory based transfer matrix method as discussed in the last section are also shown. These gratings were made using the fibre/phase mask scanning technique. They were widely used in the work carried out in this thesis due to their low cost and ease of fabrication. More importantly, they are compatible to the optical system.

3.7.1 Uniform Gratings

Gratings fabricated with a uniform periodic pattern $\Lambda = \Lambda_{PM}/2$ along their length are known as uniform gratings. They are the most common gratings which can be easily fabricated using holographic or phase mask technique. Due to the uniformity, the average effective refractive index always remains constant along the length of the fibre, thus giving its Bragg wavelength as

$$\lambda_B = 2n_{eff}\Lambda, \tag{3.28}$$

where n_{eff} is the effective refractive index of the fibre.

For a uniform grating with a reflectivity R, its coupling coefficient, κL, can be calculated as

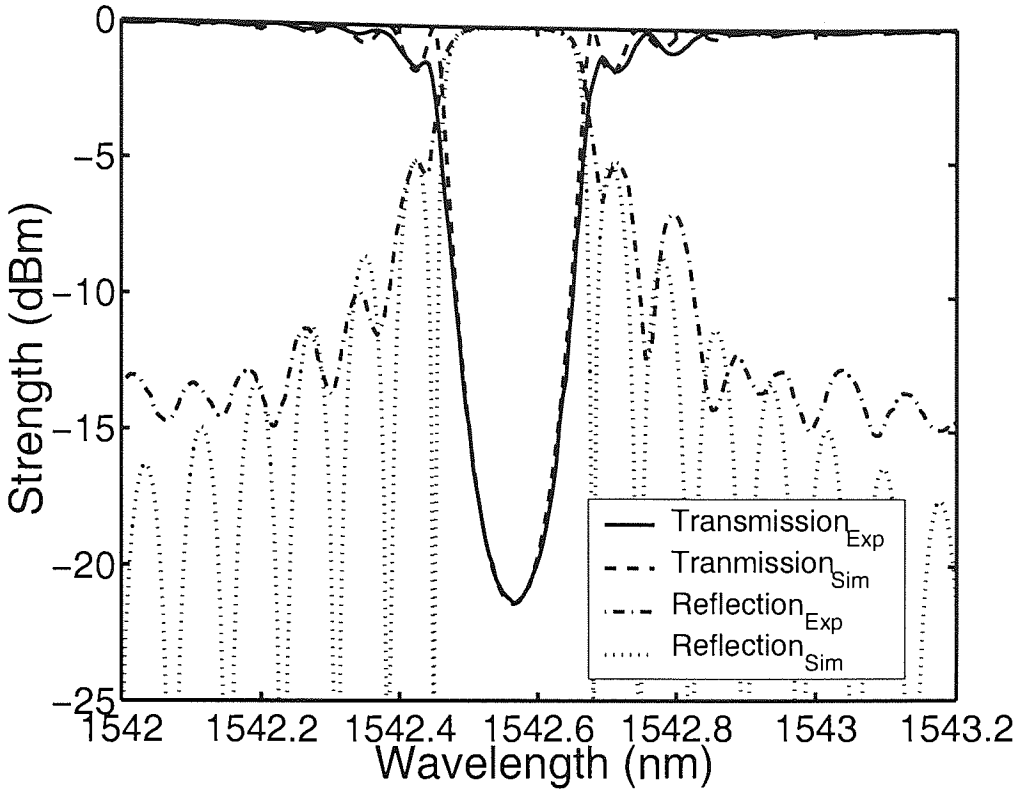

Figure 3.7: Experimental and simulated transmission spectra for a 10-mm uniform grating with κL=3.16.

$$\kappa L = \tanh^{-1}(\sqrt{R}), \tag{3.29}$$

where κ is the coupling constant and L is the grating length. Together with the measured bandwidth, $2\Delta\lambda$, between the first zeroes (FWFZ), the grating length L can be defined from

$$2\Delta\lambda = \frac{\lambda_B^2}{\pi n_{eff} L}\sqrt{(\kappa L)^2 + \pi^2}. \tag{3.30}$$

From the length, the refractive index modulation $\nu\overline{\Delta n}$, with fringe visibility ν, can be calculated from

$$\kappa = \frac{\pi\eta\nu\overline{\Delta n}}{\lambda_B}, \tag{3.31}$$

where η is the core mode overlap factor.

An example 10-mm uniform grating was fabricated using the scanning fibre/phase mask technique. The transmission spectrum is shown in figure 3.7. It can be seen that the grating was centred at 1542.57 nm. Its peak reflectivity R and κL were calculated as 99.3 % and 3.16, respectively. The measured spectrum was compared with the simulated result and there was a good agreement between them. From the simulation, the index modulation Δn was

calculated to be 1.55×10^{-4}. According to the simulated reflection spectrum, the extinction between the Bragg resonance and the first sidelobe was only 5.00 dB. This low extinction extremely limits the applications of uniform gratings. However, this type of grating is widely applied in quasi-distributed sensing of temperature, pressure, strain, et cetera.

3.7.2 Chirped Gratings

Gratings with non-uniform period along their length are known as chirped gratings. The period may vary symmetrically, either increasing or decreasing in period around a pitch in the middle of gratings. It may be linear, where the period varies linearly with length of the gratings [58], may be quadratic or even have jumps in the period [59], and it could also have a period that varies randomly along its length over and above a general trend [24]. Chirped gratings can be fabricated by exposure to UV beams of non-uniform intensity of the fringe pattern, varying the refractive index along the length of a uniform period grating, altering the coupling constant κ of the gratings as a function of position, incorporating a chirp in the inscribed gratings, fabricating gratings in a tapered fibre and applying non-uniform strain.

For linearly chirped gratings with a shortest period of Λ_{short} and longest period of Λ_{long}, the chirp in the period, can be related to the chirped bandwidth, $\Delta\lambda_{chirp}$, of the fibre gratings as

$$\begin{aligned}\Delta\lambda_{chirp} &= 2n_{eff}(\Lambda_{long}-\Lambda_{short}) \\ &= 2n_{eff}\Delta\Lambda_{chirp}.\end{aligned} \tag{3.32}$$

Equation (3.29) can be modified to accommodate a non-uniform grating by substituting the reflectivity found in equation (3.12) whose chirp is non-uniform.

An example 50-mm linearly chirped grating centred at 1557.08 nm with κ=540 was made under the exposure of a chirped phase mask to scanning UV beams. The reflection and transmission spectra are shown in figure 3.8 exhibiting there was a good agreement between the experimentally measured and simulated spectra, except the simulated result had a higher sidelobe suppression and smoother profile. The sources of this discrepancy will be pointed out at the end of this chapter.

Another discrepancy that is worth pointing out is the radiation mode loss that appeared at the short wavelength side of the Bragg wavelength, as can be seen from figure 3.8. This loss usually appears in a highly photosensitive fibre, or hydrogenated fibre and it is only observable in the transmission spectrum. Thus, this loss is resulted from light leaving the side of the fibre [46]. It becomes more significant for a stronger grating [60]. Since this effect

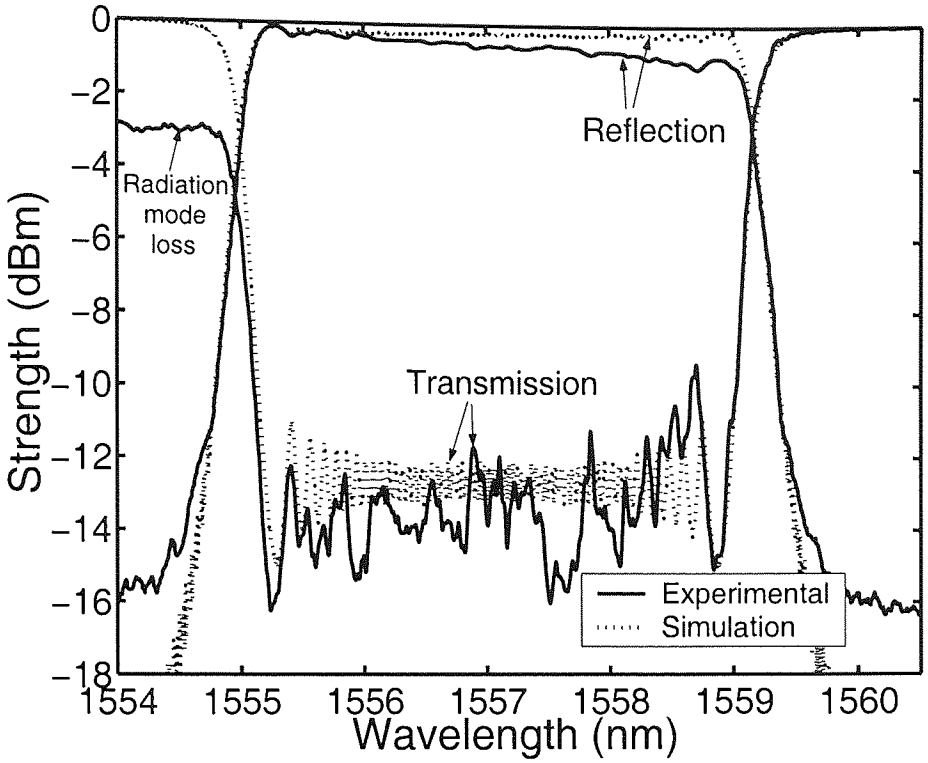

Figure 3.8: Experimental and simulated transmission and reflection spectra for a 50-mm linearly chirped grating with κ=540.

was not included in the coupled-mode formalism, there remains a discrepancy between the measured and simulated results.

The linearly chirped gratings can be applied as a dispersion-correcting and compensating device in optics. This application has also led to the fabrication of ultra-long, broad-bandwidth gratings of high quality, for high-bit-rate transmission in excess of 40 Gb/s over 100 km [61] or more [62] and in Wavelength Division Multiplexing (WDM) transmission [63]. Other applications are chirped pulse amplification [64], chirp compensation of gain-switched semiconductor lasers [65], various kinds of sensing [66], higher-order fibre dispersion compensation [67] and bandpass filtering [68].

3.7.3 Apodised Gratings

The suppression of the sidelobes in the reflection spectrum by gradually increasing the coupling coefficient with penetration into, as well as gradually decreasing on exiting from, the grating is called apodisation. Gratings with such a refractive index modulation amplitude profile diminishes the sidelobes substantially and are called apodised gratings. Apodisation is not only used to suppress the sidelobes of uniform gratings, but also to suppress the background reflection of chirped gratings to achieve a high extinction. Furthermore, it removes

the ripple effect on the dispersion [24, 60]. These suppressions are of importance in some applications, such as in dense wavelength division multiplexing (DWDM) that requires high rejection of the non-resonant light [46].

Basically, apodised gratings are fabricated based on the appropriate *shading* functions for the refractive index modulation amplitude. The only principle that needs to be followed is to maintain an unchanging average refractive index, n_0, throughout the length of the fibre while gradually altering the refractive index modulation amplitude, $\Delta n_0(z)$.

For apodised gratings, the grating coupling constant is defined as

$$\kappa(z) = \kappa \cdot f(z), \tag{3.33}$$

in which the *f(z)* refers to the selected *shading* functions. The most common *shading* are raised cosine, Gaussian, tanh, Blackman, sinc and Cauchy functions. All of them have the same purpose, which is, to eliminate the sidelobes of gratings. In these processes, the average index remains constant along the grating length because the intensity of the UV exposure is uniform. Hence, the index distribution along the grating length is given by

$$n(z,t) = n_0 + \Delta n_0(z)\cos[\frac{2\pi}{\Lambda}z + \phi(z,t)], \tag{3.34}$$

where $\phi(z,t)$ is the introduced phase shift and Λ is the grating period.

Apodised Uniform Grating

Figure 3.9 shows the transmission and reflection spectra of a 20-mm apodised uniform grating which was fabricated by phase mask dithering/shaking technique. In this technique, phase mask attached to a PZT shook according to the inverse amplitude of the applied *shading* profile, in which maximum shaking amplitude was induced at the two edges of the grating in order to erase the refractive index modulation while minimum shaking amplitude appeared at the centre of the grating. The *shading* function used to fabricate this grating was a six-order hyper-Gaussian apodisation function

$$f(z) = \exp\left[-(\frac{2z}{l})^{12}\log 2\right], \tag{3.35}$$

with its physical length at full width half maximum (FWHM), l, set at 12.2 mm. Six-order hyper-Gaussian *shading* function was used because it could give a higher sidelobe suppression. It can be seen that the grating was centred at 1550.71 nm. Its peak reflectivity R and κ were calculated as 99.9 % and 400, respectively. The experimental result was compared with

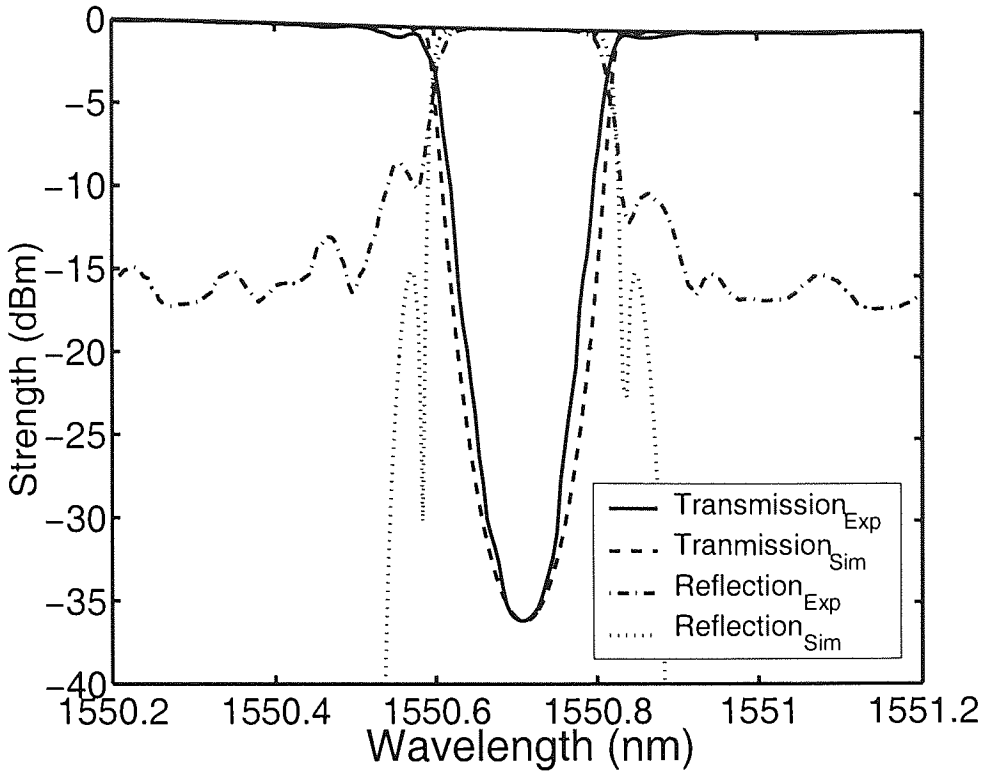

Figure 3.9: Experimental and simulated transmission and reflection spectra for a 20-mm apodised uniform grating with κ=400.

the simulated result and there was a good agreement between them. According to the simulated reflection spectrum, the extinction between the Bragg resonance and the first sidelobe was 14.90 dB. This proved that apodisation enabled higher sidelobe suppression in uniform grating fabrication. This piece of apodised uniform grating was experimentally used for sideband filtering in section 6.5.

Apodised Chirped Grating

Figure 3.10 shows the transmission and reflection spectra of a 70-mm apodised chirped grating which was fabricated by phase mask dithering/shaking technique. Again, the *shading* function used to fabricate this grating was a six-order hyper-Gaussian apodisation function as in equation 3.35 with its physical length at full width half maximum (FWHM), l, set at 37.1 mm. This *shading* function was used to produce a chirped grating with wider flattop reflectivity and higher sidelobe suppression. The apodised grating centred at 1557.23 nm had a κ=368 and sidelobe suppression of about 7.0 dB. This piece of apodised chirped grating was experimentally used as a sensing element in Chapter 4.

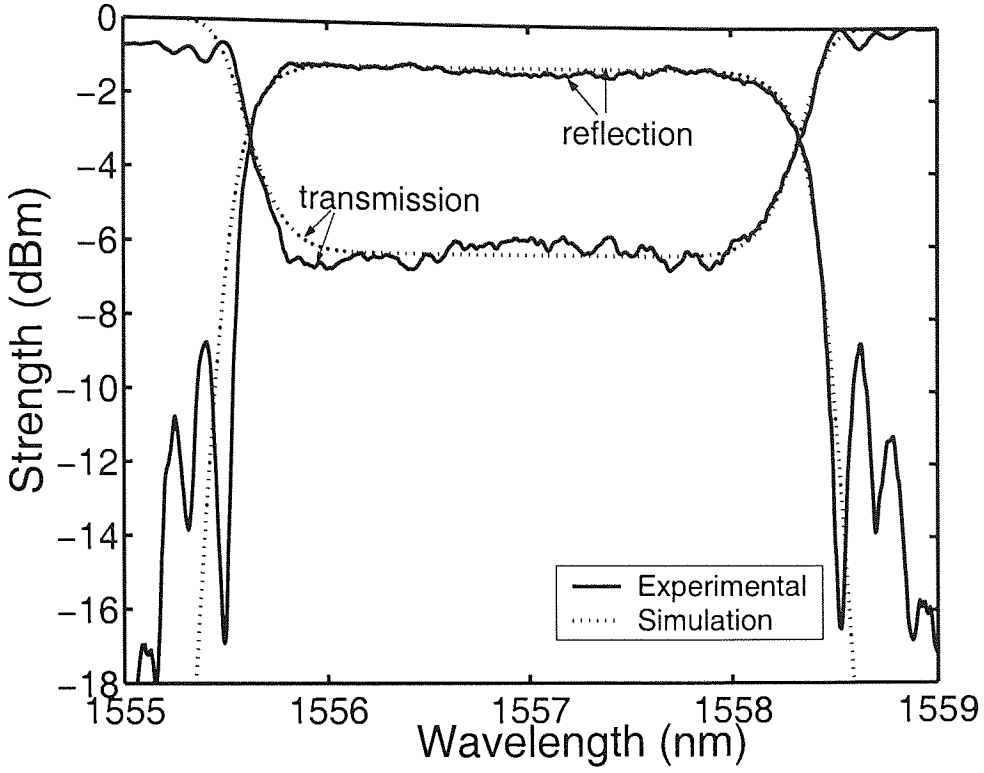

Figure 3.10: Experimental and simulated transmission and reflection spectra for a 70-mm apodised chirped grating with κ=368.

Applications

Apodised gratings are very useful, particularly in WDM system, since they eliminate cross talk problem between adjacent channels and reduce ripples in the dispersion characteristic of chirped Bragg gratings and henceforth improve the performance of system. As mentioned, in the research work carried out by the author, the apodised uniform grating shown in figure 3.9 was used as an optical filter in realising the single-sideband modulation in microwave photonics link in section 6.5, while the apodised chirped grating shown in figure 3.10 was used as a sensing element in the proposed distributed temperature sensing system in Chapter 4. Apart from that, two other apodised chirped gratings with different dispersions were used as dispersion compensator in section 6.4.3 and section 6.4.4. Their specific roles will be described in more detail in the relevant chapters.

3.8 Conclusion

The working principle of FBGs and the fabrication processes have been introduced in this chapter together with the coupled-mode theory and simulation method. Uniform gratings, chirped gratings and apodised gratings are among the common gratings used and they have been studied in this chapter. The common fabrication method is by using the phase mask technique because this technique is more flexible and more repeatable compared to the holographic and point-by-point techniques. To simulate the characteristics and the responses of gratings, transfer matrix method based on the coupled mode equations has been used.

Based on the examples, the experimental result normally exhibits higher sidelobes and a rougher profile compared with the simulated result. This is due to the reason that there may exist errors during the fabrication process, such as stitch errors in the phase mask, dirt on the phase mask, dirt on fibre, non-uniformity in photosensitivity of fibre, non-uniformity in laser source, unfocused laser source, optical misalignment, instability of scanning stage, and so on. Thus, it is impossible to gain a sidelobe suppression as high as and a reflection spectrum as smooth as the simulation result. Besides, since the radiation mode loss at shorter wavelength is not included in the coupled-mode formalism, there exists, potentially, a discrepancy between the experimentally measured and simulation results.

Chapter 4

Chirped Fibre Bragg Grating Temperature Sensor

4.1 Introduction

The optical fibre distributed temperature sensing (DTS) method is a relatively new system for temperature monitoring. It uses optical fibre instead of thermocouples or thermistors, as has typically been the case in the past. It has lately generated much attention because of its minimal dimension and the considerable advantages in hostile environments, such as in the presence of corrosive chemicals, high temperature, high electric, magnetic or strong radio frequency fields. A range of miniature optical fibre temperature sensors have been reported in recent years and a small number have been successfully commercialised. Most of them are built based on the principle of fluorescence [69], absorption of rare-earth-doped fibre [70], reflection intensity profile [71] and interferometry [72]. However, they are mainly point sensors, which only measure temperature at a small area or point rather than giving the temperature distribution over the whole area under test. Prior knowledge of the placements of the point sensors is required and it might need a large number of sensors in order to cover the whole area under test.

In this chapter, a distributed temperature sensing system consisting of an apodised chirped fibre Bragg grating (FBG) is presented. Systems proposed by others are firstly described in terms of their measurement principles and temperature profile recovery methods. Then, the least squares optimised fitting process adopted in this proposed system is described followed by the introduction of the Fabry-Perot effect induced by the temperature change within a grating, which is the working principle of the proposed sensor. To determine the grating physical parameters from its reflection response, a synthesis model based on the transfer

matrix method as detailed in the previous chapter is introduced. Through the understanding of the Fabry-Perot effect, a modified parametric model is presented to reconstruct the distributed temperature profile applied to the apodised chirped FBG. A series of experimental results are presented and are compared with the fitted results from the proposed model. The ability to measure two heated regions, factors that affect the performance of the synthesis model, ripple problem and the coverage of the proposed distributed sensing system will also be brought up in the discussion before the conclusion is made. The proposed system has successfully shown that, unlike other approaches, it is capable of providing distributed non-monotonic temperature measurements through a simple approach.

4.2 Background

As most of the temperature sensing applications need efficient, fast and accurate monitoring over the area under test, fibre-optic intracore Bragg gratings functioning as mirrors with wavelength-selective reflectivities have emerged as a promising candidate in distributed temperature sensing. These grating based sensors are popular because of their feasibility in multiplexing, higher resolution, lower cost and simplicity in signal processing based on the wavelength-encoded reflected signals.

The key issue of these sensors is the need for high resolution detection of the Bragg wavelength shift. In most FBG temperature sensing schemes, the typical value of temperature sensitivity of fibre is about 10 pm/K at 1550 nm [6]. It means that an 1-nm shift of Bragg wavelength near 1550 nm is caused by a change of 100 K in temperature. As most of the conventional optical spectrum analysers have a measuring resolution of 0.06–0.1 nm, a FBG sensor using an optical spectrum analyser as a demodulation system can not evaluate the temperature change within 6–10 K [7] if the direct wavelength shift method is used.

To overcome this limitation, different numerical methods for Bragg grating based distributed sensing systems have been reported [73–84] and they have achieved various degrees of success. Most of them have concentrated on the problem of synthesising or reconstructing a FBG structure (grating period and/or refractive index modulation) from its corresponding reflection response in obtaining information about the applied strain or temperature profiles for distributed sensing. Although some of them have predominantly focused on the measurements of strain, the numerical methods can also be applied to temperature measurements.

Among them, Huang *et al.* [73] and LeBlanc *et al.* [74] have proposed a demodulation method based on either the intensity or phase spectrum. In this method, the disturbance distribution onto a FBG can be obtained by inversely solving the close-form relation between the disturbance and the intensity or the phase spectrum. A recently proposed and efficient

method for grating reconstruction is the layer-peeling algorithm (LPA) that provides a path integral solution to the inverse problem by use of causality argument and by taking into account all the multiple reflections inside the grating [85]. However, LPA needs both the amplitudes and the phase parameters of the reflection. Although the measurement of the reflected intensity spectrum requires only an optical spectrum analyser the phase spectrum technique needs a more complex setup including an interferometric scheme. It is also worth to point out that the above-mentioned approaches are only suitable for monotonically increasing or decreasing disturbance profiles with fairly large gradients and the measurement of an arbitrary distributed disturbance profile is difficult.

The low-coherence reflectometry method reported by Volanthen *et al.* [75] has been shown able to measure the arbitrary disturbance profile but, with the extent of the position scanning, has restrictions on the sensor length. On the other hand, a fibre grating synthesis method based on the Fourier transform proposed by Ohn *et al.* [76] has proven able to measure non-monotonic arbitrary disturbance distributions within a FBG. However, this method is too sensitive to system noise, which limits the reconstruction of high disturbance gradients and discontinuities. Moreover, it is only valid for Bragg grating reflectivity of below 30% and it needs complex intensity and phase spectra. As in [76], the direct group-delay measurement technique suggested by Duck *et al.* [77] is also restricted by the system noise because it involves the calculation of the derivative of a phase function. Besides, the need of radio frequency schemes in the setup makes the system complex and costly for on-site application.

Muriel *et al.* [78], Azana *et al.* [80–82] have suggested reconstructing the grating period of an FBG from its corresponding complex reflection coefficient using time-frequency signal analysis based on Wigner-Ville (WV) and spectrogram (SP) distributions. Numerical simulations have shown that this method is able to reconstruct the grating period of arbitrary FBG structures with very high accuracy provided that the coupling is not too strong for resonant structures where the Bragg frequency is the same at different points within the device. Although the technique is not restricted to weak (reflectivity <30%) gratings, it requires FBG's complex reflection coefficient. Besides, it is difficult to measure the reflection spectra of FBG in the reported experiment.

More recently, a genetic algorithm (GA) method was reported by Casagrande [83] to inversely track the distributed disturbance based on the intensity spectrum of FBG. The numerical simulations have successfully shown the potential and versatility of the approach. However, there exist possible problems induced by the dependence of initial values of the grating parameters in the proposed algorithms. The initial values are the first values to be entered into an algorithm for simulation. The reconstruction error is limited when a large

number of interrelated parameters need to be adjusted [86], which is the bigger the number of parameters, the longer time the simulation takes. The choice of the initial values of the grating parameters also influences the convergence speed of the simulation algorithm. Moreover, the reported GA algorithm is limited to only monotonic measurement.

Another GA approach reported by Lo [84] has the same problem in choice of initial values although it has demonstrated that non-monotonic measurement is possible. Lhommé [87] reported another method based on Nelder-Mead simplex algorithm which is the combined version of LPA and GA. They have shown that the method is faster despite the convergence speed of simulation algorithm depending on the choices of initial values. However, only reconstructions of simple grating reflection response and uniform temperature determination test were presented.

All of the above-mentioned reconstruction algorithms for FBG reflection and group delay responses have shown their different degrees of successes. Nevertheless, they have only emphasised on the synthesis of FBG characteristic parameters, such as coupling coefficient, refractive index modulation and its full-width half-maximum (FWHM) bandwidth. Even when they claimed that the approaches can be applied for temperature sensing, only uniform or monotonic measurements were demonstrated. Besides, it is worth to point out that some of them are only suitable for point sensing or for quasi-distributed sensing by using many point sensors.

In the following sections, the synthesis models and the working principle of the proposed FBG based distributed sensors are presented. First, a very simple and yet accurate approach based on the transfer matrix method and the optimised least squares curve fitting algorithm is introduced. The algorithm used by the least squares curve optimised fitting is based on the interior-reflective Newton method. Then, a description about the Fabry-Perot cavities created by intra-grating wavelength shift in FBG is given followed by two synthesis models used in this proposed system. The first synthesis model is straightforward and essential. It is built to evaluate the FBG physical parameters from its reflection spectrum. The second model is a modified version of the first one. It is constructed to include the temperature change effect on a FBG both with a uniform temperature change throughout the whole FBG and with a localised temperature change on part of the FBG.

4.3 Least Squares Optimised Fitting

As least squares optimised fitting is able to solve nonlinear curve-fitting (data-fitting) problems in the least squares sense, it is used to optimally search for the grating reflection spectrum as well as the applied distributed temperature profile that can generate a reflection

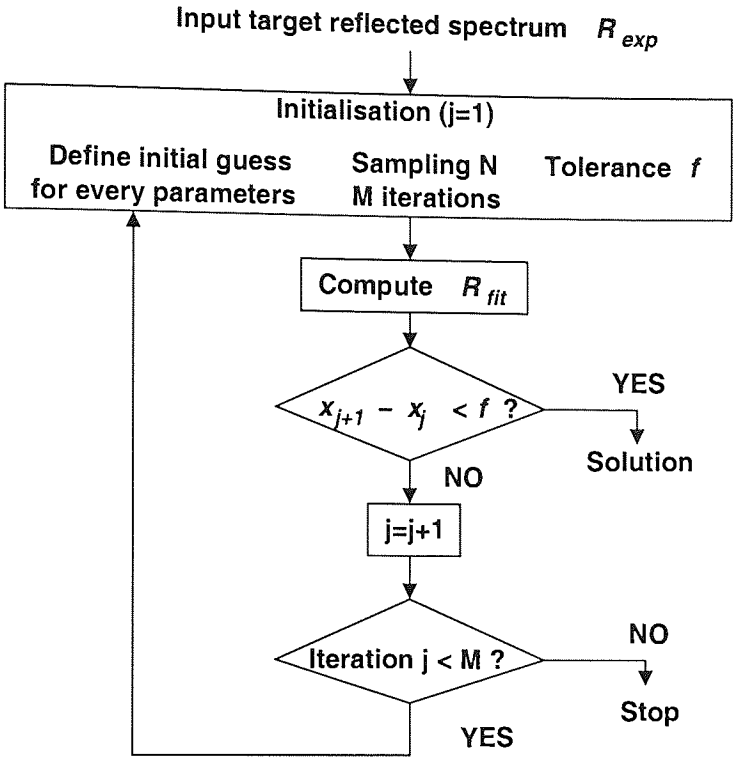

Figure 4.1: Flow chart showing the steps of the optimisation procedure.

spectrum in agreement with the experimental spectrum. Its optimisation process is shown in figure 4.1. Here, the solution is to get the parameters that can generate a reflection spectrum to "best-fit" the experimental reflection spectrum. This solution can be expressed as

$$Tol = min\frac{1}{2}|R_{fit} - R_{exp}|^2 = \frac{1}{2}\sum_{i=1}^{n}\left(R_{fit} - R_{exp}\right)^2, \tag{4.1}$$

where i is the number of iterations, R_{fit} and R_{exp} are the fitted reflection spectrum and the experimental reflection spectrum, respectively. This process can be executed by using the lsqcurvefit Matlab routine with the optimset option where optimset represents the optimisation. This optimised fitting routine utilises an algorithm based on the interior-reflective Newton method that can be easily implemented. This method is based on a subspace trust region method. Each iteration involves the approximate solution of a large linear system of equations using the method of preconditioned conjugate gradients (PCG). The PCG output direction is either a direction of negative curvature or an approximate solution to the Newton system. In either case, it is used to help to define the two-dimensional subspace used in the trust region approach. Algorithm PCG exits when a direction of negative (or zero) curvature is encountered.

In every evolution of the least squares optimised fitting, the current solution is better than the previous solution and the algorithm is iterated until the desired fitness is acquired, or it

may stop if the number of the iterations exceeds the assigned value, M. In the later case, it indicates that there is no convergence for the fitting and the process has to be abandoned in order to save time.

As can be noticed, the desired fitness must be minimised to a desired value in order to give the most accurate solution. In this optimisation process, the choice of the fitness function is fundamental in order to have a correct and efficient search of the solution. In the synthesis models, the fitness function defines the absolute difference between the previous fitted parameters x_{j-1} and the current fitted parameters x_j in producing the smallest Tol. This fitness f can be defined as

$$f = |x_j - x_{j-1}|. \tag{4.2}$$

Like other conventional optimisation methods [83, 84], the convergence speed depends on the number of unknown parameters, initial choice of values, desired fitness, number of wavelength points measured on the spectrum and certainly the processing speed of the computer.

4.4 Fabry-Perot Effect

For a restricted temperature interval from 0 K to 100 K, the dependence of Bragg wavelength to temperature T is approximated by a linear expression as [6]

$$\lambda_B(T) = \lambda_B(T_0) + A \times (T - T_0), \tag{4.3}$$

where A is the FBG temperature dependence coefficient, which can also be referred to as temperature sensitivity, and T_0 is the initial temperature. Based on this dependence, when the grating is heated, its Bragg wavelength shifts from its original wavelength to a wavelength with a higher value. For a chirped FBG, the localised heating within the grating manifests itself as a localised shift in the resonant wavelength of the grating. This intra-grating wavelength shift causes two separate regions in the grating being resonant at the same wavelength leading to the formation of the Fabry-Perot cavities within the chirped grating. This phenomenon is illustrated in figure 4.2 where the wavelength distribution of a grating with a single heated region at $\Delta T = 60$ K is shown. The same concept applies to multiple localised heated regions. As an example, the wavelength distribution for two localised heated regions at $\Delta T = 50$ K is shown in figure 4.4. These illustrations were obtained based on the coupled-mode theory implemented by the transfer matrix method with the temperature change effect which will be discussed in section 4.6.

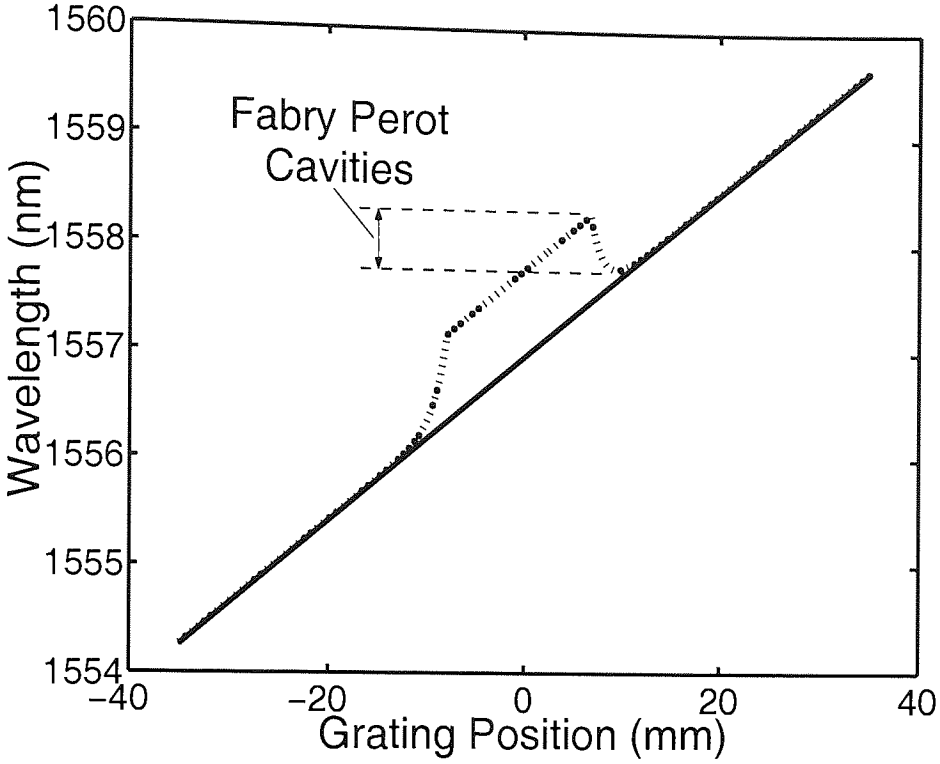

Figure 4.2: Resonant wavelength distributions at $\Delta T = 0$ K (—) and $\Delta T = 60$ K ($\cdots$) along an apodised chirped FBG.

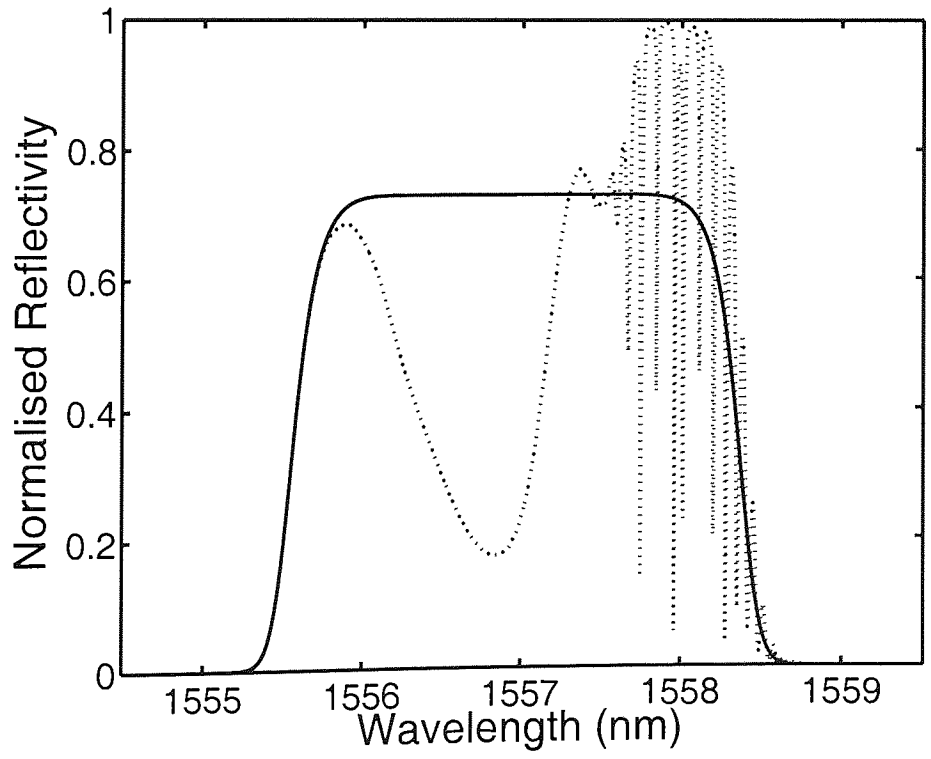

Figure 4.3: Corresponding reflection spectrum at $\Delta T = 0$ K (—) and $\Delta T = 60$ K ($\cdots$) along an apodised chirped FBG.

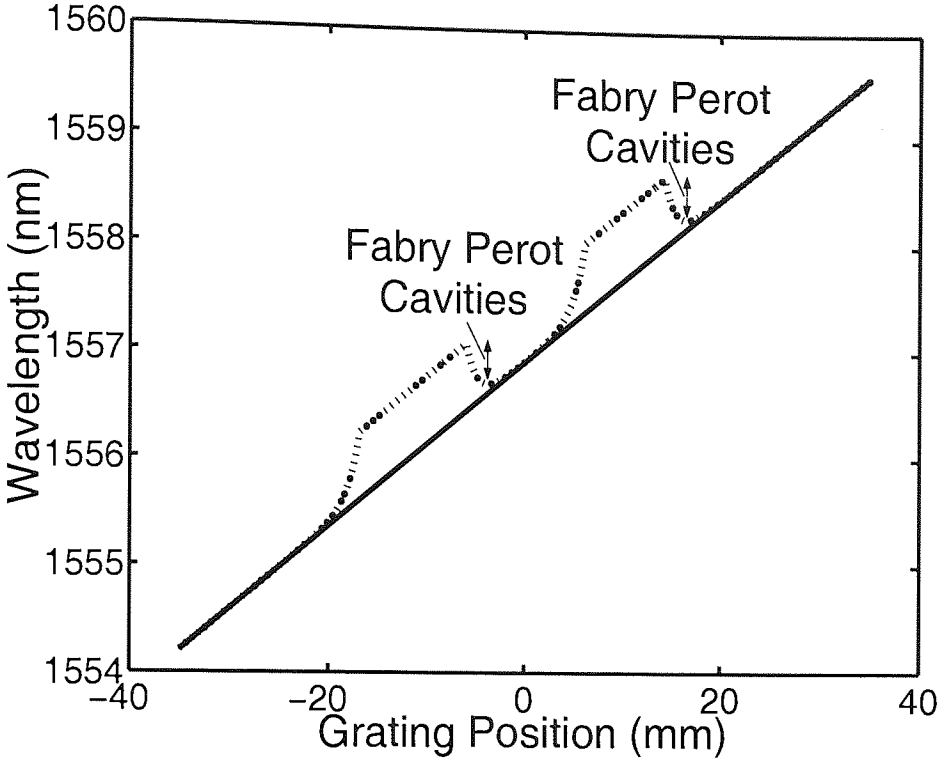

Figure 4.4: Resonant Wavelength distribution at $\Delta T = 0$ K (—) and $\Delta T = 50$ K ($\cdots$) with two heated regions along an apodised chirped FBG.

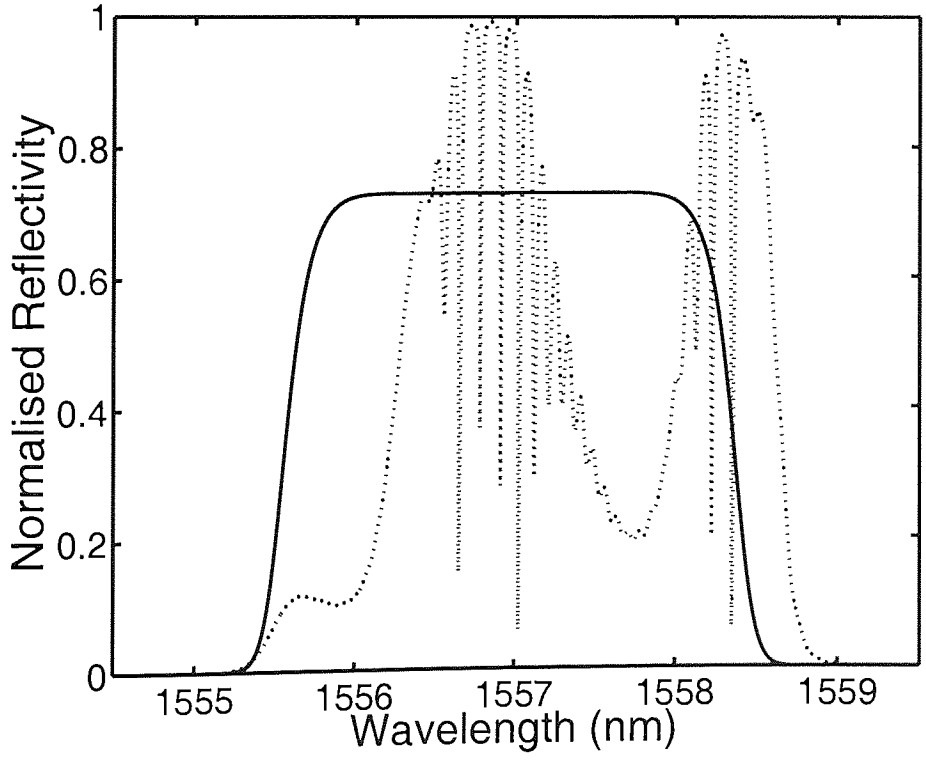

Figure 4.5: Corresponding reflection spectrum at $\Delta T = 0$ K (—) and $\Delta T = 50$ K ($\cdots$) with two heated regions along an apodised chirped FBG.

As can be seen from figure 4.2 and figure 4.4, the grating is interrupted due to the intra-grating wavelength shift. This shift reduces the reflectivities of the original wavelengths corresponding to the heating location and forms the Fabry-Perot cavities at the resonant wavelengths. Consequently, the reflectivities of the grating wavelengths at the new resonant wavelengths are deformed due to the resulting the Fabry-Perot resonant cavities. This phenomenon can be clearly seen from the corresponding reflection spectrum with single heated region in figure 4.3 and the corresponding reflection spectrum with two heated regions in figure 4.5. The free spectral range of the Fabry-Perot cavities produced in the grating depends on the magnitude of the resonant wavelength shift, which in turn, depends on the magnitude of the temperature change onto the grating.

The Fabry-Perot effect in the grating plays a very important role in the proposed system. The strong distinction in reflection profile provides a more useful and informative data for the interrogation compared to the wavelength-shift interrogation method that highly depends on the measuring resolution of the spectrum analyser. It does not only reduce the fitting time of the least squares optimised process, but also eliminates any ambiguities caused by ripples in the reflection profile. This greatly improves the accuracy and spatial resolution of the measurement.

4.5 Synthesis Model for FBG Physical Parameters

This section describes the synthesis model used to evaluate the physical parameters of the apodised chirped FBG based on its reflection spectrum. As described in the last chapter, the reflectivity ρ of a uniform grating is given by equation 3.12. Since an apodised chirped FBG is able to provide a broader band of constant reflectivity and a higher side lobe suppression, it is employed as the sensing element in the proposed system. To account for the linear chirp in the apodised chirped grating, the z-dependent resonant period becomes

$$\Lambda_B(z) = \Lambda_c + \gamma_p z, \tag{4.4}$$

where Λ_c is the grating period at the centre of the grating and γ_p is the grating period chirp with z spanning from $-L/2$ to $L/2$ where L is the physical length of grating. Consequently,

$$\lambda_B(z) = \lambda_c + \gamma z, \tag{4.5}$$

where λ_c is the central wavelength of grating and γ is the effective chirp rate. To account for the apodisation *shading* profile in the apodised chirped grating, the z-dependent coupling coefficient becomes

$$\kappa(z) = \kappa \cdot f(z), \tag{4.6}$$

where $f(z)$ is the apodisation profile. The function $f(z)$ can be any apodisation profile, for instance, raised cosine, Gaussian, tanh, Blackman or sinc functions.

In the proposed system, in order to have a wide flat top reflection spectrum, the chirped grating is apodised with a sixth-order hyper-Gaussian profile. Thus,

$$f(z) = \exp\left[-\left(\frac{2z}{l}\right)^{12}\log 2\right], \tag{4.7}$$

where l is the physical length of the grating at full-width half-maximum (FWHM) bandwidth. The broad band flat top reflectivity and high side lobe suppression of the hyper-Gaussian apodised chirped grating allows it to be used to diagnose temperature change over a large area under test with just a single piece of fibre [88].

Before a grating can be used as the sensing element, the reflection spectrum of an unperturbed case, which is at room temperature with $\Delta T = 0\ K$, is first recorded. Based on the synthesis model described above and the transfer matrix method discussed in the previous chapter, the least squares optimised fitting detailed in section 4.3 is implemented in order to determine the grating physical parameters, which are the coupling coefficient κ, FWHM bandwidth l, central wavelength λ_c and chirprate γ of the grating. This measurement is only made once and the four parameters are used to characterise the grating before the grating is used as a sensor to eliminate any cyclic ripples caused by the system and as a reference for the subsequent reflection spectra when temperature change is applied.

In this model, the fitness of the optimised fitting is set at 1×10^{-6}, which means that the iterations stop when the f value reaches 1×10^{-6}, which also implies the convergence point. At this point, the fittest values of the four parameters, κ, l, λ_c and γ are obtained. Since the grating is fabricated based on the chirped phase mask fabrication technique, the initial values of κ, l, λ_c and γ are given from a range of potential values. The number of wavelengths scanned is set at a value that is commensurate to the measurements obtained from the spectrum analyser. For example, for the next two examples, it was set at 701 and 401, respectively.

Figure 4.6 and figure 4.7 show the transmission and reflection spectra of the two apodised chirped gratings used in the proposed distributed sensing system and their parameters optimised from the synthesis model described above can be found in table 4.1 and table 4.2. Both gratings were fabricated with a chirprate of 0.773 nm/cm. This value was selected because it could provide a wide band reflectivity without losing the flat top characteristics of

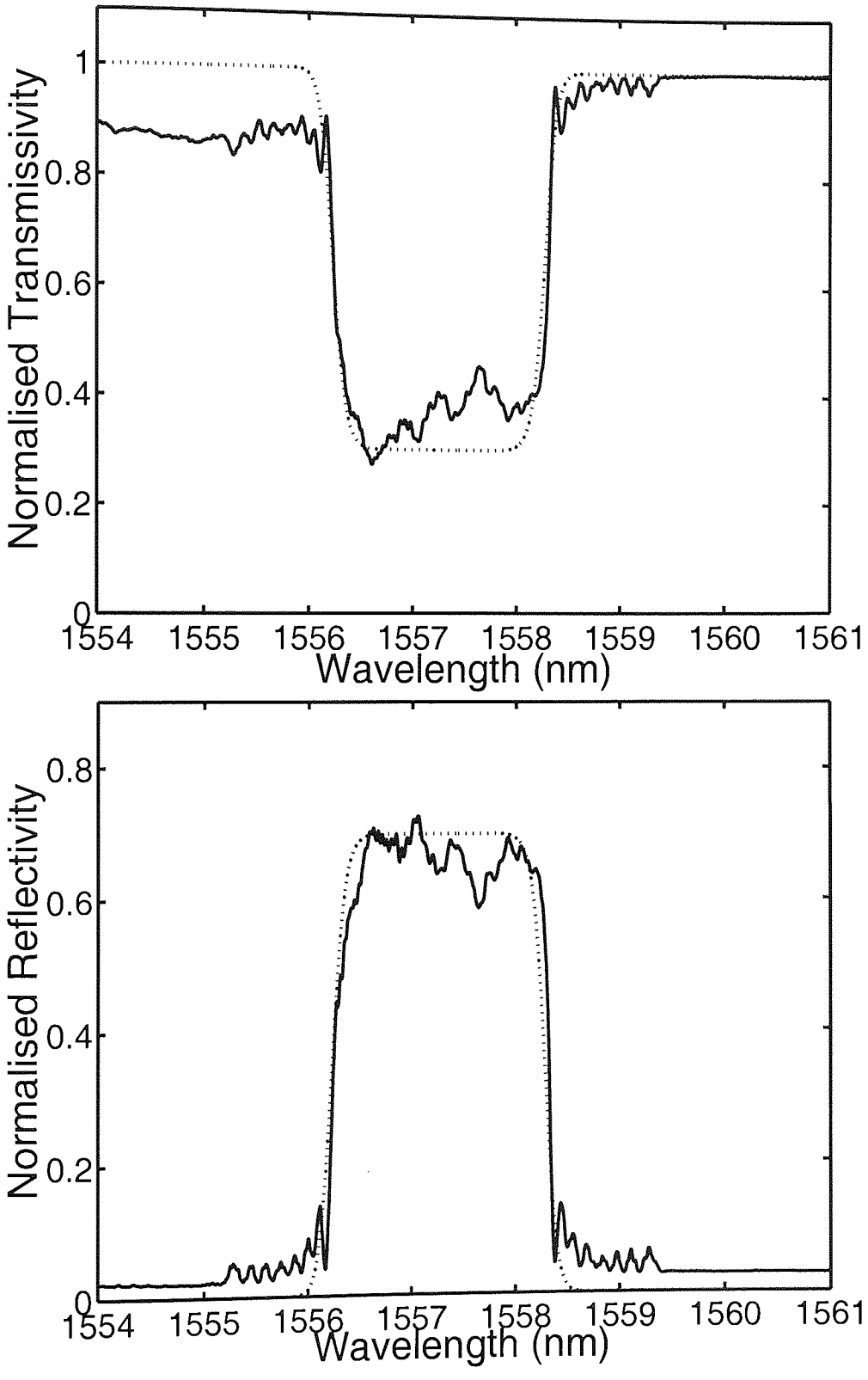

Figure 4.6: Measured (–) and fitted (···) transmission and reflection spectra of grating G1 used for uniform temperature determination test.

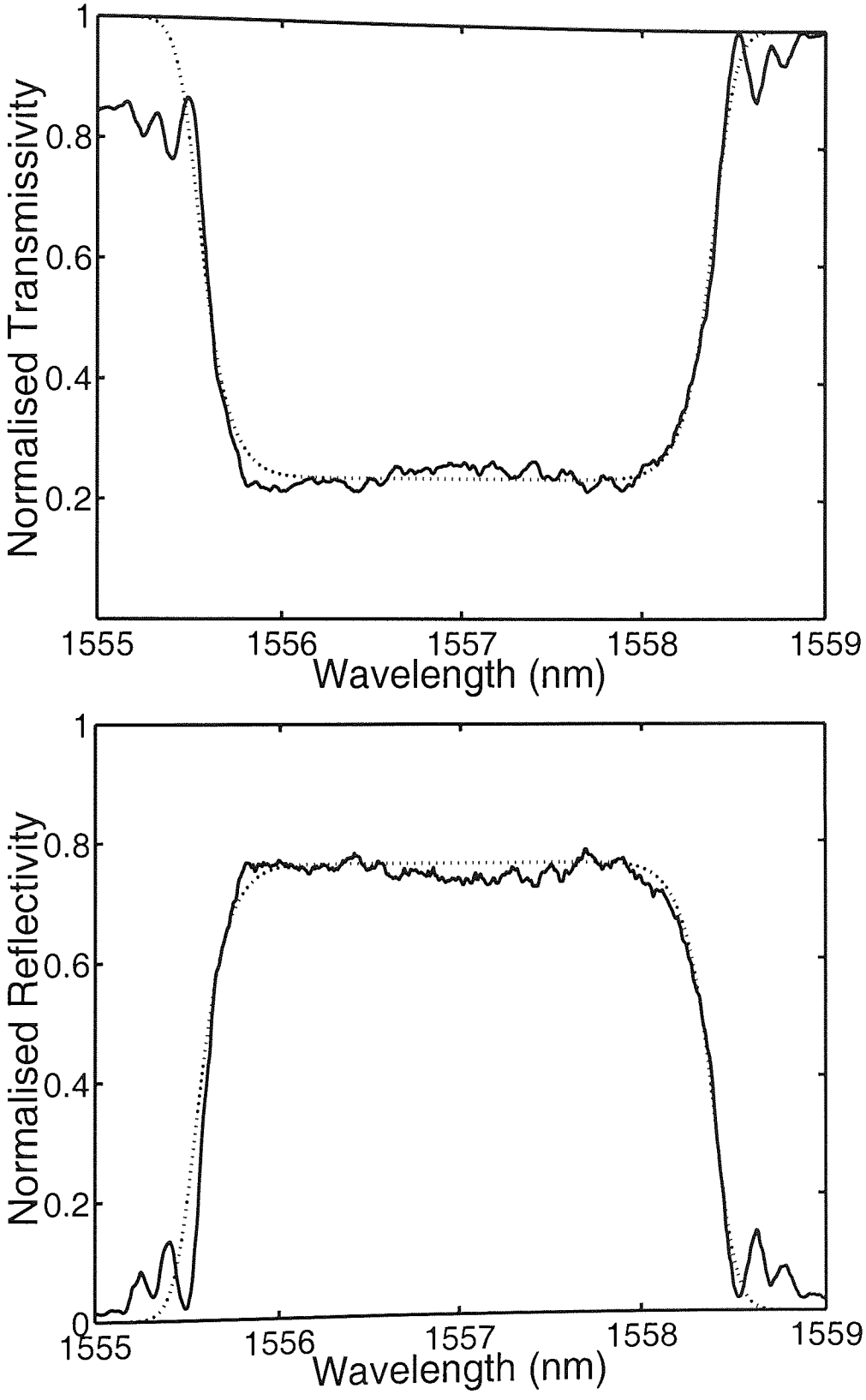

Figure 4.7: Measured (–) and fitted (···) transmission and reflection spectra of grating G2 used for localised temperature determination test.

Characteristics	G1
coupling coefficient κ	335
length of the grating L	40.0 mm
central wavelength λ_c	1557.25 nm
bandwidth	2.21 nm
FWHM bandwidth l	1.95 nm
effective chirp rate γ	0.773 nm/cm

Table 4.1: Characteristic parameters of the grating G1.

Characteristics	G2
coupling coefficient κ	368
length of the grating L	70.0 mm
central wavelength λ_c	1556.97 nm
bandwidth	3.09 nm
FWHM bandwidth l	2.87 nm
effective chirp rate γ	0.773 nm/cm

Table 4.2: Characteristic parameters of the grating G2.

the grating. As can be seen from the spectra in figure 4.6, it was quite difficult to maintain a flat top reflection profile. The irregularities in the spectra could be caused by the errors occurred during the fabrication process, such as non-parallel alignment of the fibre and the phase mask, stitch errors and dirt on the phase mask, and vibration of the stage. This situation became worse when the grating was made with higher chirprate and longer length. Thus, a compromise had to be made in order to reach an optimum balance between the wide bandwidth and flat top reflectivity. These two gratings were used for the uniform temperature sensing and the localised temperature sensing in the proposed system which will be discussed in the experimental work.

4.6 Proposed Synthesis Model for FBG as a Distributed Temperature Sensor

This section introduces the synthesis model built to include the temperature effect onto the grating reflection profile. For temperature sensing using an apodised chirped fibre grating, the z-dependent $\lambda_B(z)$ function can be modified as

$$\lambda_B(z) = \lambda_c + \gamma z + g(z, \Delta T, L_p, C_p), \tag{4.8}$$

where $g(z, \Delta T, L_p, C_p)$ is the temperature variation profile along the grating under test that gives the shift in Bragg wavelength where ΔT is the applied temperature change, L_p is the

width of the heat source and C_p is the position of the heat source with reference to the centre of the grating.

In the proposed system, a known temperature change profile is applied to the chirped grating using three contiguous peltiers. When the central peltier acts as the heat source and the rest remain at the room temperature, the temperature change profile can be modelled as

$$g(z,\Delta T,L_p,C_p)=\begin{cases} A\Delta T\exp(k_1(z-a)) & \text{if } z<a \text{ with } a=C_p-0.5L_p \\ A\Delta T & \text{if } b<z<a \\ A\Delta T\exp(k_2(b-z)) & \text{if } z>b \text{ with } b=C_p+0.5L_p, \end{cases} \tag{4.9}$$

where A is the temperature dependence coefficient of the grating, and k_1 and k_2 are the temperature decay coefficients that depend on the ΔT and account for the heat flow to the area adjacent to the heat source. In this work, with the same physical conditions for both sides of the heated region, the assumption of $k=k_1=k_2$ can be made.

By using the grating physical parameters of the unperturbed grating found from the fundamental synthesis model discussed in the last section, the calculated reflection spectrum based on equation (4.8) accounting for the effect of the temperature change profile $g(z,\Delta T,L_p,C_p)$ is least squares fitted to the experimental reflection spectrum obtained with the presence of temperature change. By optimising the fitting, the temperature variation ΔT, the location L_p, the width C_p of the heat source and the appropriate value to account for the heat flow of each specific experimental configuration can be determined. Again, a fitness function is applied and the fitting process stops only when the desired fitness is achieved.

In this proposed synthesis model, the fitness of the optimised fitting is, again, set at 1×10^{-6}. Iterations stop when the f value is achieved with the fittest values of the three parameters, ΔT, L_p and C_p. The number of wavelengths scanned is set at a value in accordance to the measurements obtained from the spectrum analyser. Generally, for a slowly varying temperature change, the previous set of values is used as the starting point for the subsequent measurement to enable the tracking of the distributed temperature changes. In this way, the temperature profile of the area under test can be predicted.

One of the applications of this system is to monitor the temperature of a tumour and its surrounding tissue during hyperthermia treatment since the area to be radiated usually includes the tumour and an area surrounding the tumour [89]. According to the American Brain Tumour Association [89], the radiation may be directed from several angles. This makes the proposed sensor more practical, since it can cover the treated area using only one piece of an apodised chirped fibre grating. More importantly, it is able to provide the temperature profile of the treated area with the information of temperature variation, location and width of the heat source.

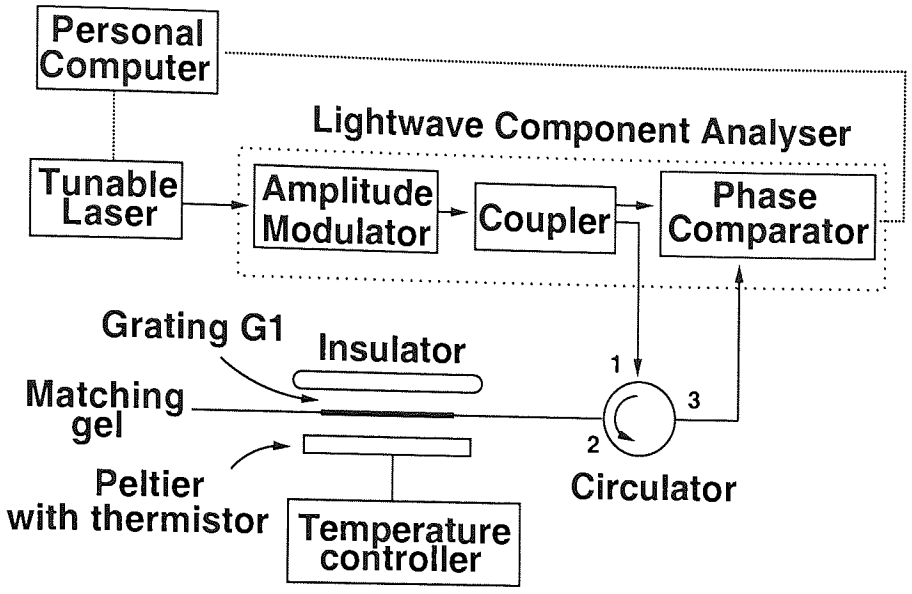

Figure 4.8: Experimental setup for uniform temperature determination test.

4.7 Experimental Setup and Procedure

Before proceeding to the validation tests for the proposed distributed temperature sensing system, a very simple but yet fundamental temperature test was carried out, in which uniform heating was applied to the whole piece of the grating under test. The aim of this test was to evaluate the efficiency of the proposed system and the least squares fitted synthesis model by verifying the temperature dependence coefficient A of the grating in use. After the uniform temperature determination test, a series of localised temperature determination tests, with a temperature variation on a certain part of the piece of the grating, were conducted to validate the proposed system and the proposed synthesis model for distributed temperature sensing.

4.7.1 Uniform Temperature Determination

The working principle of FBG temperature sensors is based on the dependence of the Bragg wavelength λ_B on the temperature T. As in equation (4.3), for a restricted temperature interval from 0 K to 100 K, the relationship between Bragg wavelength and temperature T can be estimated by a linear expression. Typically, the FBG temperature dependence coefficient is about 10–14 pm/K at 1550 nm. It has been measured in silica fibre at 800 nm and 1550 nm with values of 6.8 pm/K and 13 pm/K, respectively [90].

To verify this, a uniform temperature determination test was carried out. The experimental setup for the proposed system is shown in figure 4.8. A tunable laser with a scanning step size of 10 pm and an output power of 50 μW was used as the laser source. The laser was first

impinged to the lightwave component analyser (LCA) which has a resolution of 0.001 dB. It internally split the laser into two, one to the circulator and the other to the phase comparator as the reference arm. The laser fed through the circulator was incident to a grating from its shorter wavelength side and reflected by the grating under test to the LCA through the phase comparator.

During the test, the grating was attached to a 70-mm peltier which served as a heat source. It was used to generate uniform temperature change onto the whole piece of grating through electricity. The temperature of the peltier was controlled by a temperature controller with a resolution of 0.1 K through a thermistor attached to the peltier. A personal computer was connected to the tunable laser and the LCA in order to remotely control them and to capture the reflection spectrum of the grating as well as its group delay response. Matching gel was applied to the fibre end of the grating as to eliminate any Fresnel back reflection that would contribute about 4 % of reflectivity to the reflection spectrum. To avoid heat convection to the environment, an insulator, layers of mica, was used.

The grating in use was grating `G1`. Its characteristic parameters and spectra can be found in Table 4.1 and figure 4.6. It was a 40-mm apodised chirped grating fabricated using a chirped phase mask on a hydrogen-loaded photosensitive fibre. Undeniably, it was a low quality grating with average reflection and transmission spectra, but it is adequate considering that it was solely used in the preliminary and uniform temperature test, in which only the shift of the entire reflection spectrum would be interpreted into temperature change. Thus, the requirement of a flattop reflection profile was not crucial in this test.

To begin the test, as already described in section 4.5, the peltier was firstly set at room temperature, which was 24.0°C. The reflection spectrum and group delay response of the grating were captured at this temperature and they served as a reference for the subsequent reflection spectra in this test. The temperature of the peltier was then increased by 10.0 K above room temperature and was controlled while the spectrum was being captured. Same procedure was carried out with another temperature increment of 10.0 K until the temperature of the peltier achieved 60.0 K above the room temperature. For each temperature increment, reflection spectrum and group delay response of the grating `G1` were taken by LCA. The measured reflection spectrum was then least squares fitted based on the proposed synthesis model. Here, the initial values of the four parameters were found by manually fitting and were entered into the proposed synthesis model for least squares optmised fitting.

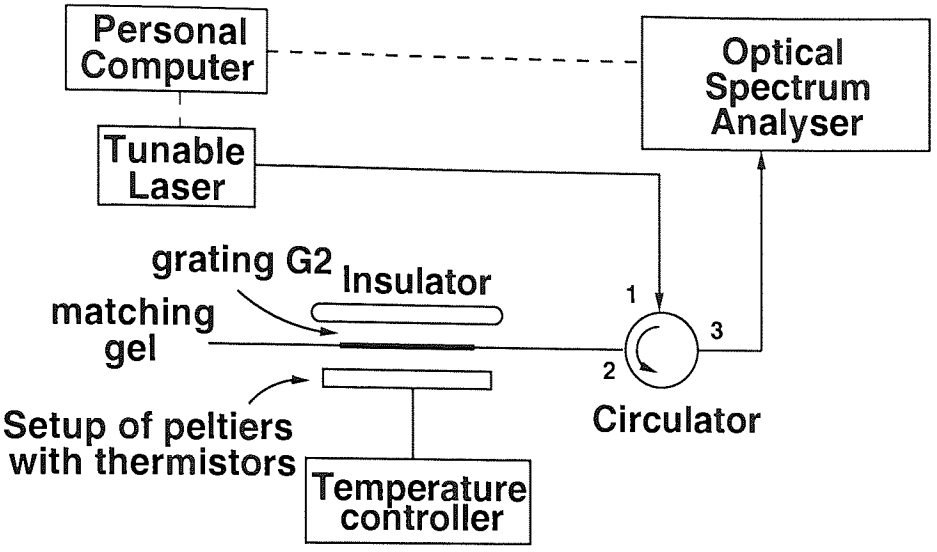

Figure 4.9: Experimental setup for localised temperature determination test.

4.7.2 Localised Temperature Determination

To validate the proposed distributed sensing system, a series of tests were carried out with localised heated region applied onto a 70-mm apodised chirped grating, G2. Again, the characteristic parameters of the grating were found based on the synthesis model in section 4.5 before the test. Its parametric values and spectra can be found in figure 4.7 and Table 4.2. The test was conducted in three stages, which were temperature determination test, location determination test and width determination test. For all the tests, the peltiers were thermally insulated from each other by layers of mica sheet. The setup of the experiment was simplified by substituting the LCA with an optical spectrum analyser (OSA) in order to speed up the measurements. In these tests, the initial values for the parameters were given based on the manual fitting before they were entered into the proposed synthesis model.

Temperature Determination

First of all, a temperature determination test in a localised region was carried out to evaluate the temperature dependence coefficient A of grating G2 and the temperature decay coefficient k of the setup. Figure 4.9 shows the experimental setup for the sensing system. As can be seen, the reflection spectrum of the grating was measured by using a fast scanning tunable laser and an OSA. To achieve the localised heating, the single peltier was replaced by a setup of peltiers as depicted in figure 4.10.

As shown, a localised heating was applied to the grating by using three contiguous temperature controlled peltiers; P1, P2 and P3 with lengths of 31.5 mm, 15.0 mm and 70.0 mm, respectively. At the beginning, all three peltiers were set to the room temperature in order to

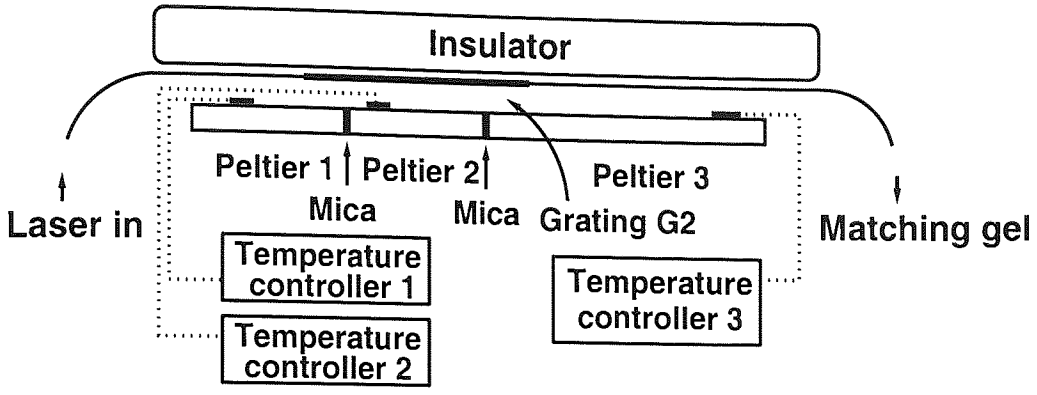

Figure 4.10: Setup of peltiers for localised temperature determination test.

obtain the reference reflection spectrum. The temperature of the central peltier P2 was then increased to 60.0 K by a step size of 5.0 K while the adjacent peltiers P1 and P3 were used to maintain a constant temperature over the remainder of the grating throughout the test by preventing any temperature diffusion from peltier P2 to peltiers P1 and P3, and by avoiding the remaining part of the grating from being heated by the peltier P2.

The measurement of reflection spectrum was taken at each increment. The reflection spectrum of the grating under test was then least squares fitted by the proposed synthesis model discussed in section 4.6 in order to find the temperature dependence coefficient A of grating G2 and the temperature decay coefficient k of the setup, as well as the corresponding location C_p and width L_p of the heat source.

Location Determination

A location determination test was carried out in order to examine the capability of the proposed system of locating the heat source along the grating. The same setup and grating G2 were used. In this test, the centre section of the 70-mm grating was attached on the peltier P2, whose temperature was maintained at 64.0°C. Meanwhile, the temperature for peltiers P1 and P3 were held at room temperature, which was at 24.0°C.

Firstly, a measurement was carried out to obtain the initial location of the heat source. Then, the grating was shifted 10 mm with a step size of 1 mm in the direction of peltier P3. It is worth noting that the centre of the heat source was changed to the shorter wavelength side of the grating every time the shift was made. The reflection spectrum for each shift was captured by using the OSA and was least squares fitted to determine the location C_p and the corresponding width L_p of the heat source. Since the same peltier setup as in temperature determination test was used, the temperature decay coefficient k in this test was referred to the value obtained from the temperature determination test whilst the initial value of the tem-

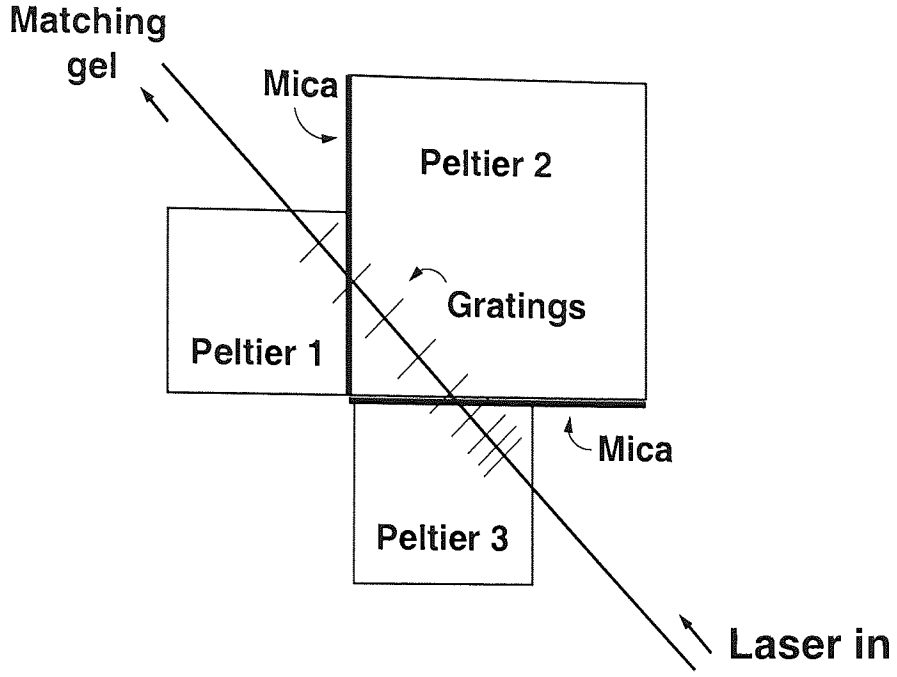

Figure 4.11: Setup of peltiers for width determination test.

perature dependence coefficient A for the optimised fitting corresponded to the temperature determination test.

Width Determination

To examine the capability of the proposed system of determining the width of the heat source, a width determination test was conducted, in which the near-centre section of the grating was attached to different widths of P2. To achieve different widths, the setup of peltiers, as shown in figure 4.11, was used. The width of the heat source could be changed easily by just moving the grating along the setup of the peltiers. In this way, it provided the flexibility in choosing different widths for the heat source. In this test, the temperature of peltier P2 was controlled at 54.0°C while peltiers P1 and P3 were maintained at room temperature. Tests with heated widths of 4.0 mm, 6.0 mm, 12.5 mm, 21.0 mm, 23.5 mm, 27.5 mm, 30.0 mm, 33.5 mm, 37.5 mm and 40.0 mm were carried out. The reflection spectrum for each width change was captured using the OSA and was least squares fitted to determine the three parameters.

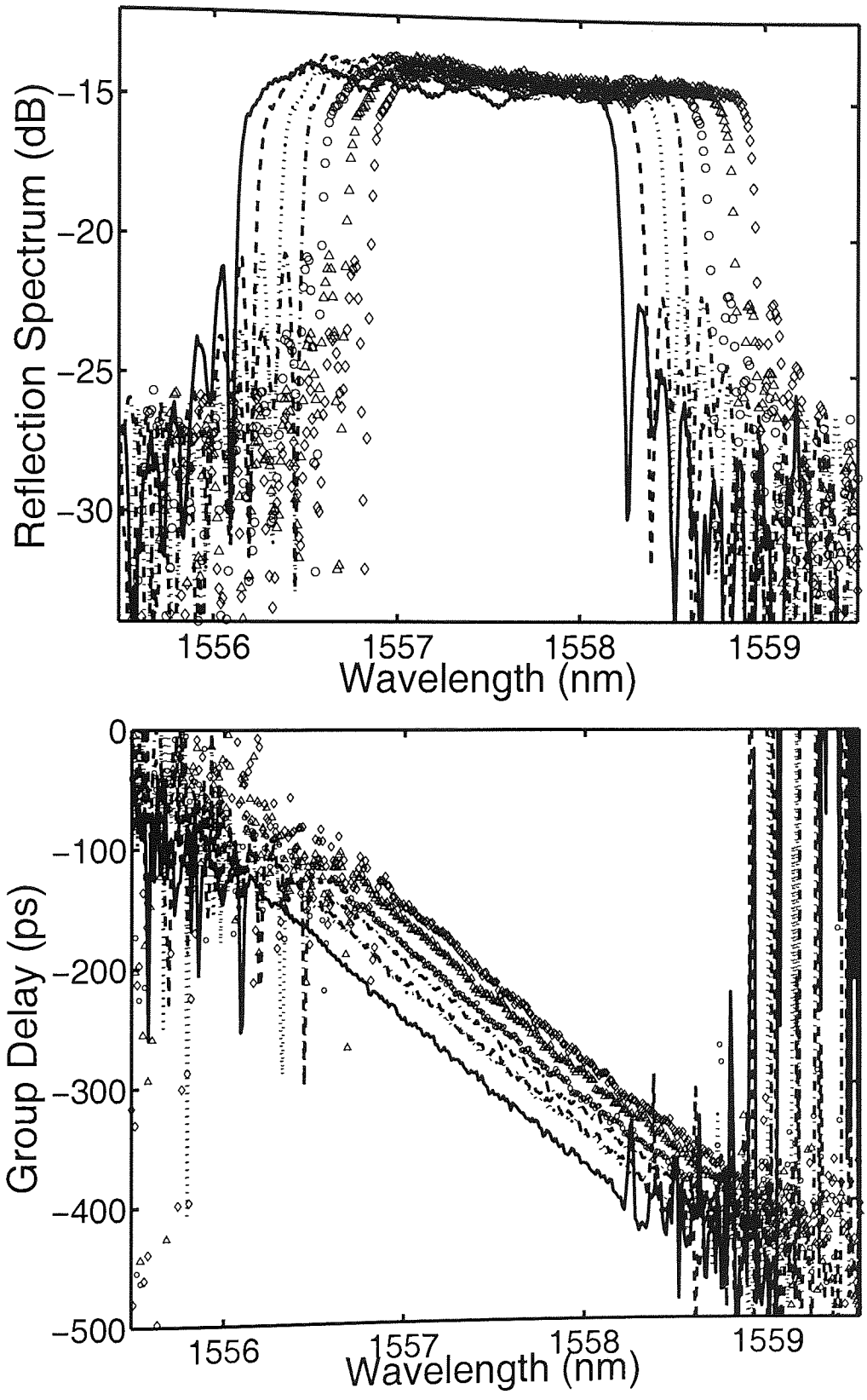

Figure 4.12: Reflection spectrum and group delay response of grating G1 in the uniform temperature determination test when the temperature of peltier P1 was set at (–) 24°C, (- -) 34°C, (···) 44°C, (-·-) 54°C, (○) 64°C, (△) 74°C and (◇) 84°C.

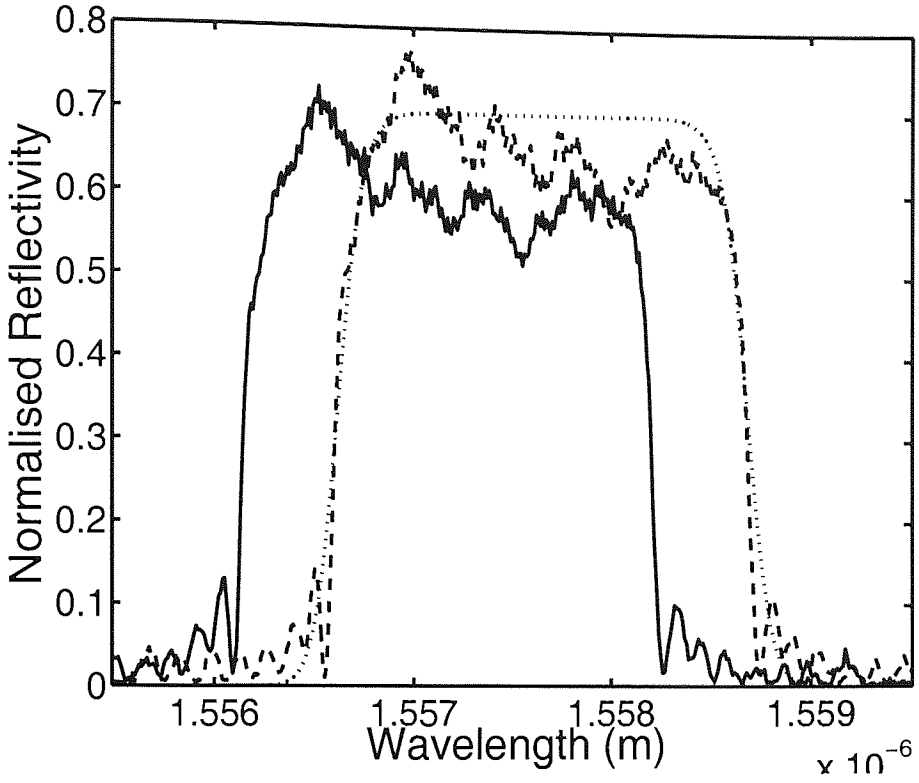

Figure 4.13: Measured reflection spectra at ΔT=0 K (–) and ΔT=40 K (- -) and its corresponded fitted spectrum at ΔT=40 K ($\cdots$).

4.8 Results

4.8.1 Uniform Temperature Determination

The reflection spectra and group delay responses for the uniform temperature determination test at different temperatures using grating `G1` are shown in figure 4.12. The proposed model for the distributed sensing was used to fit the reflection spectrum based on the grating characteristic parameters found from Table 4.1 for `G1`. As the uniform temperature change was applied to the whole piece of grating, $g(z, \Delta T, L_p, C_p)$ could be simplified to $g(z, \Delta T)$ in the proposed model because the information of position C_p and width L_p of the heat source was no longer interesting in this case.

A typical experimental result is illustrated in figure 4.13. The ΔT applied to the grating was 40.0 K. Simulated result has shown a good agreement with the experimental result. By least squares optimised fitting the measured reflection spectra, the wavelength shift of grating at each increased 10.0 K was numerically computed. The results are shown in Table 4.3 and figure 4.14. From the linear regression, the temperature dependence coefficient of the grating was computed to be 11.7 pm/K. This value matched with those cited in [6, 90] and it has proven the dependence of λ_B on temperature variation. Thus, the temperature dependence

T in °C	ΔT in K	Shift in pm
34	10.0	100
44	20.0	220
54	30.0	350
64	40.0	460
74	50.0	580
84	60.0	720

Table 4.3: Experimental wavelength shifts for uniform temperature test.

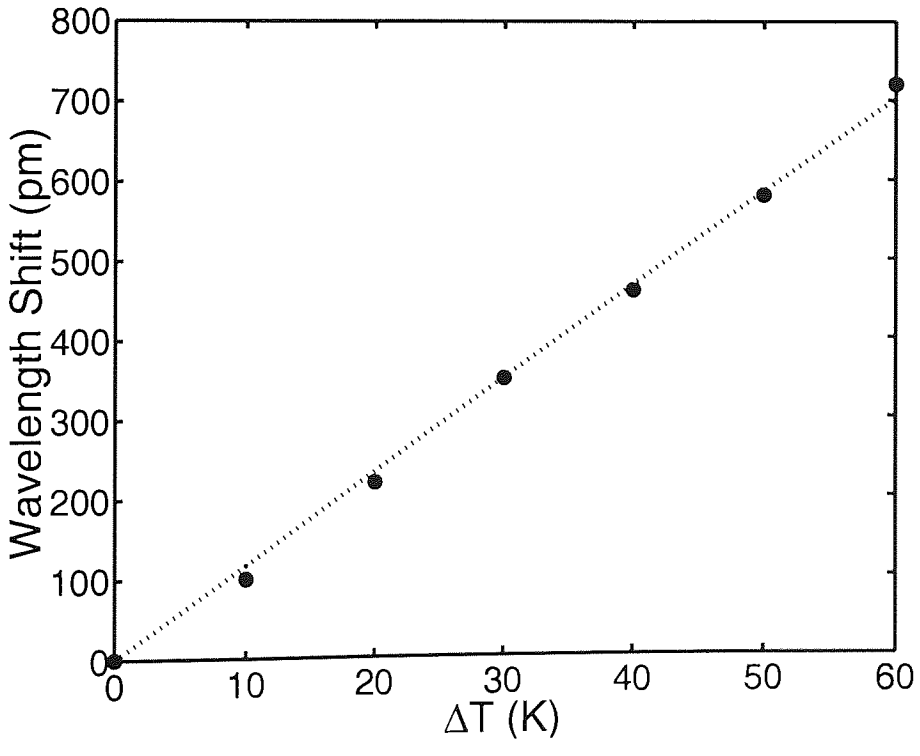

Figure 4.14: Experimental wavelength shift of grating (•) and linear regression (···) which gives the value of temperature dependence coefficient of 11.7 pm/K.

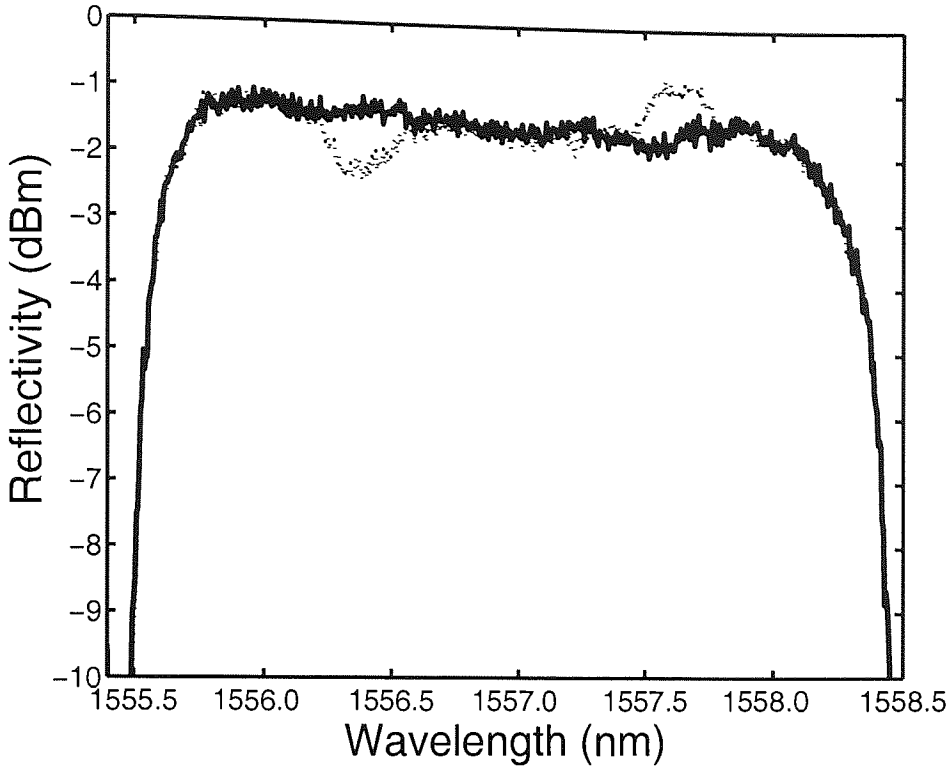

Figure 4.15: Reference (–) and reflection spectra taken when $\Delta T = 10\ K$ $(\cdots)$.

coefficient of the grating was verified.

4.8.2 Localised Temperature Determination

Temperature Determination

First of all, to provide an idea of how the reflection spectrum changes with the temperature change, figure 4.15 shows the variation between the measured reference reflection spectrum for G2 and the reflection spectrum measured with a ΔT of 10 K. It can be seen that there was a significant variation in the reflection profile when a localised temperature change was applied to part of the grating.

A plot of fitted $A\Delta T$ determined from the proposed model versus the applied temperature change is shown in figure 4.16. They were in good agreement to a straight line with a temperature dependence coefficient $A = 13.97$ pm/K. This value matched with other FBG sensor experiments [90]. The standard deviation from the linearity was 30 pm. This A determined the value of ΔT when fitted value for $A\Delta T$ was known.

On the other hand, the fitted value of C_p at each temperature variation is shown in figure 4.17. It shows that the location of the heat source ranged from -0.6 mm to 0.2 mm with an average location at 0.145 mm away from the centre of grating and in the direction towards

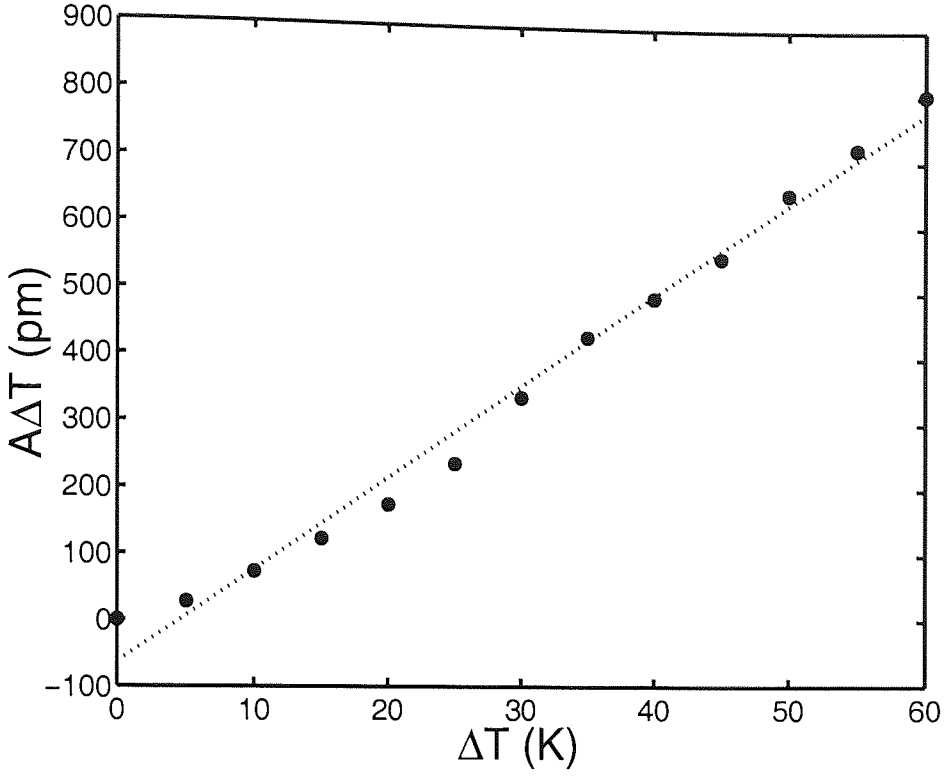

Figure 4.16: Fitted $A\Delta T$ (•) versus applied ΔT. Linear regression ($\cdots$) gives the temperature dependence coefficient of $A = 13.97$ pm/K.

the shorter wavelength side of it. This value matched well with the actual placement of the grating since the near-centre section of the grating was placed onto the centre of the peltier P2 before the test.

As can be seen from figure 4.18, the fitted value of L_p at each temperature variation is given. The slightly bigger value at ΔT=5.0 K might be due to the experimental errors that occur during the test, such as the imperfectness of peltier setup. Besides, it is worth noting that, the grating, G2, used for the test did not have a flat top reflectivity as fitted from the proposed model. This, inevitably, increased the error between the actual value and the fitted result. However, the average value of 14.89 mm did give a good agreement between the fitted and actual width of the heat source since the actual width applied was 15 mm.

Figure 4.19 shows the fitted temperature decay coefficient k for each temperature variation. From the curve, it can be observed that k was temperature dependent. It has relatively higher value (steeper curve) in the low temperature area because of the convection to the ambient was low when temperature of peltier P2 was low. When a higher temperature change was applied, k has a lower value, which meant that there was higher convection to the ambient. This was a well-understood phenomenon. The relationship between k and ΔT which indicated the temperature decay behaviour of the heat source was computed as

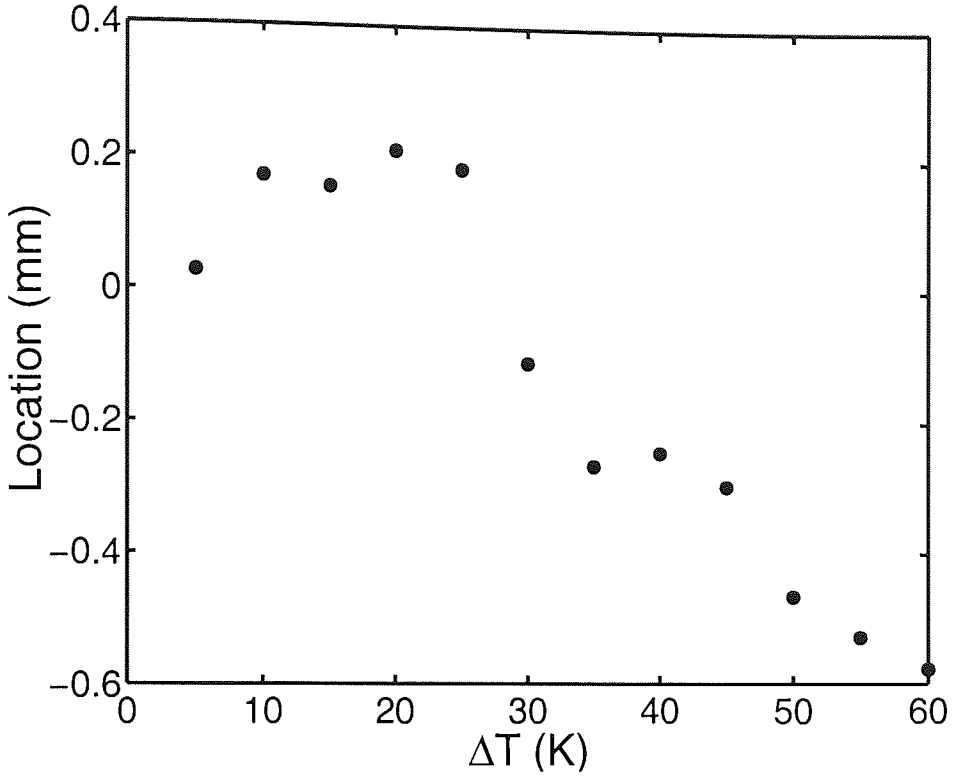

Figure 4.17: Fitted location of heat source C_p with an average value of 0.145 mm away from the centre of grating and towards the shorter wavelength side of grating.

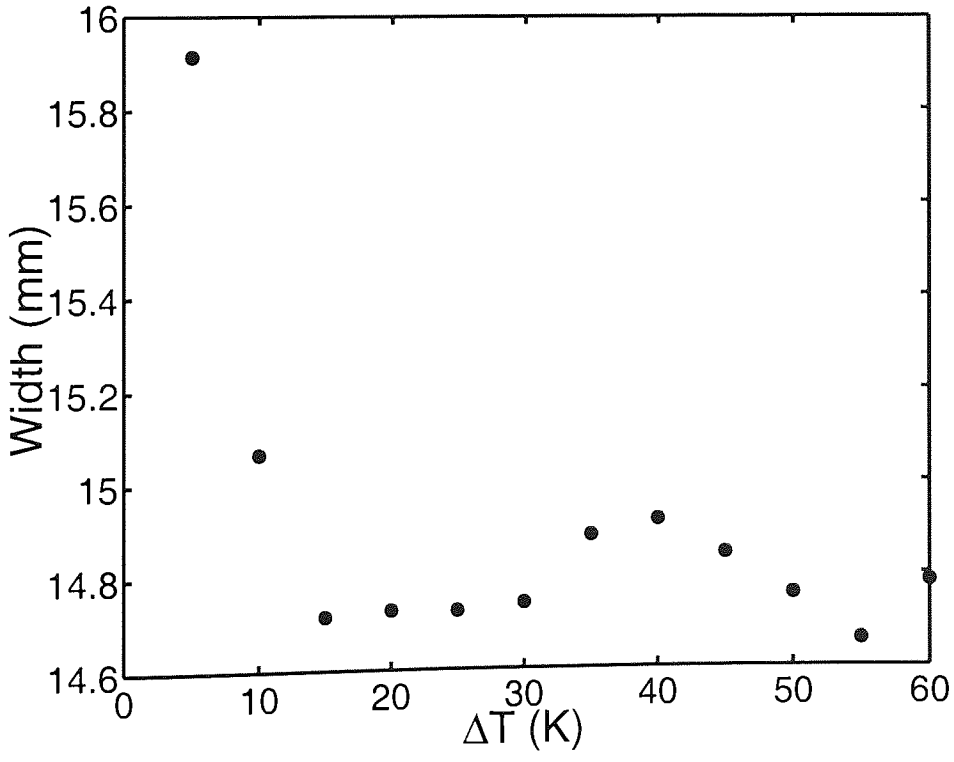

Figure 4.18: Fitted width of heat source L_p with an average value of 14.89 mm.

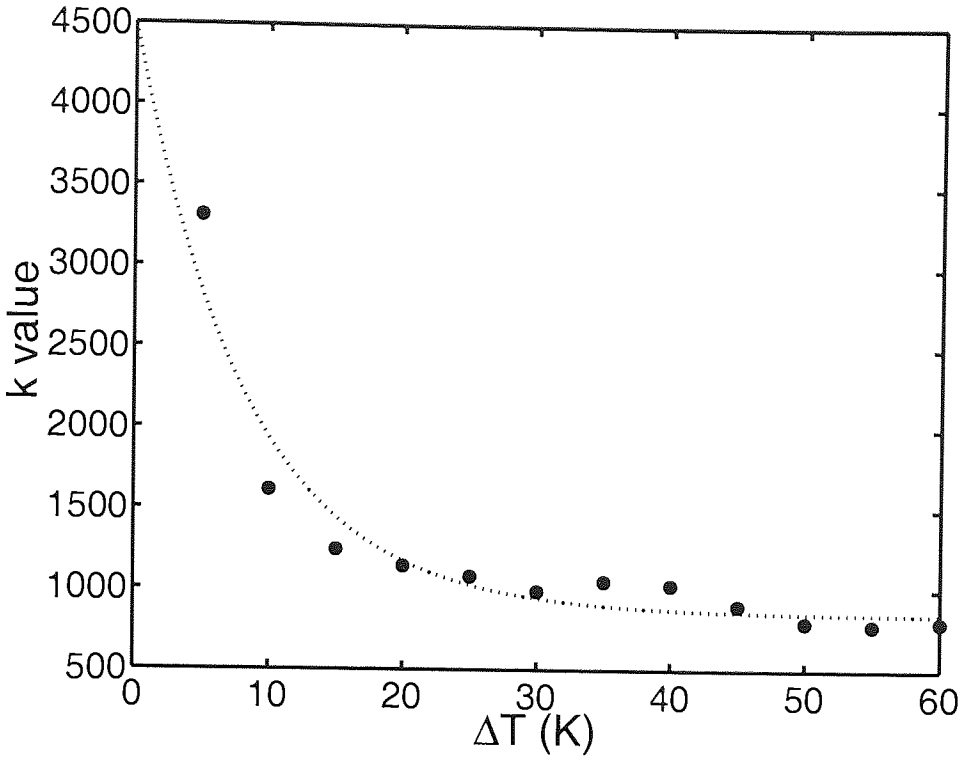

Figure 4.19: Temperature decay coefficient k at each ΔT.

$$k(\Delta T) = 845.89 + 3645.17exp(-0.1208\Delta T). \tag{4.10}$$

Typical experimental and fitted results of the reflection spectrum with $\Delta T = 45.0$ K are displayed in figure 4.20 together with its group delay response as in figure 4.21. The fitted ΔT was 45.3 K with $k = 901$. A good agreement between the experimental and fitted results was gained. Based on the fitted result of the proposed model, the heat source was located at 0.30 mm from the centre of the grating towards the shorter wavelength side of it. This matched the placement of the grating since the near-centre section of the grating was placed onto the centre of the peltier `P2` before the test. Besides, the fitted width of the heat source was 14.84 mm. There was, again, a good agreement with the actual width of the heat source, which was 15 mm in this test.

Based on the values of $A\Delta T$, L_p, C_p and k obtained from the least squares optimised fitting over the measured reflection spectrum in the example above, the temperature change profile over grating `G2` could be simulated from equation (4.9). Figure 4.22 clearly shows the temperature profile over the grating `G2` which was commensurate with the temperature profile provided by the setup of peltiers `P1`, `P2` and `P3`.

In order to further validate the fitted model, all the fitted values obtained from the example above, $A\Delta T$, L_p, C_p and k, were used to simulate the group delay response of grating. The

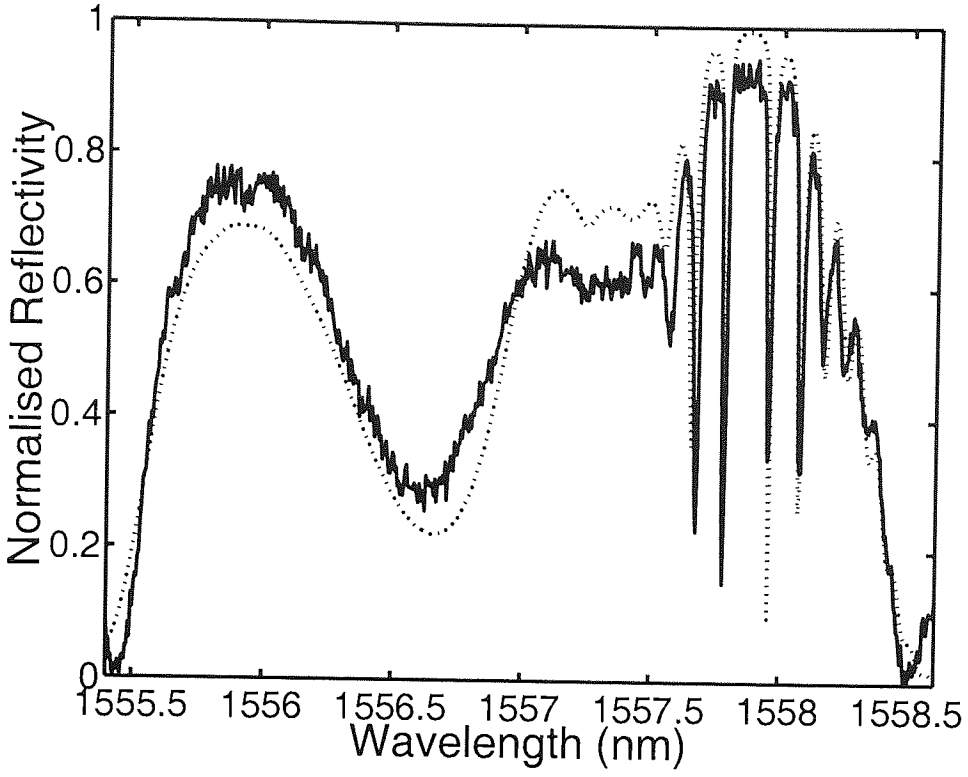

Figure 4.20: Measured (–) and fitted (···) reflection spectrum of grating at $\Delta T = 45.0\ K$.

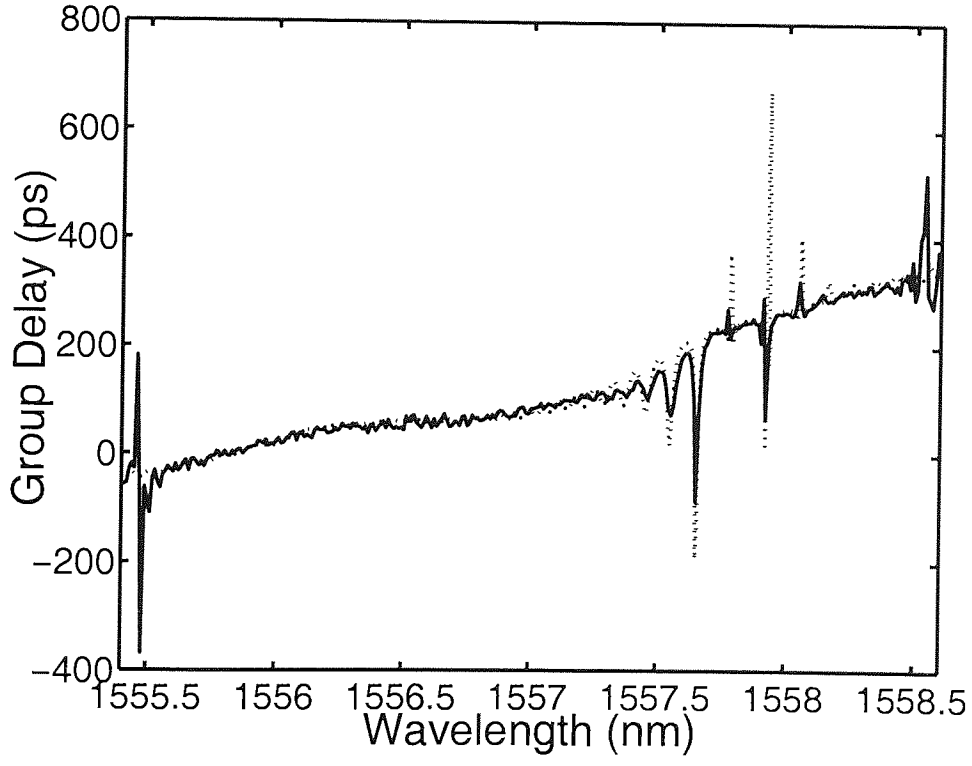

Figure 4.21: Measured (–) and fitted (···) group delay response of grating at $\Delta T = 45.0$ K.

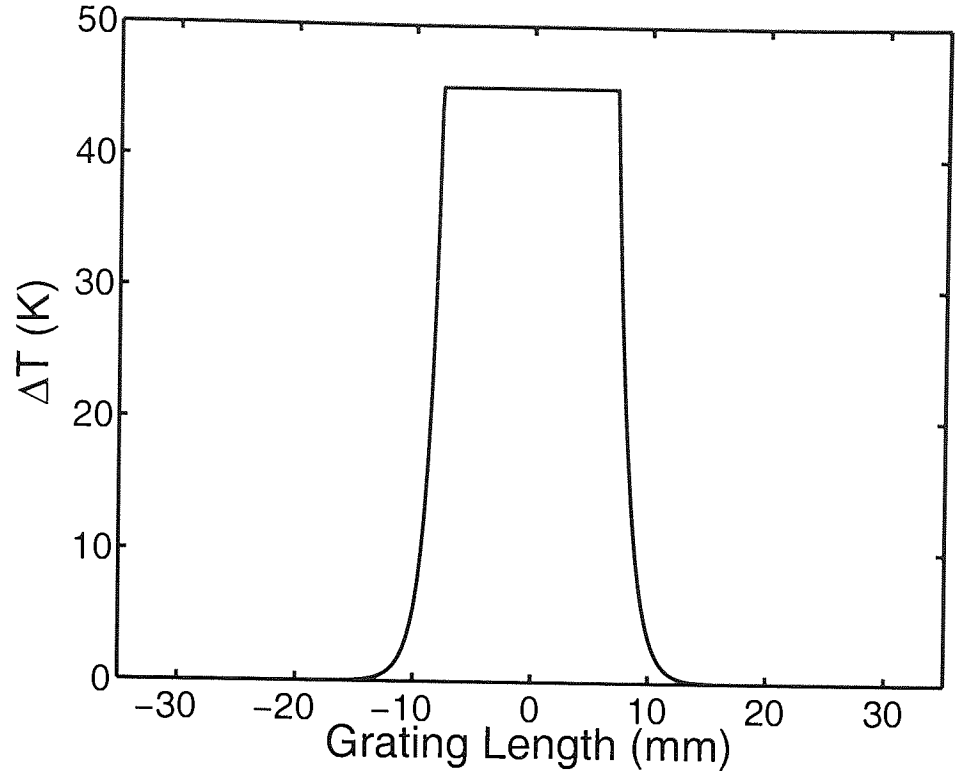

Figure 4.22: Simulated temperature change profile over grating at $\Delta T = 45.3$ K, $L_p = 14.84$ mm, C_p=0.30 mm to the shorter wavelength side of grating centre and k=901.

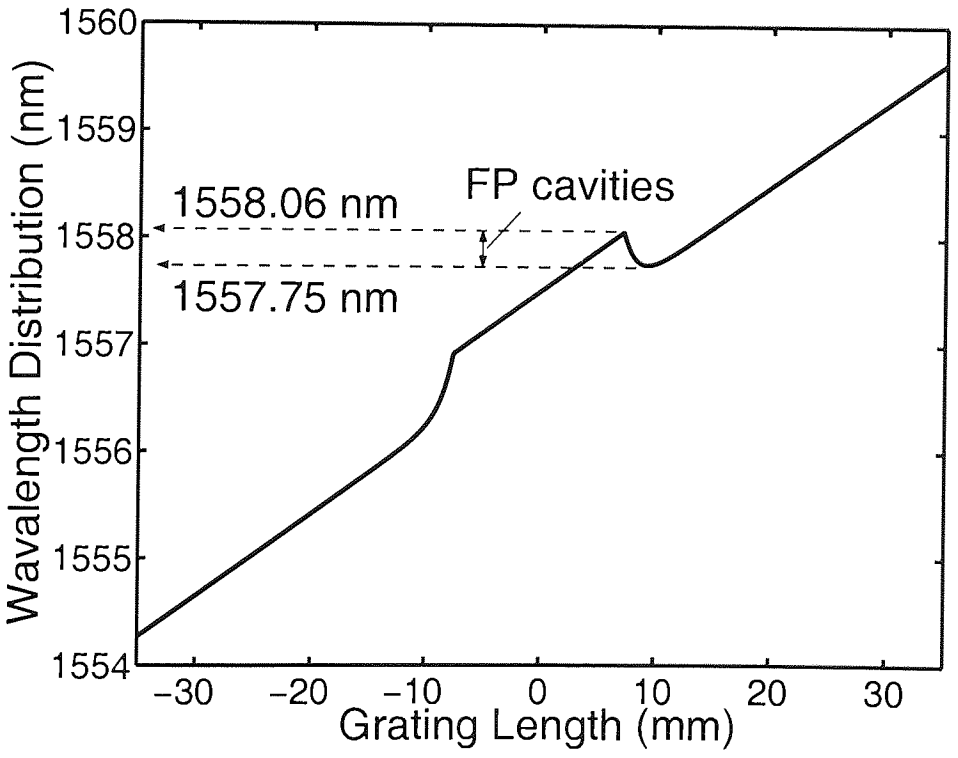

Figure 4.23: Simulated Bragg wavelength function based on the reflection spectrum obtained at $\Delta T = 45.3$ K.

simulated group delay response was then compared with the measured group delay response based on the experimental setup shown in figure 4.8. This additional measurement by LCA was made merely to evaluate the accuracy of the fitted model.

From figure 4.21, it can be seen that the simulated group delay response matched very well with the measured profile. This has verified that the proposed model is feasible to synthesise the FBG response as a distributed temperature sensor. From figure 4.20 and figure 4.21, it can also be noticed that the reflection spectrum of the grating experienced a variation in its reflectivity strength along its bandwidth while the group delay displayed a chirp at the same position. This phenomenon was due to the Fabry-Perot effect detailed in section 4.4. This effect is depicted in figure 4.23 based on the result from the example above. The Fabry-Perot cavities were basically created by the wavelength shift within the grating when temperature was increased.

Location Determination

The reflection spectrum of grating G2 for each shift at $\Delta T = 40.0$ K was least squares fitted based on the proposed synthesis model. Examples of the measured and fitted spectra for two different locations, which were -0.5 mm and -4.5 mm, are shown in figure 4.24 and figure 4.25. The negative sign in front of the location values indicated that the locations of the heat source were at the shorter wavelength side of the grating with the centre of the grating as 0.0 mm. From the plots, it can be seen that different locations raised different and distinctive profiles in the reflection spectrum of grating. The difference between these profiles was obvious. This would, inevitably, help in the optimised fitting process.

The fitted results of the locations of heat source were compared with the experimental results. From figure 4.26, it is apparent that the fitted results matched well with the shifts of the grating made before every test. In this way, the proposed system has shown its ability in locating the heat source since it has an excellent agreement with the actual measurement with a standard deviation of only 149 μm.

The corresponded fitted values for $A\Delta T$ and L_p in this location determination test are depicted in figure 4.27 and figure 4.28, respectively, giving average values of ΔT=40.7 K and L_p=14.6 mm. These values matched well with the input experimental values, which were 40.0 K and 15.0 mm, respectively. Their respective discrepancies of 1.8% and 2.7% might be caused by the error in thermistor or the temperature controller that might vary the actual applied temperature onto the grating.

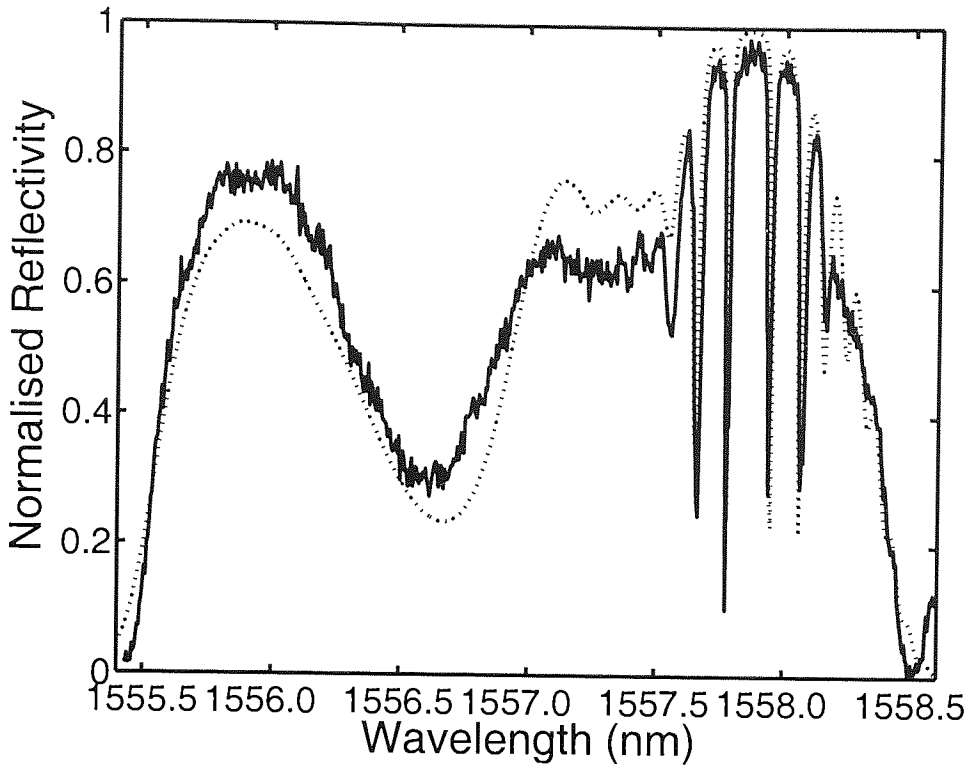

Figure 4.24: Experimental (–) and fitted ($\cdots$) spectra obtained at heating position of -0.5 mm from the centre of the grating at $\Delta T = 40.0$ K.

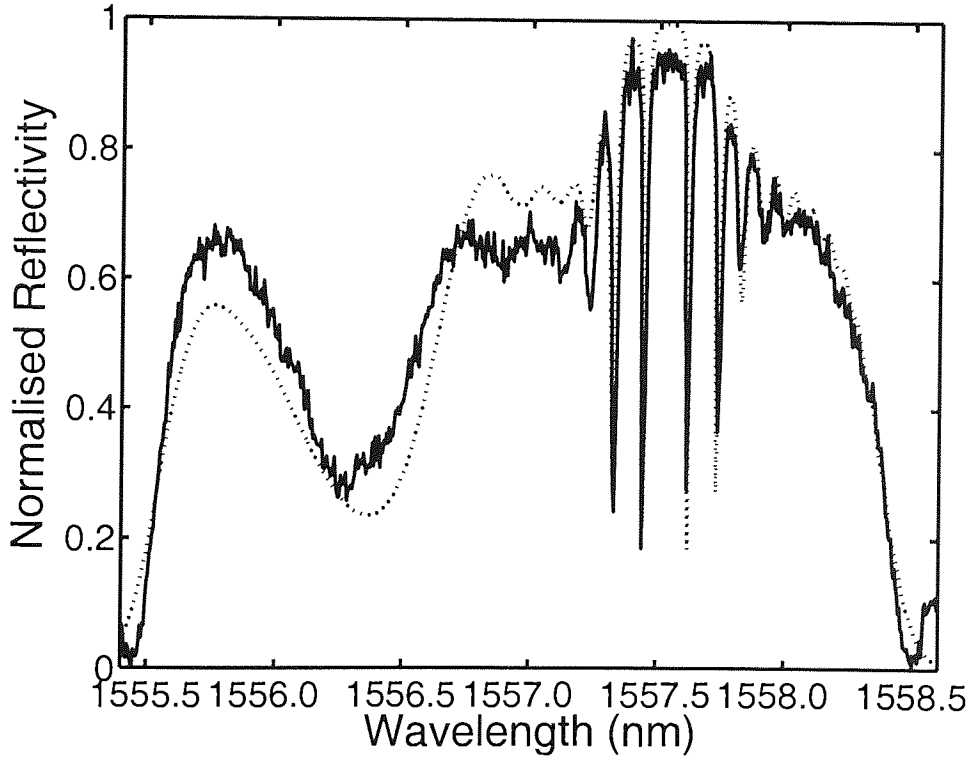

Figure 4.25: Experimental (–) and fitted ($\cdots$) spectra obtained at heating position of -4.5 mm from the centre of the grating at $\Delta T = 40.0$ K.

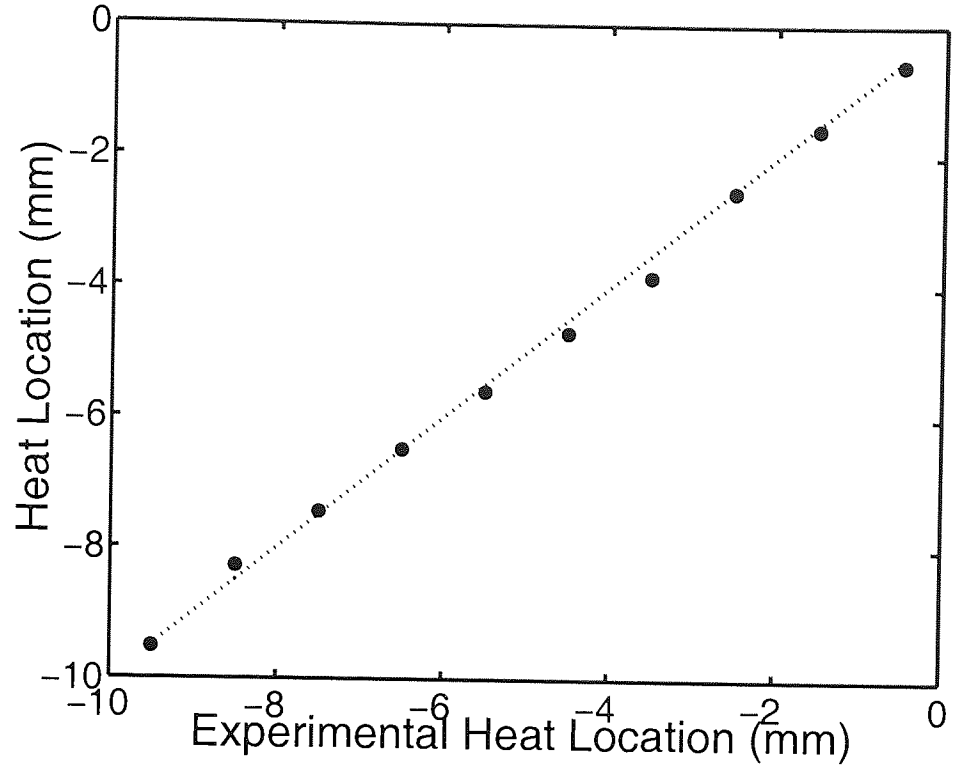

Figure 4.26: Fitted locations (•) of the heat source which gives a standard deviation of 149 μm from the unity gradient (···).

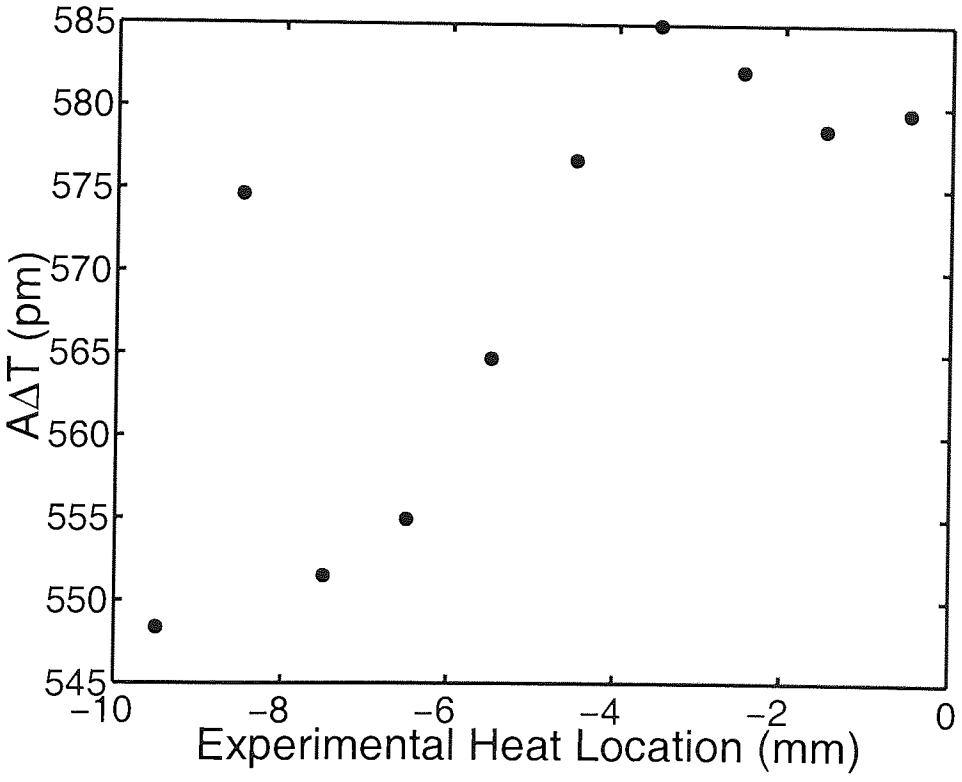

Figure 4.27: Fitted $A\Delta T$ (•) of the heat source which gives an average ΔT of 40.7 K.

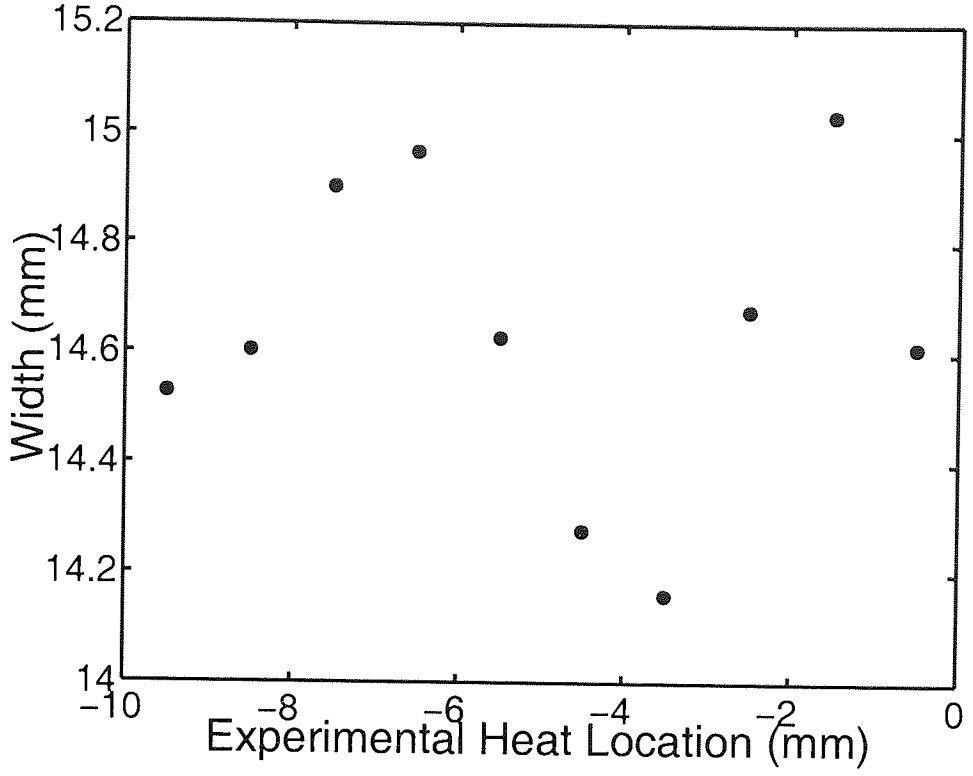

Figure 4.28: Fitted widths (•) of the heat source which gives an average L_p of 14.6 mm.

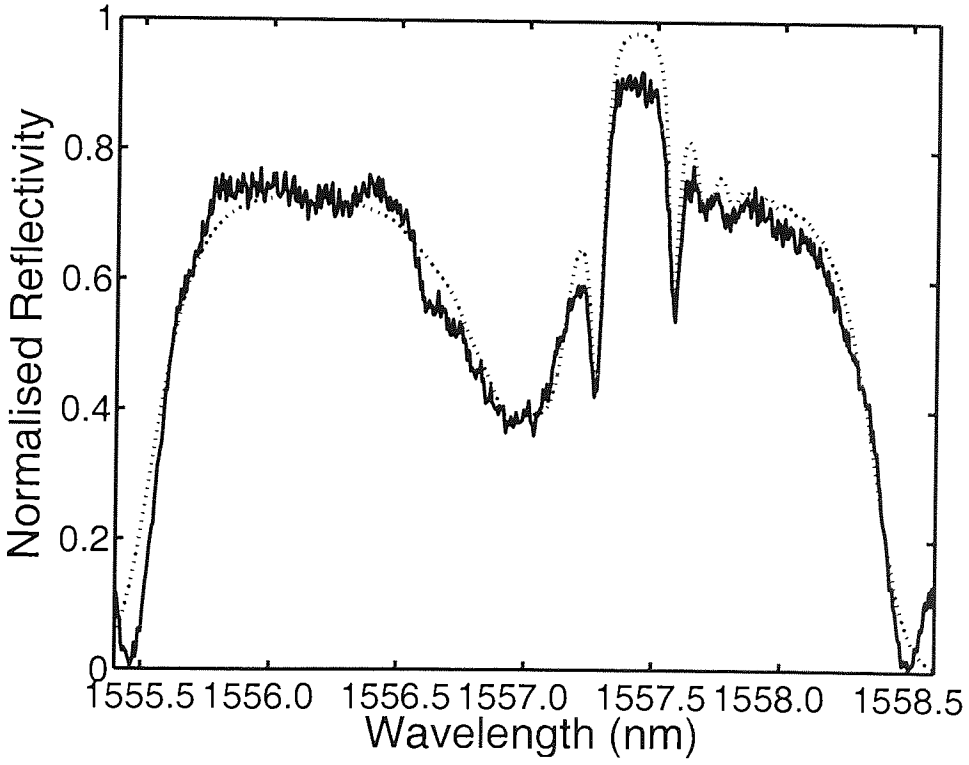

Figure 4.29: Experimental (–) and fitted (· · ·) spectra obtained with heating width of 4.0 mm at $\Delta T = 30.0$ K.

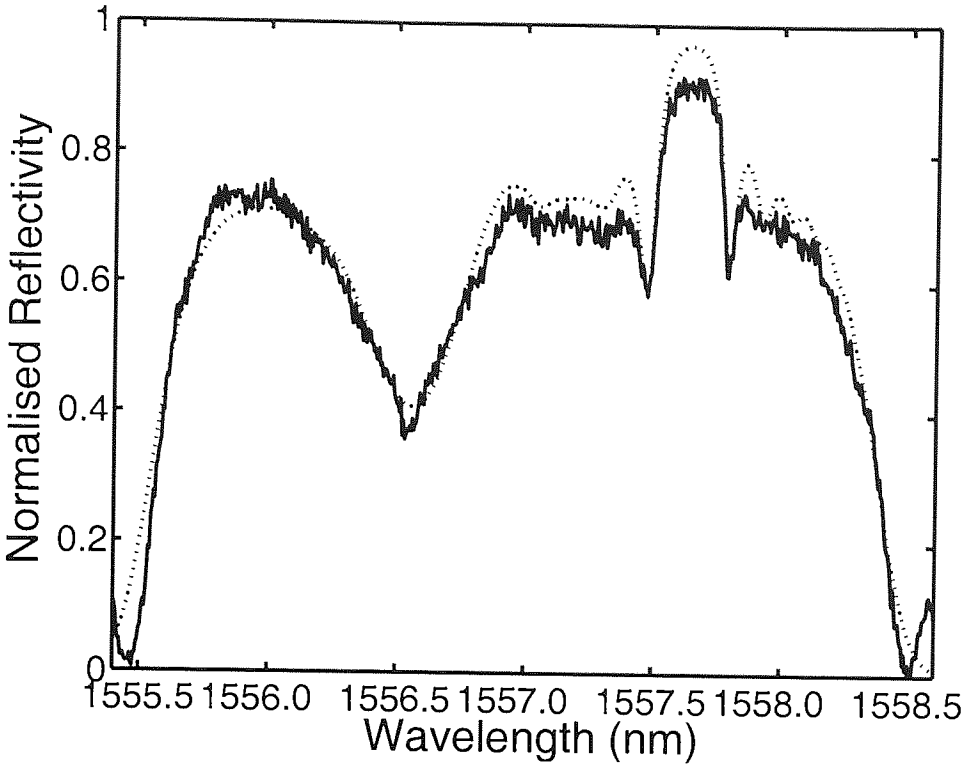

Figure 4.30: Experimental (–) and fitted ($\cdots$) spectra obtained with heating width of 12.5 mm at $\Delta T = 30.0$ K.

Width Determination

The reflection spectrum of grating G2 for each width at $\Delta T = 30.0$ K was least squares fitted based on the proposed synthesis model again. Figure 4.29 and figure 4.30 show the examples of the measured and fitted spectra for two different widths, which were 4.0 mm and 12.5 mm. It can be seen clearly that the interference part of the reflection spectrum was wider when a wider heat source was used. Loss in the reflectivity at the shorter wavelength side of grating was converted to the gain of the longer wavelength of the grating. This phenomenon was attributed to the Fabry-Perot effect within the grating which was due to the intragrating wavelength shift induced by the localised heating. Again, the distinctive pattern in the reflection spectrum gave very useful information for the least squares optimised fitting.

The comparison between the fitted and experimental values of the width is shown in figure 4.31. It can be noticed that there was an excellent agreement between them, in which a standard deviation from the unity gradient of only 306 μm was calculated. The corresponding ΔT, C_p and k in this width determination test were 29.6 K, 4.6 mm and 971, respectively. This has proven that the proposed system is able to determine the width of heat source.

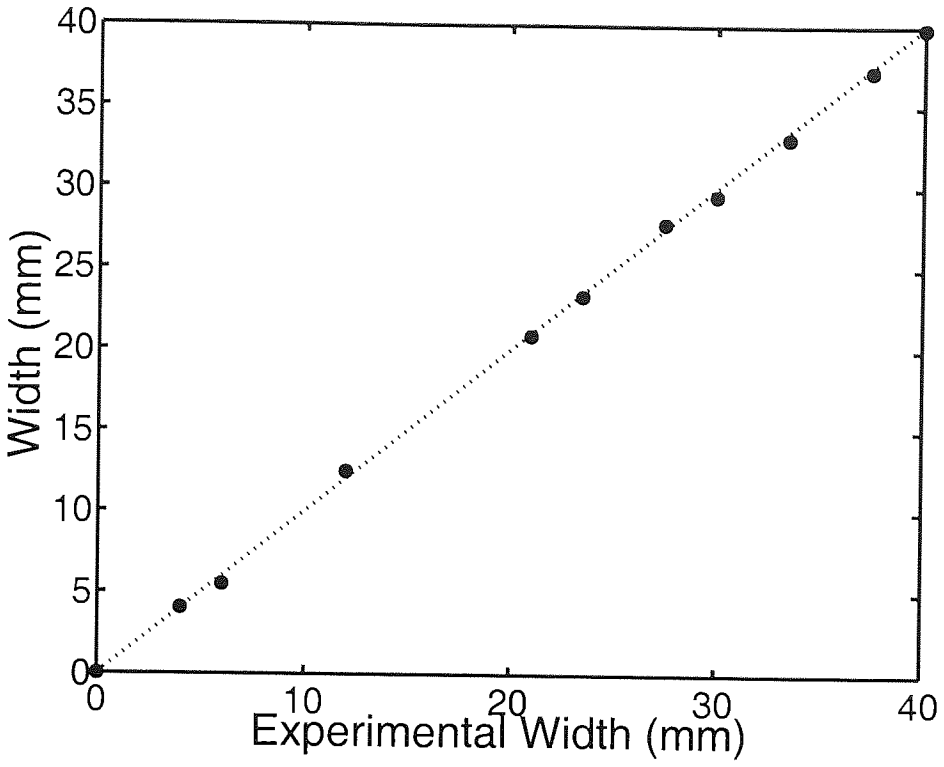

Figure 4.31: Fitted widths (•) of heat source which gives a standard deviation of 306 μm from the unity gradient ($\cdots$).

4.9 Discussion

As can be noticed in figure 4.24, figure 4.25, figure 4.29 and figure 4.30, a number of features arise in the spectra of the grating which are strongly indicative of the applied temperature profile. These features served as good indicators for the proposed synthesis model in obtaining the applied distributed temperature profile. Apart from characterising the grating in use, the synthesis models have also been demonstrated to be efficient in determining the temperature profile. Experimental and simulated results have shown that the proposed distributed temperature sensing system is not restricted to a monotonic temperature profile and that it can be used to retrieve non-monotonic temperature profile with standard deviations of 30 pm, 149 μm and 306 μm for the $A\Delta T$, location C_p and width L_p of the heat source.

Nevertheless, there remain some issues that needed to be looked into, such as, the repeatability of the system and the capability of the system of measuring two heated regions. As the speed of the fitting is crucial in making the system a fast diagnostic tool, the factors that affect the speed of algorithm are vital and needless to say the ripple problem may affect the accuracy of the simulated results. Besides, the area under test is very much dependent on the length of the grating. Thus, the grating needs to be correctly tailored to obtain an optimum design for distributed sensing. In this section, all of these are discussed in more

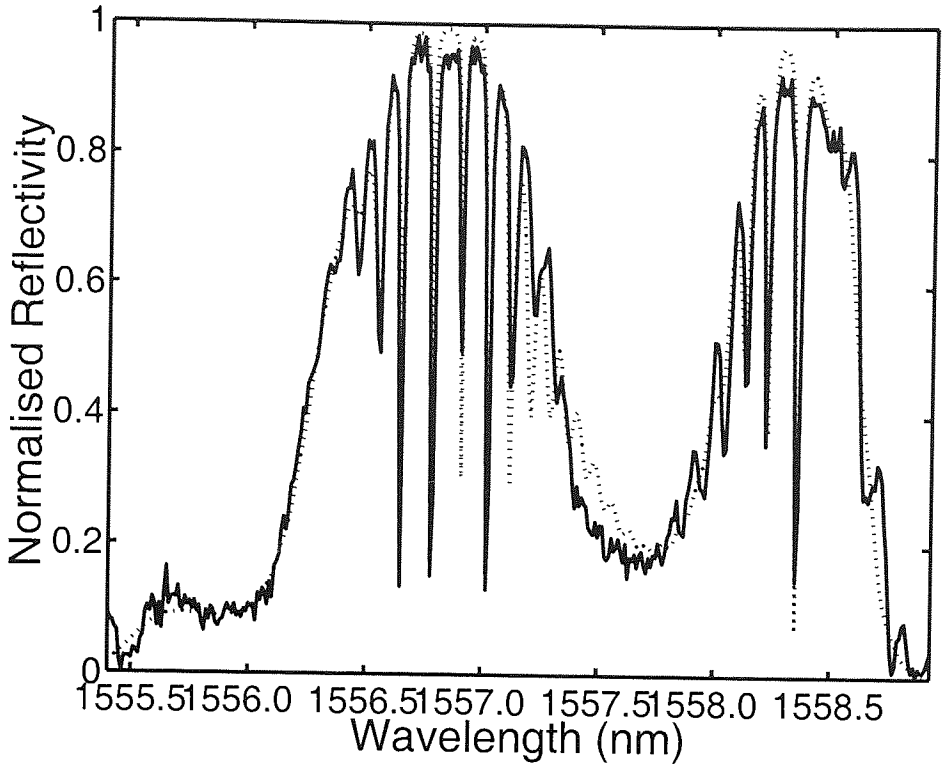

Figure 4.32: Experimental (–) and fitted (···) results for two localised heated regions with same temperature change and width but at different locations.

detail in order to seek ways to improve the proposed system.

4.9.1 Repeatability

In order to evaluate the repeatability of the proposed system, an investigation was carried out, in which a localised heating with ΔT=40 K, C_p=1.0 mm and L_p=1.5 mm was applied to grating G2. The reflection response was scanned using OSA. The same experiment was repeated 20 times and the recorded reflection spectra were least squares fitted. From the results obtained, the standard deviations for C_p, L_p and $A\Delta T$ were calculated as 29 μm, 56 μm and 8 pm (corresponding to 0.6 K for ΔT when A was taken as 13.97 pm/K), respectively. This has demonstrated that the system is reliable. Assuming that standard deviation from the linearity of each parameter, which are 30 pm for temperature dependence coefficient $A\Delta T$, 149 μm for location C_p and 306 μm for width L_p, are accounted for in making these measurements, 29 μm, 56 μm and 0.6 K are corresponding to the effective resolutions for C_p, L_p and ΔT when grating G2 is used as a distributed temperature sensor.

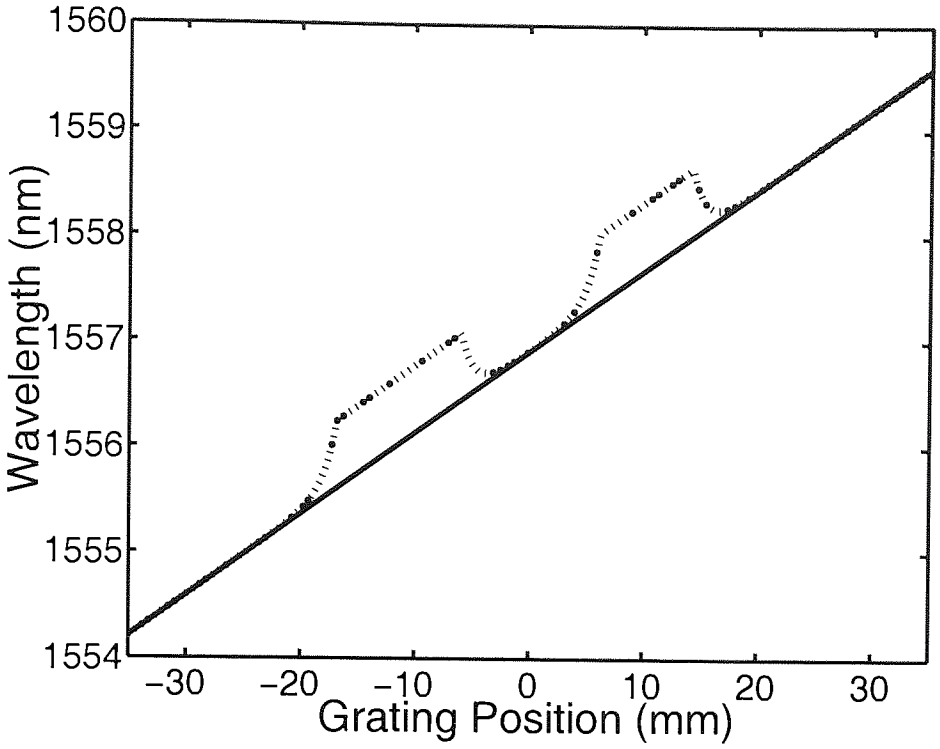

Figure 4.33: Resonant Wavelength distribution at $\Delta T = 0$ K (—) and $\Delta T = 50$ K ($\cdots$) with two heated regions along an apodised chirped FBG.

4.9.2 Capability in Measuring Two Heated Regions

In order to show the capability of the system of measuring two temperature changes along the grating, an experiment with two regions of elevated temperature was carried out by using the same experimental setup as in figure 4.9 but with a setup of five peltiers instead. Two heated peltiers with a width of 10.0 mm were separated by a 10.0 mm wide peltier fixed at room temperature. The temperature of the remaining two ends of the grating were controlled at room temperature as well by another two peltiers. Figure 4.32 shows the experimental and fitted results of two heat sources with an identical ΔT of 50.0 K and width L_p of 10.0 mm. Its wavelength distribution over the piece of grating is also plotted in figure 4.33. From the results, the positions C_{p1} and C_{p2} of the two heated regions were fitted to be -12.0 mm and 10.0 mm, respectively, which were in agreement with the arrangement of the peltiers before test. This test has successfully shown that the proposed system is able to measure temperature distribution over an area by using only a single piece of grating.

4.9.3 Factors that Affect the Algorithm Speed

The optimised fitting process of this work took about several minutes to complete. Like the problems faced by other optimisation methods [83, 84], the performance of the process de-

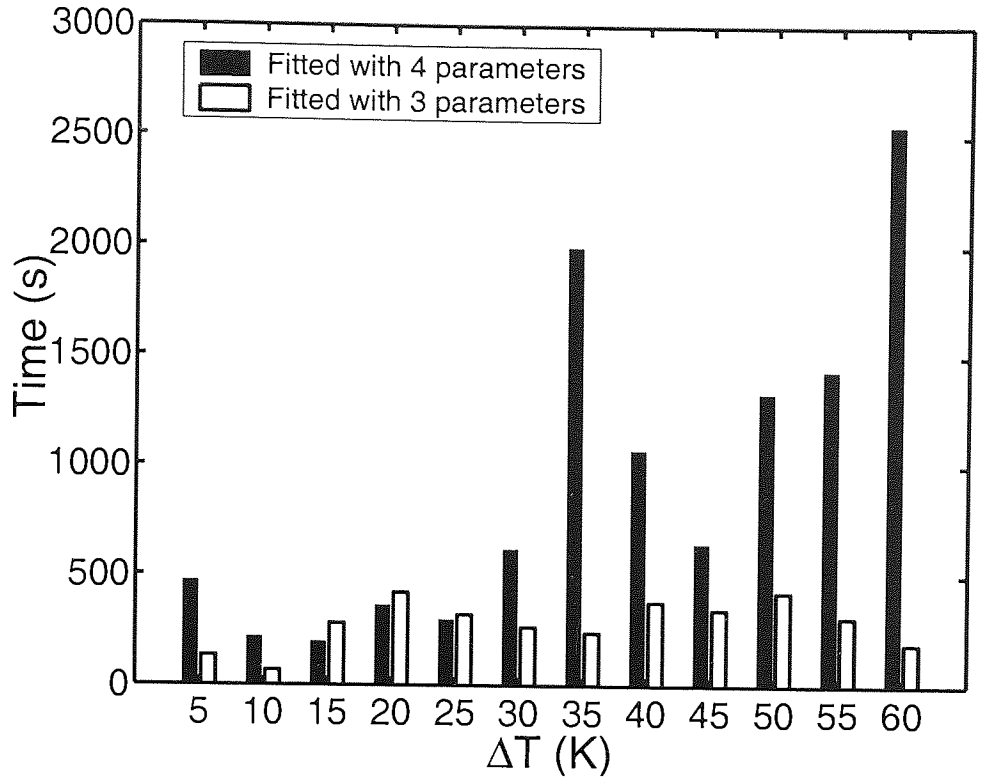

Figure 4.34: Durations taken for fitted result with three parameters and four parameters.

pends on the number of the unknown parameters, choice of the initial values, desired fitness, number of wavelength measured and the processing speed of the computer in use. These factors are influential and are needed to be well-tailored in order to improve the performance of the process. They are discussed in more detail as below:

Number of Unknown Parameters

In order to evaluate the duration taken with different number of unknown parameters, an investigation was carried out where two fittings were run onto the reflection spectra with different ΔT. Firstly, the measured results were fitted with four parameters, which were ΔT, C_p, L_p and k and the time taken was recorded for each temperature change. Secondly, the number of unknown parameters was reduced to three with the value k as stated in equation (4.10) was inserted in the proposed synthesis model. The time taken was recorded for each ΔT. Comparison was made between these two fitting processes and it is shown in figure 4.34. As can seen, the fitting process with more parameters used longer time to reach the convergence of the optimisation. The duration taken for four parameters could be reduced up to 93% if there was only three parameters to be fitted and apparently, almost the same results were obtained. This can be observed from the standard deviation calculated between the measured

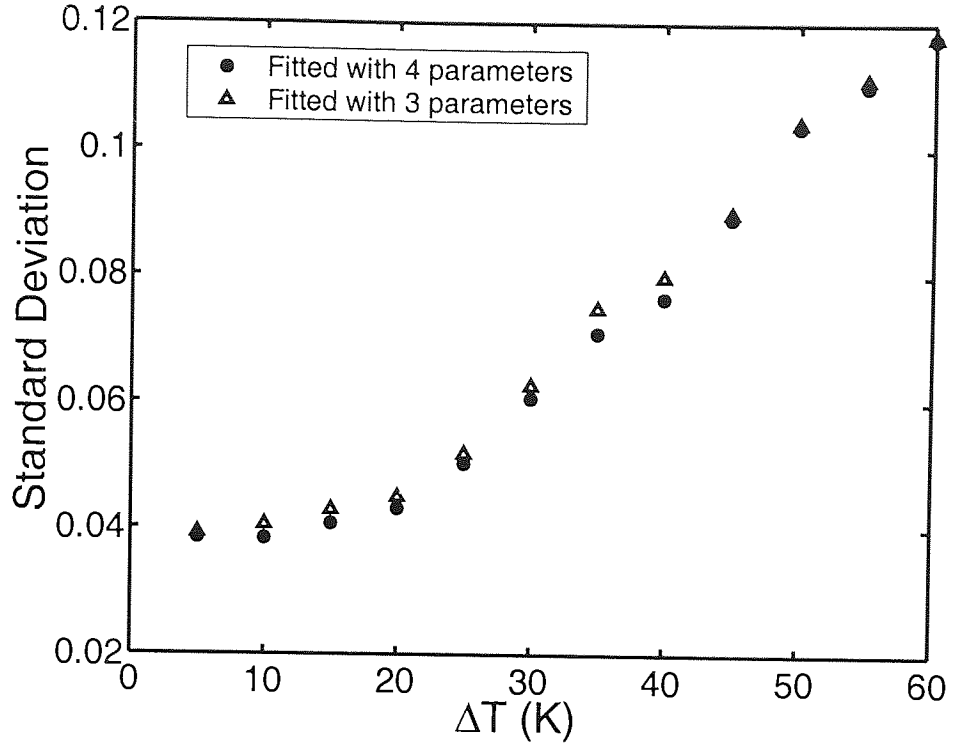

Figure 4.35: Standard deviation between the measured spectrum and the fitted profile with three parameters and four parameters at different ΔT.

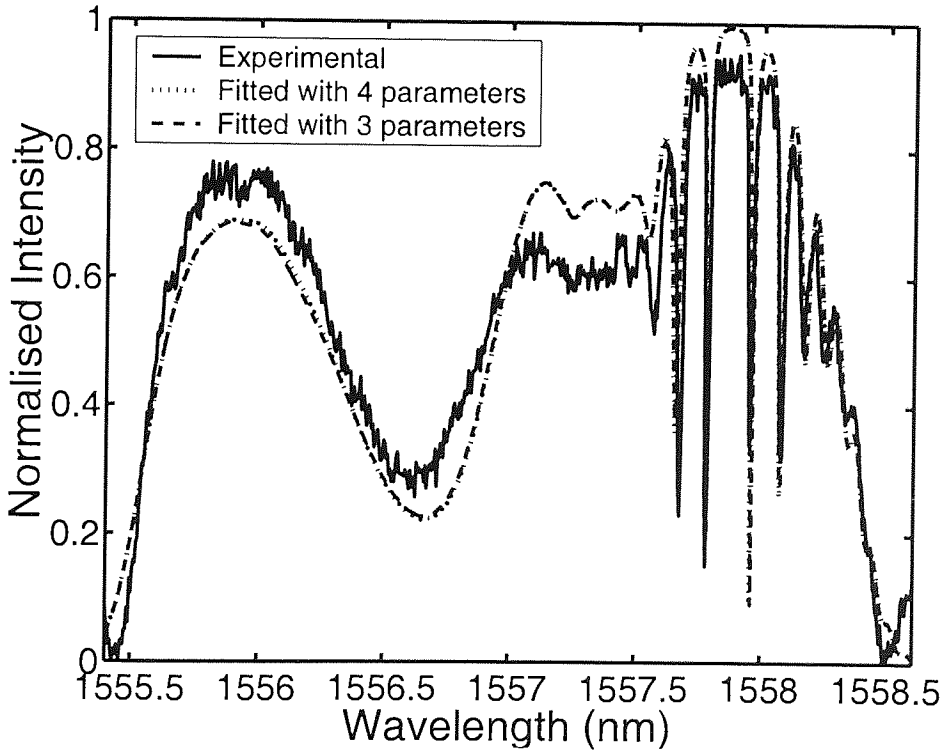

Figure 4.36: Experimental result (–), fitted result with three parameters ($\cdots$) and fitted result with four parameters (- -) at $\Delta T = 45.0$ K.

spectrum and the fitted profile with three and four parameters, as shown in figure 4.35.

For instance, the example in figure 4.20 was taken into the investigation and the comparison between the spectra is shown in figure 4.36. The time saving percentage at this particular temperature change, ΔT, was calculated to be 46% whilst the standard deviation for the fitted result with four parameters was calculated to be 0.0892 and for the three parameters, it was calculated as 0.0899. The spectra obtained were almost the same, but with very much improvement in the duration taken. Thus, it can be concluded that the less the number of unknown parameters, the shorter time the optimisation process takes to fit the targeted spectrum.

Choice of Initial Values

As can be aware of from the algorithm, the choice of the initial value for each parameters is very important as to achieve the right convergence in the optimisation process. Thus, it is crucial that the process starts with a right set of initial values. In this work, the initial values were obtained by performing a manual fitting based on the proposed synthesis model. To investigate the flexibility of the choice of initial values, several evaluations were conducted with initial values in a range of 20 % of the desired initial values obtained from the manual fitting. For each optimised fitting, the initial value of one parameter was changed at a time with all the others remained at the desired initial values.

Figure 4.37 shows the results of the evaluations. The desired initial value meant the initial value obtained from manual fitting. It is noticeable that the time taken for each evaluation with different parameter values was independent from others. This was due to the fact the different initial value would take different time to reach the convergence.

Comparisons of reflection spectra obtained from different initial values were made and they are shown in figure 4.38, figure 4.39 and figure 4.40, respectively. The standard deviation between the experimental result and the fitted result with desired initial value was calculated to be 0.0899 whilst the respective standard deviations for 0.8×desired initial value and 1.2×desired initial value for $A\Delta T$ were calculated to be 0.1360 and 0.1288. In the case of C_p, they were 0.0968 and 0.0949 for 0.8×desired initial value and 1.2×desired initial value for C_p whilst for L_p, they were 0.1455 and 0.1255 for 0.8×desired initial value and 1.2×desired initial value for L_p. It can be seen that although it took longer or shorter time to achieve the convergence, some of the optimised fittings did not actually lead to the right fitting, which were the case in $A\Delta T$ and L_p.

The only conclusion could be made was, the initial value of width L_p was most dominant in the process since it took more time for it to converge and yet gave poor result, followed by the initial value of $A\Delta T$ due to its poor result too. Thus, more care has to be taken in

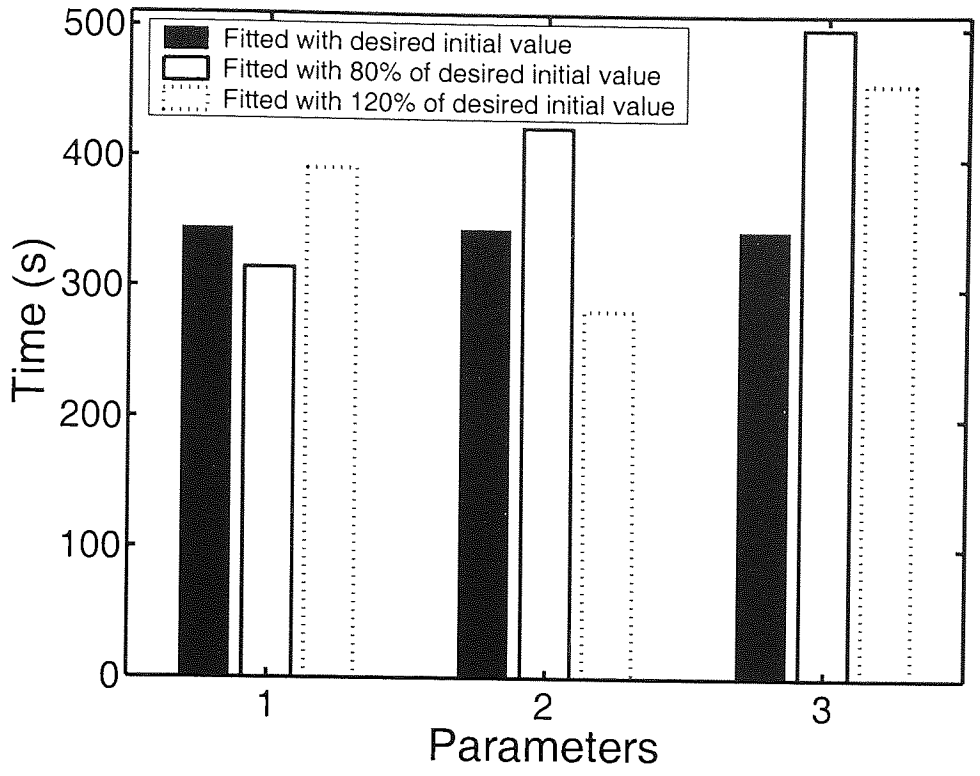

Figure 4.37: Durations taken for fitted results with different initial values for (1) $A\Delta T$, (2) C_P and (3) L_p at the example of ΔT=45°C.

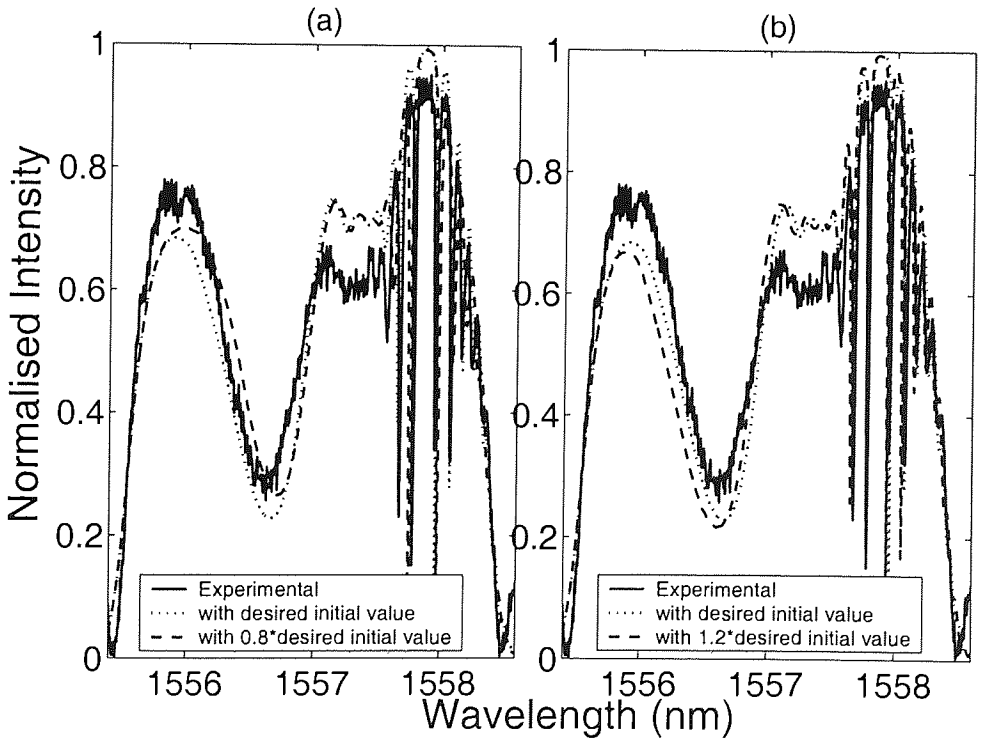

Figure 4.38: Comparison of reflection spectra (a) with 0.8×desired value and (b) with 1.2×desired initial value of $A\Delta T$ at the example of ΔT=45°C.

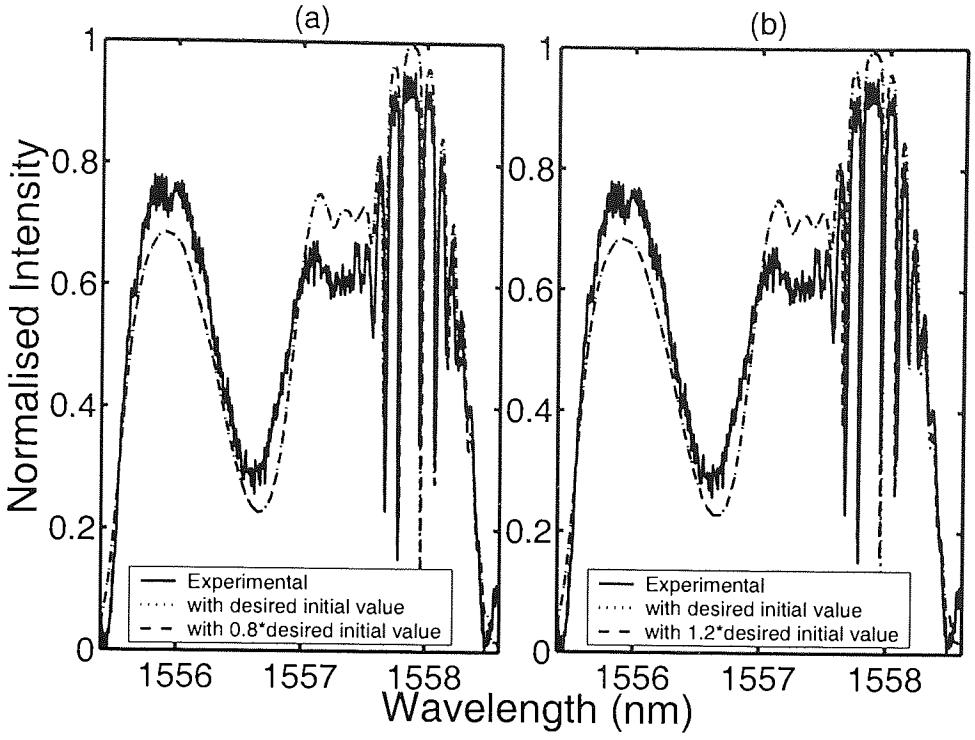

Figure 4.39: Comparison of reflection spectra (a) with 0.8×desired value and (b) with 1.2×desired initial value of C_p at the example of ΔT=45°C.

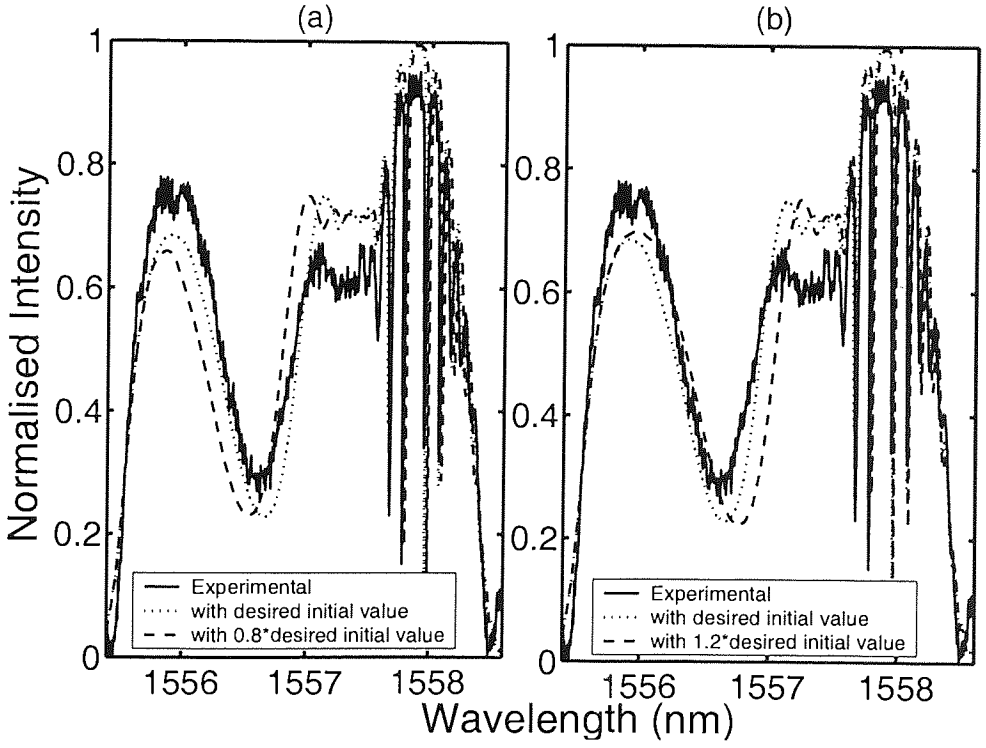

Figure 4.40: Comparison of reflection spectra (a) with 0.8×desired value and (b) with 1.2×desired initial value of L_p at the example of ΔT=45°C.

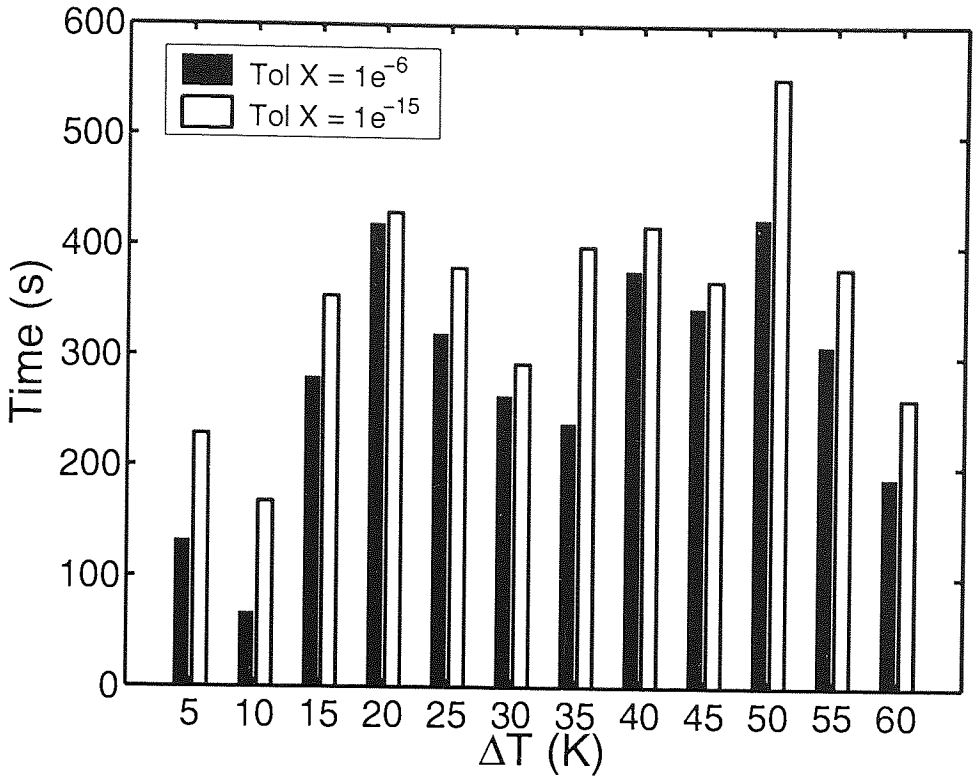

Figure 4.41: Durations taken for fitted results with $f = 1 \times 10^{-6}$ and $f = 1 \times 10^{-15}$.

the selection of the initial value of $A\Delta T$ and L_p. But, this does not mean that the choice of C_p is trivial. Alternatively, to obtain a better choice of initial values, a simple heuristic method can be used to estimate them. For example, by slowly varying temperature changes, the temperature profile can be estimated by simply using the calculated parameters of the previous measurement.

Desired Fitness

The desired fitness f was set as 1×10^{-6} in all the optimisations of this work. This value could be adjusted. As could be understood, a smaller desired fitness would take longer time to achieve. To investigate if a more stringent demand on the desired fitness would give a more accurate fitting, a series of optimisations with smaller desired fitness of 1×10^{-15} were carried out at different ΔT. Figure 4.41 shows the durations taken to obtain the fitted results with $f = 1 \times 10^{-6}$ and $f = 1 \times 10^{-15}$. Clearly, the time spent to reach the convergence when $f = 1 \times 10^{-6}$ was shorter compared to the case when $f = 1 \times 10^{-15}$.

The time saving by using lower fitness value f might not be significant, however, both fitness values gave exactly the same fitted results, as shown in figure 4.42. It is apparent that both results from $f = 1 \times 10^{-6}$ and $f = 1 \times 10^{-15}$ provided the same spectra. Thus, it can

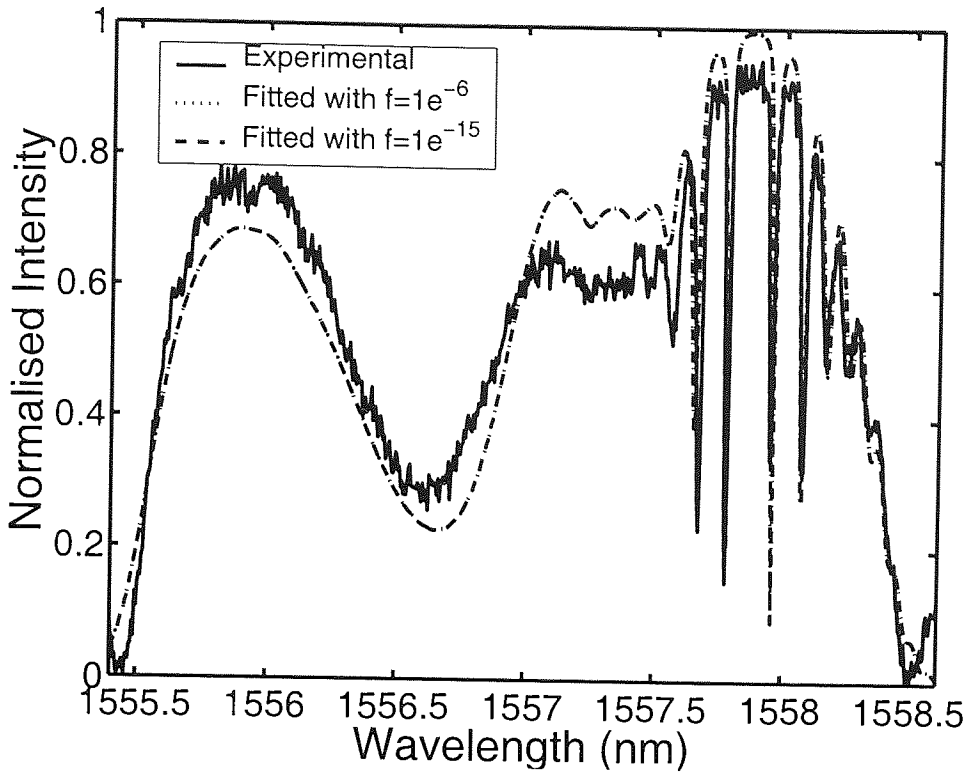

Figure 4.42: Experimental result (–), fitted result with $f = 1 \times 10^{-6}$ and fitted result with $f = 1 \times 10^{-15}$ at $\Delta T = 45.0$ K.

be claimed that the increment on the fitness value f from $f = 1 \times 10^{-6}$ to $f = 1 \times 10^{-15}$ is dispensable considering that the later needs longer time to finish the fitting process and yet gives the same result.

Number of Wavelengths Scanned

As described in section 3.4, coupled-mode equations are used to calculate the output fields of a short section δl_1 of grating, the analytical solution resulting in the amplitude reflectivity, transmission and phase. These quantities are then used as the input parameters for the adjacent section of grating of length δl_2. This process keeps going until the reflectivity, transmission and phase of the whole piece of grating are calculated. The total number of section δl is related to the number of wavelength scanned in each fitting process. It can be understood that the lower the number of layers, the faster the fitting process is. However, this may, in turn, affect the accuracy of the temperature measurement due to the poor resolution of the synthesised reflection spectrum. As depicted in figure 4.43, simulated reflection profile with smaller number of section gave limited measured profile as compared to the one with larger number of section. Thus, an optimum selection on the number of wavelength scanned is important in the empirical measurement as well as the synthesised model in order

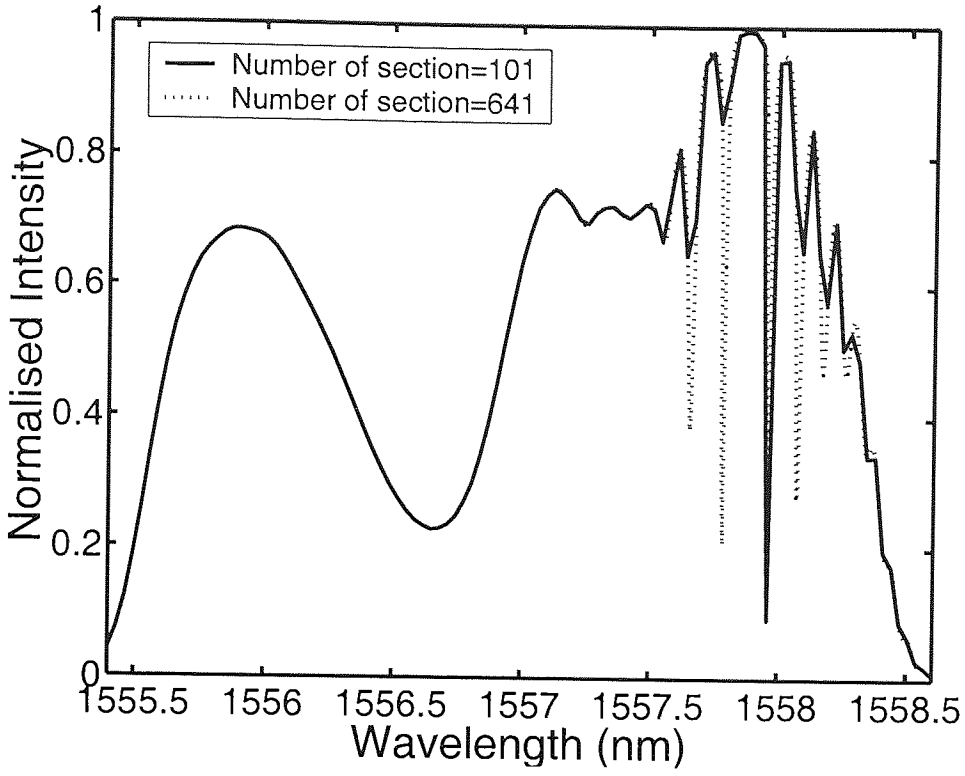

Figure 4.43: Simulated reflection spectra with different number of wavelengths.

to maintain a good accuracy of the measurement.

It is also worth noting that the number of wavelengths scanned is dependent on the value of chirprate; the higher the chirprate, the more sections of wavelength needs to be measured, since wider bandwidth needs to be measured and simulated. This can be seen from figure 4.44. Here, the value of chirprate was 0.773 nm/cm. This, inevitably, needs a longer time for the optimised fitting process. Thus, the choice of chirprate is very influential on the number of wavelength scanned and hence on the speed of the fitting process.

Processing Speed of Computer

In this work, a laptop with Intel Pentium 4 processor running at 1.2 GHz with 256 MB RAM was used to run the optimisations. Clearly, a faster processor could be used to speed up the process. To prove this, the same optimisations were carried out by using a desktop computer with AMD Athlon processor running at 1.2 GHz with 512 MB RAM. The comparison is shown in figure 4.45. As can be seen, the time taken by the desktop was shorter than the one by the laptop. Thus, it can be concluded that the duration taken for the optimised fitting process can be shortened by using a faster processor.

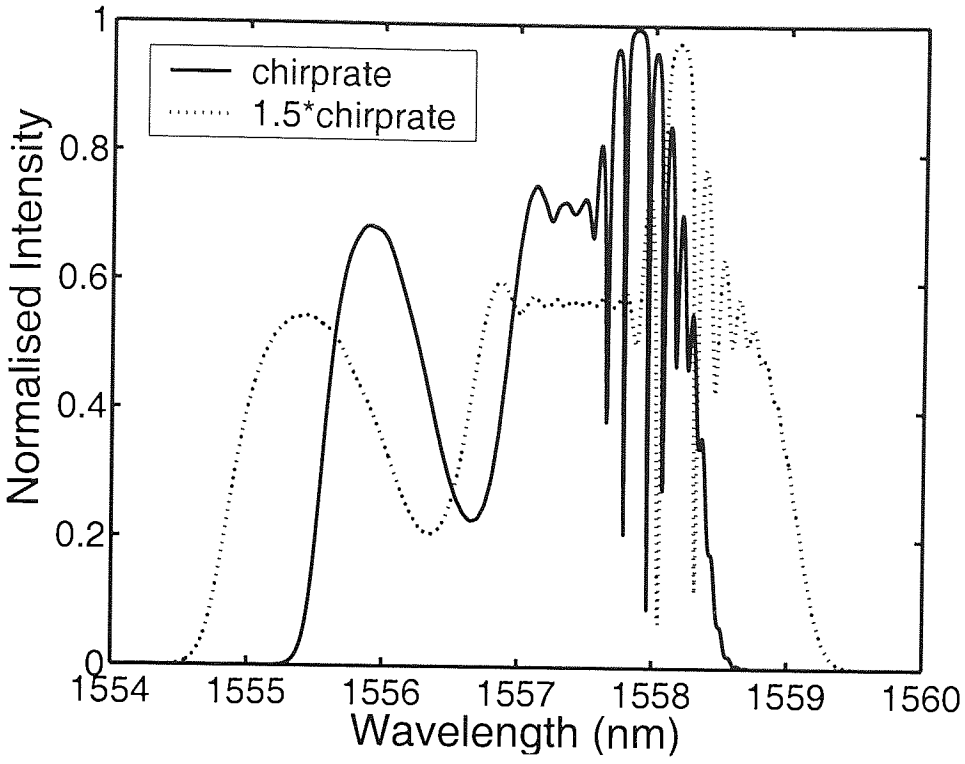

Figure 4.44: Simulated reflection spectra with different chirprates.

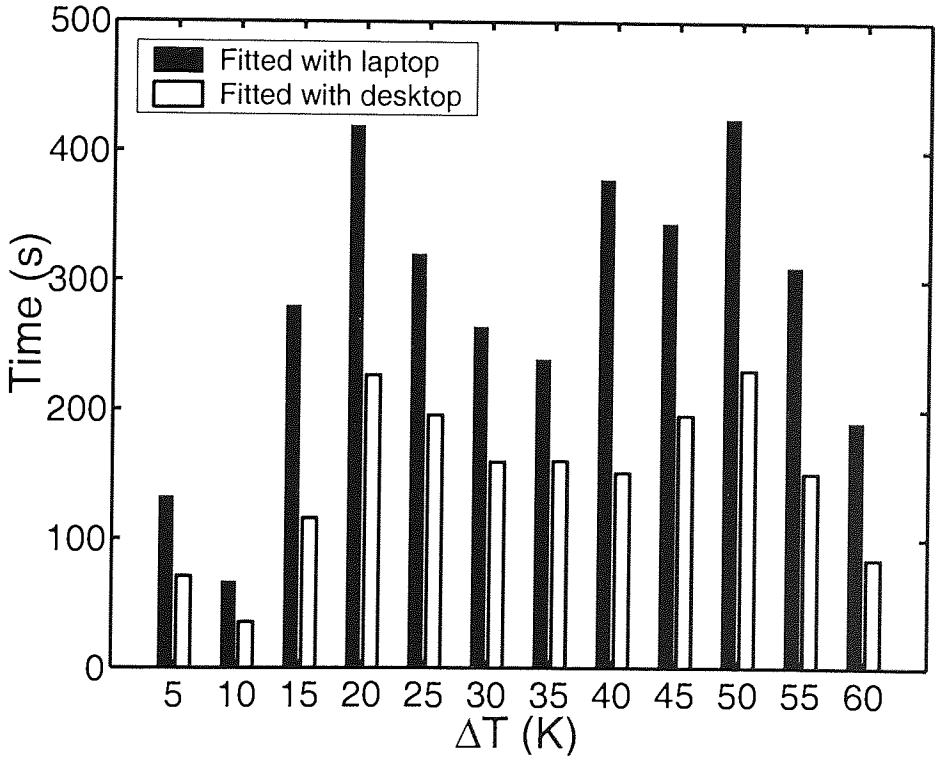

Figure 4.45: Durations taken for fitted results done by Intel Pentium laptop and AMD Athlon desktop.

4.9.4 Ripple Problem

In the experiments, ripples in the reflection spectrum were unwelcome since they formed ambiguity in data processing. The average measured ripple size for the reflection spectrum was about 0.4 dB. The ripple size was obtained after the spectrum was subtracted by the reference profile at 24.0°C. The main factor for the ripple problem was, the imperfectness of grating due to the errors occurred during the fabrication process, such as, misalignment, stitch errors and dirt on phase mask, and vibration of the stage. These errors greatly degraded the properties of the grating and its reflectivity. The subtraction process was essential since it subtracted the regular ripples caused by the imperfectness of grating. However, the subtraction process was not always reliable when there was a shift between the profile to be subtracted and the reference profile caused by the instability of the tunable laser during the scanning process. The laser stability was highly dependent on the repeatability of the tunable laser which has a tuning repeatability of ± 5 pm when the output power was at 0 dBm. Nevertheless, the data processing of the proposed model was mainly based on the Fabry-Perot effect which gave a bigger, clearer and more influential information to the simulation. Thus, the problem created by the ripple was insignificant and could be neglected.

4.9.5 Coverage

The proposed system can be tailored for different size of heat source by simply changing the length of the apodised chirped grating. The grating length has to be longer than the heat source if the information of location and width of heat source are of interest in addition to the temperature change. Otherwise, the proposed system can only provide information of the temperature variation based on the wavelength shift as it does in the uniform temperature determination test. However, it is quite difficult to maintain a flat top reflection profile when the length of grating is large. This situation becomes worse when the grating is made with higher chirprate. Thus, a compromise has to be made in order to reach an optimum balance between the coverage and the flat top reflectivity in order to have a higher accuracy.

4.10 Conclusion

A distributed temperature sensing system utilising an apodised chirped fibre Bragg grating has been proposed. Synthesis models based on the transfer matrix method have been introduced to calculate the transmissivity, reflectivity and group delay responses of grating and to include the Fabry-Perot effect induced by the temperature change within grating. Uniform and localised temperature determination tests have been carried out to verify its sensitivity

to non-monotonic temperature change and to validate the proposed system. A temperature dependence coefficient of 11.7 pm/K for grating G1, which matches the typical value, has been gained from the uniform temperature determination test whilst it has been calculated to be 13.97 pm/K for grating G2 in the localised temperature tests. On top of that, excellent agreements have been achieved from the temperature determination test, location determination test and width determination test with standard deviations of 30 pm, 149 μm and 306 μm for the temperature change, location and width of the heat source, respectively. Meanwhile, in the repeatability test, the system gave measurement with standard deviations of 8 pm (therefore 0.6 K with A=13.97 pm/K), 29 μm and 56 μm for $A\Delta T$, C_p and L_p, respectively.

The only weakness of the proposed system is the simulation speed of the synthesis model. As mentioned, it takes about several minutes to obtain the applied temperature profile. This is due to the fact that its performance depends on the number of the unknown parameters, choice of their initial values, desired fitness, number of wavelength measured and certainly, the processing speed of the computer. Simulation duration increases with more unknown parameters, higher desired fitness and higher number of wavelength. Besides, much care needs to be taken when it comes to the selection of the initial values in order to get a faster response. However, a simple heuristic way can be used to estimate them, which is, by slowly varying temperature changes, the temperature profile can be estimated by simply using the calculated parameters of the previous measurement. Thus, this proposed distributed sensing system is more practical for the applications that involve constant monitoring of slow varying temperature change.

In conclusion, a fully distributed temperature sensor consisting of an apodised chirped grating has been demonstrated. Experimental results have shown that the applied non-monotonic temperature profile to the grating can be determined by using the transfer matrix method by means of least squares optimised fitting the calculated reflection spectrum with the experimental reflection spectrum. By doing so, simultaneous determination of the temperature change, position and width of the heat sources can be achieved. Experimental results have proven that this scheme can also be applied to the simultaneous temperature measurement of multiple heat sources. The proposed system is simple and cost-effective since it can cover across the area under test by using only one piece of apodised chirped fibre grating. More importantly, it is not only able to provide the information of temperature variation, but can also give the details of location and width of the heat source, and hence, is capable of projecting a temperature profile $g(z, \Delta T, L_p, C_p)$ for the area under test.

Chapter 5

High-Birefringence Optical Fibre Based Delay Line Filter

5.1 Introduction

In fibre optics communication and microwave/millimetre-wave photonics systems, it has been recognised that it is advantageous to perform signal processing in the optical domain to overcome the limitations due to information loss, efficiency and cost because of the electro-optic and opto-electronic conversions in radio-over-fibre links. The possibility of using photonic devices to implement flexible filters for optical, microwave and radio frequency signals with larger bandwidth is preferable since conventional approaches for radio frequency processing are restrained by the electronic bottleneck and electromagnetic interference (EMU) [8, 91–93]. Particularly, optical fibre delay line filters have been extensively demonstrated and novel proposals have been reported to provide structures with higher flexibility and extended range of transfer functions [94, 95]. These also include the use of optical amplifiers [9], modulators [96] as weighting elements and the use of modulators to achieve filters with negative coefficients [97].

In this chapter, a segmented high-birefringence (Hi-Bi) optical fibre based delay line filter is presented. The basic concept of a delay line filter and the determining factors that influence the filter operation are highlighted. An introduction of the basic structure of a typical fibre delay line filter is given, followed by the working principle of high-birefringence fibre delay line filter. Then, the model employed to simulate the response of a segmented Hi-Bi fibre delay line system is detailed and the architecture of the proposed reconfigurable delay line filters is described. The results obtained from the experiments and simulations are superimposed and discussed, both for the microwave/millimetre-wave filtering and the

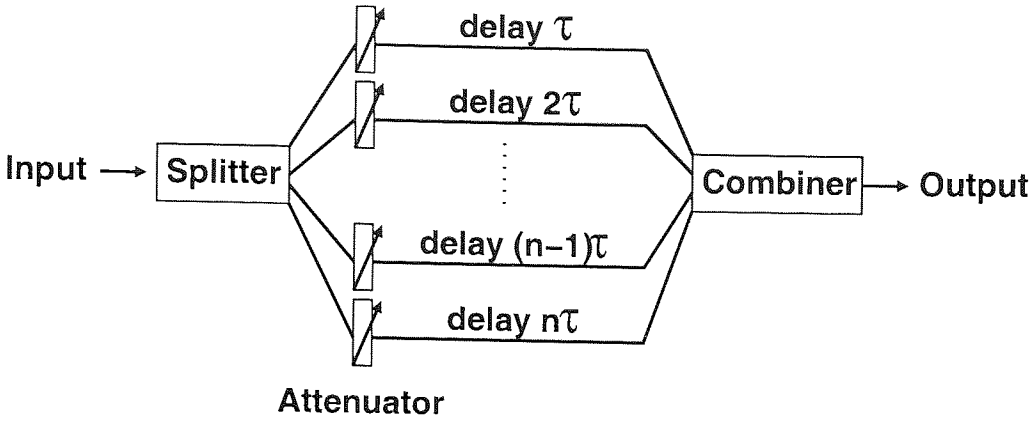

Figure 5.1: Basic setup of a delay line filter.

multichannel flattop optical bandpass filtering responses. This proposed delay line filter has successfully shown that it is capable of providing reconfigurable complex filter transfer functions with no extra care needed for the isolation from environmental disturbances.

5.2 Key Concepts

The basic structure of a delay line filter is shown in figure 5.1. It is a tapped delay line filter adopted for frequency domain signal processing where the tap weights can be adjusted to obtain the desired filtering operation [92, 98]. Basically, it consists of four key processes, which are the optical branching, tap weighting, differential time delay and summation. As shown in the figure, the input light is first split into many paths through optical branching process. The resulting paths are usually known as optical taps. In order to obtain different intensity for each path, an attenuator with appropriate weight is added to each path. The attenuated optical paths are then introduced to a differential time delay between each other. A square-law photodetector is then used to recombine all the optical paths to give the output response of the filter. This form of tapped delay line filter, which can also be called a transversal filter, is adopted for frequency domain signal processing.

An alternative approach for this form of filter is the lattice structure configuration where the filter devices consist of cascaded modules of elementary delay line filter blocks. Since optical fibres can be used to provide precise time delay, it is very easy to achieve the branching and summation in the optical domain by using $N \times N$ couplers. It should be noted that the transfer function of the lattice filter is similar to that of the transversal filter. An example of a lattice structured fibre delay line is shown in figure 5.2 where it is cascaded with two 2×2 couplers with a delay of $\Delta\tau$. This operation represents an optically coherent optical delay line filter architecture.

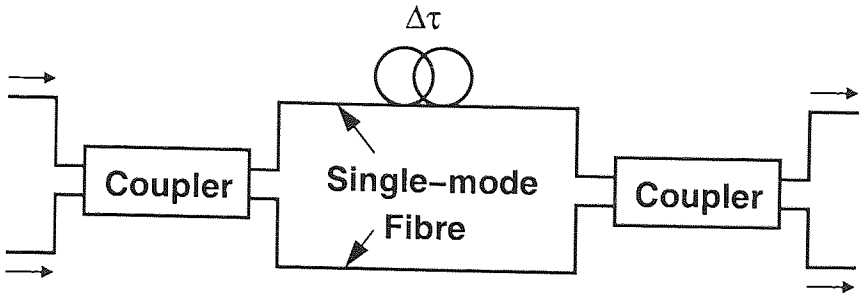

Figure 5.2: Schematic diagram of basic lattice configuration of delay line filter.

In principle, a delay line structure that coherently combines the tapped signals enables both phase and amplitude control over the output response. However, stringent stabilisation and isolation from environmental disturbances are required. Hence, coherent detection dependent on the phase of the optical carrier is avoided in delay line filters. A low coherence optical source is used simply to achieve incoherent summation to avoid the environmentally sensitive optical interference effects. But, this consequently leads to the failure to keep the phase information of the taps and thus makes the negative weighting of the optical taps not achievable. This limits the applications of incoherent fibre delay lines in flattop bandpass and high pass filtering signal processing [99].

To achieve the incoherent summing requirements, a low coherence source and large optical path difference (OPD) are imperative. As a result, the free spectral range (FSR) of the filter is restrained by the source coherence. An alternative scheme to overcome the limitation caused by the optical coherence of the source and thus to obtain a large free spectral range is to exploit the orthogonally polarised states in the fibre [26, 100]. In this way, a low coherent source and large OPD are not necessary as the two polarised states allow coherent interaction regardless of the length of the fibre. This, in turn, gives much flexibility to the free spectral range of the filter. Besides, least care on the environmental perturbation is needed since the two polarised modes within the same fibre experience the same disturbance.

To obtain two linearly orthogonal polarised beams in an optical fibre system, the simple and ideal method is to use a high-birefringence (Hi-Bi) fibre, where two linear polarisation modes travel along the fast and slow axes, respectively, with a high extinction ratio between them. A novel all-fibre transversal filter using cascaded Hi-Bi fibre structure has been proposed [101]. In this technique, every piece of Hi-Bi fibre worked as a delay line module and two separate pieces of Hi-Bi fibre were linked one after the other to form a cascaded structure. This makes the structure inflexible when higher cascaded architecture is needed since on this occasion additional pieces of Hi-Bi fibre are required for extending the delay line architecture. This inevitably affects the configurability of the filtering responses.

In this work, a single piece of high-birefringence optical fibre is exploited in order to effectively maintain a coherent fibre delay line with minimum care in environmental perturbation. The difference from [101] is that an optical fibre delay line filter constructed by a single piece of Hi-Bi fibre structure is presented. Instead of using two sections of separate fibre, the single piece of fibre can be segmented by applying a coupling stress onto it. The work aims to show that by changing the input azimuth to the fibre as well as the strength and direction of the applied stress coupling to the Hi-Bi fibre, a reconfigurable microwave/millimetre-wave filtering response can be achieved. Besides, bipolar taps can also be obtained by the optically coherent addition of the signal taps to realise more complex microwave filtering responses and multichannel flattop optical bandpass filtering for wavelength division multiplexing (WDM) applications.

5.3 Hi-Bi Fibre Delay Line Filter

As mentioned in section 2.4, Hi-Bi fibre has a high extinction ratio in its polarisation modes that can degenerate input light into slow and fast axes. These two components propagate at different speeds and interact with each other at the detector. The optical path difference (OPD) between the two polarisation modes is directly related to the birefringence Δn and the length of fibre L as in

$$OPD = \Delta nL. \tag{5.1}$$

The time delay $\Delta\tau$ and the free spectral range (FSR) of the output frequency response are hence given by

$$\Delta\tau = \frac{\Delta nL}{c} \tag{5.2}$$

and

$$FSR = \frac{1}{\Delta\tau} = \frac{c}{\Delta nL}, \tag{5.3}$$

where c is the light speed in vacuum. The phase difference $\Delta\varphi$ between the two polarisation modes can be expressed as

$$\Delta\varphi = \frac{2\Delta n\pi}{\lambda}L, \tag{5.4}$$

where λ is the optical wavelength. Due to the coherent interference between them, the detected intensity at the output $|E_0|^2$ after the detector is strongly dependent on the phase dif-

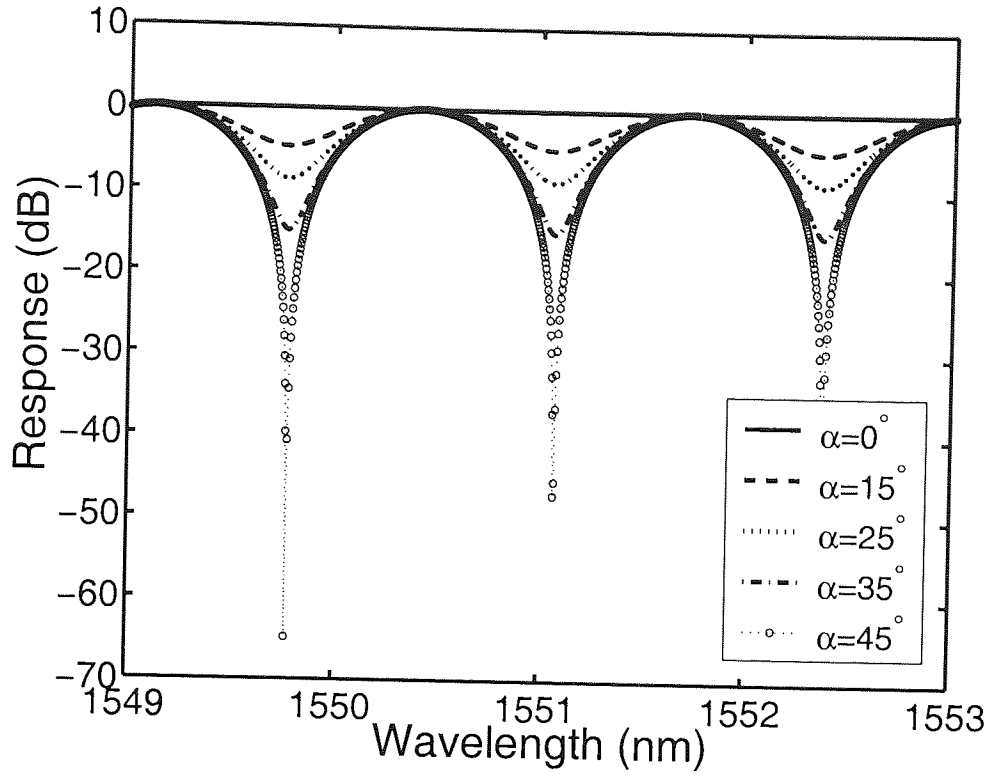

Figure 5.3: Simulated output response of a Hi-Bi fibre with different input azimuths.

ference. The output response, given the magnitude of the coherent sum of the electric field of the two polarisation modes can be expressed by

$$|E_0|^2 = \left| \sum_i^2 e_i \cdot e^{-j\left(\frac{2n_i\pi}{\lambda}L\right)} \right|^2, \tag{5.5}$$

where e_i and n_i denote the amplitude and refractive index of i-th polarisation modes with $i = x, y$. The value e_i is related directly to the relative angular rotation α between the input light and the birefringence axes of the fibre and can be written as

$$\begin{pmatrix} e_x \\ e_y \end{pmatrix} = \begin{pmatrix} \cos\alpha \\ sin\alpha \end{pmatrix}. \tag{5.6}$$

It is worth noting that equation (5.6) applies only to a single section of Hi-Bi fibre. As more sections of Hi-Bi fibre are formed, more complicated transfer functions will be involved. This will be highlighted in the forthcoming section.

The dependency of output response on the input azimuth was simulated based on equation (5.5) and the output response is shown in figure 5.3. The simulation was carried out with $n = 1.45$, $L = 5$ m and $\Delta n = 3.7 \times 10^{-4}$. As can be seen from the figure, when two polarisation modes were excited, different optical path differences caused optical power cancellation at specific wavelengths and produced notch responses [26]. When a linearly polarised light

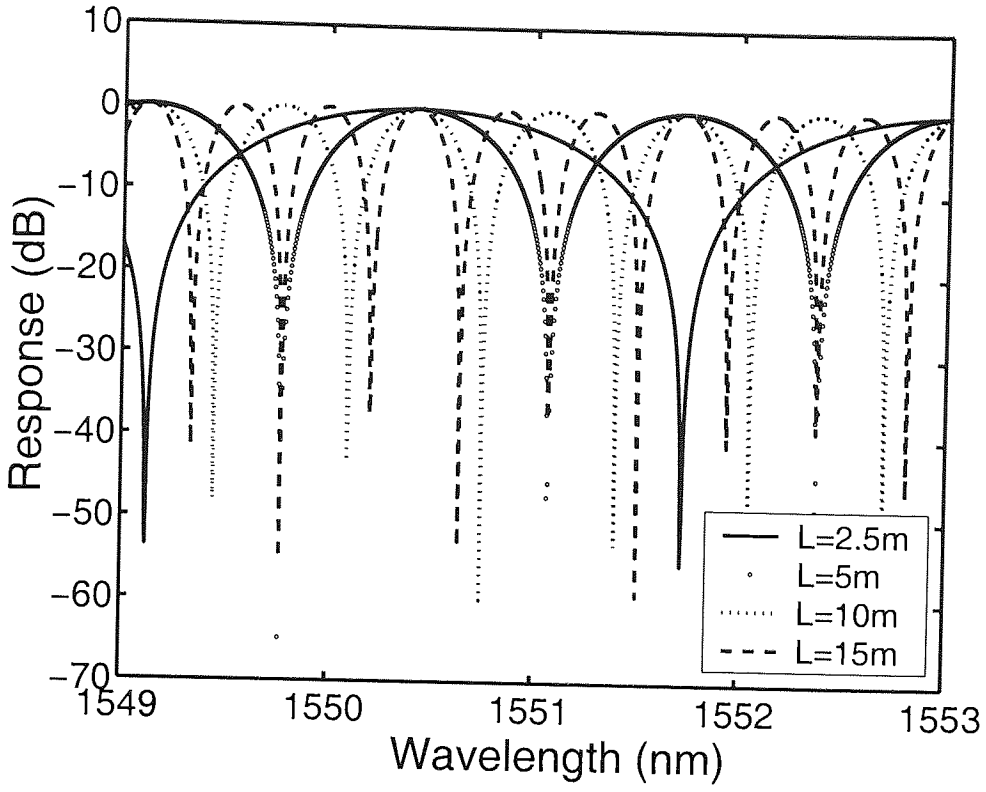

Figure 5.4: Simulated output response of a Hi-Bi fibre with different fibre lengths.

was coupled into a Hi-Bi fibre with angular rotation, or input azimuth, $\alpha = 0°$, at the fibre input, the linearly polarised light maintained its polarisation state along the Hi-Bi fibre and thus gave a flat response at the output due to no interaction between the two polarisation modes. The deepest notch appeared only when the light was coupled equally into a Hi-Bi fibre with input azimuth $\alpha = 45°$. It is obvious that the amplitude of the notch depended on the input azimuth α relative to the birefringence axes of the Hi-Bi fibre.

It is also clear from equation (5.3) and equation (5.5) that the FSR of the output response is dependent on the fibre length. This dependency was simulated and is demonstrated in figure 5.4. It can be seen that deep notches appeared at different wavelengths according to the length of fibre. Basically, longer length of fibre produced smaller FSR. In this way, the desired FSR could be obtained by changing the length of the Hi-Bi fibre.

It is evident that Hi-Bi fibre has the same working principle with the lattice filter configuration shown in figure 5.2. Each degenerated polarisation mode represents an optical branch with respective time delay or phase difference based on the fibre length and birefringence. Its advantage is, it permits easy packaging and isolation, if necessary, because it has a single-line structure design. The intensity of the polarisation modes can be controlled by applying different input azimuth and coupling onto the fibre. This single-line fibre delay line archi-

tecture allows coherent operation without limitation from the optical source coherence, and thereafter more control on the FSR. Besides, a compact filter structure with minimised environmental sensitivity typical of fibre-based optically coherent devices can also be realised. No extra control scheme is needed for optical path control in this proposed structure. Thus, the Hi-Bi fibre delay line filter is attractive because of its feasibility, stability and simplicity as demonstrated in [26].

5.4 Segmented Hi-Bi Fibre Delay Line Filter

Higher order delay line filter can be achieved by extending the basic delay line filter block to allow a complex transfer function that is not attainable by an individual elementary module. The segmented structures built by multiple basic modules induce larger number of optical taps that will provide different transfer responses. Based on the concept of the delay line filter, in this work, a segmented Hi-Bi fibre delay line filter is proposed. Before going into that, a model based on the segmented structure is presented. Here, a single section of Hi-Bi fibre is considered as an elementary module.

Polarisation evolution in a birefringent fibre is closely related to the perturbation of anisotropy along the fibre axis due to waveguide imperfections, external forces and environmental condition changes [29, 30, 102, 103]. Highly birefringent fibres are used to minimise random mixing of polarisation modes. They support two well-defined and mutually orthogonal polarisation modes, commonly referred to the slow and fast modes [102, 104]. At the output, fields orthogonal to the incident state of polarisation (SOP) can be selected and detected. For highly birefringent fibres, there is a minimal coupling between the polarisation modes in the absence of external disturbances. Thus, the fields maintain their initial SOP.

In the absence of stress, all fibre sections have the same beat length and all birefringence axes are aligned. When a birefringent fibre is subjected to a lateral force, the beat length is changed. More importantly, the birefringence axes of the stressed fibre are also rotated relative to those of the unstressed fibre. As a result, there is coupling between two polarisation modes [29]. Thus, in the presence of stress, the beat length of the stressed section is changed and the birefringence axes are rotated by an angle, β, relative to those of other sections. Therefore, in the model, a high-birefringence fibre is modelled as a concatenation of three fibre sections with different beat length (and hence different birefringence) and orientation of the birefringence axes [29, 30]. This model can be applied for microwave filtering responses as well as optical filtering responses.

As demonstrated in figure 5.5, if a linearly polarised light is launched into the fibre with an azimuth α to the x-axis of the first fibre section, L_1, the input amplitude e to the fibre and

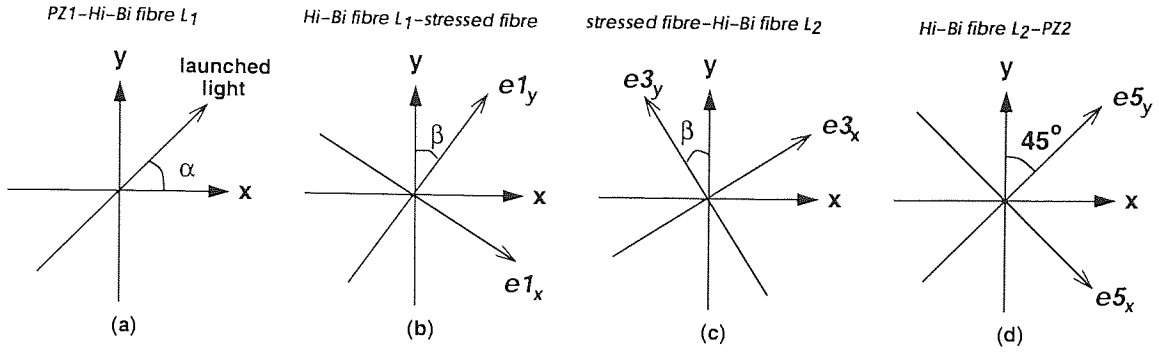

Figure 5.5: Degeneracy of light between the interface of (a) PF1 and Hi-Bi fibre L_1, (b) Hi-Bi fibre L_1 and stressed fibre l, (c) stressed fibre l and Hi-Bi fibre L_2 and (d) Hi-Bi fibre L_2 and PF2.

its output amplitude $e1$ can be expressed as

$$\begin{pmatrix} e_x \\ e_y \end{pmatrix} = \begin{pmatrix} \cos\alpha \\ \sin\alpha \end{pmatrix}, \tag{5.7}$$

and

$$\begin{pmatrix} e1_x \\ e1_y \end{pmatrix} = M_1 \begin{pmatrix} \cos\alpha \\ \sin\alpha \end{pmatrix}, \tag{5.8}$$

respectively, with

$$M_1 = \begin{pmatrix} e^{-jkn_xL_1} & 0 \\ 0 & e^{-jkn_yL_1} \end{pmatrix}, \tag{5.9}$$

which is the transfer matrix of the delay line in unstressed Hi-Bi fibre with L_1. $n_{x,y}$ is the refractive indices in x and y axes of the unstressed sections.

When the output light with $e1$ is launched into the middle section (stressed section) with rotation angle of β caused by the stress, its output $e2$ is

$$\begin{pmatrix} e2_x \\ e2_y \end{pmatrix} = M_2 \begin{pmatrix} e1_x \\ e1_y \end{pmatrix}, \tag{5.10}$$

with

$$M_2 = \begin{pmatrix} \cos\beta & \sin\beta \\ -\sin\beta & \cos\beta \end{pmatrix}, \tag{5.11}$$

which represents the intensity coupling coefficient between the unstressed and stressed sections of fibre. The output $e3$ after travelling l length of stressed fibre can then be defined as

$$\begin{pmatrix} e3_x \\ e3_y \end{pmatrix} = M_3 \begin{pmatrix} e2_x \\ e2_y \end{pmatrix}, \tag{5.12}$$

with

$$M_3 = \begin{pmatrix} e^{-jkN_x l} & 0 \\ 0 & e^{-jkN_y l} \end{pmatrix}, \tag{5.13}$$

which is the transfer matrix of the delay line in the stressed fibre that characterises the linear birefringence of the section with l. $N_{x,y}$ is the refractive indices in x and y axes of the stressed sections. Since the stressed section is relatively short and not twisted, the circular birefringence can be ignored [29]. It is evident that as a result of degeneration of the polarised modes propagating through the Hi-Bi unstressed-stressed structure, bipolar optical taps are created. These optically created negative taps hence enable the filter structure to perform periodic complex transfer function like flattop bandpass filtering which is impossible with purely positive structures [105].

When the light reaches the interface between the stressed and unstressed sections again, the output $e4$ can be expressed as

$$\begin{pmatrix} e4_x \\ e4_y \end{pmatrix} = M_4 \begin{pmatrix} e3_x \\ e3_y \end{pmatrix}, \tag{5.14}$$

with

$$M_4 = \begin{pmatrix} \cos\beta & -\sin\beta \\ \sin\beta & \cos\beta \end{pmatrix}, \tag{5.15}$$

which represents the intensity coupling coefficient between the stressed and unstressed sections of fibre. The output $e5$ after travelling L_2 length of unstressed fibre can be calculated as

$$\begin{pmatrix} e5_x \\ e5_y \end{pmatrix} = M_5 \begin{pmatrix} e4_x \\ e4_y \end{pmatrix}, \tag{5.16}$$

with

$$M_5 = \begin{pmatrix} e^{-jkn_x L_2} & 0 \\ 0 & e^{-jkn_y L_2} \end{pmatrix}, \tag{5.17}$$

which is the transfer matrix of the delay line in unstressed fibre with L_2.

Hence, the output electric fields along the fast E_x and slow E_y axes of the Hi-Bi fibre can be given as

$$\begin{pmatrix} E_x \\ E_y \end{pmatrix} = M_5 M_4 M_3 M_2 M_1 \begin{pmatrix} \cos\alpha \\ \sin\alpha \end{pmatrix}, \tag{5.18}$$

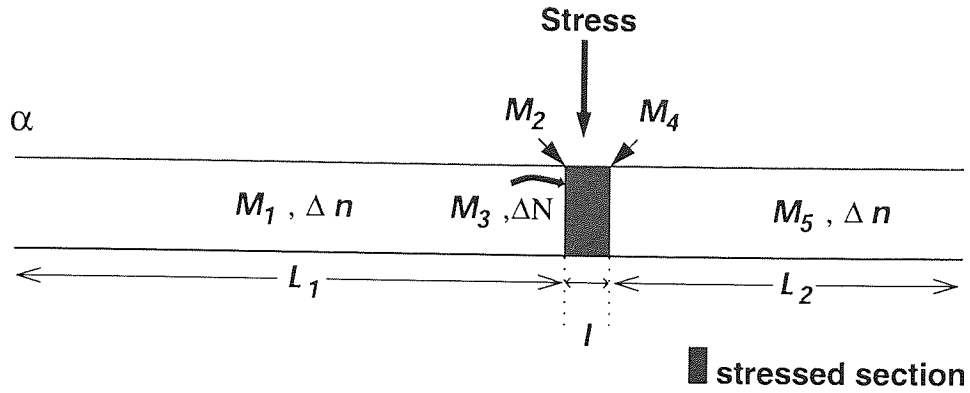

Figure 5.6: Schematic diagram of the incurred transfer matrix according to different sections.

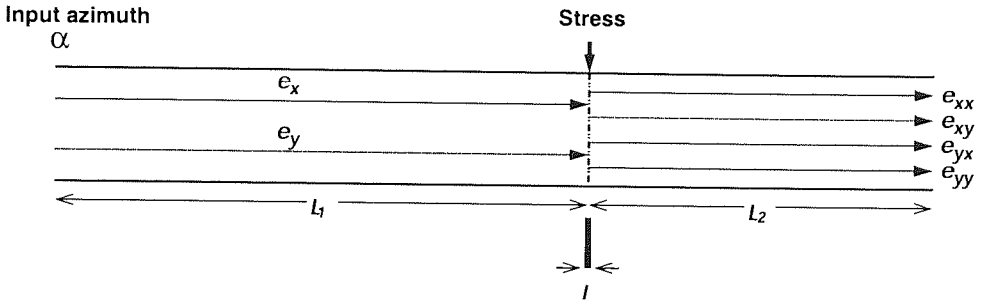

Figure 5.7: Schematic diagram of the delay line with four output taps.

where M_i (i=1, 2, 3, 4, 5) are the matrices representing the first section of the fibre, the rotation by an angle β, the stressed section, the rotation by an angle $-\beta$, and the second section of the fibre, respectively. These transfer matrices are illustrated in figure 5.6 according to respective section.

Calculating the matrices and ignoring the common phase factors, the output fields is given by

$$\begin{pmatrix} E_x \\ E_y \end{pmatrix} = \begin{pmatrix} a_1 e^{-j\theta_1} e^{-jk\Delta n(L_1+L_2)} + a_2 e^{-j\theta_2} e^{-jk\Delta n L_2} \\ a_3 e^{-j\theta_3} e^{-jk\Delta n L_1} + a_4 e^{-j\theta_4} \end{pmatrix}, \tag{5.19}$$

with

$$a_1 e^{-j\theta_1} = \cos\alpha(e^{-jk\Delta N l}\cos^2\beta + \sin^2\beta), \tag{5.20}$$

$$a_2 e^{-j\theta_2} = \frac{1}{2}\sin 2\beta \sin\alpha(e^{-jk\Delta N l} - 1), \tag{5.21}$$

$$a_3 e^{-j\theta_3} = \frac{1}{2}\sin 2\beta \cos\alpha(e^{-jk\Delta N l} - 1), \tag{5.22}$$

$$a_4 e^{-j\theta_4} = \sin\alpha(e^{-jk\Delta N l}\sin^2\beta + \cos^2\beta), \tag{5.23}$$

which represent the weighting components for the output fields of the four taps. $\Delta N = N_x - N_y$ and $\Delta n = n_x - n_y$ are the birefringence in the stressed section and unstressed sections,

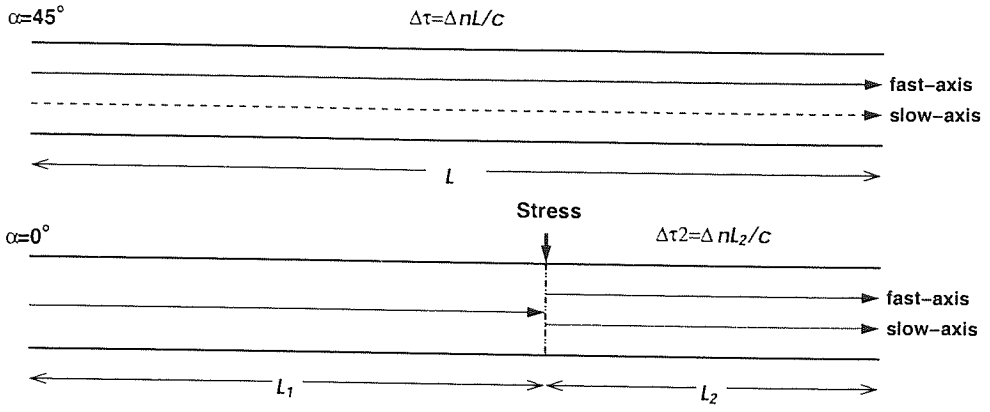

Figure 5.8: Schematic diagram of the delay line in fibre sections.

respectively. These four taps are illustrated in figure 5.7 with $E_x = e_{xx} + e_{yx}$ and $E_y = e_{xy} + e_{yy}$ related to equation (5.19). θ_i are the optical phases introduced by the input azimuth and the applied stress. They are far smaller than that introduced by the intrinsic fibre birefringence and are constants for each quadrant of the input azimuth. Note that all four taps are optical fields and they will add coherently to produce a bipolar response in the optical fields. According to the above equations, the weighting of the taps can be reconfigured by changing the input azimuth, and the strength and direction of the applied stress.

The optical coherently detected intensity output essentially takes a similar form as in equation (5.5). It is the magnitude of the coherent sum of the optical taps, which can be expressed as

$$|E_0|^2 = \left| a_1 e^{-j\theta_1} e^{-jk\Delta n(L_1+L_2)} + a_2 e^{-j\theta_2} e^{-jk\Delta nL_2} + a_3 e^{-j\theta_3} e^{-jk\Delta nL_1} + a_4 e^{-j\theta_4} \right|^2. \quad (5.24)$$

5.4.1 Uniformly Spaced Response

If the lengths of two Hi-Bi fibre sections satisfy

$$k\Delta nL_1 = 2k\Delta nL_2, \quad (5.25)$$

then the four optical field components will be uniformly spaced. Based on equation (5.25), the length ratio for L_1 and L_2 can be deduced as 2:1. The time delay between the four taps are spaced with a time delay unit of $\sim \Delta nL_s/c$, where c is the light speed in vacuum, L_s is the length of the shorter fibre section.

When a linearly polarised light is coupled equally in a Hi-Bi fibre with an input azimuth $\alpha = 45°$, it travels in the fast and slow axes of the Hi-Bi fibre with a time delay of $\Delta nL/c$ at the fibre output, as demonstrated schematically in figure 5.8. When the input azimuth is

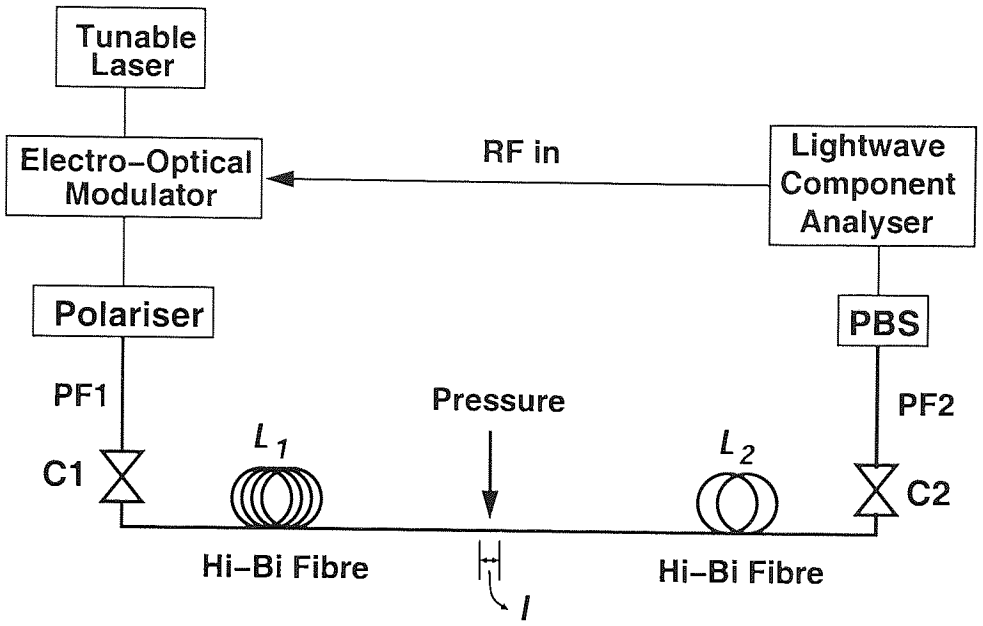

Figure 5.9: Experimental setup of Hi-Bi fibre delay line filter for microwave filtering response.

$\alpha = 0°$ at the fibre input, the linearly polarised light maintains its polarisation state along the Hi-Bi fibre and thus gives a null response until there is a presence of coupling where it is degenerated into fast and slow polarisation modes. The time delay for this situation will be the delay accumulated from the coupling point. In this case, it is $\Delta nL_2/c$.

To achieve ratio of 2:1, the FSR value obtained when stress coupling is applied at the predicted position with input azimuth $\alpha = 0°$ has to be three times larger than the FSR value obtained when no stress coupling is applied but with input azimuth $\alpha = 45°$, as can be calculated from

$$FSR_L = \frac{c}{\Delta nL} = \frac{c}{\Delta n(L_1 + L_2)} = \frac{c}{3\Delta nL_2} = \frac{FSR_{L_2}}{3}. \tag{5.26}$$

This also denotes that the time delay $\Delta nL_2/c$ with the presence of stress coupling is three times shorter than the time delay $\Delta n(L_1 + L_2)/c$ in the later case.

5.5 Microwave Filtering Response

Based on the basic concept of a Hi-Bi fibre delay line filter, a two-section delay line architecture was built. The experimental setup of the proposed delay line filter for microwave filtering response is shown schematically in figure 5.9. A single piece of Hi-Bi fibre with length L=189 m was used in the experiment. The beat length of the Hi-Bi fibre was 4.2 mm at wavelength of 1550 nm corresponding to a birefringence of 3.7×10^{-4}. Both ends of the

fibre were cleaved and butted together with connectors C1 and C2 as to give flexible angle of rotation to the input light with respect to the birefringence axes of the Hi-Bi fibre. Note that special care was not needed to isolate the experimental setup from the environmental disturbance.

A tunable laser with a wavelength of 1550 nm was modulated by a frequency ranging from 0.13 GHz to 20 GHz. With the aid of a polariser, the SOP of the input light was adjusted so that linearly polarised light could be produced. The SOP of the linearly polarised light was maintained by using a polarising fibre (PF1). The linearly polarised light was then coupled into a Hi-Bi fibre through the connector C1 with an input azimuth α. The light was split into the two polarisation modes and they travelled along the whole piece of Hi-Bi fibre $L = L_1 + L_2 = 189\ m$ continuously. At the exit, they were coupled into a short piece of Hi-Bi fibre (PF2), by the connector C2 set with an angle of birefringence $\phi = 45°$ related to that of the PF2. The connector C2 was used to realise the optical coherent addition between the light from the two polarisation modes, and the PF2 was used to spatially split the resultant component obtained from the coherent addition into the orthogonal polarisation modes. At the fibre output, a polarisation beam splitter (PBS) was employed to select the desired orthogonal polarisation mode to be detected and processed by a Light Component Analyser (LCA). The fibre can be divided into two sections by applying a coupling stress. By setting the input azimuth α with different values and by applying stress with different strengths and directions, this proposed fibre-optic delay line filter was capable of providing different frequency responses according to the desired filtering responses.

As mentioned, before a series of experiments are carried out to realise the microwave filtering, coupling at the right interaction location that gives length ratio 2:1 is imperative in order to realise an evenly spaced delay line response. To get the right ratio, a preliminary experiment was conducted. Since 189 m of fibre was used, the predicted location was calculated to be 126 m. A stress was coupled onto the predicted location by pressing the fibre through a metal block onto a length of $l \approx 10$ mm. The length ratio could be ascertained by observing the frequency response of the fibre from the LCA, with and without applied stress based on equation (5.26).

After confirming the right interaction location, a series of experiments were carried out to obtain different filtering responses by changing the input azimuth to the fibre as well as the strength and direction of the applied stress coupling to the Hi-Bi fibre. Measurements were made by using the LCA.

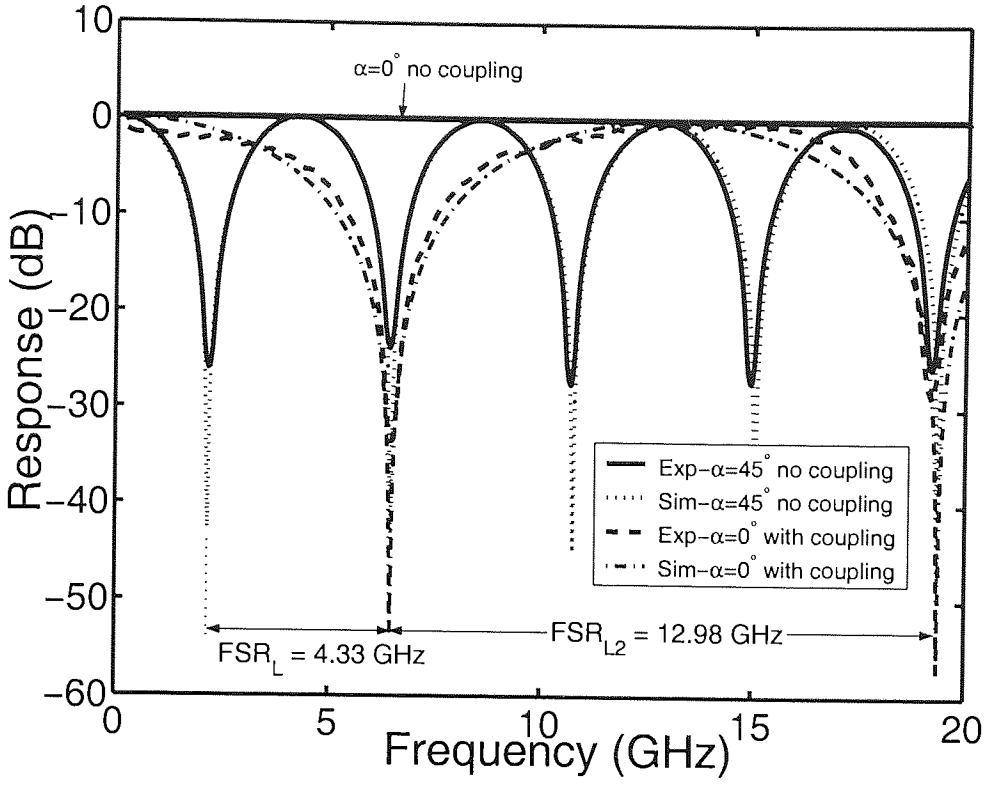

Figure 5.10: Experimental (Exp) and simulated (Sim) notch responses for fibre section ratio determination.

5.5.1 Results

To determine the length ratio of 2:1, firstly, the input azimuth α was set to 45°. This input azimuth could be confirmed easily by obtaining the deepest notch response at the anticipated notch frequency based on equation (5.26). This was because the deepest notch appears only when two polarisation modes are equally excited [26], which implies that $\alpha = 45°$ is obtained. The notch response of this condition was measured by using the LCA and the result obtained is shown in figure 5.10. It shows that the first notch of this setting appeared at about 2.17 GHz. The simulated result of this condition was superimposed onto the measured result. Then, the input azimuth was set to 0°, which allowed only one polarisation mode along x-axis or y-axis to be excited, and with no applied coupling. As can be seen from the plot, the measured response was flat since there was no interaction between the delay lines. When stress was applied to the position that was anticipated to give ratio 2:1, notch response with the first and deepest notch appeared at 6.49 GHz, as shown in figure 5.10. This notch frequency had a value of three times of 2.17 GHz, which matched with equation (5.26). These first notches also indicated that their FSR were 4.33 GHz and 12.98 GHz, respectively, corresponding to the respective time delays $\Delta\tau$ of 230.95 ps and 77.04 ps. This confirmed that

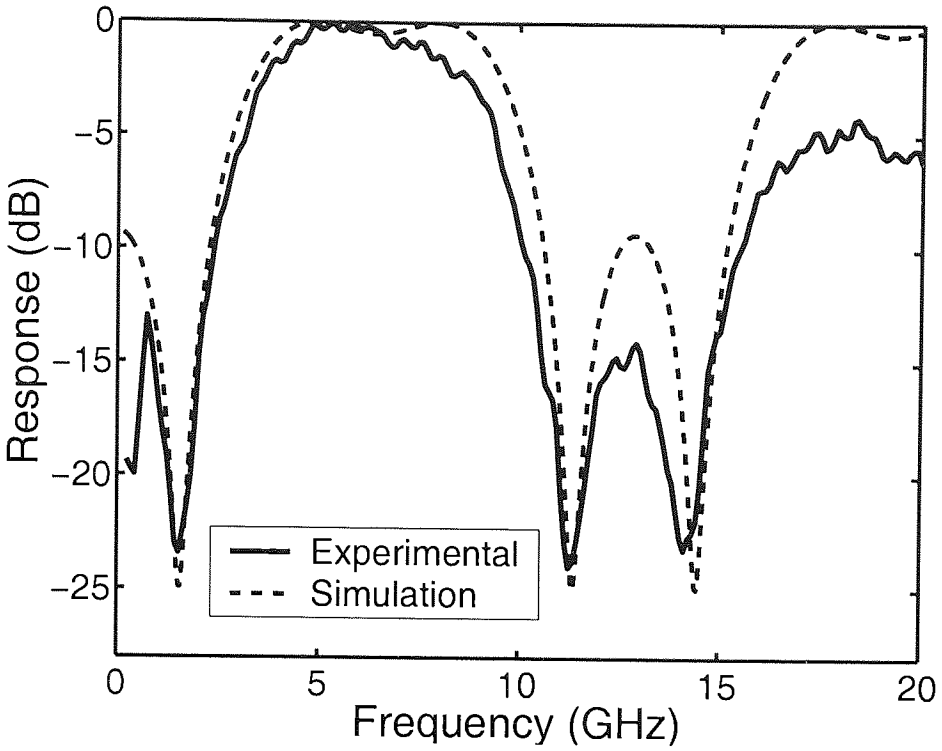

Figure 5.11: Measured filtering response with $\alpha = 19°$, $\beta = 22°$ and weighting components of [0.234, -0.657, 0.226, 0.680].

the predicted location was the location that divided the piece of Hi-Bi fibre into the length ratio 2:1.

Subsequent experiments were carried out with different input azimuth and stress to achieve different weights for the filter responses. One of the measured and simulated responses is shown in figure 5.11. Assuming $\phi = 45°$, $l = 10$ mm, $\Delta N = 7.75 \times 10^{-5}$ and $\lambda = 1550$ nm, a set of weighting components with values [0.234, -0.657, 0.226, 0.680] was obtained with $\alpha = 19°$ and $\beta = 22°$. It can be seen that the proposed delay line filter could also produce negative taps. Another example is shown in figure 5.12, with $\alpha = 24°$, $\beta = 22°$ and weighting components of [-0.293, 0.635, -0.283, -0.657]. Figure 5.13 shows the typical four-tap filter response with a set of weighting components of [0.83, 1.00, 1.00, 0.50]. Another example of negative taps can be found in figure 5.14. It has a set of weighting components of [-0.30, 1.00, 0.90, -0.30].

From the experimental and simulated results, it can be noticed that different microwave responses can be obtained by changing the input azimuth α, and the direction and strength of the stress applied to the Hi-Bi fibre. Due to the use of the Hi-Bi with two orthogonal polarisation modes, bipolar taps can be realised. Thus, filter responses with negative taps can be introduced in this proposed filter. Here, despite of the presence of coherent operation

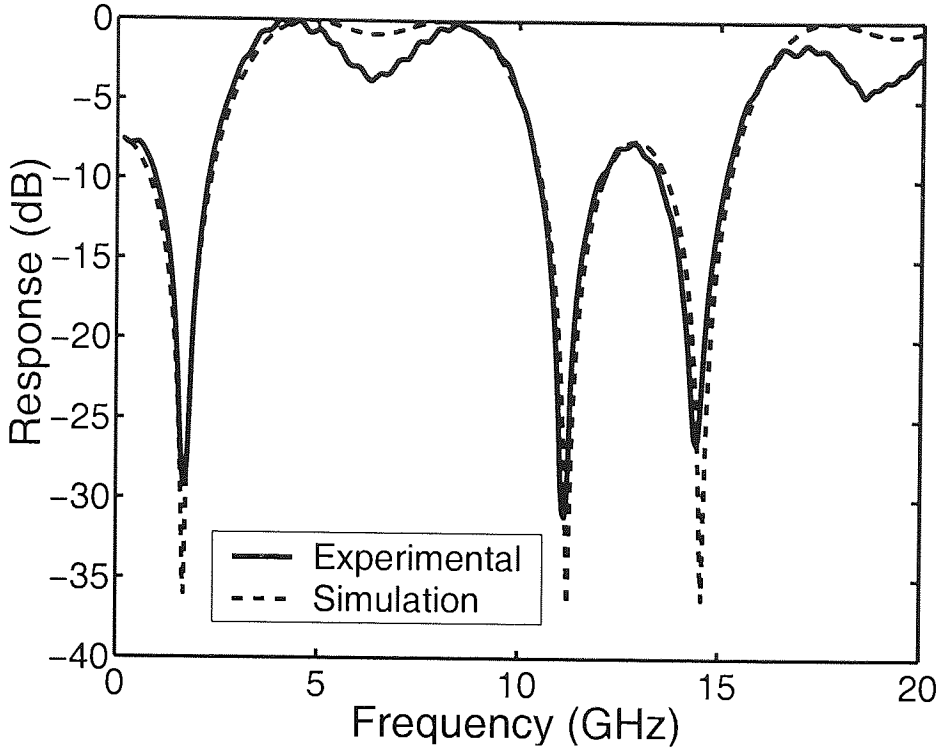

Figure 5.12: Measured filtering response with $\alpha = 24°$, $\beta = 22°$ and weighting components of [-0.293, 0.635, -0.283, -0.657].

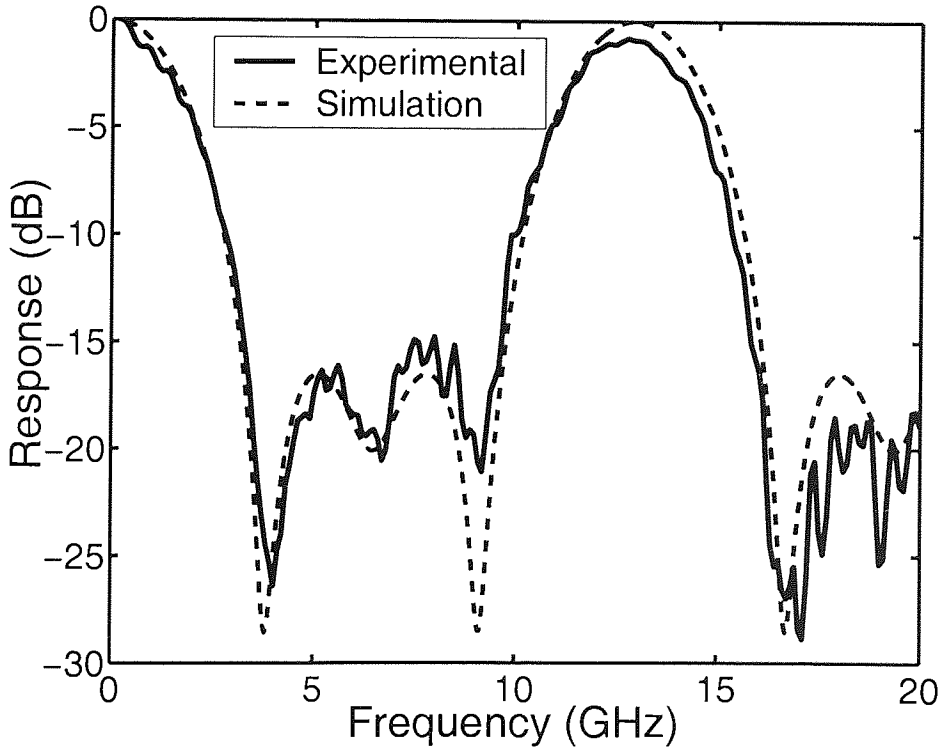

Figure 5.13: Measured filtering response with weighting components of [0.83, 1.00, 1.00, 0.50].

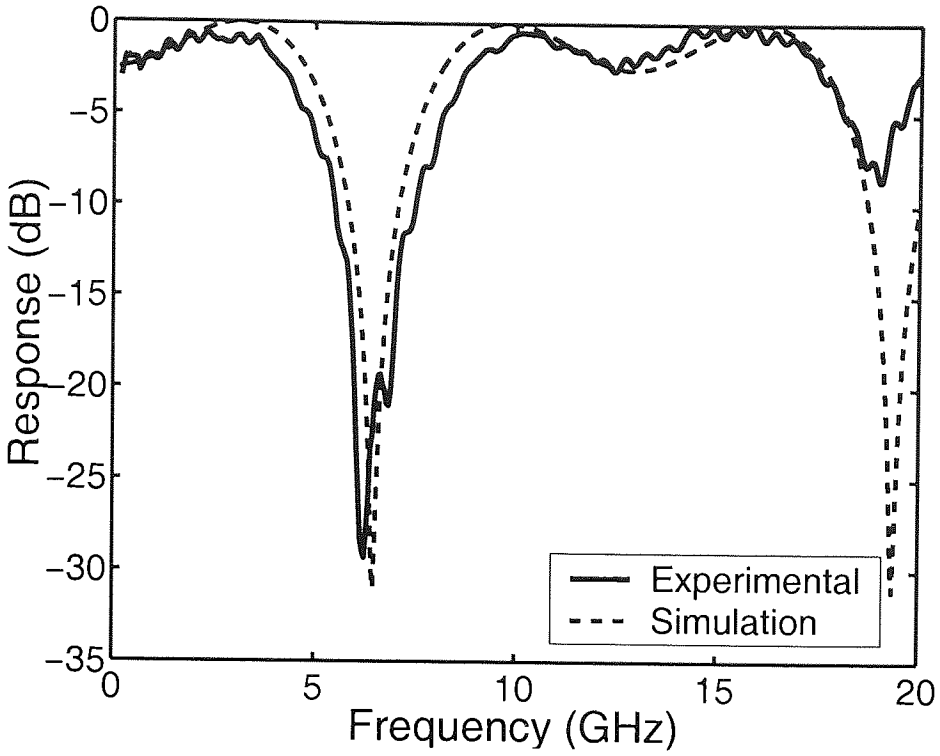

Figure 5.14: Measured filtering response with weighting components of [-0.30, 1.00, 0.90, -0.30].

in the architecture, least care is needed to prevent environmental perturbation because of the nature of the Hi-Bi fibre. The experimental results agree well with the simulated results except there are discrepancies in the amplitude of the notch depth. This could be caused by the amplitude difference between the two modulated sidebands during the experiment, as discussed in section 2.5.1 [34]. The sidelobe suppression and passband ripples obtained experimentally are less ideal than the simulated results. These could be due to the possible mismatch in the length ratio of the Hi-Bi fibre sections and angular misalignment between the fibre ends. The length ratio mismatch can be thermally compensated over a small, isolated section of the Hi-Bi fibre.

5.6 Optical Flattop Bandpass Filtering Response

The concept of Hi-Bi fibre delay line filter structure applies equally to optical filtering responses. Multi-passband optical transmission filters have numerous applications in wavelength division multiplexing (WDM) optical communications. In particular, they can be used for selecting and adding/dropping optical channels. To avoid error, high data rate systems require filters with flattop passbands (<1 dB ripple). Based on the Hi-Bi fibre delay

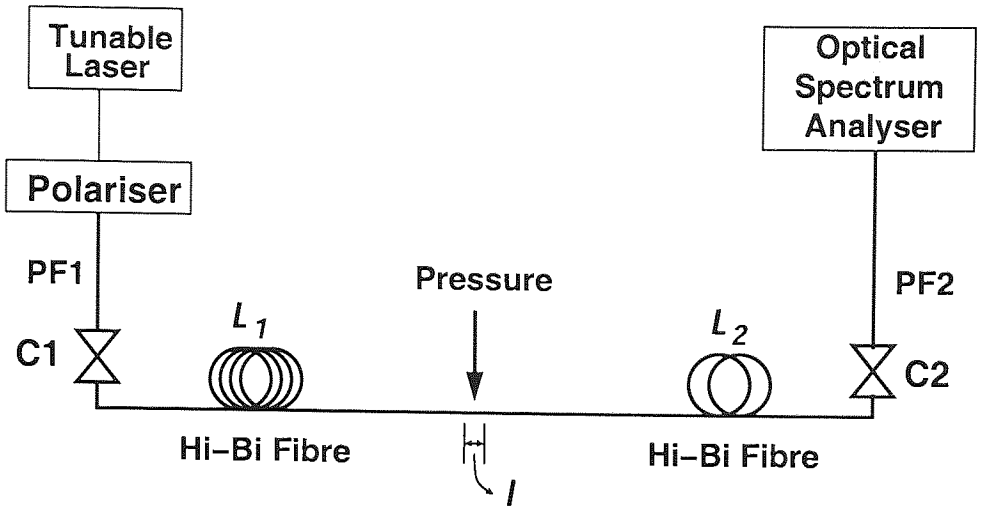

Figure 5.15: Experimental setup of Hi-Bi fibre delay line filter for optical passband filtering response.

line approach, an optical filter with flattop bandpass was assessed. Its setup is shown in figure 5.15. A piece of Hi-Bi fibre with $\Delta n = 3.7 \times 10^{-4}$ and $L = 8.12$ m was used. In order to realise a multichannel flattop filtering response, the same procedure was carried out in order to obtain the right interaction location that gave length ratio 2:1 which would divide L into $L_1 = 5.41$ m and $L_2 = 2.71$ m. After obtaining the right interaction location, an experiment was carried out to obtain flattop passband filtering response by changing the input azimuth to the fibre as well as the strength and direction of the applied coupling stress. An optical spectrum analyser (OSA) was used to measure the optical response.

It is important to mention that the flattop bandpass response is a characteristic feature of a delay line filter with bipolar taps [105]. It is not achievable in a positive system whose phase detection is not accounted for.

5.6.1 Result

Figure 5.16 depicts the measured filtering response for the optical flattop bandpass filter. It shows that multichannel flattop response could be obtained based on the proposed delay line structure. The measured sidelobe suppression was >20 dB with ripples in the passband <0.3 dB. The flattened passband width was 0.57 nm with FSR of 2.40 nm. Simulated result with $\alpha = 18°$, $\phi = 45°$, $\beta = 30°$ and $\Delta N = 7.75 \times 10^{-5}$ was superimposed onto the measured result, as shown in figure 5.16. Based on these parameters, weightings of [-0.476, -0.268, -0.824, 0.155] was obtained from the simulation. This clearly shows that negative taps can be achieved by using this delay line structure. Comparison shows that experimental and simulated results are in good agreement. The measured ripples were attributed to the

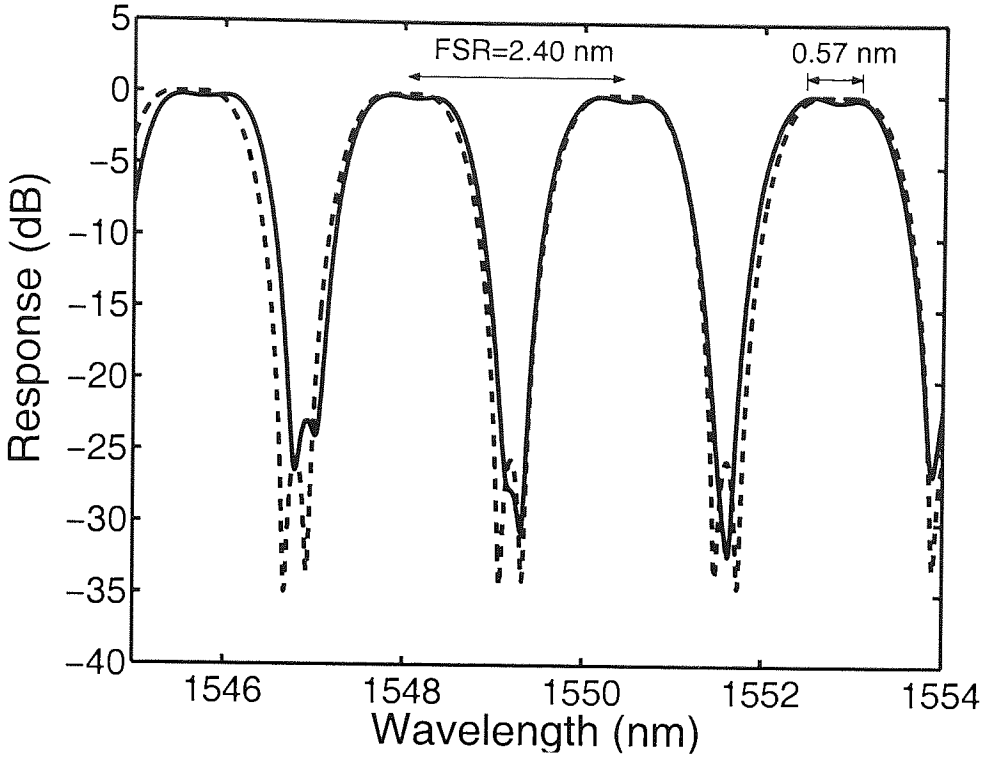

Figure 5.16: Measured (–) and simulated (- -) filtering responses of multichannel flattop optical bandpass filter with $\alpha = 18°$, $\beta = 30°$ and $\Delta N = 7.75 \times 10^{-5}$.

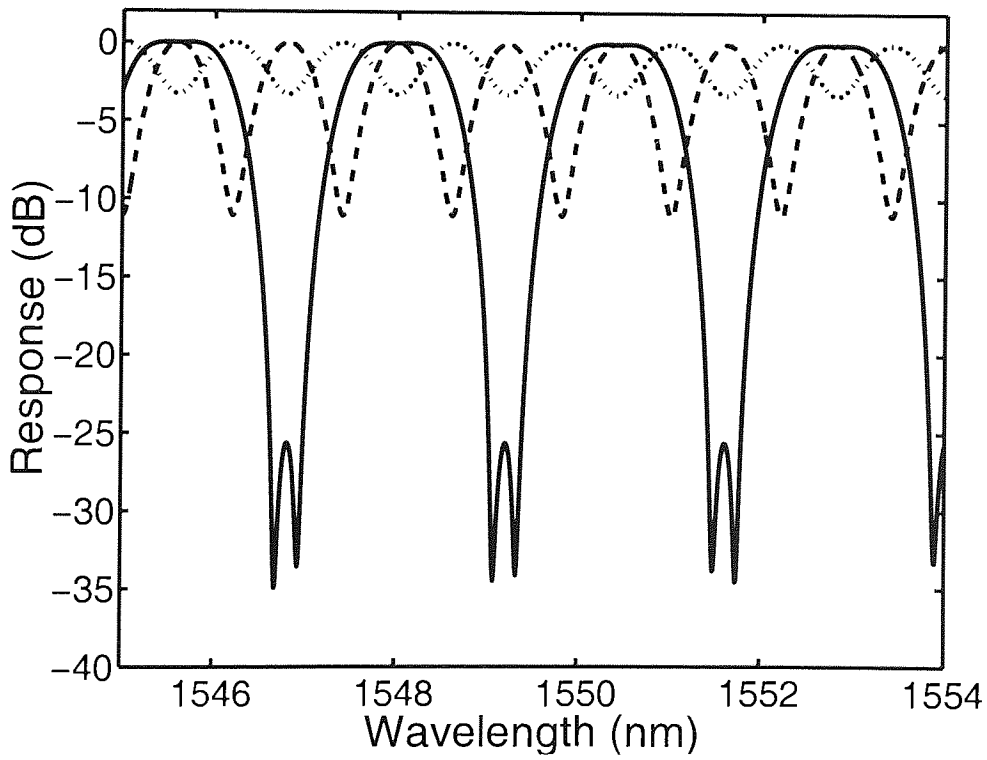

Figure 5.17: Simulated filtering responses based on $\alpha = 18°$, $\beta = 30°$ and $\Delta N = 7.75 \times 10^{-5}$ (–) together with its $|E_x|^2$ (- -) and $|E_y|^2$ ($\cdots$) components.

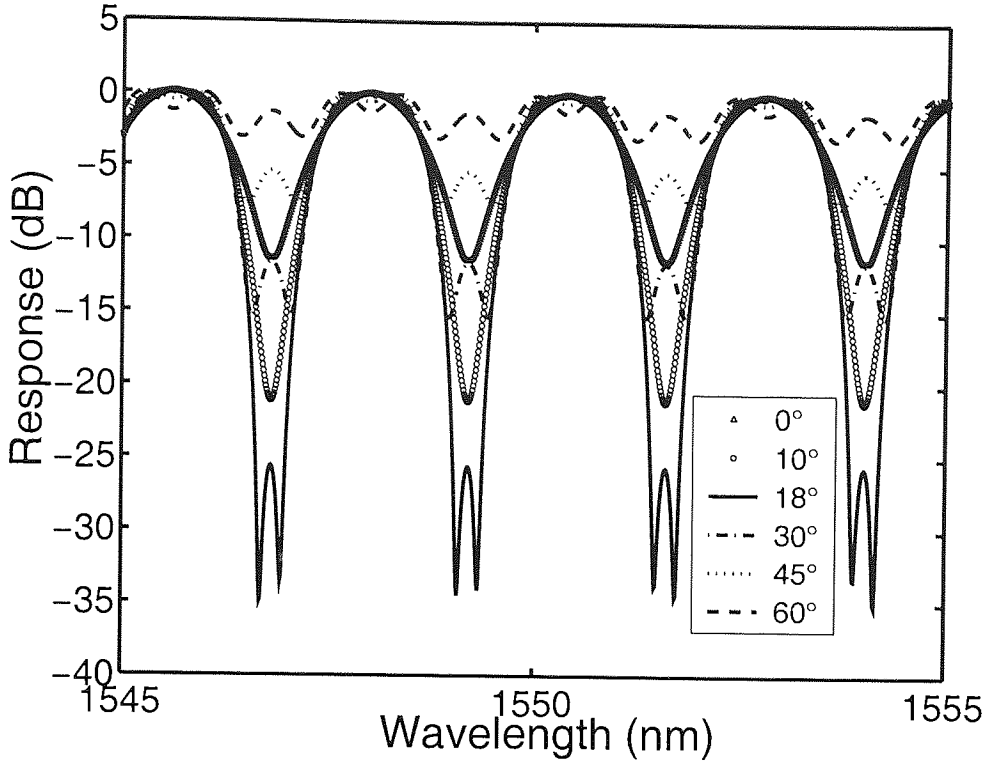

Figure 5.18: Simulated optical signal filtering responses with $\beta = 30°$, $\Delta N = 7.75 \times 10^{-5}$ and different input azimuths α.

fluctuations in the measurement laser. The less ideal sidelobe suppression in the measured response could be caused by the slight mismatch of the Hi-Bi fibre length ratio and the angular misalignments of the fibre ends. To show the interaction between the two polarised lightwaves, the simulated filtering response is also displayed in figure 5.17 together with its $|E_x|^2$ and $|E_y|^2$ components.

5.7 Discussion

From the results, it can be seen that the transfer function of Hi-Bi fibre based filter can be reconfigured by changing the input azimuth and the strength and direction of the coupling stress. To investigate the influence of each parameter, α, β and ΔN, on the transfer function, three simple evaluations based on the analysis in section 5.4 were carried out. As explained, α is the input azimuth of the launched light and β is the rotation angle caused by the coupling stress. It is also clear that ΔN is basically related to the magnitude of coupling stress. Thus, holding constant the values of β and ΔN also means that maintaining the same coupling stress with same strength and direction.

Based on the results for the optical filtering response in figure 5.16, the value of α was

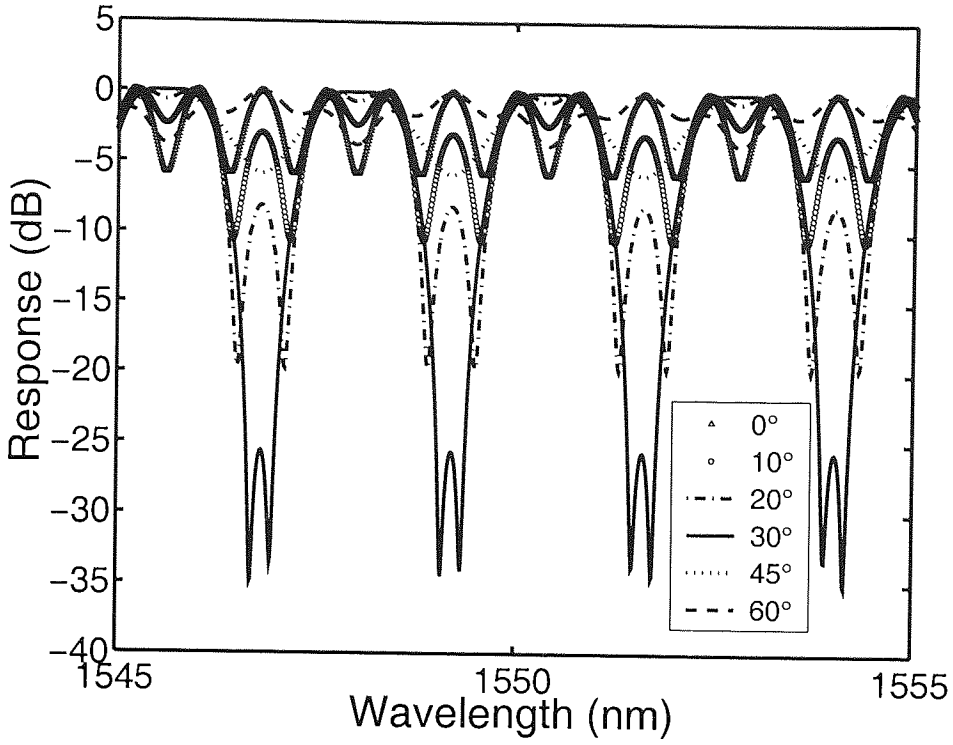

Figure 5.19: Simulated optical signal filtering responses with $\alpha = 18°$, $\Delta N = 7.75 \times 10^{-5}$ and different rotation angles caused by coupling stress β.

first changed and the values of $\beta = 30°$ and $\Delta N = 7.75 \times 10^{-5}$ were maintained. Figure 5.18 shows the transfer functions with different input azimuths α. When it was set at 0° or 90°, the transfer function represented the notch response created by the time delay of Hi-Bi fibre with length L_2=2.71 m. The calculated FSR based on equation (5.3) with L_2 was 299.7 GHz which matched with the $\Delta\lambda$ of 2.40 nm from the plot. It can be seen that α mainly affected the notch depth of the transfer function.

From figure 5.19, apart from affecting the notch depth of transfer function, β influenced the flattop bandpass of the filtering response as well. Thus, it needs to be adjusted correctly in order to produce a flattop response. Meanwhile, as can be seen from figure 5.20, the wavelengths of the notches could be changed by ΔN by varying the strength of the coupling stress onto Hi-Bi fibre.

According to the evaluation results, it can be concluded that the transfer function induced by the segmented Hi-Bi fibre delay line filter can be reconfigured by changing the input azimuth of launched light as well as the strength and direction of the coupling stress onto Hi-Bi fibre. However, due to the fact that there are only three variable parameters in the proposed system, the delay line structure is restricted from producing every arbitrary profile that needed for filtering. This is a common limitation by previously reported methods as well. But, in this proposed system, it can be overcome easily by increasing the number of

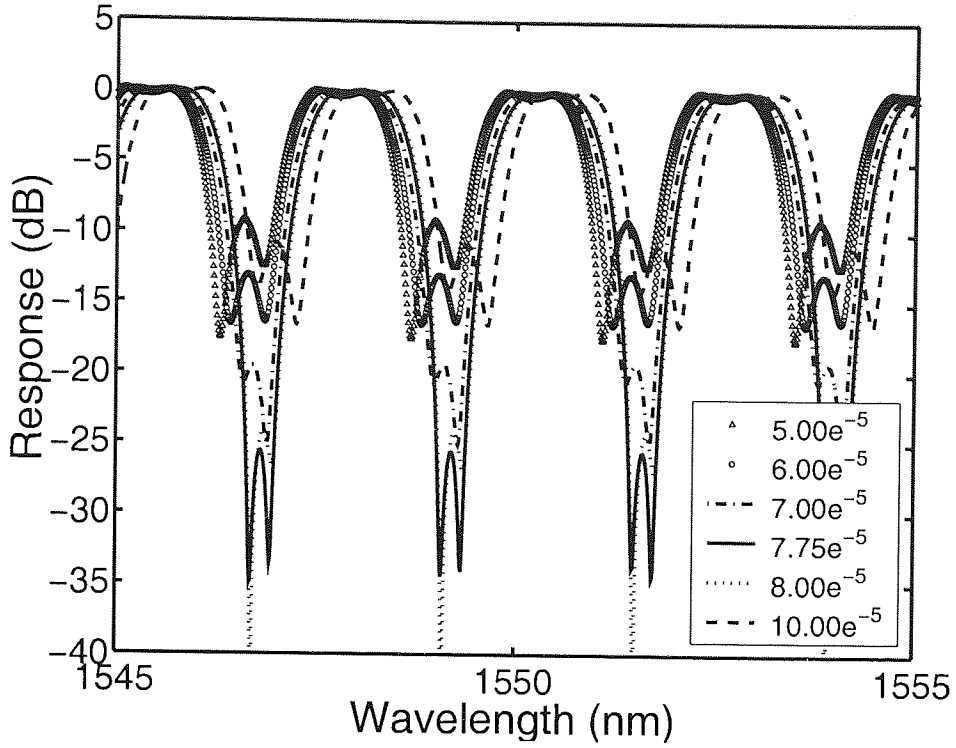

Figure 5.20: Simulated optical signal filtering responses with $\alpha = 18°$, $\beta = 30°$, and different ΔN.

segments, which in turn, increasing the number of taps as to increase the number of variable parameters. In this way, there will be more sets of values of α, β and ΔN to be adjusted to achieve different complex transfer functions.

5.8 Conclusion

A delay line filter based on the exploitation of the fibre birefringence has been reported. The proposed segmented Hi-Bi fibre delay line filter has been experimentally demonstrated and theoretically verified. As a result of the optical coherent addition between the two polarised modes propagating through the Hi-Bi fibre structure, bipolar optical taps have been created to realise periodic complex transfer function like flattop bandpass filtering. Owing to the use of the single-line Hi-Bi fibre structure, no extra control scheme is needed for optical path control in this proposed structure.

In this work, only a two-section delay line filter was demonstrated. However, due to the nature of the use of single piece Hi-Bi fibre, the concept of the filter scheme applies equally for greater number of sections. The increased number of Hi-Bi fibre sections corresponds to the increased number of polarisation mode couplings/degenerations that subsequently lead to

greater number of optical taps in the filter structure. Thus, greater number of sections can be easily realised in this proposed structure by simply adding more stress coupling points. These higher order filters are anticipated to be able to produce wider flattop bandpass channels with enhanced sidelobe suppression.

It can be concluded that the proposed filter can be reconfigured to meet the requirements of signal processing in microwave photonic and wavelength division multiplexing bandpass filter applications. Nevertheless, due to the fact that there are only three variable parameters in the proposed system, the delay line structure is restricted from producing every arbitrary profile that needed for filtering system. This, again, can be overcome by increasing the segments of Hi-Bi fibre to get more variable parameters. There are some discrepancies in the notch amplitudes and sidelobe suppressions between the experimental and simulated results. They can be reduced by using the commercially available tunable polariser, Hi-Bi fibre keyed connectors and precision rotators to effectively control the input azimuth of the launched light. Further investigation can also be done in the aspect of analysing the stress strength and its direction based on the analytical study in [29]. By doing so, the filter structure can potentially enable better free spectral range adjustments and wavelength shiftings. The speed of the filter reconfiguration can also be greatly improved.

Chapter 6

Microwave/RF Signal Transmission in Nonlinear Dispersive RoF Links

6.1 Introduction

The growing demands of bandwidth efficiency and frequency reuse investigate the deployment of radio-over-fibre (RoF) systems with smaller radio link ranges to reduce the interference between cells. This leads to the use of shorter range, higher frequency radio waves and places increased demands on the signal distribution system. There are currently unlicensed bands around 60 GHz, the candidate for future wireless systems [20]. Only a few of the bands around 60 GHz have been assigned for future broadband service provision. For instance, 62 – 63 GHz and 65 – 66 GHz bands have been identified by the European Radiocommunications Office for mobile broadband applications [12]. Microwave/millimetre-wave or radio-frequency (RF) wireless network systems are believed to be the solution for efficient delivery of video and broadband services, while optical fibre is deemed to be the ideal transmission medium between the base stations and the central station. Electronic methods for the generation and delivery of microwave/millimetre-wave or RF are complex and potentially expensive. Optical fibre based methods for generation and distribution of modulation bearing microwave/millimetre-waves or RF are, however, very attractive for this application due to the low-cost, low-loss and wide-bandwidth characteristics of fibre at microwave/millimetre-wave and RF frequencies. The combination of the deployment of the microwave/millimetre-wave or RF wireless networks and the advantages of optical fibre as the transmission medium has motivated the research work in various aspects of microwave photonics, as summarised in [14, 15].

Radio-over-fibre systems, or it can referred to as microwave photonic systems, have re-

ceived increased attention in recent years for the wide-band microwave/RF signal processing and the transmission of microwave/RF signals to remote locations (such as antennas). They are the promising candidate in the generation, distribution, transmission and processing of broadband wireless networks due to the fact that they offer solution to high frequency signal distribution problem allowing the costly optoelectronic devices to be housed in a central station remote from the transmitting antennas. By sharing the costly optoelectronic devices installed at the central station among a large number of base stations, a radio-over-fibre system can offer simple and low-cost implementations of the components required in a communication terminal for mass use [2]. Furthermore, microwave photonic systems operating near 1550 nm benefit from the low loss of standard single-mode fibre and from the use of erbium-doped fibre amplifier (EDFA). This EDFA provides RF transparency that allows signals of near arbitrary format to be distributed with small degradation that caused by the noise and amplifier nonlinearity [15]. The intrinsic properties of low loss and wide bandwidth of single-mode fibre operated near 1550 nm has made it an attractive transmission medium for microwave/RF communication systems.

Since single-mode fibre does not suffer modal dispersion as multi-mode fibre does, it is promising for long haul high bandwidth transmission. For this reason, it is more commonly used in the optical communication systems compared to multi-mode fibre [4]. On the other hand, it is inevitable that operation near 1310 nm window has its advantages of zero dispersion and low distortion over 1550 nm operation window. However, signals at 1310 nm suffer higher loss that causes them to travel 60 % shorter distance than the signals at 1550 nm. Moreover, due to the physics of the materials used in the fibre-optic amplifiers, 1550 nm amplifies much better than 1310 nm. Therefore, nearly all systems incorporating optical amplifiers are designed for 1550 nm.

The working principle of microwave/RF subcarrier signal transmission in optical fibre is adopted from microwave technology, a technology that employs microwave/RF subcarrier for signal transmission over coaxial cable or free space. It can be called a microwave photonic system, or radio-over-fibre (RoF) system since the signal is transmitted by using microwave/RF subcarriers over fibre as well as the optical carriers. Basically, microwave photonic can be defined as the study and applications of opto-electronic devices and signal processing for microwave technologies [15].

Despite the fact that the technique of RoF is borrowed from the conventional transmission in coaxial cable, it has a relatively larger total bandwidth of 10 GHz over the bandwidth of coaxial cable which is well below 1 GHz. This advantage is attributed to the high optical carrier frequencies used for lightwave systems. Besides, the characteristics of optical fibre, as can be seen from Table 6.1, make it more flexible and upgradable. These are the two key

Parameter	Optical Fibre	Coaxial Cable
Diameter (mm)	0.2	5
Weight (g/m)	0.073	30–100
Loss (dB/km)	0.2–2.0	1000–1500

Table 6.1: Comparison between optical fibre and coaxial cable.

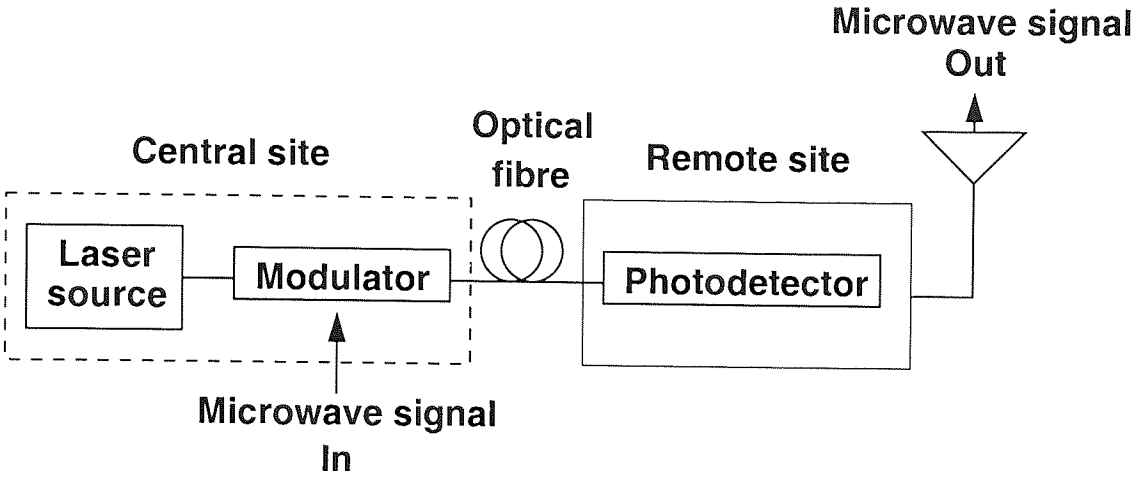

Figure 6.1: Schematic diagram of the basic microwave photonic link.

elements in the design of broadband networks. One can use analogue or digital modulation, or a combination of the two, to transmit multiple voice, data, and video signals to a large number of users. The transmission of multiple microwave/milimetre-wave or RF signals using optics is highly desired in current applications involving hybrid photonic-microwave systems such as multipoint video distribution systems, common-antenna (cable) television (CATV), remote antenna links, mobile communications networks, satellite communications, vehicle communications and control, and microcellular systems [106, 107].

The principle of the microwave photonic system is reasonably straightforward and it is an easy technique to employ in practice. The basic layout of a microwave photonic system is illustrated in figure 6.1. A RF or microwave signal is used to modulate the intensity of a semiconductor laser directly by using a modulator on the central site (central station). This results in an optical spectrum consisting of the original optical carrier plus two sidebands located at $f_0 \pm f_s$ where f_0 is the frequency of the optical carrier and f_s is the frequency of the microwave/RF subcarrier. If the microwave/RF subcarrier is modulated with digital data then sidebands centred on $f_0 + f_s$ and $f_0 - f_s$ are produced. Multiple channels can also be multiplexed onto the same optical carrier by using multiple microwave/RF subcarriers. The modulated signals are then transmitted over an optical fibre link. In order to avoid the modal noise problems due to the characteristic of multimode fibre systems, single-mode fibre is

used in most microwave photonic systems [15]. on the remote site (base station), the signals are detected.

The transmitted power can be written as

$$P(t) = P_{in}\left[1 + \sum_{j=1}^{N} m_j a_j cos(2\pi f_j t + \phi_j)\right], \tag{6.1}$$

where P_{in} is the average input power at the bias level and m_j, a_j, f_j and ϕ_j are, respectively, the modulation index, amplitude, frequency and phase associated with the jth microwave/RF subcarrier when there are more than one microwave/RF subcarrier; a_j, f_j or ϕ_j is modulated to impose the signal depending on whether amplitude modulation (AM), frequency modulation (FM) or phase modulation (PM) is used.

Due to the high demands in microwave photonic system and the importance of optical fibre as the transmission medium, this chapter seeks to investigate the transmission of microwave/RF subcarrier signals in dispersive lossy fibre link accounting for the effect of fibre dispersion, fibre loss and fibre nonlinearity. First of all, the limitations of the RoF link are addressed. The simulation algorithm used to solve the governing equation in nonlinear transmission is the generalised Schrödinger (GNLS) equation, based on the Fourier split-step method is briefly introduced. Experimental investigations on the combined effect of fibre dispersion and nonlinearity in both double-sideband (DSB) and single-sideband (SSB) modulated links are presented together with their simulated results from the GNLS equation. Lastly, further study on the intermodulation distortion caused by two-tone signals transmission in both modulation schemes is brought in.

6.2 Limitations of Microwave Photonics System

In spite of being more advantageous than the conventional transmission systems, microwave photonic systems do face some limitations that restrain their applications. This section discusses their limitations as well as solutions suggested by previous reported work.

6.2.1 Low Signal-to-noise Ratio and Responsivity

Most of the common-antenna (cable) television (CATV) networks distribute television channel by using analogue techniques based on frequency modulation (FM) or amplitude modulation with vestigial sideband (AM-VSB) formats. As the waveform of an analogue signal must be preserved during transmission, analogue subcarrier multiplexing systems require a high signal-to-noise ratio (SNR) at the receiver [15, 20]. However, microwave photonic sys-

tems do have a cost of converting from electrical to optical signals at one end of the system and then back from optical to electrical signals at the remote end.

The main component is the transmitter that consists of a laser source and a modulator. The slope efficiency of the modulator affects the SNR since poor slope efficiency means poor conversion from electrical signals to optical signals. This causes the modulated signals to travel with low power, so the signals are hard to be detected at the photodetector. Besides, since the link gain is a quadratic function of the photocurrent and thus deteriorates as the optical power incident on the photodetector is decreased; the optical power of the laser source directly contributes to the SNR. Apart from the transmitter, the photodetector that converts light into electricity through the photoelectric effect has a cost of converting signals back from optical to electrical signals. The trade-off between the bandwidth and responsivity of a photodetector [16,20] imposes limitations on the signals transfer efficiency and the operation frequency of such systems. As frequencies increase (e.g. to > 60 GHz for micro-cellular applications), there is a need to increase the optical power in the fibre link to maintain a certain level of SNR performance at the receiver. An effective solution to this problem is to increase the optical power in the transmission link [17, 18, 40]. Therefore, the use of an optical amplifier, such as EDFA, is more or less a must in optical distribution systems in order to improve the SNR and to compensate the distribution loss. As a result, higher optical power is needed in microwave photonic systems with higher operating microwave/RF subcarrier frequencies.

6.2.2 Chromatic Dispersion Induced Modulation Suppression

As explained in section 2.5.1, the performance of analogue signal transmission in single-mode fibre is severely limited by the chromatic dispersion of standard single-mode fibre. This phenomenon is caused by the phase cancellation between the two sidebands of a double-sideband (DSB) modulated signal when they arrive at the photodetector [32, 33]. This suppression sharply limits the frequency-length product of fibre-optic links.

To overcome this limitation, several dispersion-tolerant and dispersion equalisation techniques have been investigated. The most attractive method is to employ the optical single-sideband (SSB) modulation approach to eliminate one of the sidebands so that the power fading existing in conventional DSB modulation will no longer appear. To realise SSB modulated signal, the use of dual-electrode Mach-Zehnder electro-optical modulator (MZ-EOM) [108], tapered linearly chirped fibre gratings [109] and chirped fibre Bragg grating filtering [110, 111] have been proposed. It has also been shown that by varying the chirp parameter of a dual-drive MZ-EOM [112], the frequency-length product of an analogue

fibre-optic link may be extended. Another promising technique is by the use of optical dispersion compensating fibres (DCF) [113] to compensate the fibre dispersion. The use of an electroabsorption modulator based transmitters [114], a midway optical phase conjugation (OPC) [115] and a semiconductor optical amplifier (SOA) booster [116, 117] have also been reported. Negative chirp generation in externally modulated lasers using electroabsorption modulators (EAM) has also been investigated in the frame of digital transmissions [118,119], showing that it is possible to extend the transmission length beyond the dispersion limit. All these approaches have proven to be able to eliminate the dispersion-induced modulation suppression effect in linear single channel transmissions.

6.2.3 Considerations and Investigations

As mentioned earlier, the employment of optical amplifier before the fibre link is essential in order to improve the SNR while in section 2.6 , it explains that fibre nonlinearity emerges in fibre due to the high power, long length and small effective area of fibre, as can be seen from equation (2.25). Thus, a consequence of having an optical amplifier is that nonlinear effects start to become significant [19]. In this case, the fibre link with optical amplifier will operate in nonlinear propagation regime. While the impact of fibre nonlinearity on pulse transmission systems has been very extensively studied, the influence of fibre nonlinearity in analogue systems such as radio-over-fibre system has not been given much attention. Most research in the microwave signal/radio-over-fibre transmission area has treated the fibre as a linear dispersive medium only. The frequency response solely for dispersive optical communication systems has been analysed in depth [120]. But, when the optical power at the fibre input increases, nonlinear effects can not be further neglected and nonlinear dispersive propagation must be considered.

To date, the joint effect of the fibre nonlinearity and fibre dispersion has not been considered in depth. Nevertheless, a small amount of work has been reported in the use of fibre nonlinearities to improve the frequency-length product of microwave/RF signal transmission systems, such as by the use of fibre-induced self-phase modulation (SPM) whose behaviour is opposite to that of the chromatic dispersion [121,122] and by the use of four-wave mixing (FWM) in dispersion-shifted fibres [123]. Theoretical expression and experimental analysis for analogue signal propagation in dispersive and nonlinear fibre links have been presented [124, 125]. These proposals have stimulated the exploration of the effect of fibre nonlinearity in dispersive fibre links.

In parallel with the effect of fibre nonlinearity in single channel transmission, fibre nonlinearity gives impact to the two-channel transmission as well. Intermodulation products

(IMPs) are produced when there is more than one frequency present at the input of a nonlinear device. In practice, the analogue signals are distorted during their transmission through the fibre link (nonlinear device). The distortion is referred to as intermodulation distortion (IMD) and is similar in the nature of the FWM distortion discussed in section 2.6.3 [40]. The new frequencies are referred to as the intermodulation products. These are further subdivided as second order IMPs and third order IMPs. The third order IMPs tend to be the major source of distortion because of their large number and they are always in-band. The second order IMPs must also be considered if the microwave/RF subcarriers occupy a large bandwidth.

Investigations on the joint effect of fibre dispersion and nonlinearity in transmission of single unmodulated microwave/RF subcarrier have been reported [121, 122]. However, they only looked at the transfer efficiency for single microwave/RF subcarrier and did not account for the unwanted signal distortion and the generation of new frequencies which would be produced if more microwave/RF subcarriers exist. The generation of unwanted intermodulation distortion between multi-tone microwave/RF signals has not previously been investigated.

In this work, the single-tone microwave/RF signal transmission in DSB and SSB modulated fibre links, accounting for the effects of the fibre dispersion, nonlinearity and loss, are experimentally investigated and theoretically verified. Simulation study on combined effect of fibre dispersion and nonlinearity at fixed modulation frequency in different lengths of lossless and lossy links are also included. Experimental demonstrations of the influence of the fibre-induced SPM effect on dispersion compensated RoF link using chirped fibre Bragg grating are presented together with the simulated results. In order to understand the influence of nonlinear distortion in RoF links, the generation of new frequencies due to the nonlinearity is examined and in particular, a standard two-tone frequency test is simulated to investigate third-order intermodulation distortion. The performance of these systems is evaluated based on the third order intercept point which is fibre length and power dependent.

6.3 Simulation Algorithm

The equation that governs the signal propagation in a fibre link accounted for the effects of fibre dispersion, fibre nonlinearity and fibre loss is the generalised nonlinear Schrödinger (GNLS) equation which can be simplified as [19, 38]

$$i\frac{\partial U}{\partial z} + \frac{i\alpha}{2}U - \frac{\beta_2}{2}\frac{\partial^2 U}{\partial T^2} + \gamma|U|^2 U = 0, \tag{6.2}$$

where U is the slowing varying envelope, α is the fibre loss, β_2 is the group delay velocity, z is the fibre length, T is the time and γ is the nonlinear coefficient given by

$$\gamma = \frac{n_2 \omega}{c A_{\text{eff}}}, \tag{6.3}$$

with n_2 is the nonlinear refractive index, ω is the angular modulation frequency, c is the light speed in vacuum and A_{eff} is the effective fibre core area. β_3 is omitted from equation (6.2) because the wavelength window used in this entire chapter is at 1550 nm and not close to zero-dispersion wavelength.

In solving equation (6.2), the optical amplitude field is assumed to be normalised such that $|U|^2$ represents the optical incident power. $\gamma|U|^2$ is then measured in unit m^{-1} if n_2 takes the unit of m^2/W. A_{eff} is measured in unit m^2 and clearly depends on the fibre parameters such as core radius and the core-cladding index difference.

The GNLS equation is a nonlinear partial differential equation that can not be solved analytically. It normally needs a numerical approach to solve and explore the nonlinear effects in optical fibres. The most straightforward way to do this is by employing the Fourier split-step method [19, 39] which is based on the use of fast-Fourier-transform (FFT). To do this, equation (6.2) has to be divided into linear and nonlinear parts as [19]

$$\frac{\partial U}{\partial z} = (D+N)U. \tag{6.4}$$

D is a linear differential operator that accounts for the fibre dispersion and loss in linear regime and it is given by

$$D = -i\frac{\beta_2}{2}\frac{\partial^2}{\partial T^2} - \frac{\alpha}{2}. \tag{6.5}$$

N is a nonlinear differential operator that rules the fibre nonlinearity effect on signal propagation and it is expressed as

$$N = i\gamma|U|^2. \tag{6.6}$$

Generally, these two elements act together along the length of the fibre. The approximate solution from the split-step Fourier method is obtained by assuming that the dispersive and nonlinear effects can be assumed to act independently over a small propagation distance h. This leads to two steps: $D = 0$ when nonlinearity is taking effect, followed by $N = 0$ when dispersion is acting on the small distance.

The implementation of the split-step Fourier method is relatively fast and easy. As shown in figure 6.2, the fibre length is divided into a large number of sections that need not be spaced equally. The optical signal is first transmitted for a distance $h/2$ with dispersion only using the FFT algorithm. At the middle of the section $z+h/2$, the field is multiplied by a nonlinear term that represents the nonlinearity of the whole section of length h. The field is propagated

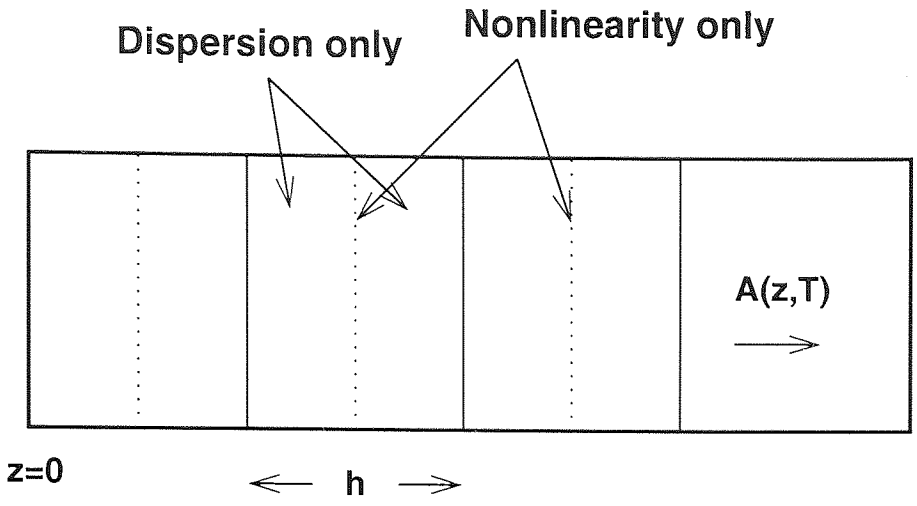

Figure 6.2: Schematic diagram of the symmetrised split-step Fourier method.

in the remaining $h/2$ with only dispersion. Effectively, the nonlinearity is assumed to be summed up at the middle of each section.

The in-house implementation of split-step Fourier method applied to GNLS equation basically is a C++ library that can be used to construct an optical fibre system from different system modules and propagate a signal through that system. These system modules include devices used to generate signal, propagate a signal through a fibre or through a linear dispersive element, to read a field from a data file, to find output of parameters like the power and frequency of signal, and so on. Thus, it is very easy and straightforward to build up a transmission system that is commensurate with experiment.

Nevertheless, care has to be taken for the selection of the time and frequency resolutions for the numerical integration because this library is implemented in terms of two vectors, one for the field as a function of time, U, and one for its Fourier transform, fU. The desired frequency resolution needs to be set as half of the value of the inverse of time window of field U, which is

$$\Delta f = \frac{1}{2}\frac{1}{t_{max}}, \tag{6.7}$$

where Δf is the frequency resolution and t_{max} is the time window of field U. This is to make sure that the time resolution is small enough to give a continuous profile of the field U since

$$dt = \frac{t_{max}}{npts}, \tag{6.8}$$

where dt is the time resolution and $npts = N/2$ with N is the number of sections to be solved. A continuous profile is important for the Fourier transformation in the library.

One may find from equation (6.8) that dt can be reduced by increasing the number of the sections N. Investigations has been done to evaluate this and the results have shown that $N = 4096$ gives artifacts (noise) in the spectrum due to the discontinuities in the time window, $N = 8192$ and $N = 16384$ give nearly identical results but the latter uses more time to complete a simulation. On the other hand, increasing the Δf will indeed provide a smaller dt. However, there is a loss of information in the frequency domain. Thus, the N and Δf for the simulated results carried out in this work have been chosen optimally, based on the considerations on the trade-off between the simulation time and artifacts, to be 8192 and 0.01 GHz, respectively.

Taking U_{out} as the output optical field obtained from the GNLS simulation in time domain, the simulated output optical amplitude field $A_{optical}$ and output optical power spectrum $P_{optical}$ in frequency domain can be calculated as

$$A_{optical} = \sum_{j=1}^{N} U_{out}(j)\omega_N^{(j-1)(k-1)} \tag{6.9}$$

and

$$P_{optical} = |A_{optical}|^2, \tag{6.10}$$

respectively, N is the length of vector U_{out} and ω_N is given as

$$\omega_N = e^{(-2\pi i)/N}. \tag{6.11}$$

The above process can be realised by the implementation of FFT algorithm from Matlab in which can be written as

$$P_{optical} = \mathsf{abs}(\mathsf{fftshift}(\mathsf{fft}(U_{out}(j)))).2. \tag{6.12}$$

The fftshift in Matlab rearranges the outputs of fft by moving the zero-frequency component to the centre of the array. It is useful for visualising a Fourier transform with the zero-frequency component in the middle of the spectrum.

Meanwhile, the simulated electrical amplitude field $A_{electrical}$ and electrical power spectrum $P_{electrical}$ in frequency domain can be calculated as

$$A_{electrical} = \sum_{j=1}^{N} |U_{out}(j)|^2 \omega_N^{(j-1)(k-1)} \tag{6.13}$$

and

$$P_{electrical} = |A_{electrical}|^2. \tag{6.14}$$

Again, this can be realised with the FFT algorithm from Matlab as in

$$P_{electrical} = \text{abs}(\text{fftshift}(\text{fft}(\text{abs}(U_{out}(j)).2))).2. \tag{6.15}$$

To summarise, the simulated detected optical power and electrical power spectra can be expressed by equation (6.12) and equation (6.15). They were used throughout the simulation studies of this chapter. In the subsequent simulation of the links, the input optical amplitude field is quoted as U_{in}. It varies according to the applied modulation scheme and the total number of the fundamental signal components. Thus, it will be defined in the beginning of each section.

6.4 Investigations on DSB Modulated Links

In the series of simulations on single-tone DSB modulated link, the input optical field U_{in} was defined as

$$U_{in} = U_{av}(1 + m\sin(2\pi f_1 t)), \tag{6.16}$$

where U_{av} was the average amplitude of incident optical field given by

$$U_{av} = \sqrt{\frac{P_{incident}}{1 + \frac{m^2}{2}}}, \tag{6.17}$$

where $P_{incident}$ was the desired optical power incident onto the fibre input, m was the modulation index and f_1 was the microwave/RF subcarrier frequency used to modulate the optical carrier. This frequency was regarded as the modulation frequency, and modulation suppression was then referred to as subcarrier suppression in the context of this work. The number of the points measured by the Light Component Analyser (LCA) in all the experiments in this section was set as 401.

6.4.1 Joint Effect of Fibre Dispersion and Fibre-Induced Self-Phase Modulation

In order to investigate the joint effect of the fibre dispersion and fibre nonlinearity in microwave/RF signal transmission link, a single-tone signal transmission at high optical incident power was carried out. Experimental results were compared with simulated results.

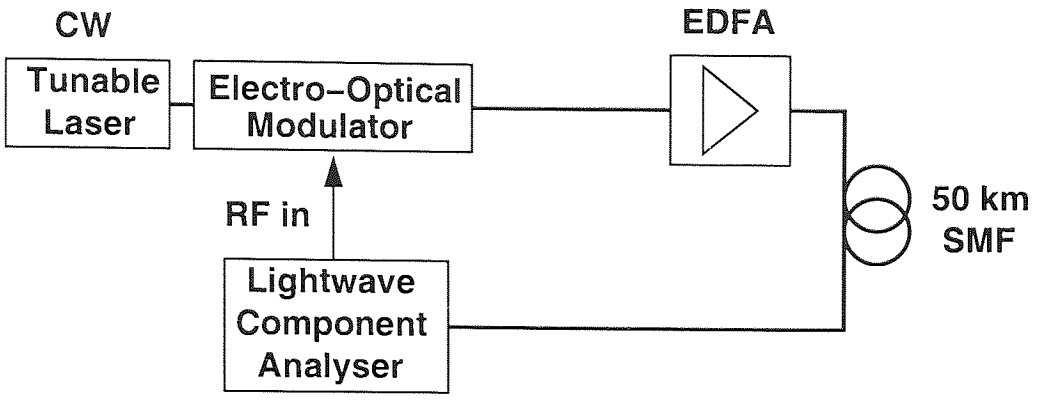

Figure 6.3: Experimental setup of single-tone 50-km DSB modulated link.

Experimental Setup

The experimental setup is shown in figure 6.3. A tunable continuous-wave (CW) source operating at 1550.9 nm was externally modulated by a microwave/RF frequency ranged from 0.13 GHz to 20 GHz using an electro-optic modulator (EOM). The modulated optical signal was then amplified in an EDFA with adjustable gain before its transmission on a 50 km length of fibre. A Lightwave Component Analyser (LCA) was used to measure the frequency transfer function of the transmitted signal in the link. In order to avoid the frequency roll-off of the EOM transfer function and the responses of the microwave/RF generator and the photodetector on measurements, a calibration of the setup was carried to obtain the transfer function of the system without the optical fibre.

The most limiting factor on these measurements was the stimulated Brillouin scattering (SBS) due to both the high optical power levels and narrow optical linewidth involved in the experiment. To overcome this effect and allow maximum influence of SPM, the laser was operated in the low coherence mode with linewidth of about 200 MHz giving rise to a SBS threshold power P_B of about 13.0 dBm that was sufficient to demonstrate the SPM effect.

Numerical Simulation

The transmission through the fibre link was simulated by using an in-house implementation of the split-step Fourier method [39] applied to the generalised nonlinear Schrödinger equation [38] as in equation (6.2) including fibre loss, fibre dispersion and the nonlinear effect. Noise, either from amplification in the link or in the receiver was not accounted for in the model. Other nonlinear terms, dispersion slope and polarisation effects were ignored in these simulations simply to investigate the effect of the fibre nonlinearity onto the dispersive fibre. To clearly see the nonlinear effect on the system, frequency transfer functions of fibre

Parameters			
Effective area	A_{eff}	80	μm^2
Nonlinear refractive index	n_2	2.6×10^{-20}	m^2/W
Group delay dispersion	D	18	ps/nm/km
Fibre loss	α	0.2	dB/km

Table 6.2: Simulation parameters for 50 km of standard single-mode fibre for DSB modulated link.

link with optical incident power above P_B were also simulated considering that the Brillouin scattering effect could be suppressed by employing the well-known techniques from [126].

In the simulation, the transmitted signal comprised a monochromatic CW at 1550.9 nm amplitude modulated using single pure sinusoidal waveform with microwave/RF frequency f_1 ranged from 0.13 GHz to 20 GHz with a frequency step of 0.5 GHz. A perfect noiseless square-law detector was assumed at the receiver end. The fibre parameters used were commensurate with transmission at 1550 nm in standard single-mode fibre, as in Table 6.2. The modulation index was set at $m = 0.178$ in accordance to the experiment. Simulations were carried out with different amounts of optical incident power ranged from -3.0 dBm to 20.0 dBm onto 50 km of fibre link.

Results and Discussion

The experimental results obtained at optical incident power of 0.0 dBm, 10.0 dBm and 12.8 dBm were normalised and are shown in figure 6.4. At 0.0 dBm, the degradation was only due to the chromatic dispersion while for 10.0 dBm and 12.8 dBm, fibre-induced SPM was generated. The first notch with $P_{incident}$ = 0.0 dBm appeared at 8.5 GHz and this limited the usable frequency-length product of the transmission link.

However, as optical incident power increased, in which the system was no longer linear, the occurrence of first notch was shifted to a higher microwave/RF frequency. As can be seen, they were at 9.4 GHz and 10.5 GHz for $P_{incident}$=10.0 dBm and 12.8 dBm, respectively. These shifts were caused by the interactions between new frequencies generated by the fibre-induced SPM effect. This phenomenon was simulated with 0.13 GHz and is shown in figure 6.5. As can be seen, the optical spectrum at 0 km only consisted of the optical carrier and the two sidebands. After travelling 50 km of fibre, optical spectrum appeared to have more sidebands due to the SPM induced four-wave mixing. The explanation of this phenomenon can be found in section 2.6.3. These new frequencies cancelled and interfered with each other at the receiver, as happened in the modulation suppression effect, and affected the detected electrical power.

From figure 6.4, there was a good agreement between the experimental and simulated

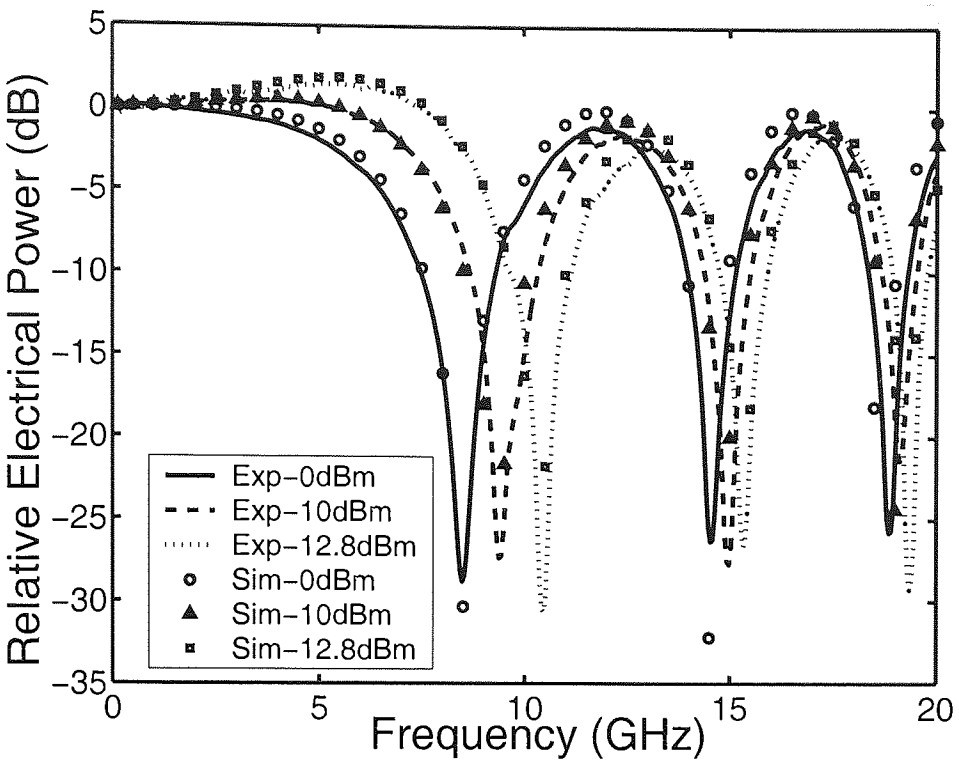

Figure 6.4: Experimental (Exp) and simulated (Sim) detected electrical power with different $P_{incident}$.

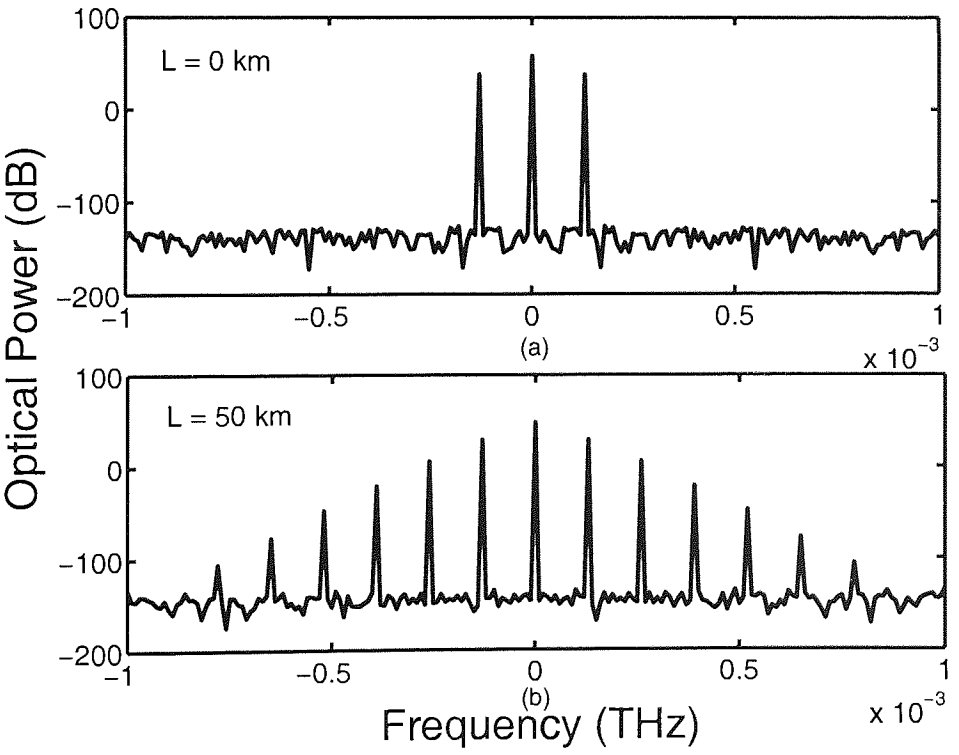

Figure 6.5: Simulated detected optical power with 0.13 GHz at $P_{incident}$ = 10.0 dBm in DSB modulated link.

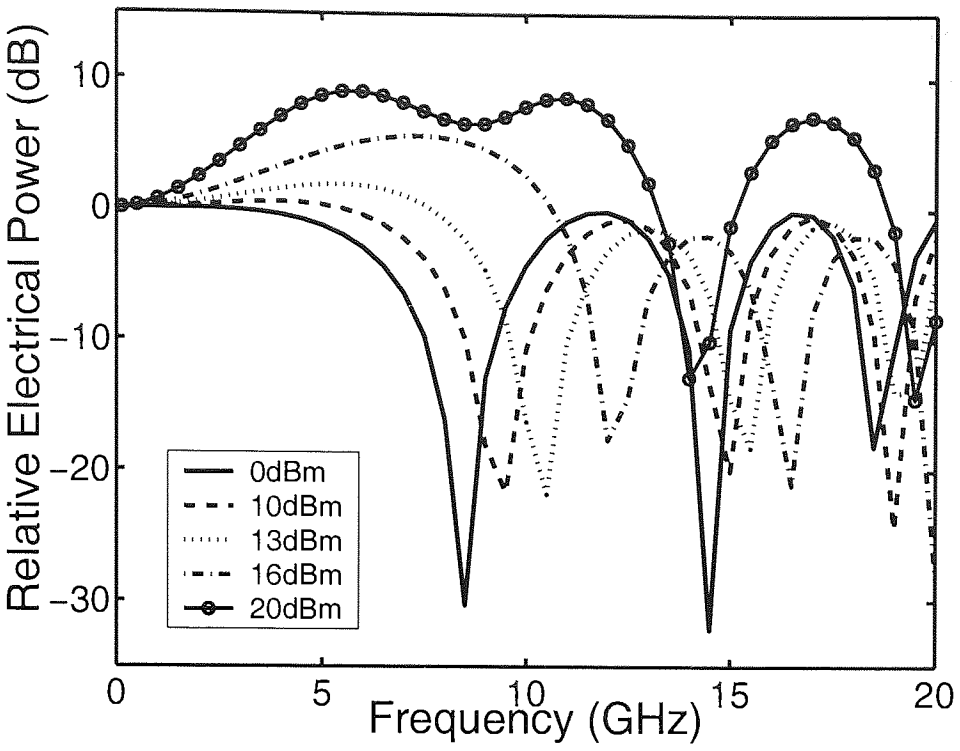

Figure 6.6: Simulated detected electrical power with different $P_{incident}$ in 50 km DSB modulated link.

results. The discrepancy in the notch power between the experimental and simulated results could be caused by the different amplitude of the two sidebands in the experimental DSB modulated signal propagated in the fibre link as discussed in section 2.5.1 [34]. Note that, relatively, there was even a link gain at the lower microwave/RF range when power was increased. This gain was obtained from the phase modulation (PM) conversion into intensity modulation (IM) [124, 125] as power increased. This showed that fibre nonlinearity induced self-phase modulation improved the usable frequency-length of the link. Or in another way, the fibre dispersion in the link was partly compensated by the fibre-induced nonlinear SPM effect at high power level.

To further investigate the combined effect of fibre dispersion and nonlinearity in nonlinear regime, simulations with higher $P_{incident}$ were carried out. The normalised results are shown in figure 6.6. It can be observed that the dispersion-induced microwave/RF signal power penalty could be sharply reduced by increasing the optical incident power. This resulted in augmenting the frequency-length product in the microwave/RF signal transmission link. It is worth noting that there was a wide bandwidth of nearly-flat response at optical incident power of 20.0 dBm which was potentially useful for transmission.

In this work, theoretical and experimental demonstrations have proven that fibre-induced SPM can be used in an efficient way to compensate for chromatic dispersion effects that

appear in amplitude modulated microwave/millimetre-wave radio-over-fibre systems. The nonlinear SPM effect combines with chromatic dispersion in such a manner that leads to an improvement of the frequency-length product. If the main limitation to go beyond 13 dBm of optical incident power, in which it is imposed by the SBS, can be overcome in practical, there exists wider bandwidth with nearly constant response for transmission.

6.4.2 Investigations on RoF Link at Fixed Modulation Frequency in Length Domain

As can be noticed, the previous experiment concentrates in investigating the joint effect in frequency domain. To clearly see the joint effect response in the fibre length domain, simulation studies with different fibre lengths and fixed modulation frequency were carried out. Investigations were directed to both lossy (α = 0.2 dB/km) and lossless fibre link. The latter case was assessed so as to look into the potential of nonlinear dispersive link if lossless fibre was used.

Numerical Simulation

The transmitted signal comprised a monochromatic CW 1550 nm optical wave amplitude modulated using a single pure sinusoidal waveform with a modulation index of $m = 0.178$ at a fixed modulation frequency f_1 of 10 GHz. The input optical field U_{in} was represented as in equation (6.16). In the first instance, the fibre parameters as in the previous experiment were used. Simulations were carried out with different amounts of optical incident power ranged from 0.0 dBm to 20.0 dBm onto different fibre lengths ranged from 0 km to 100 km with a step size of 0.2 km. Secondly, simulation with a modulation frequency of 20 GHz was conducted. Finally, to investigate the pure effect of fibre-induced SPM onto dispersive fibre link, a lossless fibre link was assessed.

Results and Discussion

Figure 6.7 and figure 6.8 show the simulated results for the detected electrical power at 10 GHz and 20 GHz with different amounts optical incident power in lossy fibre link. Both figures depicted that significant reduction of chromatic dispersion could be achieved by increasing the $P_{incident}$, which resulted in augmenting the frequency-length product of the fibre-optic link. The reduction on the detected power was certainly due to the fibre loss.

For the case with lossless fibre link, the dependence of the detected microwave/RF signal power on the optical incident power and the fibre length can be found in figure 6.9. At

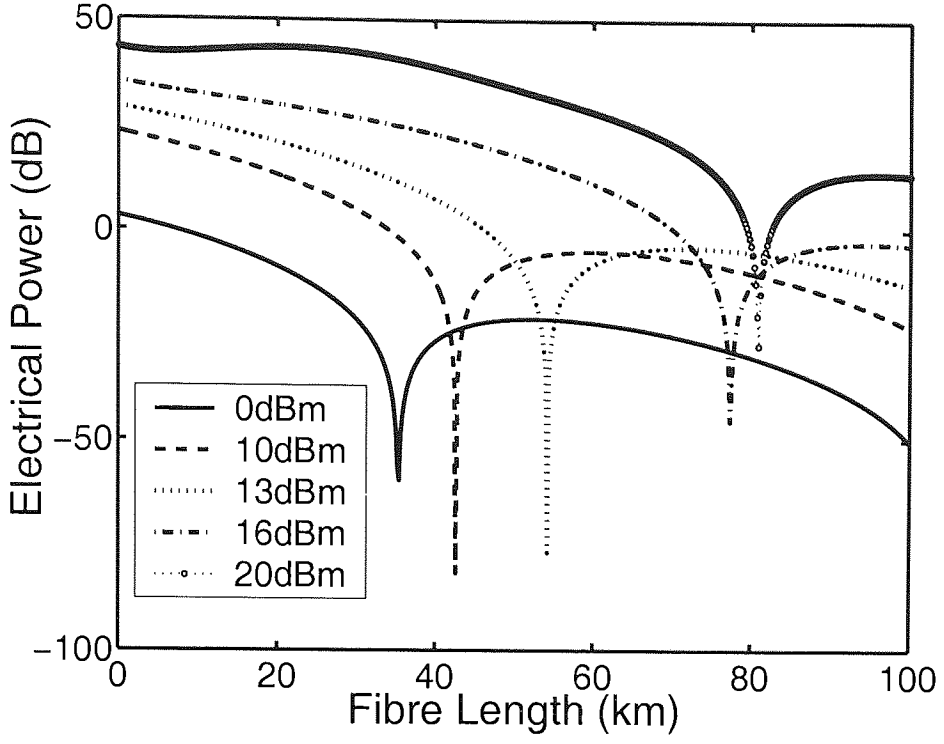

Figure 6.7: Simulated detected electrical power of DSB modulated link at 10 GHz versus propagation distance for 0.0 – 20.0 dBm of optical incident power.

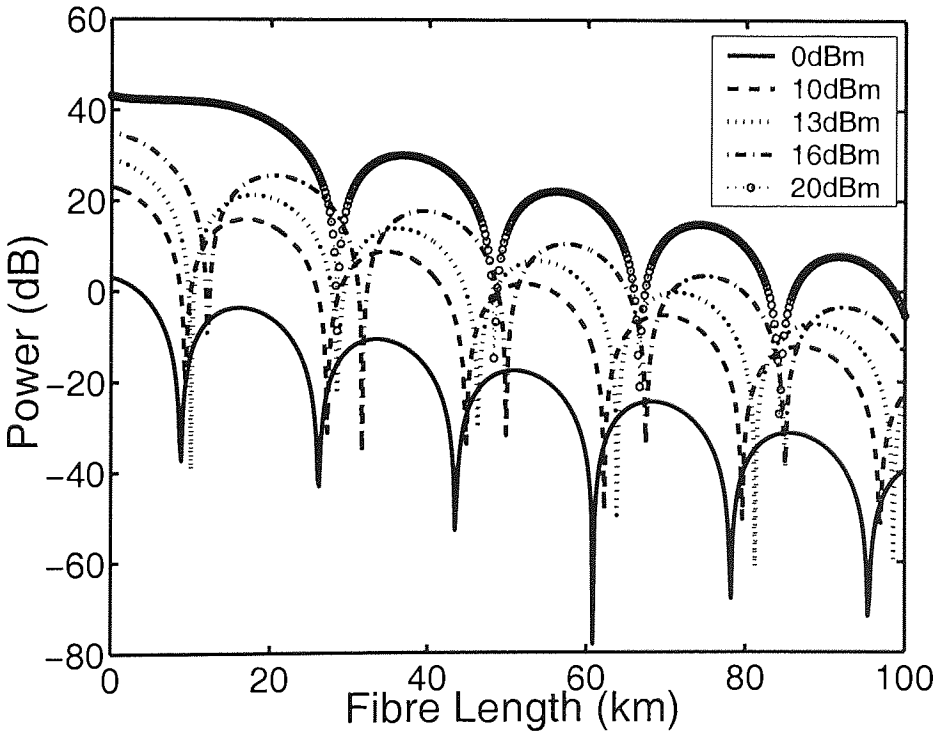

Figure 6.8: Simulated detected electrical power of DSB modulated link at 20 GHz versus propagation distance for 0.0 – 20.0 dBm of optical incident power.

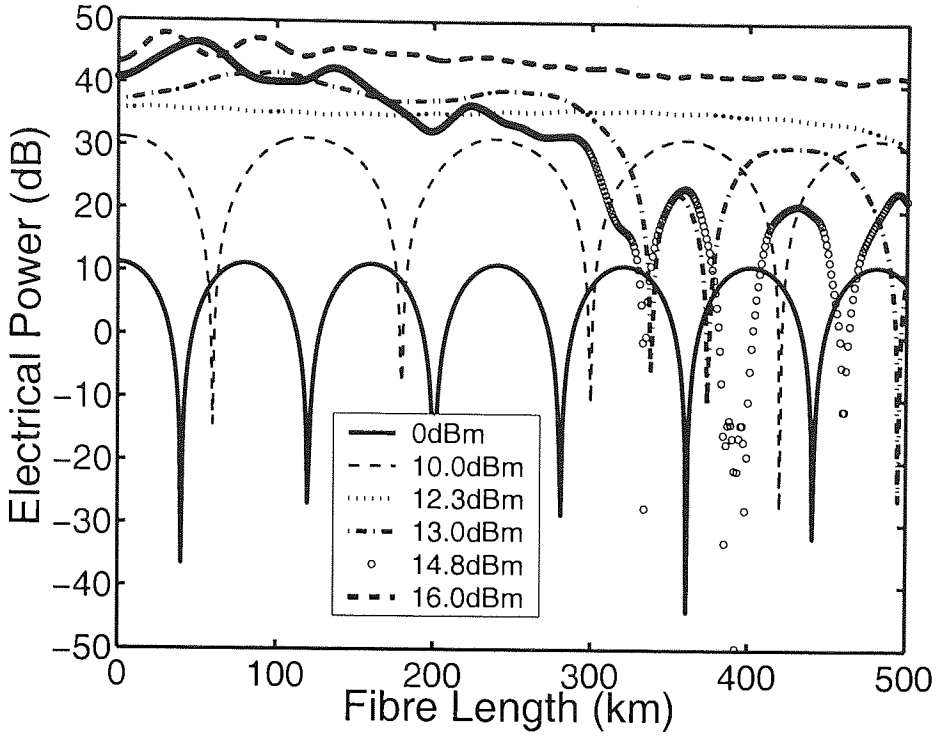

Figure 6.9: Simulated detected electrical power of DSB modulated microwave/RF signal at 10 GHz versus propagation distance for 0.0 – 16.0 dBm of optical incident power in lossless RoF link.

low optical incident power levels, the behaviour remained linear with dispersion induced fading effects until about 10.0 dBm where nonlinear effects started to become apparent. At a critical power level of ≈12.3 dBm, in agreement with the results of [122], the nonlinear effects counterbalanced the dispersion that the detected microwave/RF signal power showed only a small fluctuation (<1.0 dB) with propagation, and only appeared to deteriorate when it reached about 400 km. At higher power levels, complex nonlinear behaviour was exhibited and the response was more unpredictable.

This study has shown the improvement of frequency-length product in the fibre length domain as optical incident power increases. Theoretically, it is of high interest on the capabilities of the response at the critical power level of ≈12.3 dBm if a lossless RoF link is used.

6.4.3 Joint Effect of Fibre Dispersion and Fibre-induced SPM with the Presence of Incomplete Dispersion Compensation

Radio-over-fibre (RoF) systems serve as a promising candidate for broadband service provision. The fibre lengths do however face limitations in the usable frequency-length product

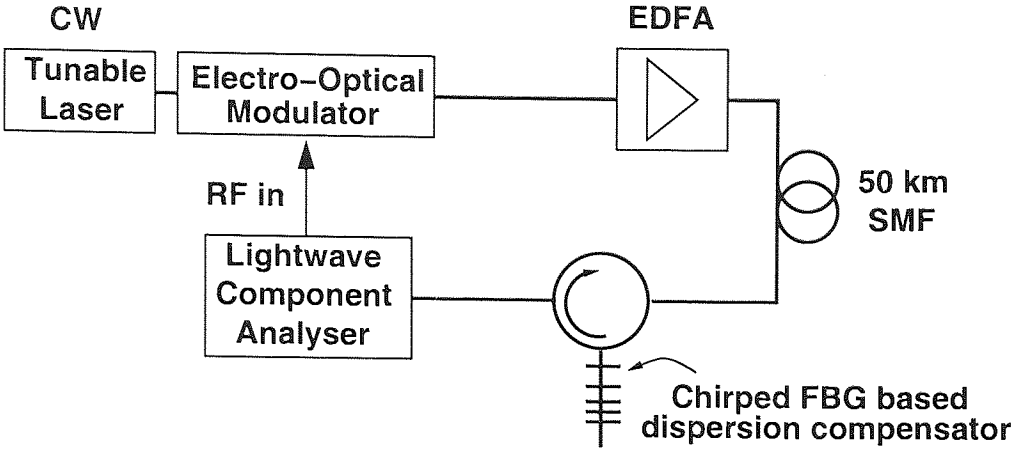

Figure 6.10: Experimental setup of single-tone 50-km DSB modulated link with fibre Bragg grating based dispersion compensation.

due to dispersion induced fading at microwave and millimetre wave frequencies [33]. The most straightforward way to overcome this limitation is to use either dispersion compensating fibre (DCF) [113] or chirped fibre Bragg gratings (CFBG) to compensate the dispersion in fibre [109]. Generally, a linear chirped fibre grating is preferred due to its linearity, compactness, low insertion loss and easy fabrication [110]. This problem has been examined extensively in the linear propagation regime [127–129]. Interesting simulation work investigating the impact of CFBG characteristics on dispersion compensation has also been reported in the nonlinear propagation regime [130].

In this work, the influence of a incomplete dispersion compensation from a CFBG onto a nonlinear dispersive RoF link was experimentally investigated in order to have a preliminary idea on the joint effect of fibre dispersion and fibre-induced SPM with the presence of dispersion compensation. Experimental results were compared with the simulated results from GNLS equation. In this context, incomplete dispersion compensation can be defined as: when -900 ps/nm of dispersion compensation is needed for 50 km fibre link, a supply of -500 ps/nm is considered as incomplete dispersion compensation.

Experimental Setup

The experimental setup is shown in figure 6.10 with a CW at 1557.0 nm emitted from a tunable laser. It was then externally modulated by an electro-optical modulator with frequencies ranged from 0.13 GHz to 20 GHz. To get the desired optical incident power, the modulated signal was amplified by an erbium-doped fibre amplifier (EDFA) with controllable gain before it was impinged into the input of 50 km of single-mode fibre (SMF). The transmitted signal was then dispersion-compensated by an apodised chirped fibre Bragg grat-

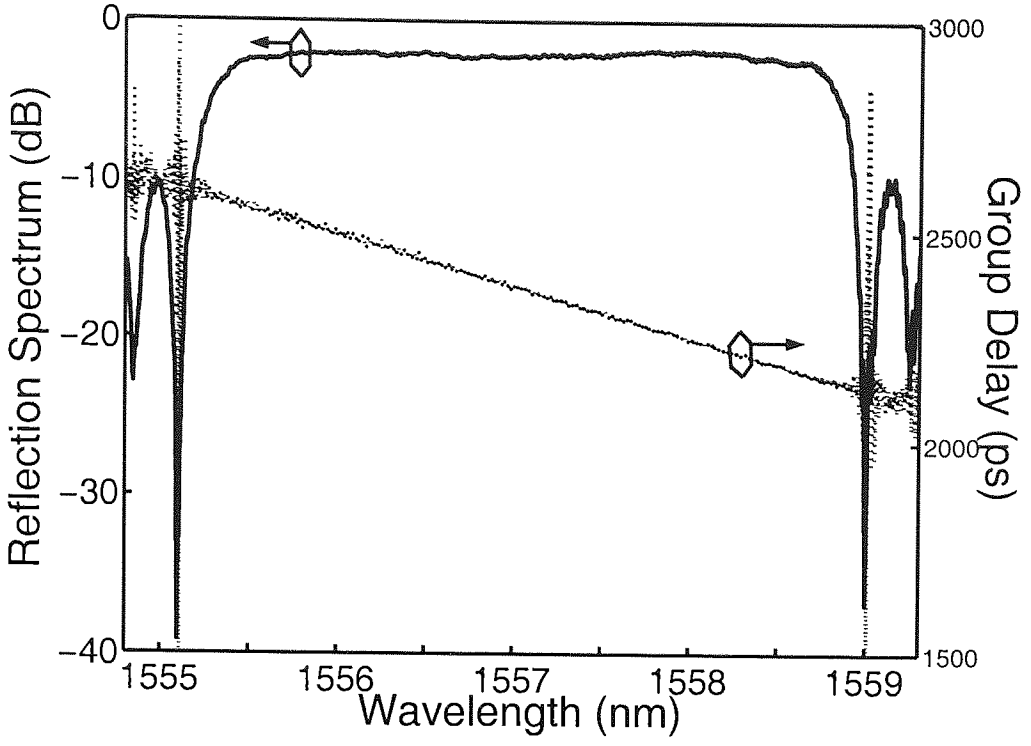

Figure 6.11: Reflection spectrum (–) and group delay (···) of the apodised chirped fibre Bragg grating which provides -120 ps/nm of dispersion compensation.

ing (ACFBG) through a circulator. A Lightwave Component Analyser was used to measure the frequency response of the reflected signal from the ACFBG.

The grating in use had a dispersion of about -120 ps/nm, which was much lower than the ideal dispersion compensation of -900 ps/nm for the dispersion suffered in a 50 km of RoF link. This ACFBG was fabricated based on the phase-mask dithering technique with a sixth-order hyper-gaussian apodisation profile. Its reflection spectrum and group delay profile are shown in figure 6.11.

Numerical Simulation

To simulate the propagation of a modulated signal in the RoF link, an in-house implementation of Fourier split-step method applied to the GNLS equation was employed. Parameters of standard single-mode fibre were set to be: effective area $A_{\text{eff}} = 80$ m^2, nonlinear coefficient $n_2 = 2.6\times10^{-20}$ m^2/W, loss $\alpha = 0.2$ dB/km, dispersion $D = 18$ ps/nm/km. Apart from the fibre dispersion, nonlinearity and loss, dispersion compensation of -120 ps/nm/km was also included in the simulation. The dispersion compensator was modelled as a perfect dispersive device that gave linear compensation of -120 ps/nm throughout the range of radio frequencies.

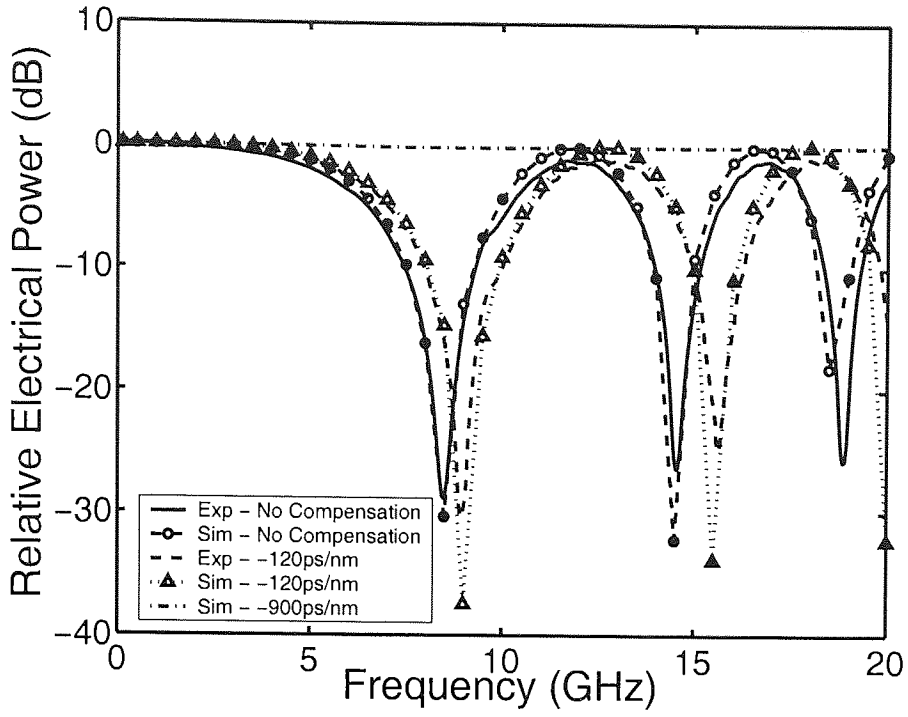

Figure 6.12: Experimental (Exp) and simulated (Sim) detected electrical power with optical incident power of 0.0 dBm in 50 km DSB modulated link with and without -120 ps/nm of dispersion compensation.

Results and Discussion

All the results above were normalised and compared. From figure 6.12, figure 6.13 and figure 6.14, it can be clearly seen that power degradation could be improved by the use of a CFBG based dispersion compensator with a incomplete dispersion compensation. Experimental results matched well with the simulated results. For comparison, plotted alongside with every figure are the simulated responses without dispersion compensation and with ideal dispersion compensation of -900 ps/nm. In the linear regime, in which when low optical incident power was used, expectedly, there was a total elimination of power degradation in the detected power when ideal dispersion compensation was used. However, when the power level increased, power penalty started to appear and reduced the frequency-length product of the link. In contrary, while frequency-length product was being improved with the presence of high optical incident power, the use of incomplete dispersion compensation enhanced the effect by extending the frequency-length product of the link to a higher value.

Due to the limitation of SBS in the experiment, the responses with higher optical incident power were simulated and normalised, as shown in figure 6.15. It shows that, apart from improving the frequency-length product of the link, employment of incomplete dispersion compensation from CFBG gave a nearly-flat response in the frequency range of up

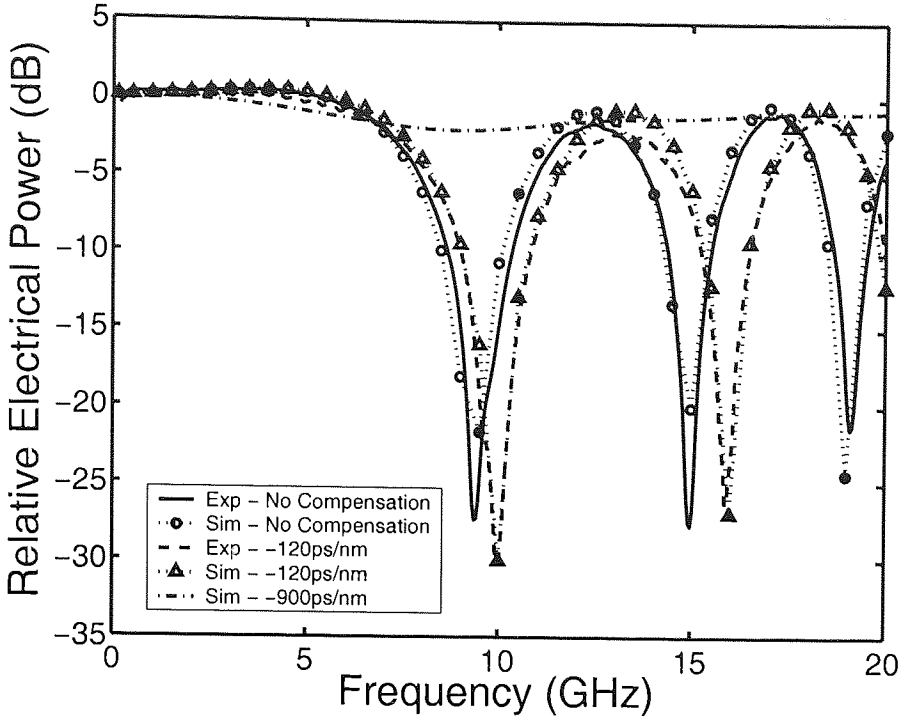

Figure 6.13: Experimental (Exp) and simulated (Sim) detected electrical power with optical incident power of 10.0 dBm in 50 km DSB modulated link with and without -120 ps/nm of dispersion compensation.

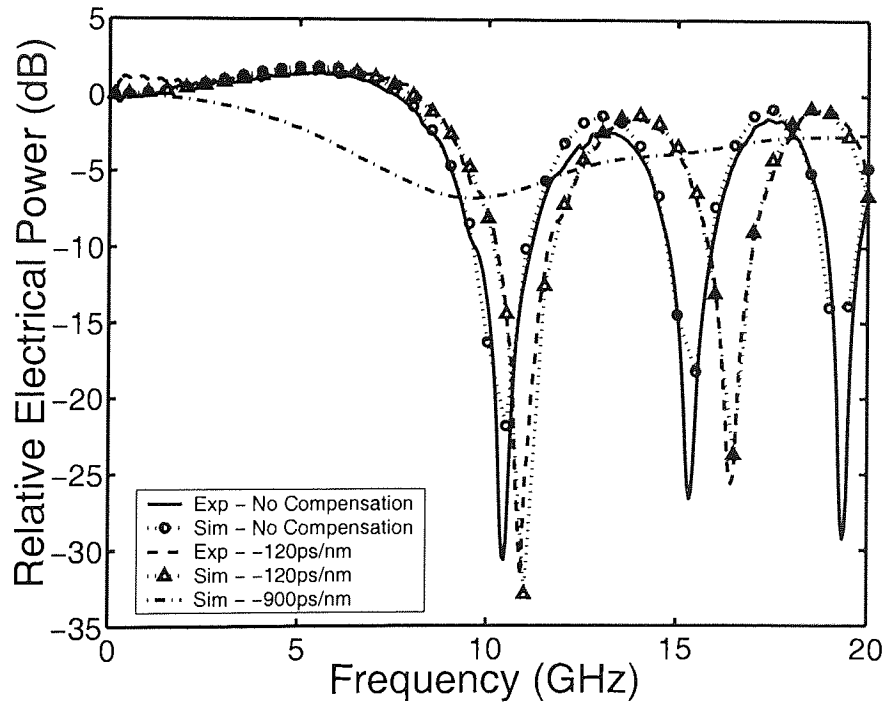

Figure 6.14: Experimental (Exp) and simulated (Sim) detected electrical power with optical incident power of 12.8 dBm in 50 km DSB modulated link with and without -120 ps/nm of dispersion compensation.

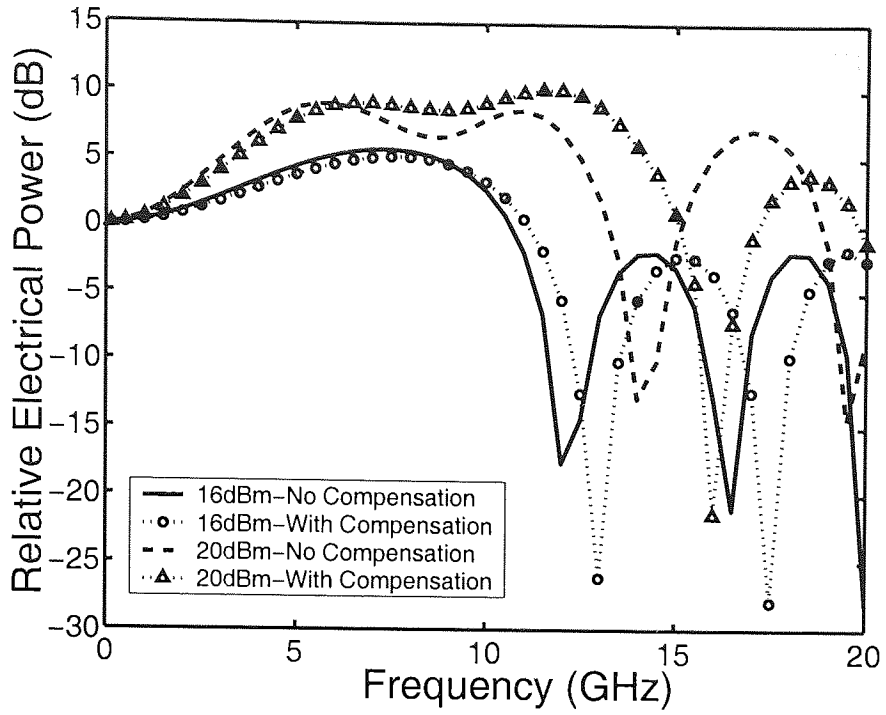

Figure 6.15: Simulated detected electrical power with optical incident power of 16.0 dBm and 20.0 dBm in 50 km DSB modulated link with and without -120 ps/nm of dispersion compensation.

to ≈13 GHz when 20 dBm was incident to the fibre. Thus, it can be concluded that the potential of employing the CFBG based dispersion compensator with incomplete dispersion compensation in high power transmission links has been proven whilst the use of the ideal dispersion compensation in high power transmission needs to be reconsidered.

6.4.4 Influence of Fibre-induced SPM in Dispersive RoF Link with the Presence of Ideal Dispersion Compensation

In order to further look into the impact from the ideal dispersion compensation, in this work, the influence of the fibre-induced SPM effect on a dispersion compensated RoF link using CFBG based ideal dispersion compensation was experimentally demonstrated. Experimental results were compared with the simulated results from the GNLS equation. In this context, ideal dispersion compensation means the complete dispersion compensation. For instance, the ideal dispersion compensation for a 72 km link with fibre dispersion of 18 ps/nm/km is 1296 ps/nm.

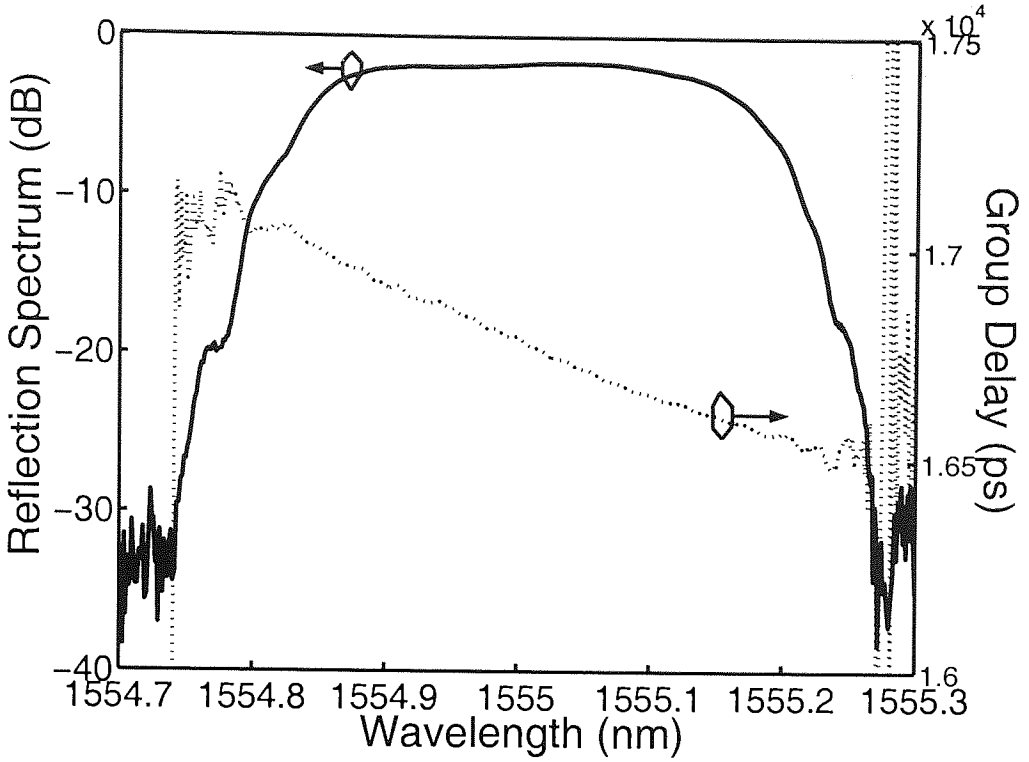

Figure 6.16: Reflection spectrum (–) and group delay (···) of the apodised chirped fibre Bragg grating which provides ≈ -1300 ps/nm of dispersion compensation.

Experimental Setup and Numerical Simulation

The experimental setup for this work was similar to the previous one as in figure 6.10, but CW laser source tuned at 1555.1 nm and 72 km of fibre were used instead. In this case, a different ACFBG with a dispersion of ≈-1300 ps/nm was used. This ACFBG was fabricated based on the phase-mask dithering technique with a sixth-order hyper-gaussian apodisation profile. Its reflection spectrum and group delay profile are shown in figure 6.16. To overcome the effect of Stimulated Brillouin Scattering (SBS) due to the high optical power levels, the tunable laser was operated in coherence controlled mode. In the simulation, the dispersion compensator was modelled as a perfect dispersive device that gave linear compensation of -1300 ps/nm throughout the range of modulation frequencies.

Results and Discussion

In the first incidence, an optical incident power of -3.0 dBm was used to measure the linear frequency transfer function of the RoF link without the dispersion compensation. The normalised results are shown in figure 6.17 with a good match between measured and expected results for the dispersion induced nulls in the frequency response. This suppression was then

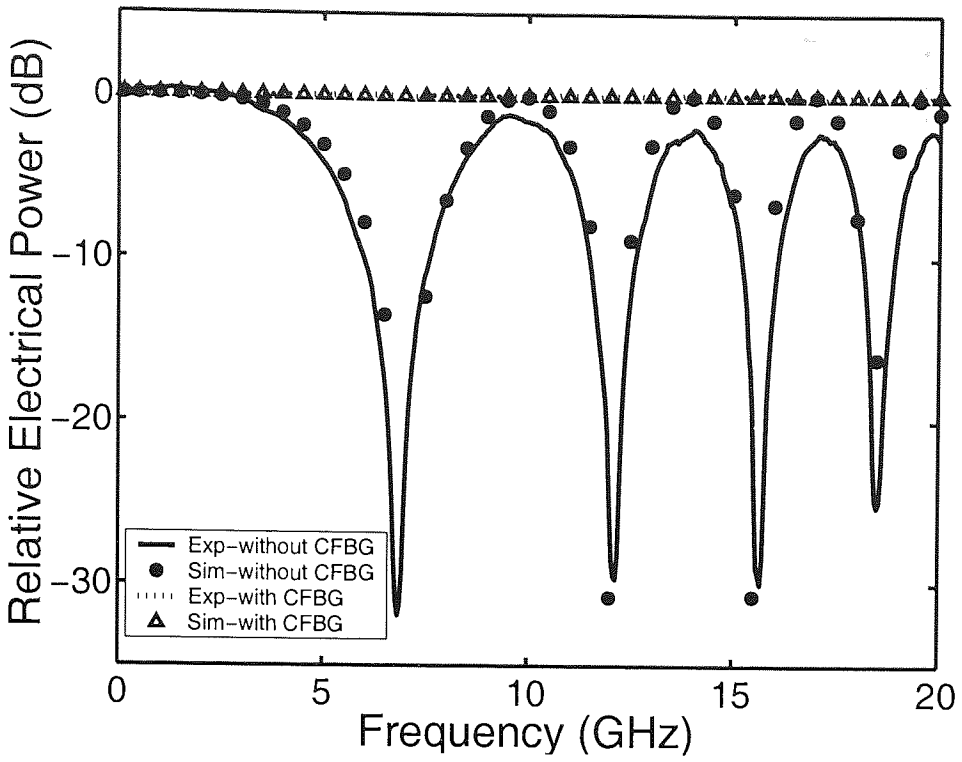

Figure 6.17: Experimental (Exp) and simulated (Sim) detected electrical power at receiver with and without CFBG dispersion compensation at -3.0 dBm.

eliminated by adding a CFBG based dispersion compensator in the link, as can be seen in figure 6.17, where a flat link response was achieved at input power level of -3.0 dBm.

However, when higher optical incident power was applied, the optical fibre link worked in nonlinear regime and the dispersion compensation was no longer ideal. Figure 6.18 shows the normalised measured and simulated responses for the link with dispersion compensation for different amounts of optical incident power. It can be clearly seen that as the optical power increased, a dip of up to 4.7 dB at 12.5 dBm of optical incident power appeared reducing the frequency-length product of the link. Note that the small ripples in the measured response at high frequencies were due to the non-ideal dispersion characteristics of the CFBG close to the reflection band edge [130]. However, in contrast to the results in [130], the ripples in our experimental results had smaller amplitudes and a periodic pattern throughout the experiments and were similar for both linear and nonlinear propagation.

Simulations without SBS effect at higher power levels are summarised in figure 6.19. It can be observed that power penalty varied with modulation frequency and that at 20.0 dBm the first notch appeared at a modulation frequency of 3 GHz, which was half the frequency of that in the linear system without dispersion compensation. More serious impact is anticipated if the baseband signal is frequency-modulated onto the intensity-modulated RoF link

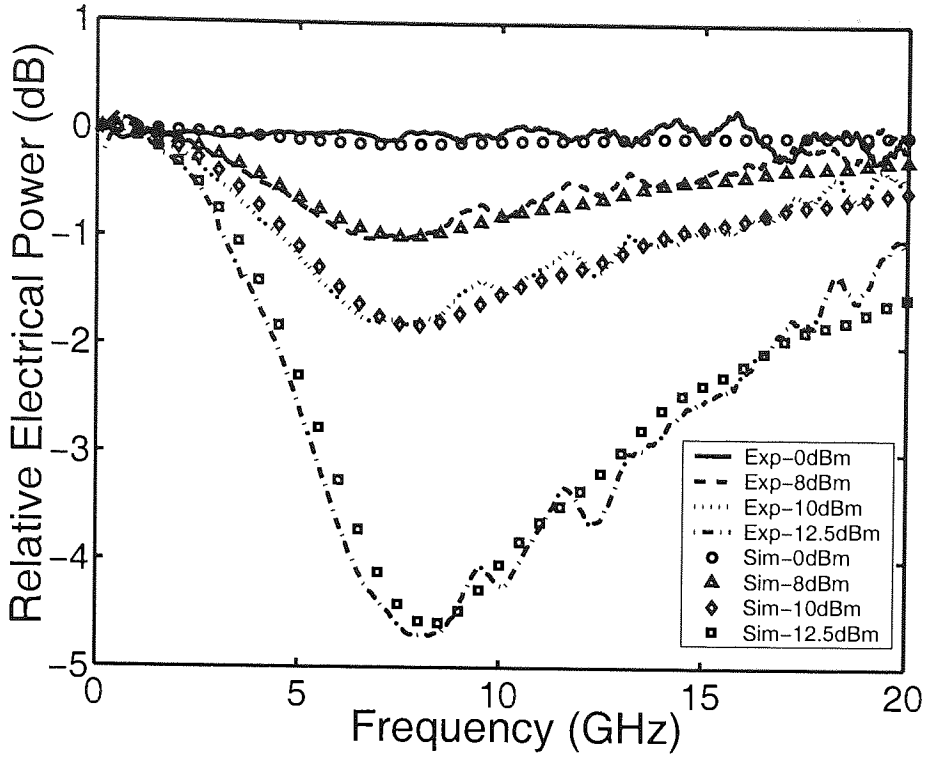

Figure 6.18: Experimental (Exp) and simulated (Sim) detected electrical power with different $P_{incident}$ in 72 km DSB modulated link with ≈-1300 ps/nm of dispersion compensation.

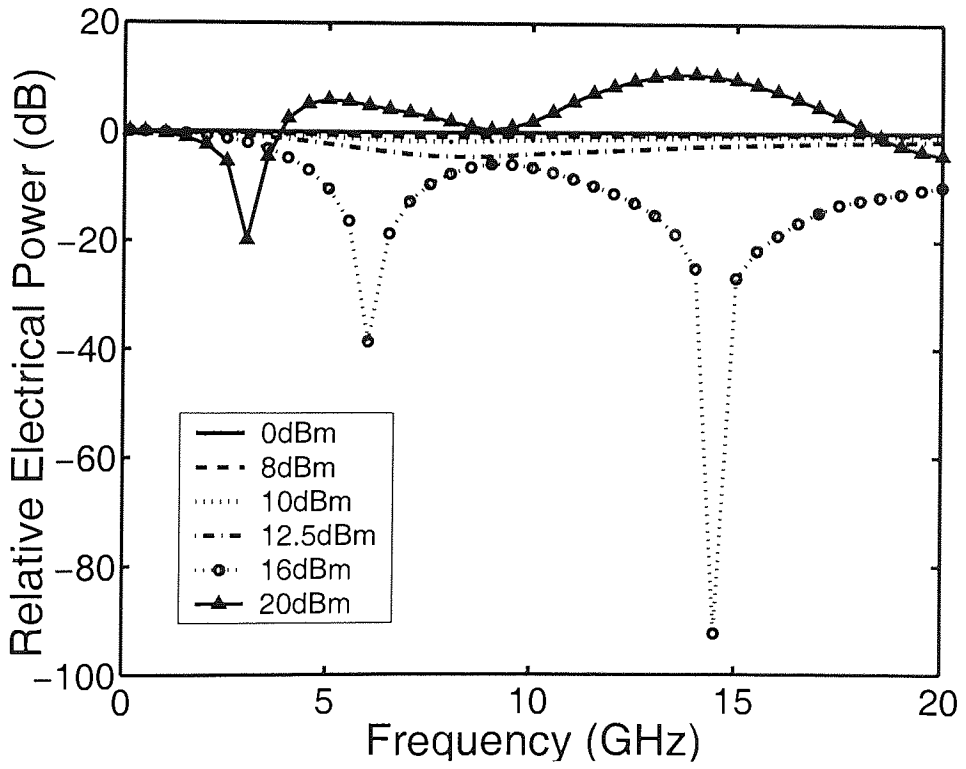

Figure 6.19: Simulated detected electrical power with different $P_{incident}$ in 72 km DSB modulated link with -1300 ps/nm of dispersion compensation.

since the nonlinear distortion in this modulation scheme is more dominant or considerable compared to other sources of noise in the system [20].

In this work, the impact of fibre nonlinearity induced SPM in a CFBG compensated RoF link was experimentally demonstrated. Both experimental and simulated results have shown that the power penalty in frequency transfer function appears and increases with the optical incident power when ideal dispersion compensation is employed. The experimental and simulated results have also led to a conclusion that ideal dispersion compensation eliminates the dispersion induced power penalty in the linear transmission regime and deteriorates the frequency-length product in the nonlinear transmission regime.

6.5 Investigations on SSB Modulated Links

As mentioned, the frequency-length product of RoF links is rigorously restricted by the fibre chromatic dispersion. Many approaches have been employed to overcome this problem. The optical SSB modulation is a very promising technique, compared to the techniques using optical dispersion compensating fibres (DCF) [113], electroabsorption modulator based transmitters [114], optical phase conjugation (OPC) [115] and semiconductor optical amplifier (SOA) booster [116, 117]. It overcomes the chromatic dispersion induced modulation suppression and further increases the bandwidth efficiency. To compensate system loss and enhance system performance, erbium-doped fibre amplifiers (EDFA) is usually employed, consequently resulting in high input power level to the fibre link. This usually is the case where fibre nonlinear effect begins to take part. Theoretical studies about SSB modulation approach have been done [124, 131]. Nevertheless, no experimental investigation has been reported for the exploration in the high optical input power levels when the system is nonlinear.

In this work, the fibre nonlinear effect onto the signal transmission in dispersive RoF link was experimentally investigated. In the series of simulations for single-tone SSB modulated link, the input optical field U_{in} and the average amplitude of input optical field U_{av} were defined as

$$U_{in} = U_{av}(1 + m(\sin(2\pi f_1 t) - i\cos(2\pi f_1 t))) \tag{6.18}$$

and

$$U_{av} = \sqrt{\frac{P_{incident}}{1+m^2}}, \tag{6.19}$$

respectively, where $P_{incident}$, m and f_1 were defined previously as in equation (6.16) and

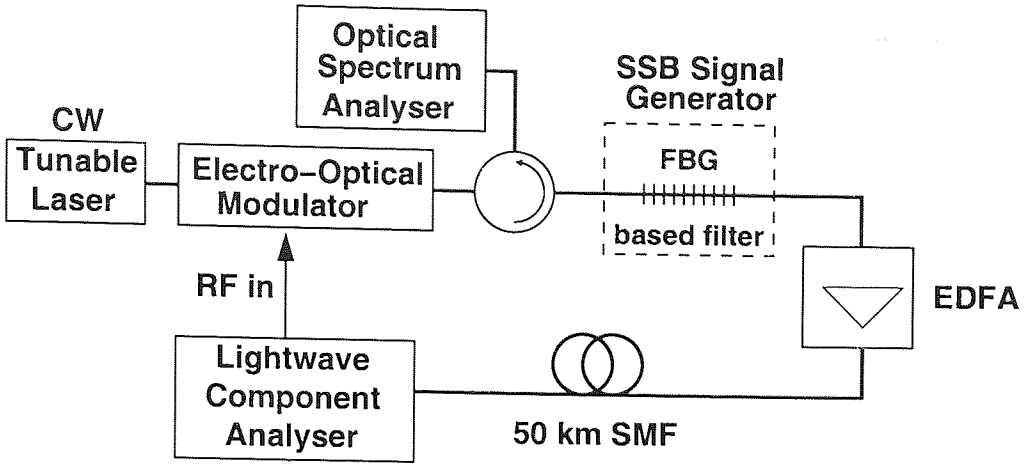

Figure 6.20: Experimental setup for single-tone 50-km SSB modulated link.

equation (6.17). The number of the points measured by the Light Component Analyser (LCA) in all the experiments in this section was also set as 401.

6.5.1 Elimination of Chromatic Dispersion Induced Modulation Suppression in Low Power Transmission

This section seeks to experimentally verify the elimination of chromatic dispersion induced modulation suppression by the SSB modulation approach in linear transmission regime.

Experimental Setup

The experimental setup is shown in figure 6.20, in which the optical CW carrier was supplied by a tunable laser tuned at 1550.9 nm and was externally modulated by an electro-optical modulator. Since the external modulator generated double-sideband signal, an apodised fibre Bragg grating based filter was employed to filter one of the sidebands of the modulated signal in order to realise the SSB modulated signal. The apodised grating in use was fabricated by phase mask scanning technique. Its measured and simulated transmission and reflection spectra are shown in figure 6.21.

An optical spectrum analyser was used to monitor the reflected spectrum from grating as well as the stimulated Brillouin scattering (SBS) in the fibre link. The transmitted signal was amplified by an erbium-doped fibre amplifier (EDFA) with adjustable gain to achieve the desired optical incident power at the fibre input. The frequency response of the SSB modulated signal after the 50 km fibre link was then measured by a Lightwave Component Analyser. To overcome the effect of SBS, the tunable laser was operated in coherence controlled mode with a linewidth of about 200 MHz. Experiments were carried out with a SSB

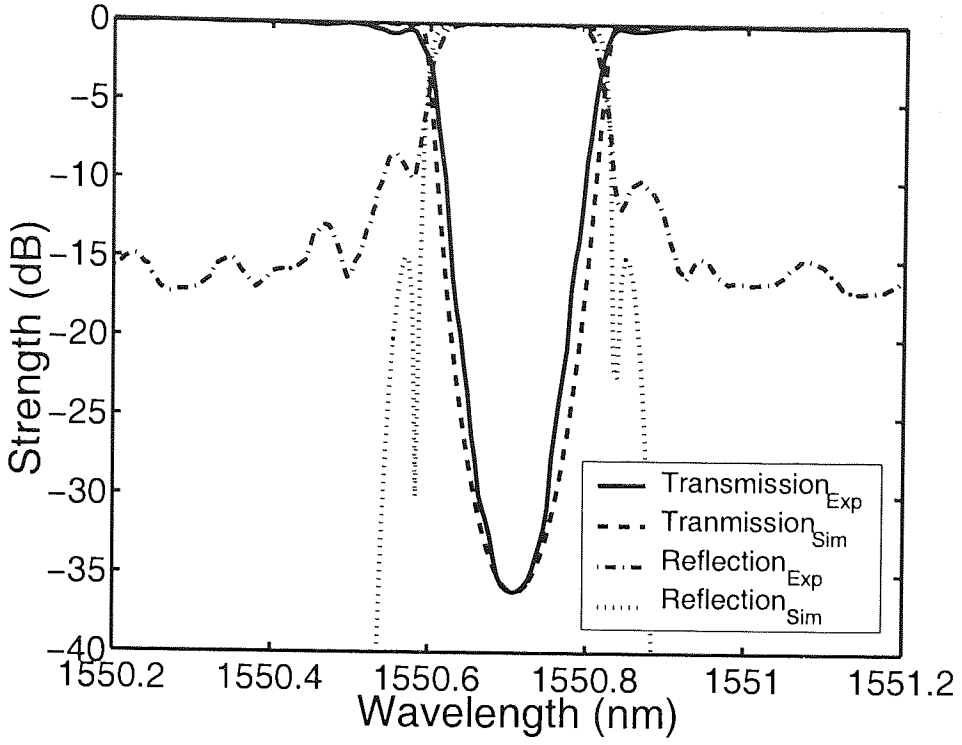

Figure 6.21: Transmission and reflection spectra of the apodised uniform FBG used as sideband filter in single-tone SSB modulated link.

Parameters		
Effective area A_{eff}	80	μm^2
Nonlinear refractive index n_2	2.6×10^{-20}	m^2/W
Group delay dispersion D	18	ps/nm/km
Fibre loss α	0.2	dB/km

Table 6.3: Simulation parameters for 50 km of standard single-mode fibre for SSB modulated link.

signal modulated from 0.13 GHz to 20 GHz at optical incident power of -3.0 dBm where the optical link still represented a linear system.

Numerical Simulation

The same in-house implementation of the split-step Fourier method applied to the GNLS equation including loss, fibre dispersion and the nonlinear effect was used to simulate the single-tone microwave/RF signal transmission through the fibre link. The simulations were carried out with SSB modulation scheme over a 50 km optical fibre link with different modulation frequencies ranged from 0.13 GHz to 20 GHz. The fibre parameters used are shown in Table 6.3 and the modulation index was set at m=0.07 to commensurate with the experiment.

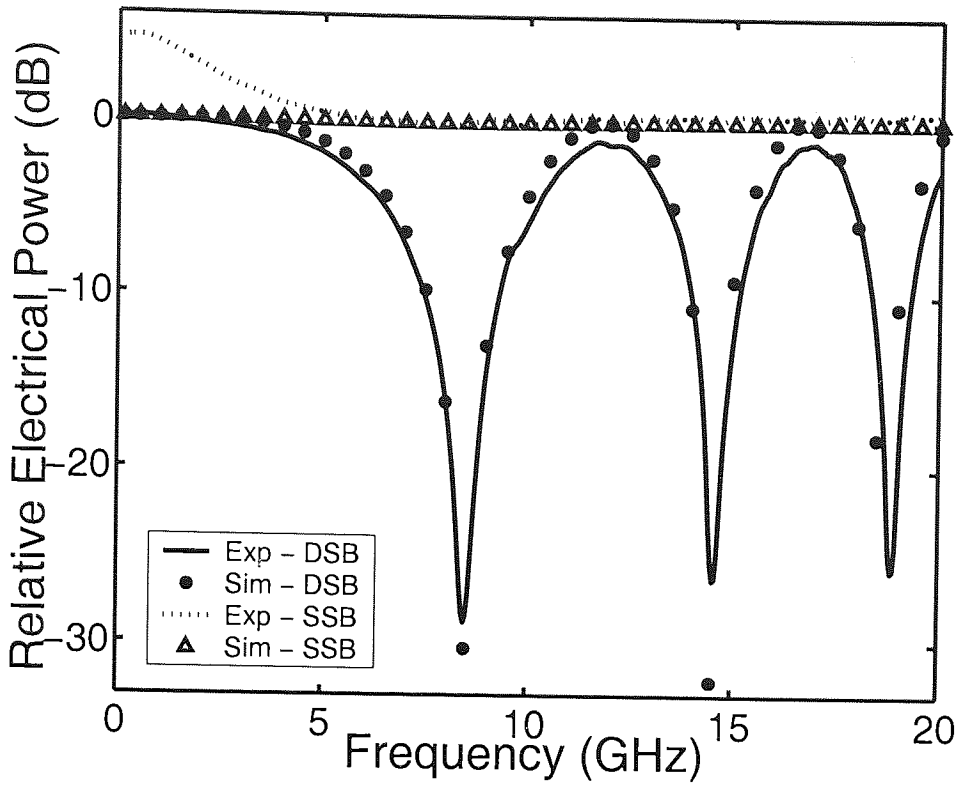

Figure 6.22: Experimental (Exp) and simulated (Sim) detected electrical power with optical incident power of -3.0 dBm in 50 km DSB and SSB modulated link.

Results and Discussion

Figure 6.22 shows the electrical modulation suppression effect suffered in a conventional DSB modulated link and the power penalty mitigation offered by the SSB modulated link at optical incident power of -3.0 dBm where the optical link still represented a linear system. It can be seen that there was no chromatic dispersion induced modulation suppression in the measured response of the SSB modulation at low input power level. This showed that the power penalty could be successfully eliminated by employing the SSB approach as stated in [108,111,132]. Note that the response in the lower frequency range was higher than that in the higher frequency range. This was due to the dual sideband transmission within the limited bandwidth of the fibre grating used. Other than that, there was a good agreement between the experimental results and the simulated results. They have demonstrated that chromatic dispersion induced power penalty can be eliminated by employing SSB modulation approach in the low power signal transmission.

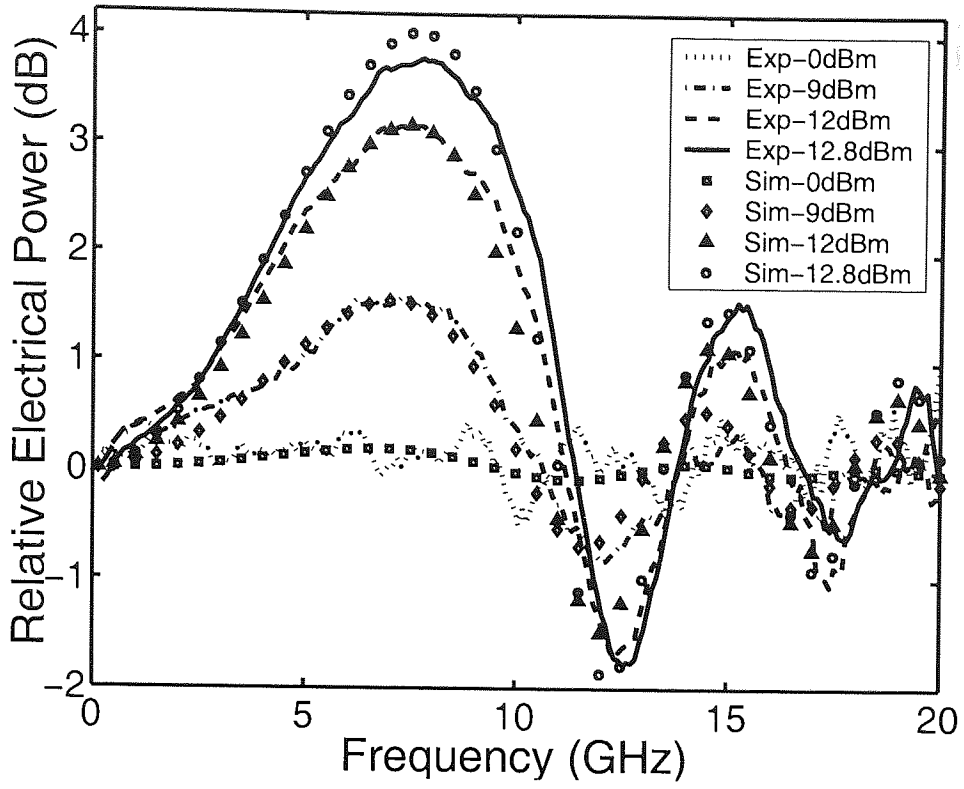

Figure 6.23: Experimental (Exp) and simulated (Sim) detected electrical power with different $P_{incident}$ in 50 km SSB modulated link.

6.5.2 Influence of Fibre-Induced SPM in High Power Transmission

The previous investigation focuses on the SSB modulated signal transmission in linear regime. To investigate the effect of fibre nonlinearity induced self-phase modulation on dispersive RoF link, experiments with higher optical incident power were carried out by using the same setup as in figure 6.20 and the same parameters for the simulations as in previous investigation.

Results and Discussion

The experimental and simulated results with different amounts of optical incident power of 0.0 dBm, 9.0 dBm, 12.0 dBm and 12.8 dBm are shown in figure 6.23. All the measured responses for SSB modulation scheme were normalised with regard to the response of SSB modulation at -3.0 dBm input power. Experimental results had good agreement with simulated results from GNLS equation. It indicated that the elimination as shown in figure 6.22, however, only happened when optical incident power was low where the system was treated as linear. When higher optical incident power was impinged at the fibre input, some fluctuations appeared in the fibre response with respect to linear SSB propagation, as can be seen in

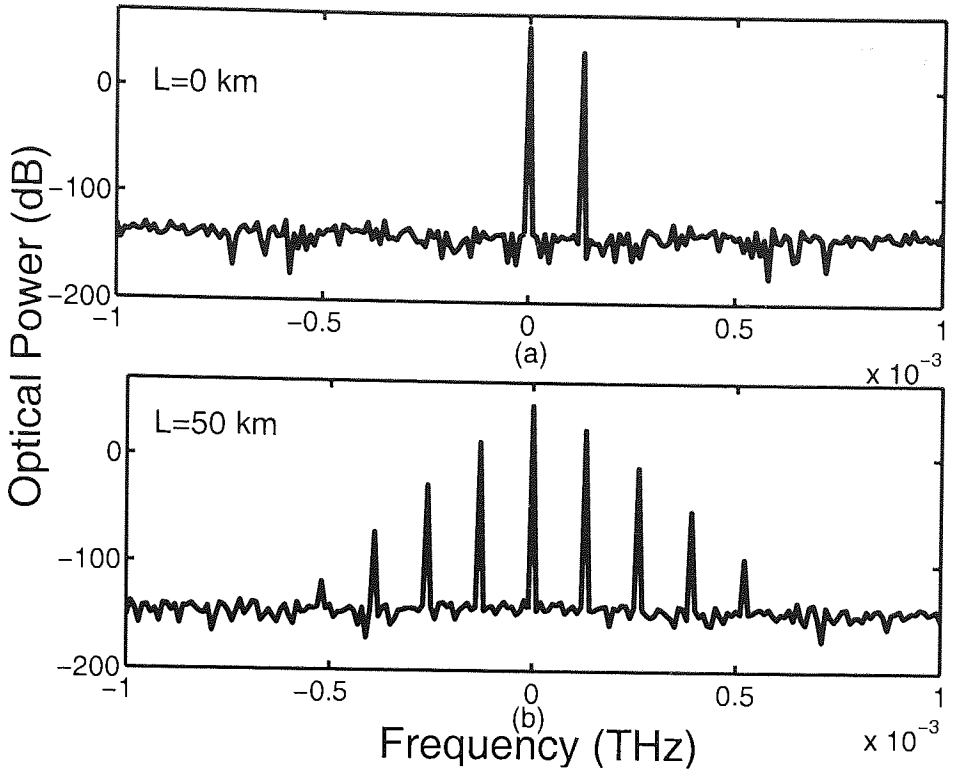

Figure 6.24: Simulated optical spectra of SSB signal modulated at 0.13 GHz with incident optical power of 10.0 dBm (a) at 0 km and (b) after 50km.

figure 6.23. Response fluctuations started to appear even at 0.0 dBm level and increased as input power was increased. This was in contrast with previous conclusions based on linear transmission using SSB modulation [108, 111, 132].

The cause of this phenomenon was that the dispersion mitigation is SPM-dependent. When SSB modulated signal transmitted through long length of fibre with high optical power, the nonlinear interaction between SPM and chromatic dispersion generated the other modulation sidebands. This phenomenon was simulated using modulation frequency of 0.13 GHz and is depicted in figure 6.24 where it shows new frequencies were generated after travelling 50 km of fibre with optical incident power of 10.0 dBm. These sidebands were generated by the four-wave mixing phenomenon that was phase-matched by the self-phase modulation. They interfered with each other when they arrived at the photodetector, as happened in DSB approach, and cancelled each other whenever there was a π-phase difference between each other.

Due to the limitation from SBS effect, the frequency transfer function for higher optical power beyond the SBS threshold were simulated in order to further look into the impact of the nonlinear effect. The simulated results at different $P_{incident}$ is shown in figure 6.25 whilst figure 6.26 summaries the maximum fluctuation amplitudes at each input power level. It

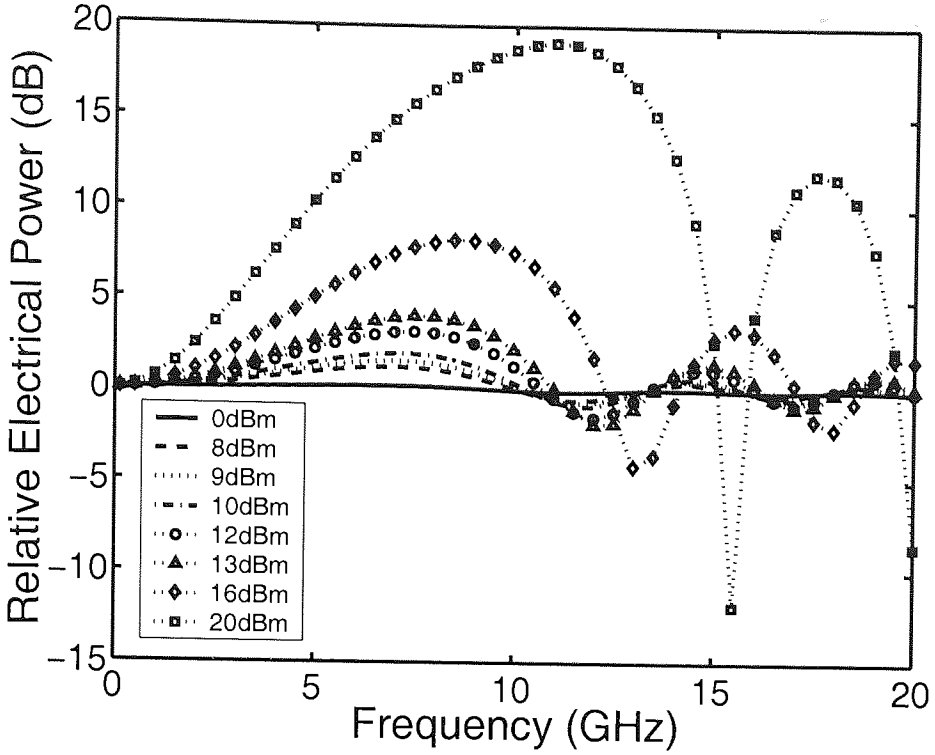

Figure 6.25: Simulated detected electrical power with different $P_{incident}$ in 50 km SSB modulated link.

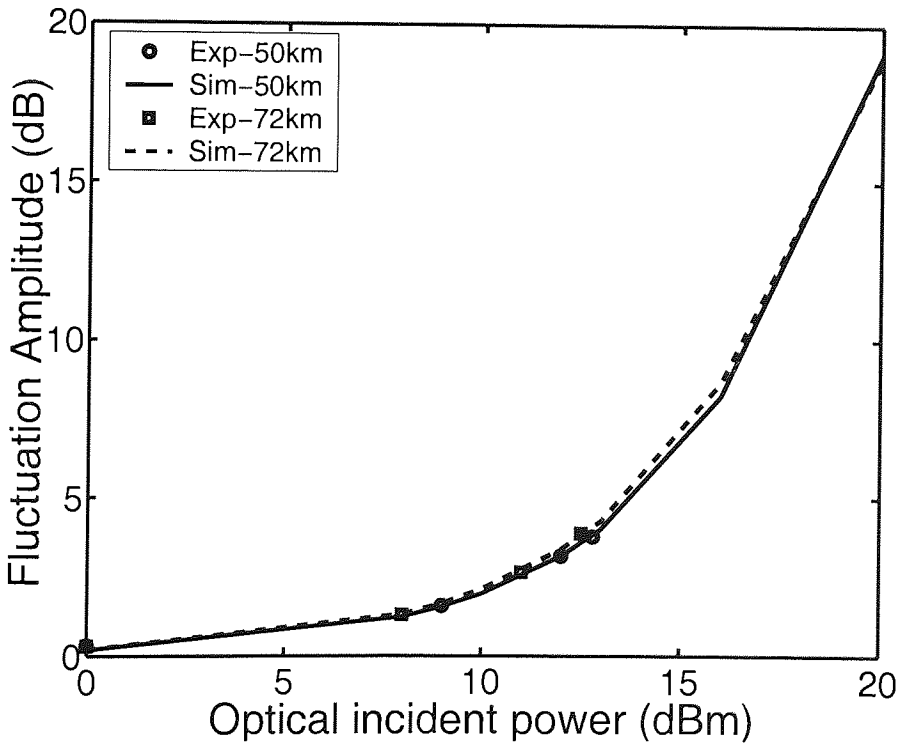

Figure 6.26: Fluctuation amplitudes for 50 km and 72 km of SSB modulated fibre link versus $P_{incident}$.

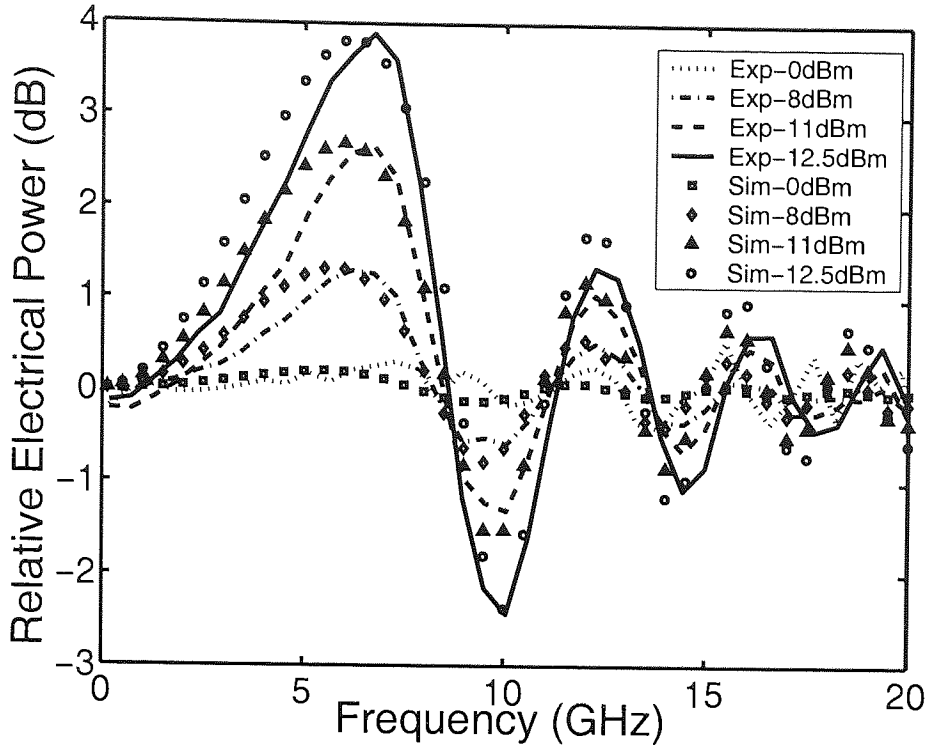

Figure 6.27: Experimental (Exp) and simulated (Sim) detected electrical power with different $P_{incident}$ in 72 km SSB modulated link.

can be seen that the maximum fluctuation amplitude was exponentially proportional to the optical incident power. At about 8.0 dBm, the maximum fluctuation amplitude was about 1.23 dB whilst it was about 1.97 dB when the optical incident power was 10.0 dBm. It could be further increased to 19.10 dB when 20.0 dBm of optical incident power was used. The results have shown that the maximum amplitude of the fluctuation is dependent to the optical input power, which in turn, SPM-dependent.

The same experiment was also conducted onto 72 km of optical fibre link in order to see the length dependency of the power fluctuation of SSB modulated link at high power level. Figure 6.27 shows the comparison between the experimental results and simulated results at $P_{incident}$ of 0.0 dBm, 8.0 dBm, 11.0 dBm and 12.5 dBm.

For higher input power levels, their detected electrical power was simulated and is shown in figure 6.28. The maximum fluctuation amplitude is summarised in figure 6.26. From the plot, it can be noticed that the maximum fluctuation amplitude in 72 km appeared to be slightly higher than that in 50 km with the same optical incident power. But, they became identical at higher power level. As in 50 km link, the results with 72 km have shown that the dispersion induced power fluctuation exists in high power SSB modulated link and it is SPM-dependent. The dependency of power fluctuation on length is small and can be

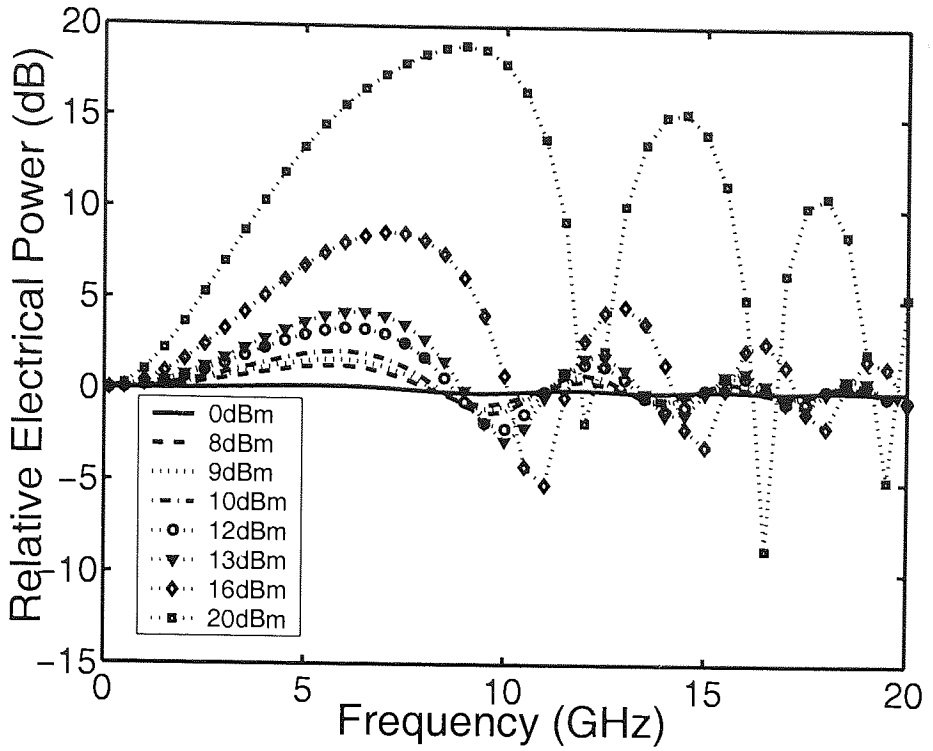

Figure 6.28: Simulated detected electrical power with different $P_{incident}$ in 72 km SSB modulated link.

neglected when optical incident power reaches 20 dBm.

6.5.3 Joint Effect of Fibre Dispersion and Fibre-induced SPM with the Presence of Incomplete Dispersion Compensation

Based on the results obtained in section 6.4.3 and section 6.4.4, in high power transmission links, the use of CFBG based dispersion compensator with incomplete dispersion compensation generally gives better frequency response than does the ideal dispersion compensation. And from section 6.5.2, it has concluded that when higher optical incident power is fed at the fibre input, fluctuations appear in the response and the dispersion mitigation is SPM-dependent.

Based on these observations, the employment of incomplete dispersion compensation in high power SSB modulated links was assessed. Simulation study was carried out with the presence of SPM effect in 50 km and 72 km of SSB modulated links which had total dispersion of 900 ps/nm and 1296 ps/nm, respectively. Similar setup as in figure 6.20 was referred to in the simulation, except a dispersion compensator was added right before the signal was detected by the LCA. A series of simulations were carried out with different dispersion compensation values started from 0 ps/nm to the respective ideal dispersion compensation for

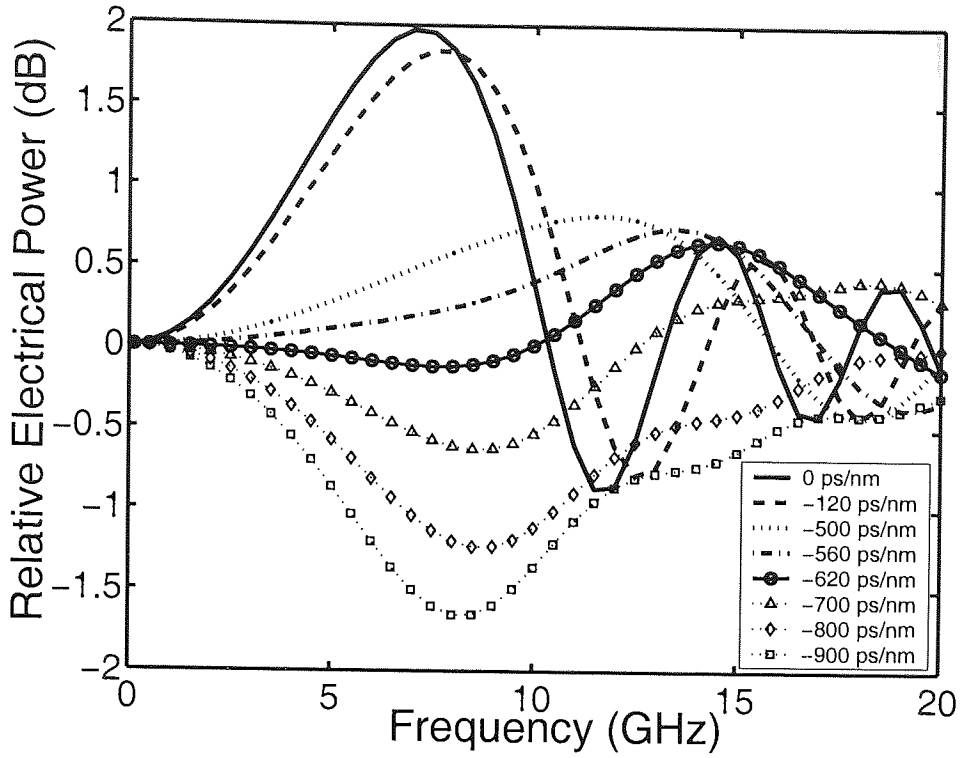

Figure 6.29: Simulated frequency transfer function with different dispersion compensations in a 50 km SSB modulated link at 10.0 dBm.

the two links. Simulations were carried out at 0.0 dBm, 10.0 dBm and 12.5 dBm. To get the best improvement that has the least magnitude of fluctuation, standard deviation of each simulation was calculated and compared.

Results and Discussion

Simulated results at 10.0 dBm are shown as an example of the frequency transfer response in 50 km and 72 km RoF links with the presence of incomplete dispersion compensation. The frequency transfer functions and the calculated standard deviation with 50 km link are shown in figure 6.29 and figure 6.30, respectively. Both of them clearly indicated that dispersion compensation with a value of -620 ps/nm successfully gave an improvement with least standard deviation to the frequency transfer function as compared to the link without dispersion compensation and the link with ideal dispersion compensation of -900 ps/nm. Standard deviation was calculated as only 0.265 dB, which was the minimum point in figure 6.30. Thus, it can be said that -620 ps/nm of dispersion compensation can be used to mimimise the power fluctuation in a 50 km SSB modulated link at 10.0 dBm of optical incident power.

For 72 km link at 10.0 dBm, the frequency transfer functions and the calculated standard deviation of simulation are illustrated in figure 6.31 and figure 6.32, respectively. Apparently,

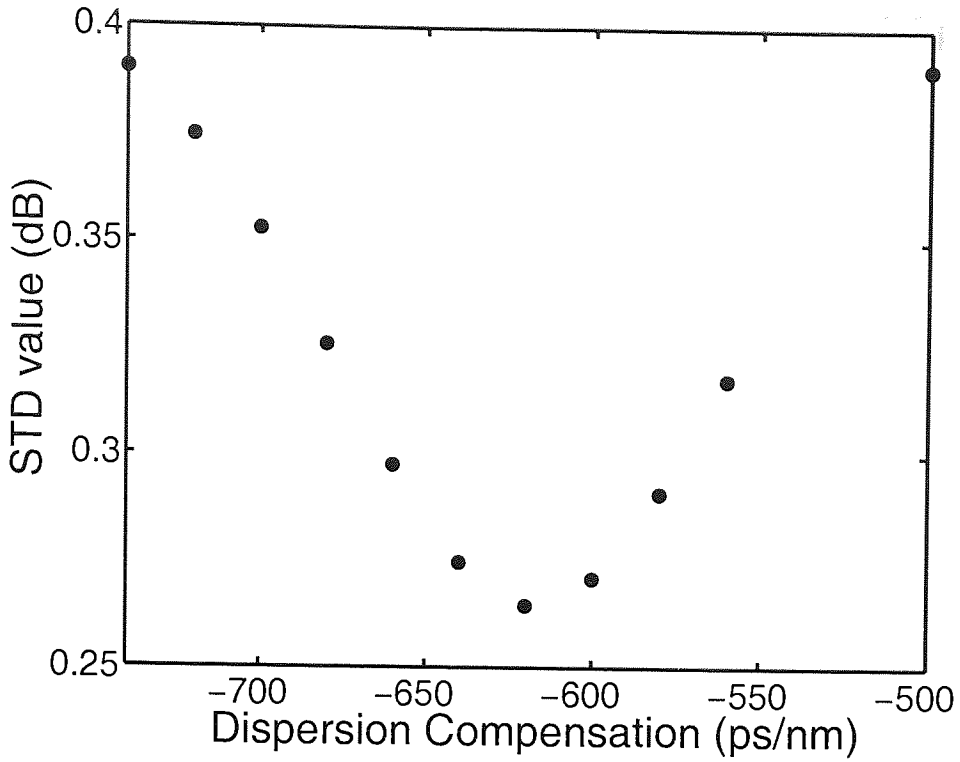

Figure 6.30: Standard deviation with different dispersion compensations in a 50 km SSB modulated link at 10.0 dBm.

dispersion compensation with a value of -1000 ps/nm successfully reduced the fluctuation amplitude of the nonlinear SSB modulated link as compared to the link without dispersion compensation and the link with the ideal dispersion compensation of -1296 ps/nm. Standard deviation was calculated as only 0.310 dB, which was the minimum point in figure 6.32. Thus, for the case of 72 km, the use of -1000 ps/nm of dispersion compensation is recommended to minimise the power fluctuation.

In figure 6.33, the calculated standard deviations at different amounts of optical incident power in 50 km and 72 km nonlinear SSB modulated link were plotted against the magnitude of residual dispersion compensation. Here, the residual dispersion magnitude was defined as the difference between the ideal dispersion compensation and the incomplete dispersion compensation in use. For instance, for 50 km link suffered from -900 ps/nm of dispersion, zero residual dispersion magnitude meant -900 ps/nm of dispersion compensation was used whereas 280 ps/nm of residual dispersion magnitude implied that -620 ps/nm of dispersion compensation was employed.

From figure 6.33, it is obvious that the residual dispersion magnitude that gave minimum standard deviation for 50 km and 72 km links were very similar at corresponded power level, but they were very dependent on the optical incident power. Generally, the value for the

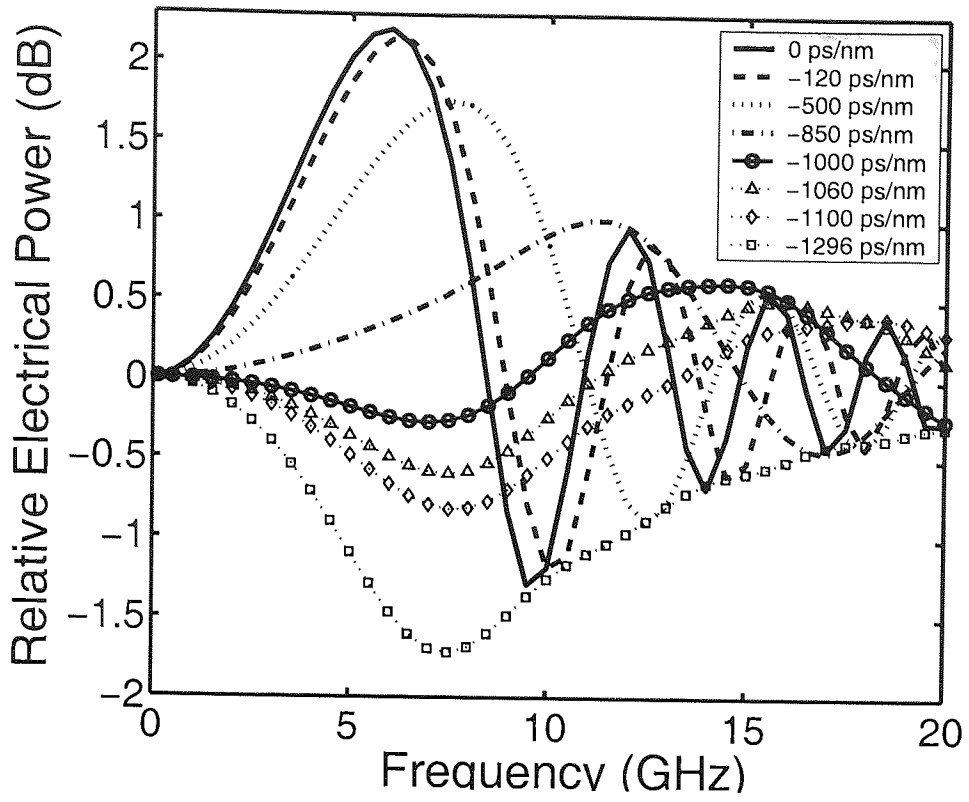

Figure 6.31: Simulated frequency transfer function with different dispersion compensations in a 72 km SSB modulated link at 10.0 dBm.

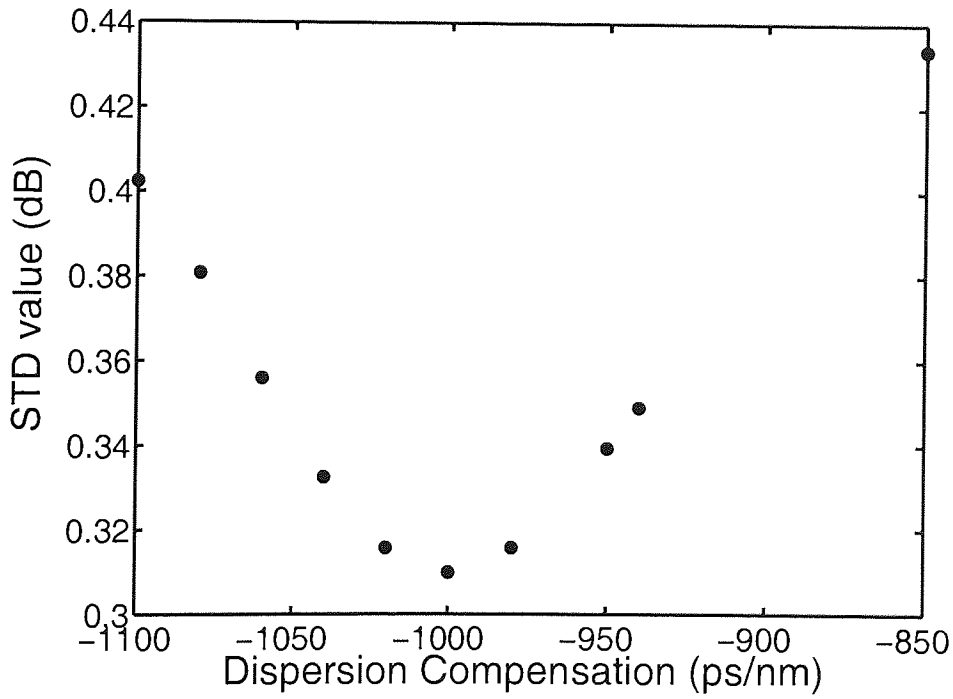

Figure 6.32: Standard deviation with different dispersion compensations in a 72 km SSB modulated link at 10.0 dBm.

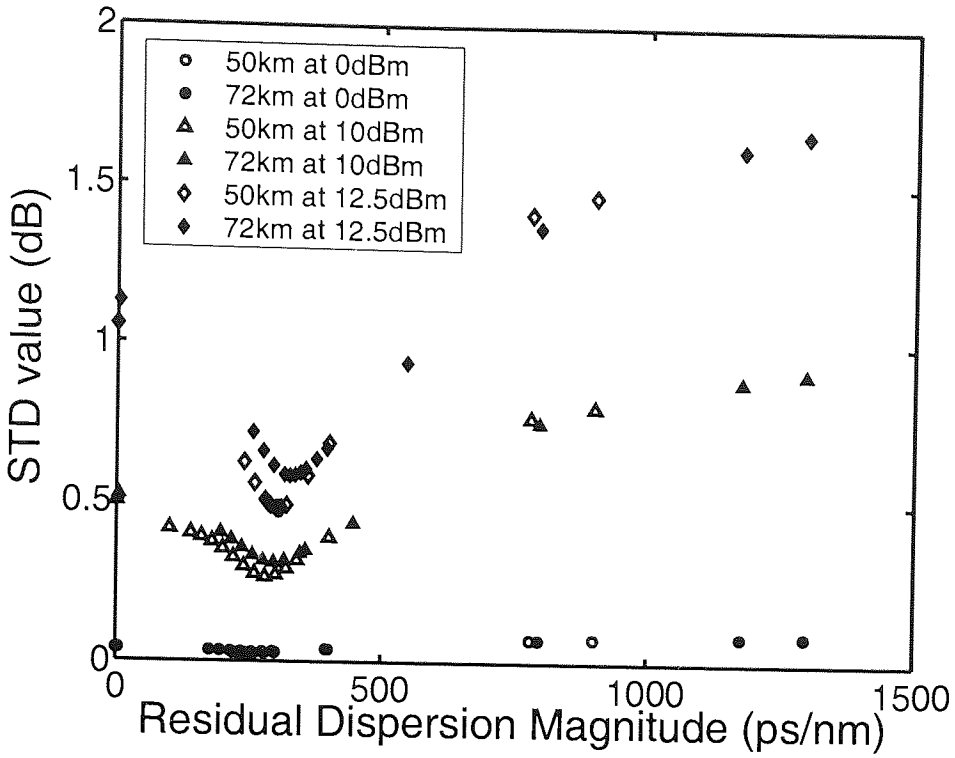

Figure 6.33: Standard deviation versus residual dispersion magnitude in 50 km and 72 km nonlinear SSB modulated link at different amounts of optical incident power.

residual dispersion magnitude increased with the optical incident power. This phenomenon was anticipated because fibre dispersion in the link was partly compensated by the nonlinear SPM effect that augmented with high power level, analogous to DSB modulated link in section 6.4.1, and henceforth less dispersion compensation from CFBG was needed.

The simulated results of the best residual dispersion magnitudes and the corresponded standard deviations for both links are summarised in figure 6.34 and figure 6.35 with reference to the optical incident power. Linear regression was also included in the figures in order to give an approximation at high power levels. It can be noticed from the simulated results and their approximations in figure 6.34 that, as power increased, incomplete dispersion compensation was needed to give the maximum reduction to the fluctuation amplitude in SSB modulated links. However, this was at the cost of a higher standard deviation value as well, as can be seen from figure 6.35.

Based on the results obtained, it can be concluded that incomplete dispersion compensation can be used to improve the power fluctuation occurred in high power SSB modulated link. The residual dispersion magnitude and the corresponded standard deviation increase with the optical incident power and the length of fibre link.

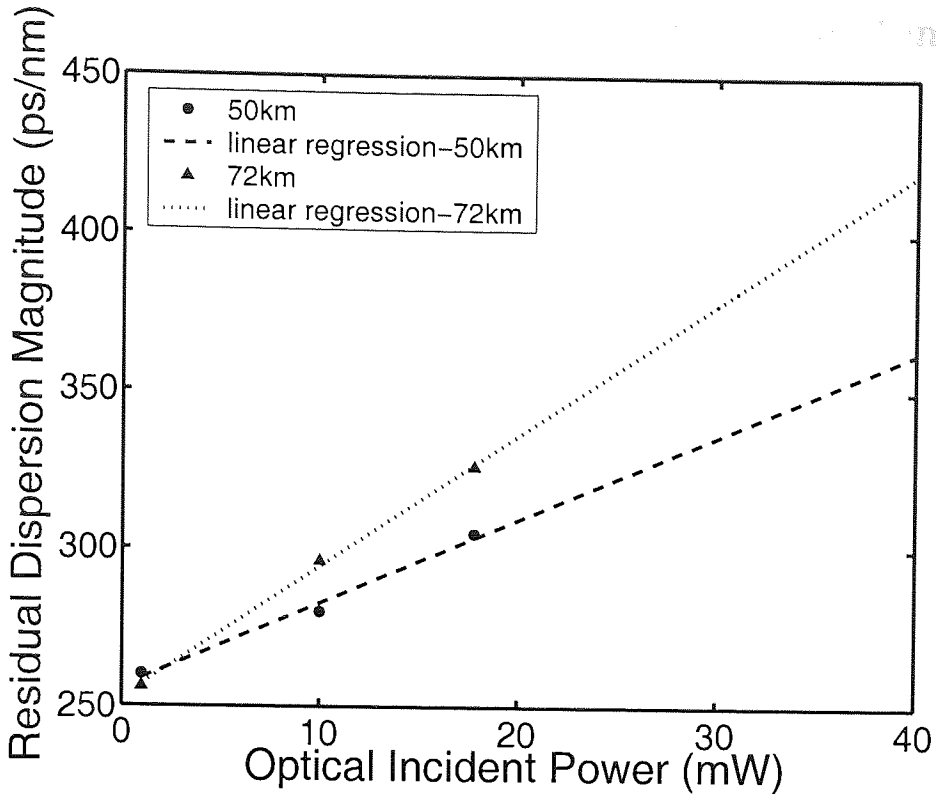

Figure 6.34: Best residual dispersion magnitude and its approximation in 50 km and 72 km nonlinear SSB modulated link.

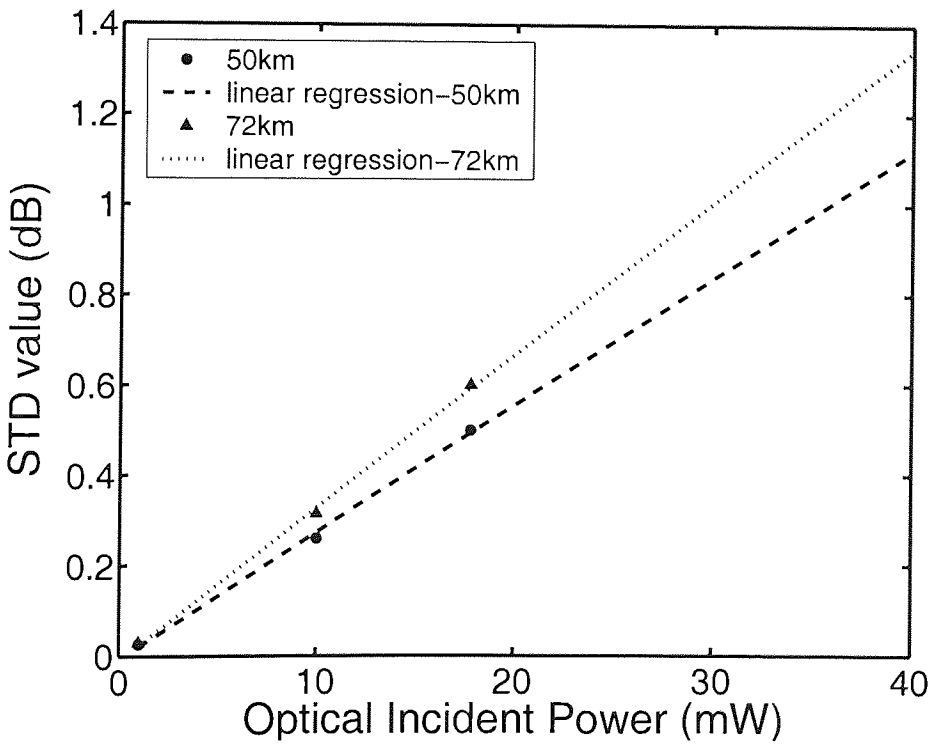

Figure 6.35: Standard deviation corresponded to the best residual dispersion magnitude and its approximation in 50 km and 72 km nonlinear SSB modulated link.

6.6 Study of Intermodulation Distortion in Two-Tone Microwave/RF Signals Transmission Links

Device performance has advanced to a point where system capabilities can be limited by the fibre transmission. With the existing high output power provided by EDFAs, fibre-induced nonlinear effect is a potential problem. When more than one signal transmits in the high power link, fibre dispersion interplays with fibre-induced self-phase modulation to produce intermodulation distortions [133, 134].

In this work, a study of intermodulation distortion focusing on the combined effect of chromatic dispersion and fibre nonlinearity in two-tone microwave/RF signals transmission was conducted to evaluate the system performance of nonlinear DSB and SSB modulated RoF links. The performance of these systems was evaluated based on the third order intercept point (TOI), which is fibre length and power dependent.

6.6.1 Intermodulation Distortion and Third Order Intercept Point

Intermodulation distortion occurs when the nonlinearity of a device or system with multiple input frequencies causes undesired outputs at other frequencies. In a communications system, this means that a signal in one channel can cause interference with adjacent channels. The spurious products generated due to the nonlinearity of a device are mathematically related to the original input signals. As the spectrum becomes highly demanded, leading to the channels to be tightly spaced, minimising the intermodulation distortion becomes more critical.

The frequencies of the two-tone intermodulation products with original input frequencies of f_1 and f_2 can be computed by the equation:

$$Mf_1 \pm Nf_2 \qquad M,N = 0,1,2,3,\ldots \quad . \tag{6.20}$$

The order of the distortion product is given by the sum of M+N. The second order intermodulation products of two signals at f_1 and f_2 would occur at f_1+f_2, f_2-f_1, $2f_1$ and $2f_2$, as can be seen from figure 6.36. Third order intermodulation products of the two signals f_1 and f_2 would be $2f_1+f_2$, $2f_1-f_2$, f_1+2f_2 and f_1-2f_2 where $2f_1$ is the second harmonic of f_1 and $2f_2$ is the second harmonic of f_2. The level of these undesired products is a function of the power received and the linearity of device under test.

The important distortion terms in radio-over-fibre analogue links are those which have frequencies close to the fundamental signals and cannot be filtered. These can be the third

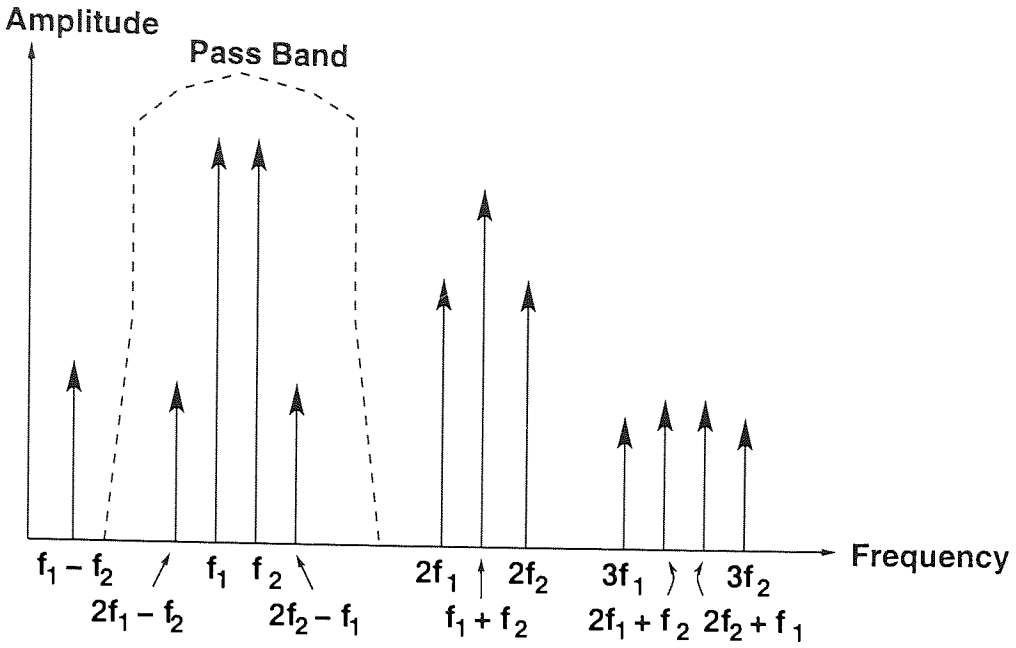

Figure 6.36: Schematic diagram of third order intermodulation products in pass band.

order intermodulation (IM3) products, $2f_1 - f_2$ and $2f_2 - f_1$, since they are usually in the pass band of the transmission as shown in figure 6.36 [135].

The third-order intercept point (TOI) is typically used to characterise the relative importance of these third order intermodulation products. It helps quantify a device's intermodulation distortion performance and indicates how well a device performs in the presence of strong signals. It is a point that is an extrapolated convergence, not directly measurable, of the third order intermodulation term with one of the fundamental tones, as shown in figure 6.37 [20]. It can also be calculated by applying the equation [20]

$$TOI = P_{output} + |\frac{IP_{dBc}}{2}|, \tag{6.21}$$

where P_{output} is the output power of the fundamental signal and IP_{dBc} is the level in dBc of the third order intermodulation product relative to the fundamental since the power slope is known for both the fundamental signal (slope of 1) and the third order intermodulation product (slope of 3). In our calculations, the worst case difference, which is the smallest IP_{dBc}, between the fundamental and generated tones was used.

6.6.2 DSB Modulated Links

The same in-house simulator was used to simulate the signal transmission through the fibre link including loss, fibre dispersion and fibre nonlinear effect. The optical source was represented as a monochromatic CW source at 1550 nm, amplitude modulated using two pure

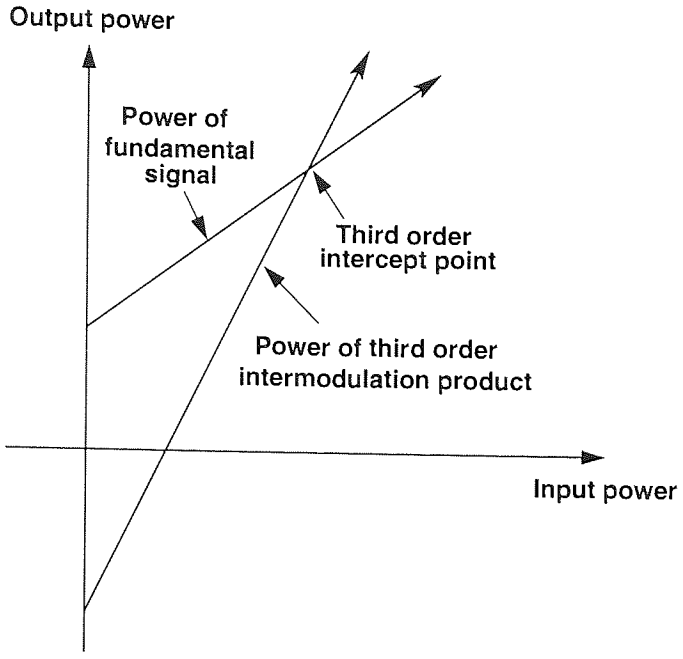

Figure 6.37: Schematic diagram for third order interception point.

sinusoidal waveforms with a modulation index of $m = 0.5$ at frequencies of f_1=10 GHz and f_2=10.1 GHz [136]. The parameters in this simulation were the same as in the single-tone transmission. Particular care was taken to ensure that these tones and the inter-harmonic components they would generate could be accurately represented in the simulation. Noise, either from amplification in the link or in the receiver was not accounted for in the simulation and fibre loss was included simply to account for its influence on the power and thus nonlinear terms with distance. Again, to simplify the interpretation of the results, other nonlinear terms, dispersion slope and polarization effects were ignored.

For two-tone signals transmission with DSB modulation scheme, the input optical field U_{in} and the average amplitude of input optical field U_{av} were represented by

$$U_{in} = U_{av}\left(1 + \frac{m}{2}\left(\sin\left(2\pi f_1 t\right) + \sin\left(2\pi f_2 t\right)\right)\right) \tag{6.22}$$

and

$$U_{av} = \sqrt{\frac{P_{incident}}{1 + \frac{m^2}{4}}}, \tag{6.23}$$

respectively.

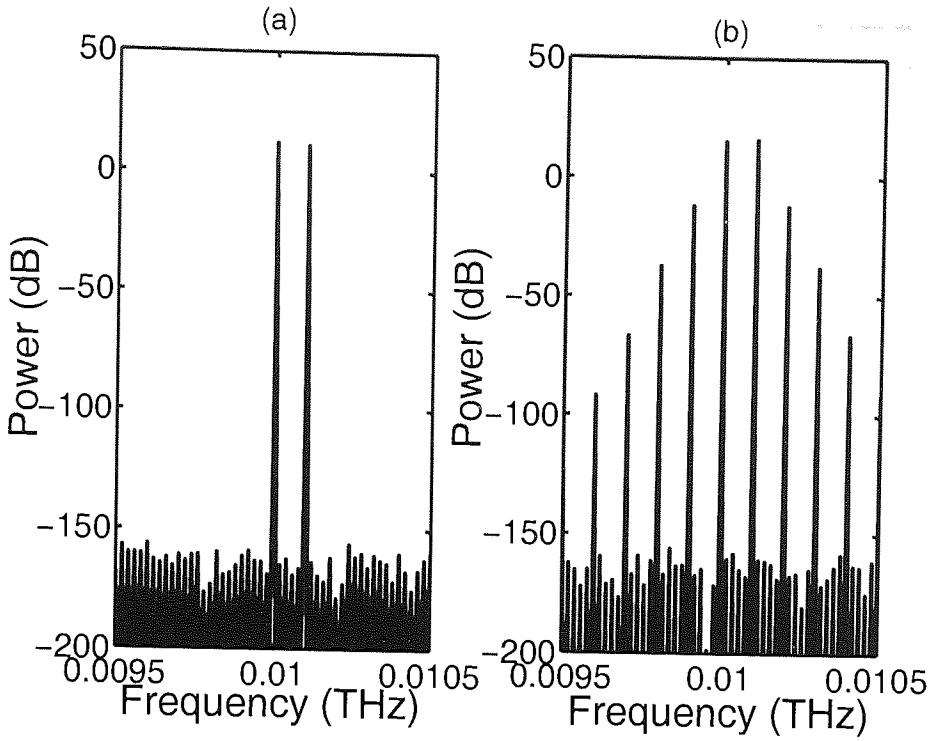

Figure 6.38: Simulated detected optical power spectra of 10.0 GHz and 10.1 GHz microwave/RF signals in a 100 km of fibre at $P_{incident}$ = 16.0 dBm in (a) linear and (b) nonlinear regimes.

Results and Discussion

To clearly see the growth of IM3 products, in the first incidence, simulations were carried out with $n_2 = 0 \times 10^{-20}\text{m}^2/\text{W}$ and $n_2 = 2.6 \times 10^{-20}\text{m}^2/\text{W}$ which represented linear and nonlinear systems, respectively. Figure 6.38 shows the received optical power spectra for both linear and nonlinear signal transmissions over 100 km of fibre at the optical incident power of 16.0 dBm. It can be seen that there was no spurious tone even when the optical incident power was as high as 16.0 dBm in the linear regime whereas spurious tones appeared in the nonlinear regime with the same optical incident power. This clearly showed the generation of third-order intermodulation distortion terms due to the nonlinearity in the fibre.

Figure 6.39 shows the detected output microwave/RF signal power retrieved at the two fundamental signals, $f_1 = 10.0$ GHz and $f_2 = 10.1$ GHz, and the resulted IM3 products at $2f_1 - f_2 = 9.9$ GHz and $2f_2 - f_1 = 10.2$ GHz, corresponding to the optical incident power of 16.0 dBm. For comparison, the amounts of the detected signal power in linear transmission at 10.0 GHz and 10.1 GHz are plotted alongside the nonlinear results. Note that the amounts of the detected optical power at 9.9 GHz and 10.2 GHz in linear system were not plotted because basically they were just noise. It can be observed that there were signifi-

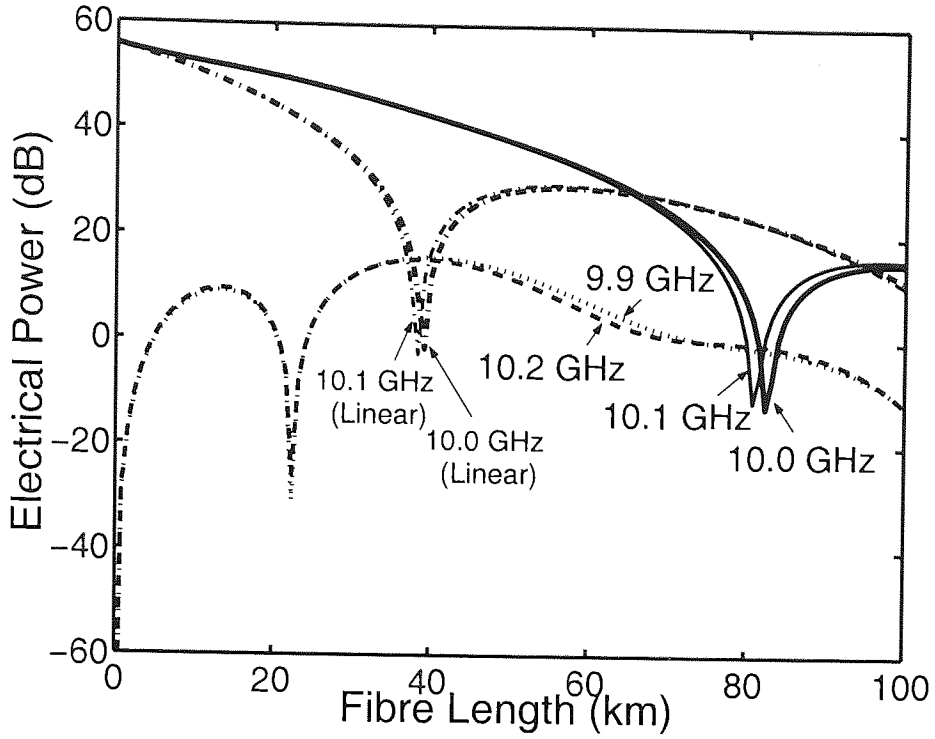

Figure 6.39: Simulated detected electrical power of 10.0 GHz and 10.1 GHz microwave/RF signals and their distortion tones versus propagation distance at optical incident power of 16 dBm in DSB modulated link.

cant shifts in the positions of the dispersion induced notches in the signal at 10.0 GHz and 10.1 GHz in the nonlinear system as compared to those in the linear system. These shifts were recognised as dispersion mitigation caused by the self-phase modulation effects of fibre nonlinearity [121, 122]. Besides, the initial high rate for growth of the IM3 products at 10.2 GHz and 9.9 GHz was observed as well as some fluctuations as fibre length increased. It is worth noting that at certain fibre lengths, where IM3 products reached minimum, an optimum system performance could be achieved. In this case, the link provided an optimum system performance at 22.4 km, as can be seen from figure 6.39. On the contrary, when the dispersion induced fading greatly reduced the signals, the IM3 distortion terms were dominant. From the plot, this IM3 dominance happened between 80.5 km and 82.5 km due to the occurrence of double notches from the fundamental signals.

In the calculations of the TOI point, as in equation (6.21), the smallest difference between the fundamental outputs and IM3 products was used at each fibre length and power level in order to predict the worst case value. The results are plotted in figure 6.40. As expected, the TOI increased with optical incident power level and decreased with fibre length due to the combined effect of nonlinearity and dispersion. There was, however, a peak in the TOI output due to the dispersion induced suppression of the IM3 terms and subsequently a dip in

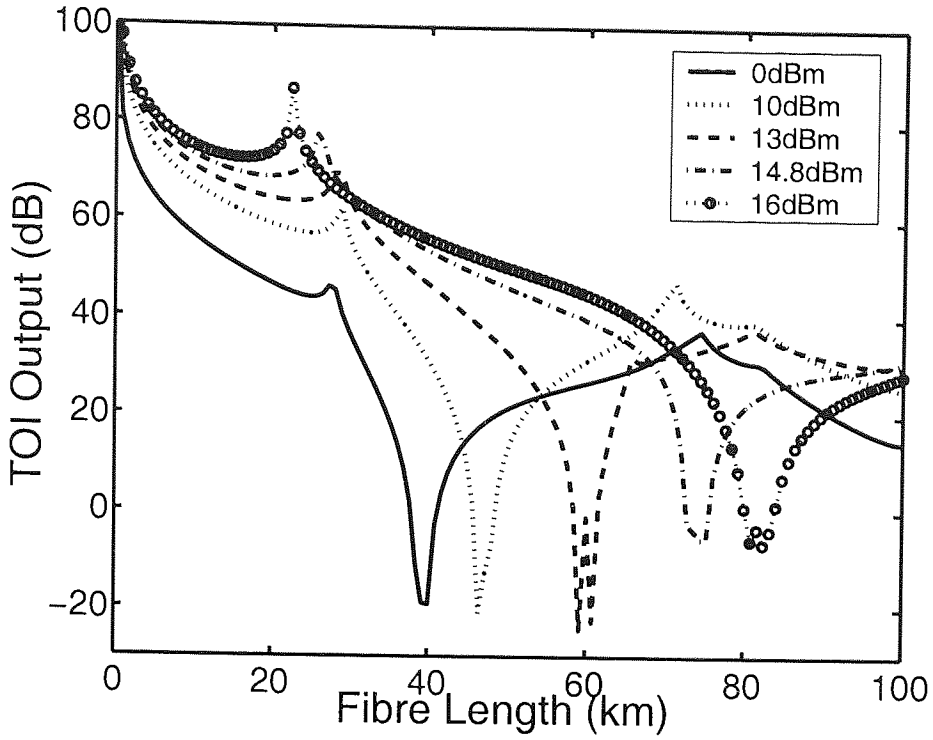

Figure 6.40: TOI output versus propagation distance for different amounts of optical incident power in two-tone signals transmission with DSB modulation scheme.

the TOI where the two fundamental signal frequencies suffered dispersion induced fading. This, respectively, indicated the best and the worst performances for a two-tone system. The double notch observed in the plots corresponded to the slightly different distances at which the two signal frequency components suffered dispersion induced fading.

6.6.3 SSB Modulated Links

After the investigation on DSB modulation scheme, simulations on two-tone signals transmission were repeated with SSB modulated optical field. In the simulations, the input optical field U_{in} and the average amplitude of input optical field U_{av} were represented by

$$\begin{aligned} U_{in} &= U_{av}(1+\frac{m}{2}(\sin(2\pi f_1 t) - i\cos(2\pi f_1 t) \\ &\quad + \sin(2\pi f_2 t) - i\cos(2\pi f_2 t))) \end{aligned} \tag{6.24}$$

and

$$U_{av} = \sqrt{\frac{P_{incident}}{1+\frac{m^2}{2}}}, \tag{6.25}$$

respectively.

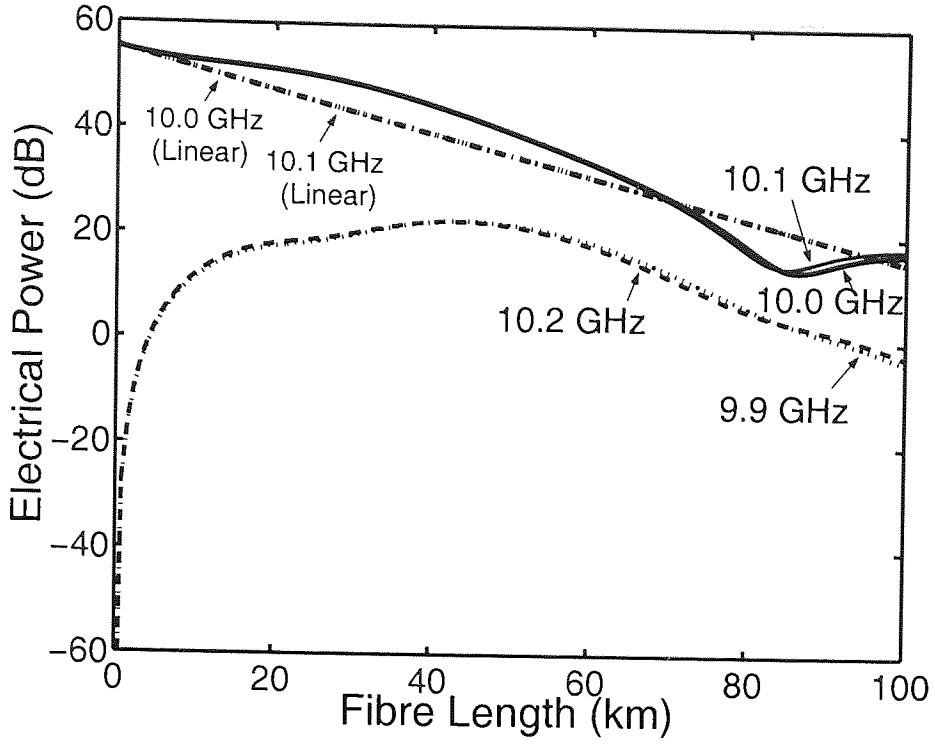

Figure 6.41: Simulated detected electrical power of 10.0 GHz and 10.1 GHz microwave/RF signals and their distortion tones versus propagation distance at optical incident power of 16.0 dBm in SSB modulated link.

Results and Discussion

For the case of SSB modulation, the simulated results are shown in figure 6.41. For comparison purpose, the amounts of the detected microwave/RF signal power at the two fundamental signals in a linear SSB modulation system are plotted in the same plot. Again, the amounts of the detected optical power at 9.9 GHz and 10.2 GHz in linear system were not plotted because they were just noise. It can be seen that there was a successful elimination of dispersion induced power penalty if a linear system was assessed. The amounts of the detected power in linear system only responded to fibre loss which was 0.2 dB/km. On the contrary, in the nonlinear system, the combined effect of dispersion and nonlinearity led the detected output power of the fundamental signals to a depression point. This meant that power penalty still existed. This phenomenon was well-explained in section 6.5.2.

The results also showed that there was a high growth rate for the IM3 products. Nevertheless, they never overwhelmed the fundamental signals. This occurrence was due to the fact that, unlike those in the DSB modulated link, the dispersion induced fading in the fundamental signals were solely caused by the interaction between the fundamental signals and the newly generated frequencies induced by the nonlinear SPM effect on the other side of the optical carrier. Thus, weaker power penalty was anticipated. Besides, much weaker or even

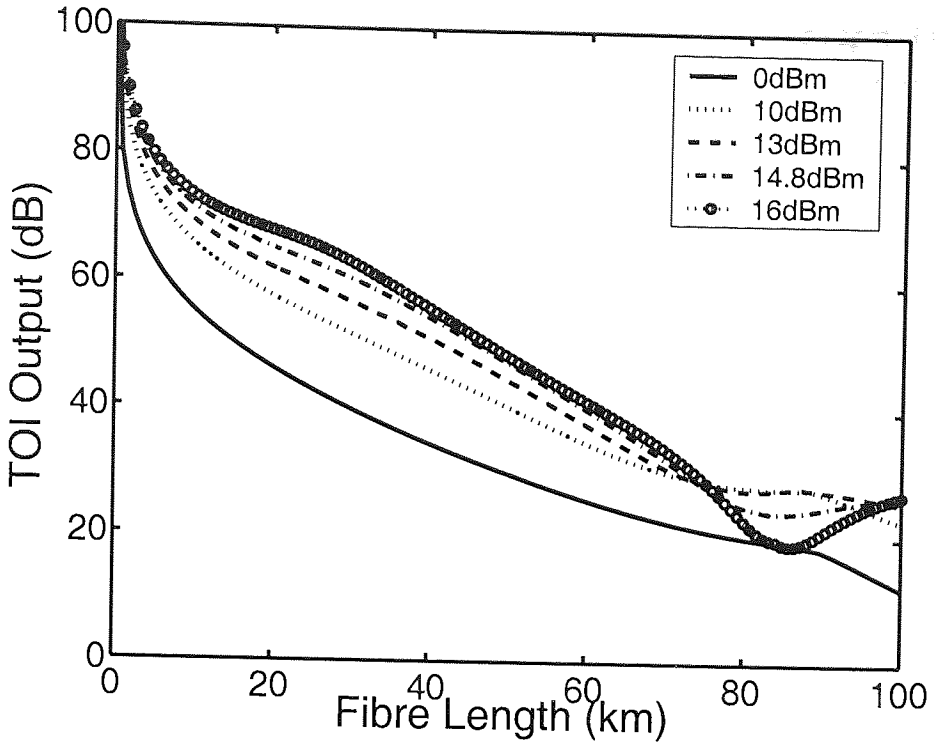

Figure 6.42: TOI point versus propagation distance for different amounts of optical incident power in two-tone signals transmission with SSB modulation scheme.

no dispersion induced fading was found in the IM3 products because of the same scenario. These were the two differences between the DSB and SSB modulated links.

The calculated TOI is depicted in figure 6.42. Results showed that TOI of SSB modulated link had a very different trend compared to the result from DSB modulated link. The TOI value increased with optical incident power but decreased monotonously with fibre length. Dips appeared at some fibre lengths indicating that the fundamental signals were suffering from dispersion induced power penalty due to the interaction between fibre dispersion and nonlinearity as discussed above. As predicted, these depression points were deepened when higher power levels were used.

6.7 Conclusion

In this chapter, a series of investigations based on the DSB and SSB modulated links were carried out. For DSB modulated link, theoretical and experimental demonstrations have proven that fibre-induced SPM can be used as an efficient way to compensate for chromatic dispersion effect that appear in externally modulated microwave/millimetre-wave radio-over-fibre systems. The interplay between the nonlinear SPM effect and the anomalous dispersion leads to an improvement of the frequency-length product. Certainly, this also applies to the

responses in length domain. Theoretically, there is a high interest on the capabilities of the response at the critical power level of ≈12.3 dBm which gives a constant detected power up to a length of 400 km. However, this phenomenon only happens if lossless RoF link is used. Apart from improving the frequency-length product of the link, the employment of incomplete dispersion compensation by CFBG gives a nearly-flat response in the frequency range of up to ≈13 GHz when high optical incident power is used. The potential of the use of CFBG based dispersion compensator with incomplete dispersion compensation in high power transmission links has been proven. On the other hand, further investigations have indicated that ideal dispersion compensation only gives precise compensation in the linear transmission regime. When higher optical incident power is applied, the optical fibre link works in nonlinear regime and the dispersion compensation is no longer ideal. Techniques to overcome this issue need to be investigated.

The investigations in SSB modulated link have concluded that SSB modulation approach successfully eliminates the chromatic dispersion induced power penalty in the linear regime. However, power fluctuation exists when high power transmission is employed. This attributes to new frequencies generated by the interaction between SPM and chromatic dispersion while the signal is travelling along the dispersive fibre. Experimental and simulated results have shown that the power fluctuation is exponentially proportional to the optical incident power and the length dependency can be neglected at power level above 20 dBm. This shows that the mitigation of modulation suppression is SPM-dependent. Thus, fibre nonlinearity induced SPM effects must also be considered in a SSB modulation approach to accurately characterise the signal propagation in dispersive and nonlinear RoF links. However, with the use of incomplete dispersion compensation, the power fluctuation in the nonlinear SSB modulated links can be reduced. Further study has concluded that the residual dispersion magnitude are dependent on the optical incident power. As optical incident power and length increase, incomplete dispersion compensation is needed and this is accompanied with higher standard deviation.

Note that simulation studies below SBS threshold were carried out without the SBS effect which was compliance with the experiments. The SBS effect in the simulation studies above the SBS threshold were, however, ignored since the main purpose of the simulation at high power levels was to look into the potential of the nonlinear link response. And considering that this limitation can be suppressed by using the well-known techniques suggested in [126] at a later stage, the inclusion of SBS effect is dispensable in the simulation study.

The intermodulation performance of amplitude modulated microwave/RF signals at 10.0 GHz and 10.1 GHz transmitted over a fibre optic link including nonlinearity, dispersion and loss was also studied. The investigations into the third order intermodulation distortion have

indicated that for a fixed fibre length, increasing input power level in the DSB modulation scheme generally enhances the TOI until the dispersion related power penalty appears; a similar trend for the SSB modulation scheme. However, the DSB can provide a better system performance for fibre link with certain length because peak of TOI output can be found if appropriate fibre length is used with appropriate optical incident power level. This peak provides a possibility for optimising the system performance. Studies in SSB modulated link have shown that nonlinear effect induced in high power link causes TOI to have depression points at around 82 km length of link. Thus, the nonlinear effect should be considered in designing and characterising high power fibre links when the SSB modulation approach is used.

Chapter 7

Thesis Conclusions

This thesis has focused in exploiting the characteristics of single-mode fibre, namely, its thermal sensitivity, birefringence, dispersion and nonlinearity, in the applications of distributed temperature sensing and radio-over-fibre. The challenge of optical sensing technology to realise the temperature monitoring system and the challenges of microwave/millimetre-wave technologies for the future signal processing and broadband photonics communication network have been identified and constituted as the main focus of the studies of this thesis.

The fibre transmission characteristics have been outlined in detail in the first incidence in order to give the relation and the joint effects that they may possess. Fibre Bragg grating technology has also been reviewed since it has been widely used in most of the work in this thesis. It has successfully shown its effectiveness as a temperature sensing element, a bandpass filter and a dispersion compensator throughout the experiments with its tailored design for each role.

A fully distributed temperature sensor consisting of an apodised chirped fibre Bragg grating has been demonstrated. It has shown that the applied temperature profile to the grating can be determined by using the transfer matrix method by means of least squares optimised fitting the calculated reflection spectrum with the experimental reflection spectrum. Simultaneous determination of the temperature change, position and width of the heat sources can be achieved to a standard deviation of 0.6 K, 29 μm and 56 μm, respectively. The proposed system has proven to be efficient in characterising grating and providing the information of temperature variation, location and width of the heat source, and henceforth, is capable to project a temperature profile $g(z, \Delta T, L_p, C_p)$ for the area under test. Experimental and simulated results have shown that the proposed system is not restricted to monotonic temperature profile. On the contrary, it can be used to retrieve non-monotonic temperature profile. With an optimum design of longer grating, this system can be used for distributed temperature

sensing over a larger region. The proposed system has also proven itself to be capable of simultaneous temperature measurement of multiple heat sources. The only concern is, the process takes minutes to determine the parametric profile depending on the number of parameters to be fitted, choice of initial values, desired fitness, number of wavelength scanned and the speed of the processor in use. These factors appear to be the same concern in other conventional optimisation methods as well [83, 84]. To improve this, a simple heuristic way can be used to estimate them. For example, slowly varying changes in the temperature profile can be estimated by simply using the calculated parameters of the previous measurement. Thus, this proposed distributed sensing system is more practical for the applications that involve slow varying temperature change.

In achieving the optical signal processing for microwave/millimetre-wave and optical communication systems, the key concepts of the fibre delay line filter have been reviewed and the analysis based on the delay line filter transfer function has also been presented. Based on the basic concept, a reconfigurable optical fibre delay line filter constructed by a single piece of high-birefringence (Hi-Bi) fibre structure has been presented. Segmented architecture has been realised by applying transverse force onto the Hi-Bi fibre as to divide the single piece Hi-Bi fibre into sections without breaking the fibre. By changing the input azimuth to the fibre, as well as the strength and direction of the applied stress coupling to the Hi-Bi fibre, reconfigurable microwave filtering and optical bandpass filtering responses can be achieved. Bipolar taps, which are not achievable by positive systems, have also been realised in this segmented Hi-Bi fibre structure by the optically coherent addition of the signal taps. Owing to the use of the single-line Hi-Bi fibre structure, no extra control scheme is needed for optical path control in this proposed structure. The experimental and simulated results have successfully shown that the proposed filter can be reconfigured to meet the requirements of signal processing for microwave photonic and optical filtering applications. This system is attractive because of its simple and cost effective feature. However, there are some discrepancies in the notch amplitudes and sidelobe suppressions between the experimental and simulated results. These could be due to the possible mismatch in the length ratio of the Hi-Bi fibre sections and angular misalignment between the fibre ends.

Owing to the high demands in microwave photonic provision system and the importance of optical fibre as the transmission medium, microwave/RF signals transmission in dispersive lossy fibre link accounting for the effect of fibre dispersion, fibre loss and fibre nonlinearity has been investigated. The generalised Schrödinger (GNLS) equation solved by the Fourier split-step method has been reviewed. Experimental investigations on the combined effect of fibre dispersion and nonlinearity in both double-sideband (DSB) and single-sideband (SSB) modulated links have been conducted and superimposed onto the results

obtained from GNLS equation.

For signal transmission in DSB modulated link, experimental and theoretical investigations have proven that fibre-induced self-phase modulation (SPM) can be used as an efficient way to compensate for the chromatic dispersion induced power penalty that appears in the externally modulated microwave/RF radio-over-fibre systems. Further investigation has also shown that ideal dispersion compensation is only able to eliminate the dispersion induced power penalty in the linear transmission regime. When higher optical incident power is applied, the optical fibre link works in nonlinear regime and the dispersion compensation is no longer ideal. Power penalties start to appear and their amplitudes increase with the optical incident power. Instead, the employment of incomplete dispersion compensation from a chirped fibre Bragg grating is recommended because it enhances the joint effect and leads to a further improvement in the frequency-length product.

For signal transmission in SSB modulated link, experimental and simulated results have shown that SSB modulation approach successfully eliminates the power penalty due to the fibre chromatic dispersion, however, only at low optical incident power. At higher power level, power fluctuation exists and the fluctuation amplitude increase with the optical incident power. This phenomenon attributes to the new frequencies generated by the interaction between fibre nonlinearity induced SPM and chromatic dispersion while the signal is travelling along the dispersive fibre. The dependency of power fluctuation on the optical incident power indicates that the mitigation of modulation suppression in high power SSB modulated link is SPM-dependent. These power fluctuations can be reduced by using a incomplete dispersion compensation from a chirped fibre Bragg grating. The residual dispersion magnitudes increase with the optical incident power and the length of fibre link, however, at the cost of having a higher standard deviation. Based on the investigations, the joint effect of fibre dispersion and fibre nonlinearity induced SPM effects in SSB modulated link must be taken into account in a high power SSB modulated RoF link in order to accurately characterise the signal propagation.

For the intermodulation performance of an amplitude modulated microwave/RF signal transmitted over a fibre optic link, investigations into the third order intermodulation distortion indicate that for a fixed fibre length, the TOI output can be improved by increasing the optical incident power level of the DSB and SSB modulated links. Generally, DSB modulation scheme provides a better system performance for the fibre link with shorter length as there is a peak of TOI output for certain fibre length at certain power level. This peak provides a way to optimise the system performance. On the other hand, simulation study in SSB modulated link has discovered that nonlinear effect induced in high power link causes TOI to have a depression point at around 82 km length of link. This has, again, concluded

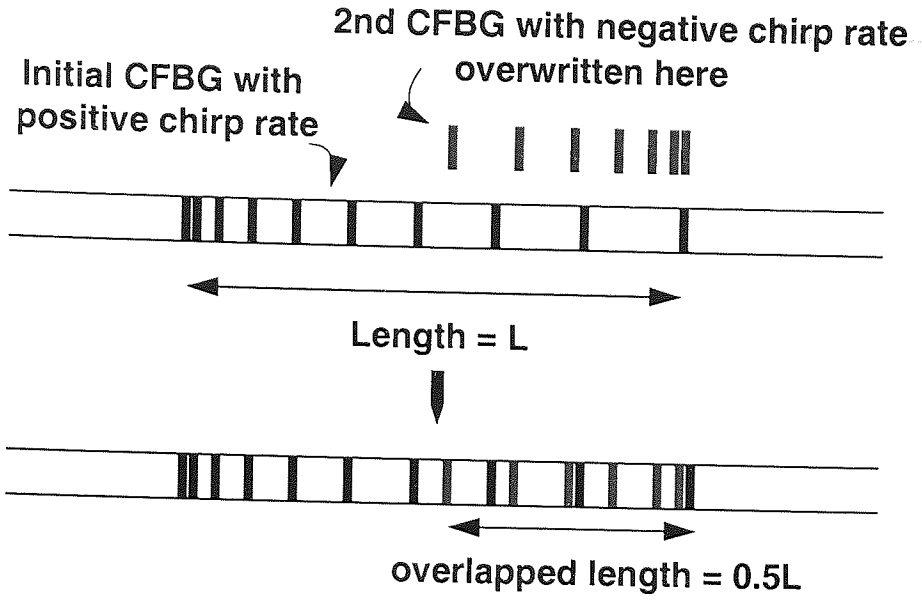

Figure 7.1: Structure of two overlapped gratings.

that nonlinear effect should be considered in designing and characterising high power fibre links when SSB modulation approach is used.

7.1 Future Work

7.1.1 Chirped Fibre Bragg Grating Temperature Sensor

It is important to point out that the concept of using chirped FBG (CFBG) for distributed temperature sensing applications is not restricted to the single-grating structure design. Different grating architectures based on CFBG can be implemented to improve the effectiveness of the measurements. An example of a simple extension to the concept is by overlapping a second CFBG of the opposite chirp rate over half of the first CFBG. The grating structure is illustrated schematically in figure 7.1. As can be seen, a grating of length of 35.0 mm and chirp rate of -0.35 nm/cm is superimposed over half of a CFBG (at the long wavelength side) of length of 70.0 mm with a chirp rate of 0.35 nm/mm. The spectral overlap between the two superimposed chirped gratings creates the distributed Fabry-Perot cavities that lead to the high interference fringes at the short wavelength side of the grating stopband. Taking note that the perturbations to the grating structure directly translate to cavity length variations of the distributed Fabry-Perot cavities within the grating structure, the length of the perturbed region can be computed by examining the variations of the free spectral ranges of the interference fringes. Similar data fitting and optimisation technique are then used to compute

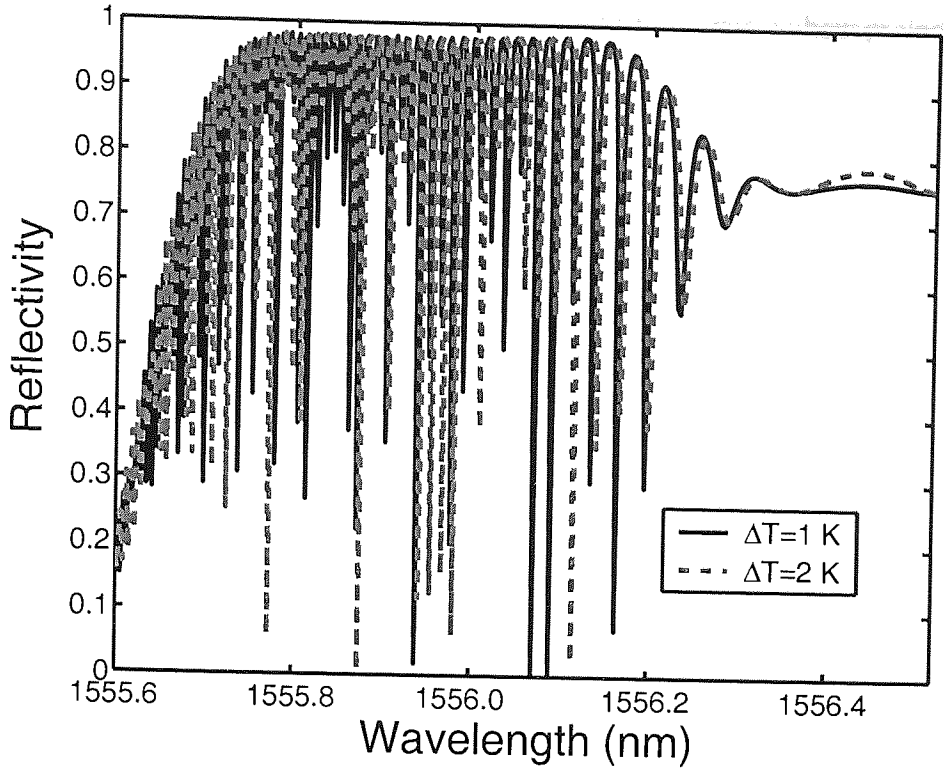

Figure 7.2: Reflection spectra of overlapped apodised CFBG with temperature change of 1 K (–) and 2 K (···). Note that only part of the reflection spectra is shown.

the temperature variations without the need for initial values in the optimisation algorithm. Simulation study was carried out by setting a 15.0 mm heat source with $\Delta T = 1.0°C$ at the centre section of the grating followed by another simulation with $\Delta T = 2.0°C$. The simulated spectral are shown in figure 7.2. It can be noticed that there is a clear variation between the two spectral by just a 1.0°C of difference. By observing the shifts between the two spectra and relating them with location and width of heat source, the values obtained can be used as the initial values for the synthesis models. This shows that this overlapped grating design can potentially be used to further improve the distributed temperature sensing system.

As mentioned in section 4.9.5, the coverage of the proposed distributed temperature sensing system depends on the length of the apodised CFBG. Certainly, the straightforward way to extend the coverage is to increase the length of the apodised CFBG. But, this will inevitably increases the duration for the optimised fitting process and reduces the accuracy due to the possibility of having long apodised CFBG with poor reflectivity. To extend the coverage without using a long apodised CFBG, a distributed architecture is suggested, in which a number of apodised CFBGs with different central wavelengths are placed at different locations on a piece of fibre. In this way, temperature change at any part of the fibre can be interrogated easily since the apodised CFBGs have different reflective wavelengths. This

architecture can be used to extend the coverage of the sensing system without prolonging the processing time and affecting the accuracy of the measurements.

7.1.2 High-Birefringence Optical Fibre Based Delay Line Filter

Since the wavelength-selective element in the filter configuration comprises of high-birefringence fibres and the spectral responses depend strongly on the birefringence of the fibres adopted, the physical size and simplicity of the filter configuration can be further improved by using photonic crystal fibres that exhibit very high birefringence. To have better control on the input and output azimuths of the launched light, commercially available tunable polariser, Hi-Bi fibre keyed connectors and precision rotators are recommended. Further investigations can also be done in the aspect of analysing the stress strength and the direction based on the analytical study in [29] as to have a more effective control on the coupling induced by the applied stress. By doing so, the filter structure can potentially enable better free spectral range adjustments as well as wavelength shiftings. Needless to say about the speed and performance of the filter reconfiguration will be greatly improved if controlled variations on the azimuths, the strengths and directions of stress can be achieved.

On the other hand, due to the fact that there are only three variable parameters in the proposed system, the delay line structure is restricted from producing every arbitrary profile needed for filtering system or more complex transfer functions. Further work can be done to overcome this limitation by increasing the number of variable input azimuths as well as the numbers of variable strengths and directions of the coupling stress. The increased number of variable parameters corresponds to the increased number of polarisation mode couplings/degenerations that subsequently leads to the increased number of optical taps in the filter structure. This structure, with more taps, can be realised by simply increasing the number of stress coupling points onto the Hi-Bi fibre. These higher order filters are anticipated to be able to produce wider flattop bandpass channels with enhanced sidelobe suppression.

7.1.3 Microwave/RF Signal Transmission in Nonlinear Dispersive RoF Links

As can be seen from the results obtained from the nonlinear transmission of microwave/RF signal in optical fibre, fibre dispersion interplays with fibre nonlinearity, giving interesting and remarkable responses. Further investigations can be carried out to explore the potential contributions of the joint effect of fibre dispersion and fibre nonlinearity to the radio-over-fibre links. Considering that the employment of dispersion compensation significantly affects

the performance of the transmission in nonlinear RoF links, the exact value required for every link length with different optical incident power needs to be investigated. Subsequently, a more adaptive scheme for controlling dispersion compensation is suggested to constantly provide the *in-situ* compensation to the links accounted for the changes of length, optical incident power and loss along the RoF links.

Apart from this, the intermodulation distortion of multi-tone system needs to be studied in more detail in order to solve, or perhaps to explore, the induced problems. Since dispersion compensation can be used to reduce the power fluctuations in the DSB and SSB transmission links carrying single microwave/RF modulated signal, integrating dispersion compensation into the two-tone system is anticipated to give a better intermodulation performance. Thus, further study is needed to explore this potential improvement. In addition, the impacts of fibre nonlinearity onto the frequency modulated RoF link as well as the real data transmission are the areas that are worth being investigated.

Bibliography

[1] A. D. Kersey, M. A. Davis, H. J. Patrick, M. LeBlanc, K. P. Koo, C. G. Askins, M. A. Putnam, and E. J. Friebele, "Fiber grating sensors," *IEEE Journal of Lightwave Technology*, vol. 15, no. 8, pp. 1442–1463, 1997.

[2] J. R. Forrest, "Communication networks for the new millennium," *IEEE Transactions on Microwave Theory and Techniques*, vol. 12, no. 47, pp. 2195–2201, 1999.

[3] M. Tsuchiya and T. Hoshida, "Nonlinear photodetection scheme and its system applications to fibre-optic millimetre-wave wireless down links," *IEEE Transactions on Microwave Theory and Techniques*, vol. 7, no. 47, pp. 1342–1350, 1999.

[4] J. Senior, *Optical Fiber Communications - Principles and Practice.* Prentice Hall, 1985.

[5] G. P. Agrawal, *Fiber-optic Communication Systems.* Wiley-Interscience, 2002.

[6] A. I. Gusarov, F. Berghmans, O. Deparis, A. F. Fernandez, Y. Defosse, P. Mégret, M. Décreton, and M. Blondel, "High total dose radiation effects on temperature sensing fiber Bragg gratings," *IEEE Photonics Technology Letters*, vol. 11, no. 9, pp. 1159–1161, 1999.

[7] J. Jung, H. Nam, B. Lee, J. O. Byun, and N. S. Kim, "Fiber Bragg grating temperature sensor with controllable sensitivity," *Applied Optics*, vol. 38, no. 13, pp. 2752–2754, 1999.

[8] K. Jackson, S. Newton, B. Moslehi, M. Tur, C. Cutler, J. Goodman, and H. J. Shaw, "Optical fiber delay-line signal processing," *IEEE Transactions on Microwave Theory and Techniques*, vol. 33, no. 3, pp. 193–210, 1985.

[9] B. Moslehi, "Fiber-optic filters employing optical amplifiers to provide design flexibility," *IEE Electronics Letters*, vol. 28, no. 3, pp. 226–228, 1992.

[10] S. Sales, J. Capmany, J. Marti, and D. Pastor, "Solutions to the synthesis problem of optical delay line filters," *Optics Letters*, vol. 20, no. 23, pp. 2438–2440, 1995.

[11] S. Tedjini, A. Ho-Quoc, and D. A. M. Khalil, "All-optical networks as microwave and millimeter-wave circuits," *IEEE Transactions on Microwave Theory and Techniques*, vol. 43, no. 9, pp. 2428–2434, 1995.

[12] European Radiocommunication Office, *url:www.efis.dk/search/general.*

[13] L. Noël, D. Wake, D. G. Moodie, D. D. Marcenac, L. D. Westbrook, and D. Nesset, "Novel techniques for high capacity 60 GHz fibre radio transmission systems," *IEEE Transactions on Microwave Theory and Techniques*, vol. 45, no. 8, pp. 1416–1423, 1997.

[14] J. O'Reilly and P. Lane, "Remote delivery of video services using mm-waves and optics," *IEEE Journal of Lightwave Technology*, vol. 12, no. 2, pp. 369–375, 1994.

[15] A. J. Seeds, "Microwave photonics," *Transactions on Microwave Theory and Techniques*, vol. 50, no. 3, pp. 877–887, 2002.

[16] G. P. Agrawal, *Fiber-Optics Communication Systems*, 3rd ed. John Wiley and Sons, 2002.

[17] I. Frigyes, A. Hilt, and S. Csernyin, "Investigations in microwave optical links-accent on QAM," in *International Topical Meeting on Microwave Photonics*, 2000, pp. 156–159.

[18] C. H. Cox, E. I. Ackerman, and G. E. Betts, "Relationship between gain and noise figure of an optical analog link," in *IEEE MTT-S International Microwave Symposium Digest*, vol. 3, 1996, pp. 1551–1554.

[19] G. P. Agrawal, *Nonlinear Fiber Optics*. Academic Press, 2001.

[20] H. Al-Raweshidy, *Radio over Fiber Technologies for Mobile Communications Networks*. Artech House, 2002.

[21] G. P. Agrawal, *Nonlinear Fiber Optics*. Academic Press, 2001.

[22] R. J. Mears, L. Reekie, I. M. Jauncy, and D. N. Payne, "High gain rare-earth doped fibre amplifier at 1.54 μm," in *Proceedings of Optical Fiber Communication Conference*, 1987, p. W11.

[23] R. J. Mears, L. Reekie, S. B. Poole, and D. N. Payne, "Low threshold tunable CW and Q-switched fibre laser operating at 1.55 μm," *IEE Electronics Letters*, vol. 22, no. 3, pp. 159–160, 1986.

[24] R. Kashyap, *Fiber Bragg Gratings*. Academic Press, 1999.

[25] D. N. Payne, A. J. Barlow, and J. J. R. Hansen, "Development of low- and high-birefringence optical fibers," *IEEE Journal of Quantum Electronics*, vol. QE-18, no. 4, pp. 477–488, 1982.

[26] W. Zhang, J. A. R. Williams, and I. Bennion, "Optical fibre delay line filter free of limitation imposed by optical coherence," *IEE Electronics Letters*, vol. 35, no. 24, pp. 2133–2134, 1999.

[27] M. Douay, T. Feng, P. Bernage, P. Niay, E. Delevaque, and T. Georges, "Birefringence effect of optical fiber laser with intracore fiber bragg grating," *IEEE Photonics Technology Letters*, vol. 4, no. 8, pp. 844–846, 1992.

[28] J. Hernandez-Cordero, V. A. Kozlov, A. L. G. Carter, and T. F. Morse, "Fiber laser polarization tuning using a bragg grating in a hi-bi fiber," *IEEE Photonics Technology Letters*, vol. 10, no. 7, pp. 941–943, 1998.

[29] T. H. Chua and C. Chen, "Fiber polarimetric stress sensors," *Applied Optics*, vol. 28, no. 15, pp. 3158–3165, 1989.

[30] J. Sakai and T. Kimura, "Birefringence and polarization characteristics of single-mode optical fibers under elastic deformations," *IEEE Journal of Quantum Electronics*, vol. QE-17, no. 6, pp. 1041–1051, 1981.

[31] G. Meslener, "Chromatic dispersion induced distortion of modulated monochromatic light employing direct detection," *IEEE Journal of Quantum Electronics*, vol. QE-20, no. 10, pp. 1208–1216, 1984.

[32] B. Christensen, J. Mark, G. Jacobsen, and E. Bødtker, "Simple dispersion measurement technique with high resolution," *IEE Electronics Letters*, vol. 29, no. 1, pp. 132–134, 1993.

[33] H. Schmuck, "Comparison of optical millimetre-wave concepts with regard to chromatic dispersion," *IEE Electronics Letters*, vol. 31, no. 21, pp. 1848–1849, 1995.

[34] F. Coppinger, S. Yegnanarayanan, P. Trinh, and B. Jalali, "Continuously tunable photonic radio-frequency notch filter," *IEEE Photonics Technology Letters*, vol. 9, no. 3, pp. 339–341, 1997.

[35] Y. R. Shen, *The Principles of Nonlinear Optics*. Wiley-Interscience, 1984.

[36] G. P. Agrawal, *Applications of Nonlinear Fiber Optics*. Academic Press, 2001.

[37] "www.fiber-optics.info/articles/nonlinearities.htm," 2004.

[38] V. E. Zakharov and A. B. Shabat, "Exact theory of two-dimensional self-focusing and one-dimensional self-modulation of waves in nonlinear media," *Soviet Physics JETP*, vol. 34, pp. 62–69, 1972.

[39] A. Hasegawa and F. Tappert, "Transmission of stationary nonlinear optical pulses in dispersive dielectric fibers I. Anomalous Dispersion," *Applied Physics Letters*, vol. 23, pp. 142–144, 1973.

[40] A. R. Chraplyvy, "Limitations on lightwave communications imposed by optical-fiber nonlinearities," *IEEE Journal of Lightwave Technology*, vol. 8, no. 10, pp. 1548–1557, 1990.

[41] K. O. Hill, Y. Fujii, D. C. Johnson, and B. S. Kawasaki, "Photosensitivity in optical waveguides: Application to reflection filter fabrication," *Applied Physics Letters*, vol. 32, no. 10, p. 647, 1978.

[42] W. W. Morey, G. Meltz, and W. H. Glen, "Fiber optic Bragg grating sensors," in *Proceedings of SPIE*, vol. 1169, 1989, pp. 98–107.

[43] S. Melle, T. Coroy, S. Karr, T. Alavie, and R. Measures, "Structural sensing using a fiber laser strain sensor," in *Proceedings of SPIE*, vol. 1798, 1992, pp. 227–236.

[44] E. Hecht, *Optics*. Addison-Wesley Longman, 2002.

[45] I. Bennion, J. A. R. Williams, L. Zhang, K. Sugden, and N. J. Doran, "UV-written in-fibre Bragg gratings," *Optical and Quantum Electronics*, no. 28, pp. 93–135, 1996.

[46] A. Othonos and K. Kalli, *Fiber Bragg Gratings-Fundamentals and Applications in Telecommunications and Sensing*. Artech House, 1999.

[47] K. Sugden, I. Bennion, A. Malony, and N. J. Copner, "Chirped gratings produced in photosensitive optical fibre by fibre deformation during exposure," *IEE Electronics Letters*, vol. 30, no. 5, pp. 440–442, 1994.

[48] B. Malo, K. O. Hill, F. Bilodeau, D. C. Johnson, and J. Albert, "Point-by-point fabrication of micro-bragg gratings in photosensitive fibre using single excimer pulse refractive index modification techniques," *IEE Electronics Letters*, vol. 29, no. 18, pp. 1668–1669, 1993.

[49] A. Martinez, M. Dubov, I. Khrushchev, and I. Bennion, "Direct writing of fibre bragg gratings by femtosecond laser," *IEE Electronics Letters*, vol. 40, no. 19, pp. 1170–1172, 2004.

[50] A. Martinez, I. Y. Khrushchev, and I. Bennion, "Thermal properties of fibre Bragg gratings inscribed point-by-point by infrared femtosecond laser," *IEE Electronics Letters*, vol. 41, no. 4, pp. 176–177, 2005.

[51] K. O. Hill, B. Malo, F. Bilodeau, D. C. Johnson, and J. Albert, "Bragg grating fabricated in monomode photosensitive optical fibre by UV exposure through a phase mask," *Applied Physics Letters*, vol. 62, no. 10, pp. 1035–1037, 1993.

[52] D. Z. Anderson, V. Mizrahi, T. Erdogan, and A. E. White, "Production of in-fibre grating using a diffractive element," *IEE Electronics Letters*, vol. 29, no. 6, pp. 566–568, 1993.

[53] J. D. Prohaska, E. Snitzer, S. Rishton, and V. Boegli, "Magnification off mask fabricated fiber Bragg gratings," *IEE Electronics Letters*, vol. 29, no. 18, pp. 1614–1615, 1993.

[54] R. J. Campbell and R. Kashyap, "Spectral profile and multiplexing of Bragg gratings in photosensitive fiber," *Optics Letters*, vol. 16, no. 12, pp. 898–900, 1991.

[55] Q. Zhang, D. A. Brown, L. Reinhart, T. F. Morse, J. Q. Wang, and G. Xiao, "Tuning Bragg wavelength by writing gratings on prestrained fibers," *IEEE Photonics Technological Letters*, vol. 6, no. 7, pp. 839–841, 1994.

[56] W. H. Loh, M. J. Cole, M. N. Zervas, S. Barcelos, and R. I. Laming, "Complex grating structures with uniform phase mask based on the moving fibre-scanning beam technique," *Optics Letters*, vol. 20, no. 20, pp. 2051–2053, 1995.

[57] M. J. Cole, W. H. Loh, R. I. Laming, M. N. Zervas, and S. Barcelos, "Moving fibre/phase mask scanning beam technique for enhanced flexibility in producing fibre gratings with uniform phase mask," *IEE Electronics Letters*, vol. 31, no. 17, pp. 1488–1490, 1995.

[58] K. C. Byron, K. Sugden, T. Bircheno, and I. Bennion, "Fabrication of chirped Bragg gratings in photosensitive fibre," *IEE Electronics Letters*, vol. 29, no. 18, pp. 1659–1660, 1993.

[59] M. C. Farries, K. Sugden, D. C. J. Reid, I. Bennion, A. Molony, and M. J. Goodwin, "Very broad reflection bandwidth (44 nm) chirped fibre gratings and narrow-bandpass filters produced by the use of an amplitude mask," *IEE Electronics Letters*, vol. 30, no. 11, pp. 891–892, 1994.

[60] Y. Liu, "Advanced fibre gratings and their applications," Ph.D. dissertation, Aston University, April 2001.

[61] R. I. Laming, M. Ibsen, M. Durkin, M. J. Cole, M. N. Zervas, K. E. Ennser, and V. Gusmeroli, "Dispersion compensation gratings," in *Bragg gratings, Photosensitivity and Poling in Glass Fibers and Waveguides: Applications and Fundamentals*, vol. 17, 1997, pp. 271–273.

[62] W. H. Loh, R. I. Laming, N. Robinson, A. Cavaciuti, F. Vaninetti, C. J. Anderson, M. N. Zervas, and M. J. Cole, "Dispersion compensation over distances in excess of 500 km for 10 Gb/s systems using chirped fibre gratings," *IEEE Photonics Technology Letters*, vol. 8, no. 7, p. 944, 1996.

[63] L. D. Garrette, A. H. Gnauck, Forgherieri, and D. Socrano, "8×20 Gb/s-315 km–480 km WDM transmission over conventional fiber using multiple broadband fiber gratings," in *Technical Digest of Conference on Optical Fiber Communication*, 1998, pp. 1–4.

[64] A. Boskovic, M. J. Guy, S. V. Chernikov, J. R. Taylor, and R. Kashyap, "All-fiber diode pumped, femtosecond chirped pulse amplification system," *IEE Electronics Letters*, vol. 31, no. 11, pp. 877–879, 1995.

[65] P. Gunning, R. Kashyap, A. S. Sidiqui, and K. Smith, "Picosecond pulse generation of <5 ps from gain-switched DFB semiconductor laser diode using linearly step-chirped fiber grating," *IEE Electronics Letters*, vol. 31, no. 13, pp. 1066–1067, 1995.

[66] A. D. Kersey and M. A. Davis, "Interferometric fiber sensor with a chirped grating distributed sensor element," in *Proceedings of OFC*, 1994, pp. 319–322.

[67] J. A. R. Williams, I. Bennion, and N. J. Doran, "The design of in-fiber Bragg grating systems for cubic and quadratic dispersion compensation," in *Optical Communication*, vol. 116, 1995, pp. 62–66.

[68] L. Zhang, K. Sugden, J. A. R. Williams, and I. Bennion, "Post fabrication exposure of gap-type bandpass filters in broadly chirped fiber gratings," *Optics Letters*, vol. 20, no. 18, pp. 1927–1929, 1995.

[69] M. H. Sun, K. A. Wickersheim, and J. Kim, "Fiber-optic temperature sensors in the medical setting," in *Proceedings of SPIE*, vol. 1067, 1989, pp. 15–21.

[70] J. Castrellon, G. Paez, and M. Strojnik, "Remote temperature sensor employing erbium-doped silica fiber," *Infrared Physics and Technology*, vol. 43, pp. 219–222, 2002.

[71] R. A. Wolthuis, G. L. Mitchell, E. Saaski, J. C. Hartl, and A. Afromowitz, "Development of medical pressure and temperature sensors employing optical spectrum modulation," *IEEE Transactions on Biomedical Engineering*, vol. 38, no. 10, pp. 974–981, 1991.

[72] D. A. Jackson and J. D. C. Jones, "Optical fiber sensors," *Optical Acta*, vol. 33, pp. 1469–1503, 1987.

[73] S. Huang, M. Ohn, and R. Measures, "Phase-based Bragg intragrating distributed strain sensor," *Applied Optics*, vol. 35, no. 7, pp. 1135–1142, 1996.

[74] M. LeBlanc, S. Y. Huang, M. Ohn, and R. M. Measures, "Distributed strain measurement based on a fiber Bragg grating and its reflection spectrum analysis," *Optics Letters*, vol. 21, no. 17, pp. 1405–1407, 1996.

[75] M. Volanthen, H. Geiger, M. J. Cole, and J. P. Dakin, "Measurement of arbitrary strain profiles within fibre gratings," *IEE Electronics Letters*, vol. 32, no. 11, pp. 1028–1029, 1996.

[76] M. M. Ohn, S. Y. Huang, R. M. Measures, and J. Chwang, "Arbitrary strain profile measurement within fibre gratings using interferometric Fourier transform technique," *IEE Electronics Letters*, vol. 33, no. 14, pp. 1242–1243, 1997.

[77] G. Duck and M. Ohn, "Distributed Bragg grating sensing with a direct group-delay measurement technique," *Optics Letters*, vol. 24, no. 2, pp. 90–92, 2000.

[78] M. A. Muriel, J. Azana, and A. Carballar, "Fiber gratings synthesis by use of time-frequency representations," *Optics Letters*, vol. 23, no. 19, pp. 1526–1528, 1998.

[79] R. Feced, M. N. Zervas, and M. M. Muriel, "An efficient inverse scattering algorithm for the design of nonuniform fiber Bragg gratings," *IEEE Journal of Quantum Electronics*, vol. 35, no. 8, pp. 1105–1115, 1999.

[80] J. Azana and M. A. Muriel, "Reconstructing arbitrary strain distributions within fiber gratings by time-frequency signal analysis," *Optics Letters*, vol. 25, no. 10, pp. 698–700, 2000.

[81] J. Azana, M. A. Muriel, L. R. Chen, and P. W. E. Smith, "Fiber Bragg grating period reconstruction using time-frequency signal analysis and application to distributed sensing," *IEEE Journal of Lightwave Technology*, vol. 19, no. 5, pp. 646–654, 2001.

[82] J. Azana and M. A. Muriel, "Reconstruction of fiber grating period profiles by use of Wigner-Ville distributions and spectrograms," *Journal of the Optical Society of America A*, vol. 17, no. 12, pp. 2496–2505, 2000.

[83] F. Casagrande, P. Crespi, A. M. Grassi, A. Lulli, R. P. Kenny, and M. P. Whelan, "From the reflected spectrum to the properties of a fiber Bragg grating: a genetic algorithm approach with application to distributed strain sensing," *Applied Optics*, vol. 41, no. 25, pp. 5238–5244, 2002.

[84] Y.-L. Lo and H.-C. Cheng, "Arbitrary distributed strain sensing technique with genetic algorithm by using two fiber Bragg gratings," in *16th Optical Fiber Sensors Conference Technical Digest*, 2003, pp. 368–371.

[85] J. Skaar, L. Wang, and T. Erdogan, "On the synthesis of fiber Bragg gratings by layer peeling," *IEEE Journal of Quantum Electronics*, vol. 37, no. 2, pp. 165–173, 2001.

[86] P. L. Swart, A. P. Kotze, and B. M. Lacquet, "Effects of the nature of the starting population on the properties of rugate filters designed with the genetic algorithm," *IEEE Journal of Lightwave Technology*, vol. 18, pp. 853–859, 2000.

[87] F. Lhommé, C. Caucheteur, K. Chah, M. Blondel, and P. Mégret, "Synthesis of fiber Bragg grating parameters from experimental reflectivity: a simplex approach and its application to the determination of temperature-dependent properties," *Applied Optics*, vol. 44, no. 4, pp. 493–497, 2005.

[88] P. C. Won, J. Leng, Y. Lai, and J. A. R. Williams, "Distributed temperature sensing using a chirped fibre bragg grating," *Measurement Science and Technology*, vol. 15, pp. 1501–1505, 2004.

[89] American Brain Tumour Association, *url:www.abta.org*.

[90] A. B. L. Ribeiro, Y. J. Rao, L. Zhang, I. Bennion, and D. A. Jackson, "A combined spatial- and time-division-multiplexing tree topology for fiber grating sensor systems," *Applied Optics*, vol. 35, pp. 2267–2273, 1996.

[91] K. Wilner and A. P. V. D. Heuvel, "Fiber-optic delay lines for microwave signal processing," in *Proceedings of IEEE*, vol. 64, 1976, pp. 805–807.

[92] C. Chang, J. A. Cassaboom, and H. F. Taylor, "Fibre optic delay line devices for RF signal processing," *IEE Electronics Letters*, vol. 13, pp. 678–680, 1977.

[93] H. F. Taylor, "Fiber and integrated optical devices for signal processing," in *Proceedings of SPIE*, vol. 176, 1979, pp. 17–27.

[94] D. B. Hunter and R. A. Minasian, "Photonic signal processing of microwave signals using an active-fiber Bragg-grating-pair structure," *IEEE Transactions on Microwave Theory and Techniques*, vol. 45, no. 8, pp. 1463–1466, 1997.

[95] D. Pastor and J. Capmany, "Fiber optical tunable transversal filter using laser array and linearly chirped fiber grating," *IEE Electronics Letters*, vol. 34, no. 17, pp. 1684–1685, 1998.

[96] J. Capmany, J. Cascón, D. Pastor, and B. Ortega, "Reconfigurable fiber-optic delay line filters incorporating electrooptic and electroabsorption modulators," *IEEE Photonics Technology Letters*, vol. 11, no. 9, pp. 1174–1176, 1999.

[97] J. Capmany, D. Pastor, A. Martinez, B. Ortega, and S. Sales, "Microwave photonic filters with negative coefficients based on phase inversion in an electro-optic modulator," *Optics Letters*, vol. 28, no. 16, pp. 1415–1417, 2003.

[98] K. P. Jackson, J. E. Bowers, S. A. Newton, and C. C. Cutler, "Microbend optical fibre tapped delay line for gigahertz signal processing," *Applied Physics Letters*, vol. 41, p. 139, 1982.

[99] B. Moslehi, J. W. Goodman, and M. T. H. J. Shaw, "Fibre optic lattice signal processing," in *Proceedings of IEEE*, vol. 72, 1984, p. 909.

[100] W. Zhang, J. A. R. Williams, and I. Bennion, "Polarization synthesized optical transversal filter employing high birefringence fiber gratings," *IEEE Photonics Technology Letters*, vol. 13, no. 5, pp. 523–525, 2001.

[101] Y. Lai, W. Zhang, and J. A. R. Williams, "All fibre multichannel flattop filter based on coherent fibre delay line structure," *IEE Electronics Letters*, vol. 38, no. 10, pp. 473–474, 2002.

[102] I. P. Kaminow, "Polarization in optical fibers," *IEEE Journal of Quantum Electronics*, vol. QE-17, no. 1, pp. 15–22, 1981.

[103] M. Tsubokawa, T. Higashi, and Y. Negishi, "Mode couplings due to external forces distributed along a polarization-maintaining fiber: an evaluation," *Applied Optics*, vol. 27, no. 1, pp. 166–173, 1988.

[104] S. C. Rashleigh, "Origin and control of polarization effects in single-mode fibers," *IEEE Journal of Lightwave Technology*, vol. LT-1, no. 2, pp. 312–331, 1983.

[105] S. Sales, J. Capmany, J. Marti, and D. Pastor, "Experimental demonstration of fibre-optic delay line filter with negative coefficients," *IEE Electronics Letters*, vol. 31, no. 13, pp. 1095–1096, 1995.

[106] S. Komaki, K. Tsukamoto, and M. Okada, "Requirements for radio-wave photonic devices from the viewpoint of future mobile radio system," *IEEE Transactions of Microwave Theory Technology*, vol. 43, pp. 2222–2228, 1995.

[107] J. Park, A. F. Elrefaie, and K. Y. Lau, "1550 nm transmission of digitally modulated 28 GHz subcarriers over 77 km of nondispersion shifted fiber," *IEEE Photonics Technology Letters*, vol. 9, no. 2, pp. 256–258, 1997.

[108] G. H. Smith, D. Novak, and Z. Ahmed, "Technique for optical SSB generation to overcome dispersion penalties in fibre-radio systems," *IEE Electronics Letters*, vol. 33, no. 1, pp. 74–75, 1997.

[109] J. Marti, J. M. Fuster, and R. I. Laming, "Experimental reduction of chromatic dispersion effects in lightwave microwave/millimetre-wave transmissions using tapered linearly fibre gratings," *IEE Electronics Letters*, vol. 33, no. 13, pp. 1170–1171, 1997.

[110] F. Ouellette, "Dispersion cancellation using linearly chirped bragg grating filters in optical waveguides," *Optics Letters*, vol. 12, no. 10, pp. 847–849, 1987.

[111] W. Zhang, J. A. R. Williams, L. A. Everall, L. Zhang, and I. Bennion, "Investigation of fibre grating single sideband filtering in radio-fibre system," in *Proceeding of Conference on Lasers and Electro-Optics*, 1999, pp. 133–134.

[112] G. H. Smith, D. Novak, and Z. Ahmed, "Overcoming chromatic-dispersion effects in fiber-wireless systems incorporating external modulators," *IEEE Transactions of Microwave Theory Technology*, vol. 45, pp. 1410–1415, 1997.

[113] H. Ibrahim, J. F. Bayon, A. Madani, J. Moalic, L. Rivoallan, D. Ronarc'h, and E. le Coquil, "Fiber-equaliser second order distortion compensation in 1.55 μm lightwave CATV transmission system," *IEE Electronics Letters*, vol. 29, no. 3, pp. 315–317, 1993.

[114] V. Polo, J. Marti, F. Ramos, and D. Moodie, "Mitigation of chromatic dispersion effects employing electroabsorption modulator-based transmitters," *IEEE Photonics Technology Letters*, vol. 11, no. 7, pp. 883–885, 1999.

[115] H. Sotobayashi and K. Kitayama, "Cancellation of the signal fading for 60 GHz subcarrier multiplexed optical DSB signal transmission in nondispersion shifted fiber using midway optical phase conjugation," *IEEE Journal of Lightwave Technology*, vol. 17, no. 12, pp. 2488–2497, 1999.

[116] J. Marti, F. Ramos, and J. Herrera, "Experimental reduction of dispersion-induced effects in microwave optical links employing SOA boosters," *IEEE Photonics Technology Letters*, vol. 13, no. 9, pp. 999–1001, 2001.

[117] D. Jeon, H. Jung, and S. Han, "Mitigation of dispersion-induced effects using SOA in analog optical transmission," *IEEE Photonics Technology Letters*, vol. 14, no. 8, pp. 1166–1168, 2002.

[118] J. A. J. Fells, M. A. Gibbon, I. H. White, G. H. B. Thompson, R. V. Penty, E. M. Kimber, D. J. Moule, and E. J. Thrush, "Transmission beyond the dispersion limit using a negative chirp electroabsorption modulator," *IEE Electronics Letters*, vol. 30, no. 14, pp. 1168–1169, 1994.

[119] J. C. Cartledge and B. Christensen, "Optimum operating points for electroabsorption modulators in 10 Gb/s transmission systems using nondispersion shifted fiber," *IEEE Journal of Lightwave Technology*, vol. 10, pp. 349–357, 1998.

[120] J. Wang and K. Petermann, "Small signal analysis for dispersive optical fiber communication systems," *IEEE Journal of Lightwave Technology*, vol. 10, no. 1, pp. 96–100, 1992.

[121] F. Ramos, J. Marti, V. Polo, and J. M. Fuster, "On the use fiber-induced self-phase modulation to reduce chromatic dispersion effects in microwave/millimeter-wave optical systems," *IEEE Photonics Technology Letters*, vol. 10, no. 10, pp. 1473–1475, 1998.

[122] I. Frigyes, Z. Várallyay, O. Schwelb, L. Jakab, and P. Richter, "Investigation in the joint effect of fiber dispersion and nonlinear refraction in microwave optical links," in *International Topical Meeting on Microwave Photonics*, 2003, pp. 299–302.

[123] F. Ramos, J. Marti, and V. Polo, "Compensation of chromatic dispersion effects in microwave/millimeter-wave optical systems using four-wave-mixing induced in dispersion-shifted fibers," *IEEE Photonics Technology Letters*, vol. 11, no. 9, pp. 1171–1173, 1999.

[124] F. Ramos and J. Marti, "Frequency transfer function of dispersive and nonlinear single-mode optical fibers in microwave optical systems," *IEEE Photonics Technology Letters*, vol. 12, no. 5, pp. 549–551, 2000.

[125] A. V. T. Cartaxo, B. Wedding, and W. Idler, "Influence of fiber nonlinearity on the fiber transfer function: theoretical and experimental analysis," *IEEE Journal of Lightwave Technology*, vol. 17, no. 10, pp. 1806–1813, 1999.

[126] F. W. Willems, W. Muys, and J. S. Leong, "Simultaneous suppression of stimulated Brillouin scattering and interferometric noise in externally modulated lightwave AM-SCM systems," *IEEE Photonics Technology Letters*, vol. 6, no. 12, pp. 1476–1479, 1994.

[127] D. Pastor, J. Capmany, D. Ortega, V. Tatay, and J. Marti, "Design of apodized linearly chirped fiber gratings for dispersion compensation," *IEEE Journal of Lightwave Technology*, vol. 14, no. 11, pp. 2581–2588, 1996.

[128] K. Ennser, M. Ibsen, M. Durkin, M. N. Zervas, and R. I. Laming, "Influence of non-ideal chirped fiber grating characteristics on dispersion cancellation," *IEEE Photonics Technology Letters*, vol. 10, no. 10, pp. 1476–1478, 2003.

[129] S. Bonino, M. Norgia, and E. Riccardi, "Spectral behaviour analysis of chirped fibre Bragg gratings for optical dispersion compensation," in *Proceedings of European Conference on Optical Communications*, 1997, pp. 194–197.

[130] F. Ramos and J. Marti, "Influence of non-ideal chirped fibre grating characteristics on dispersion-compensated analogue optical links in presence of fibre-induced SPM," *IEE Electronics Letters*, vol. 39, no. 4, pp. 353–354, 2003.

[131] ——, "Comparison of optical single-sideband modulation and chirped fiber gratings as dispersion mitigating techniques in optical millimeter-wave multichannel systems," *IEEE Photonics Technology Letters*, vol. 11, no. 11, pp. 1479–1481, 1999.

[132] A. Loayssa, D. Benito, and M. J. Garde, "Single-sideband suppressed-carrier modulation using a single-electrode electro-optic modulator," *IEEE Photonics Technology Letters*, vol. 13, no. 8, pp. 869–871, 2001.

[133] M. R. Philips, T. E. Darcie, D. Marcuse, G. E. Bodeep, and N. J. Frigo, "Nonlinear distortion generated by dispersive transmission of chirped intensity-modulated signals," *IEEE Photonics Technology Letters*, vol. 3, no. 5, pp. 481–483, 1991.

[134] E. E. Bergman, C. Y. Kuo, and S. Y. Huang, "Dispersion-induced composite second-order distortion at 1.5 μm," *IEEE Photonics Technology Letters*, vol. 3, pp. 59–61, 1999.

[135] B. Wilson, Z. Ghassemlooy, and I. Darwazeh, *Analogue Optical Fibre Communications*. The Institution of Electrical Engineers, 1995.

[136] P. C. Won and J. A. R. Williams, "Third order intermodulation products generated on transmission through a nonlinear radio-on-fibre link," *IEE Electronics Letters*, vol. 40, pp. 1290–1291, 2004.

List of Publications

1 **P. C. Won**, L. K. Seah and A. Asundi, "FMCW reflectometric optical fiber strain sensor", 2^{nd} *International Conference on Experimental Mechanics (ICEM)*. Proceedings of SPIE, V. 4317, pp. 217–222, Singapore, 2001.

2 **P. C. Won**, L. K. Seah and A. Asundi, "FMCW reflectometric optical fiber strain sensor", *SPIE's* 8^{th} *Symposium on Smart Structures and Materials*. Proceedings of SPIE, V. 4328, pp. 54–62, Los Angeles, USA, 2001.

3 L. K. Seah and **P. C. Won**, "Distributed FMCW reflectometric optical fiber strain sensor", *Optical Engineering for Sensing and Nanotechnology (ICOSN)*, Proceedings of SPIE, V. 4416, pp. 66–69, Yokohama, Japan, 2001.

4 **P. C. Won**, L. K. Seah and G. Xie, "Quasi-distributed FMCW reflectometric optical fibre strain sensor", *Optical Engineering of SPIE*, V. 41 (4), pp. 788–795, 2002.

5 L. K. Seah and **P. C. Won**, "Distributed strain sensing using frequency-modulated continuous-wave reflectometric optical technique", *Experimental Mechanics of Society of Experimental Mechanics*, V. 42 (3), pp. 288–294, 2002.

6 **P. C. Won**, J. Leng, Y. Lai and J. A. R. Williams. "Distributed Temperature Sensing Based on a Chirped Fibre Bragg Grating", *Institute of Physics Meeting on In-fibre Gratings and Special Fibres (Photonex'03)*, Stoneleigh, Warwickshire, UK, 2003.

7 **P. C. Won**, J. Leng, Y. Lai and J. A. R. Williams. "Determination of Localised Temperature Changes using a Chirped Fibre Bragg Grating", 16^{th} *International Conference of Optical Fiber Sensors (OFS-16)*, pp. 244–247, Nara, Japan, 2003.

8 **P. C. Won**, J. Leng, Y. Lai and J. A. R. Williams. "Distributed Temperature Sensing Using a Chirped Fibre Bragg Grating", *Measurement Science and Technology*, V. 15, pp. 1501–1505, 2004.

9 **P. C. Won**, W. Zhang, J. A. R. Williams and I. Bennion. "Reconfigurable Fiber-Optic Delay Line Filter Based on Polarisation Mode Coupling", 17^{th} *Annual Meeting of IEEE Lasers and Electro-optics Society (LEOS 2004)*, V. 1, pp. 272–273, Puerto Rico, 2004.

10 **P. C. Won** and J. A. R. Williams. "Third Order Intermodulation Products Generated on Transmission through a Nonlinear Radio-on-fibre Link", *IEE Electronics Letters*, V. 40 (20), pp. 1290–1291, 2004.

11 **P. C. Won** and J. A. R. Williams. "RF Signal Transmission in Nonlinear Dispersive Optical Fibre", *"Summer School on Optical Architectures For RF Signal, Processing and Signal Mixing" by European Union funded IST Project NEFERTITI*, Zaragoza, Spain, 2004.

12 **P. C. Won**, W. Zhang, J. A. R. Williams and I. Bennion. "Third Order Intermodulation in Nonlinear Dispersive Radio-on-Fiber Links", *Conference on Lasers and Electro-Optics 2005 (CLEO 2005)*, JThE47, Baltimore, Maryland, USA, 2005.

13 **P. C. Won**, W. Zhang, J. A. R. Williams and I. Bennion. "Imperfect Mitigation of Dispersion Induced Power Penalty in High Power Single-sideband Modulated Radio-on-Fiber Links", *Conference on Lasers and Electro-Optics 2005 (CLEO 2005)*, JThE61, Baltimore, Maryland, USA, 2005.

14 **P. C. Won**, W. Zhang and J. A. R. Williams. "Self-Phase Modulation Dependent Dispersion Mitigation in High Power Single-sideband Modulated Radio-on-fiber Links", 12^{th} *"Photonics in Wireless Communication" by European Union funded IST Project NEFERTITI*, Gotebörg, Sweden, 2005.

15 **P. C. Won**, W. Zhang, J. A. R. Williams and I. Bennion. "Investigation on Nonlinear Effect in High Power Single-Sideband Modulated Radio-on-Fiber Links", *Australian Conference on Optical Fibre Technology 2005 (ACOFT 2005)*, WED-WON, Sydney, Australia, 2005.